FORMATION OF SMALL-SCALE IRREGULARITIES IN THE AURORAL E REGION

A THESIS

SUBMITTED TO THE COLLEGE OF GRADUATE STUDIES AND RESEARCH

IN PARTIAL FULFILLMENT OF THE REQUIREMENTS

FOR THE DEGREE OF

DOCTOR OF PHILOSOPHY

IN THE

DEPARTMENT OF PHYSICS AND ENGINEERING PHYSICS

UNIVERSITY OF SASKATCHEWAN

SASKATOON

By

Roman Makarevitch

Spring 2003

Permission to Use

In presenting this thesis in partial fulfilment of the requirements for a Postgraduate degree from the University of Saskatchewan, I agree that the Libraries of this University may make it freely available for inspection. I further agree that permission for copying of this thesis in any manner, in whole or in part, for scholarly purposes may be granted by the professor or professors who supervised my thesis work or, in their absence, by the Head of the Department or the Dean of the College in which my thesis work was done. It is understood that any copying or publication or use of this thesis or parts thereof for financial gain shall not be allowed without my written permission. It is also understood that due recognition shall be given to me and to the University of Saskatchewan in any scholarly use which may be made of any material in my thesis.

Requests for permission to copy or to make other use of material in this thesis in whole or part should be addressed to:

Head of the Department of Physics and Engineering Physics
University of Saskatchewan
Saskatoon, Saskatchewan
Canada S7N 5E2

Abstract

In this thesis, knowledge on the production mechanisms of small scale (meter and decameter) irregularities in the auroral E region is advanced, both theoretically and experimentally.

In the theoretical part of the thesis, the linear fluid theory of the Farley-Buneman (F-B) and gradient drift (G-D) plasma instabilities is considered. A general 2-D dispersion equation is derived and analyzed. Then, a review of existing nonlinear theories is given. The thrust is on the theory predictions with respect to the phase velocity of plasma waves. As an expansion of the theory, one new effect in the F-B instability evolution is considered, a secondary instability of a turbulent background of the primary F-B waves. It is shown that in a system of F-B modes the energy can flow from the short-wavelength (primary) to long-wavelength (secondary) structures (inverse cascade), contrary to the currently dominating idea that the energy of unstable waves is transferred to the smaller-scale structures. The phase velocity of the secondary waves propagating along the electron flow was found to be close to the electron streaming velocity and not saturated at the ion acoustic speed of the plasma. A possibility of decameter wave generation through this mechanism is envisioned.

Experimentally, data of 2 separate experiments carried out in the auroral E region to study phase velocity of meter and decameter irregularities are considered. First, nearly simultaneous measurements of two Super Dual Auroral Radar Network (SuperDARN) HF radars (12 MHz, scatter from decameter waves, $\lambda = 12$ m) and one VHF radar (50 MHz, scatter from meter waves, $\lambda = 3$ m) at the Antarctic Syowa station are compared. It is demonstrated that HF echoes exhibit quite different characteristics as compared to VHF echoes so that HF echoes with low (< 350 m s^{-1}) and high (> 350 m s^{-1}) Doppler velocities are proposed to consider separately. Observations indicate that the high-velocity HF echoes exhibit properties similar to VHF echoes while the low-velocity HF echoes do not have a VHF counterpart. Other echo characteristics are also studied. For example, the preferential direction for the HF echo occurrence was found to be shifted by 45° from the direction of the electron flow and this shift was related to the existence of the low-velocity echoes in the data statistics. In the

second experiment, the characteristics of decameter irregularities at 5 very close scales (between 10 and 16 m) are investigated by considering SuperDARN observations at Prince George, British Columbia, Canada. It is shown that the measured Doppler velocity (and hence the phase velocity of plasma waves) depends on the irregularity scale but only for irregularities propagating within the F-B instability cone. For these directions, the phase velocity was also found to decrease with the aspect angle and the rate of the decrease was found to be scale sensitive. Very little velocity variation with the aspect angle was discovered for observations outside of the F-B instability cone. Several factors potentially contributing to the observed HF and VHF echo characteristics in both experiments are identified and discussed. These are the geophysical conditions during measurements (details of large-scale convection patterns, a possibility of scatter from meteor trails), propagation effects (focusing of the HF radio waves onto various parts of the electrojet layer) and the plasma physics of irregularity formation (effects of strong gradients of the background electron density, ion and neutral particle motions, mode coupling, anomalous collisions). It is argued that the high-velocity HF echoes and VHF echoes are generated through traditional F-B and G-D instabilities, while the low-velocity HF echoes can have additional sources. Finally, several suggestions for further research are presented.

Acknowledgements

This thesis has only been made possible thanks to the outstanding supervision of Dr. Sasha Koustov. His influence has been enormous, his support omnipresent, and his guidance invaluable. To work with him has been a great fun and tremendous challenge. I would like also to express my sincere gratitude to my co-supervisor Dr. Andrei Smolyakov for his time and effort to make me understand the theory better; Dr. George Sofko for his support of my work and insightful contributions; Dr. Jean-Pierre St.-Maurice for his helpful comments and suggestions during my PhD studies; Dr. Glenn Hussey for his genuine interest, help, and advice; Dr. Christos Haldoupis for numerous discussions, criticism, and also for giving me the opportunity to present some results of this study. Many thanks go to my fellow doctoral students Don Danskin, Leo Benkevitch, and Yuriy Tyshetskiy for creating a very special stimulating environment I was broiling in. I also appreciate all the help I got from the colleagues in the SuperDARN group, Institute of Space and Atmospheric Studies, and Department of Physics and Engineering Physics at the University of Saskatchewan.

Financial support, for which I am grateful, was provided from the NSERC Team Research Grant, the University of Saskatchewan Graduate Studies PhD Scholarship, and the J. S. Kim Graduate Scholarship. My special thanks for the extensive financial support from the Gerhard Herzberg Fund in the form of Gerhard Herzberg Memorial Scholarships and Travel Award.

To my family: Mom, Dad, and my little sister, who have been a constant source of support, encouragement, and inspiration I wish to say my fondest, greatest and dearest thanks.

Contents

List of Tables

List of Figures

List of Abbreviations

ACF	Auto-Correlation Function
CRL	Communications Research Laboratory
CUTLASS	Co-ordinated UK Twin-Located Auroral Sounding System
CW	Continuous Wave
DIA	Direct Interaction Approximation
DMSP	Defense Meteorologic Satellite Program
EDQNM	Eddy-Damped Quasi-Normal Markovian
EIC	Electrostatic Ion Cyclotron
EISCAT	European Incoherent Scatter
F-B	Farley-Buneman
FFT	Fast Fourier Transform
FOV	Field of View
IGY	International Geophysical Year
IMF	Interplanetary Magnetic Field

IRI	International Reference Ionosphere
IZMEM	Institute of Terrestrial Magnetism, Ionosphere and Radiowave Propagation
G-D	gradient drift
HF	High Frequency
MF	Medium Frequency
MLT	Magnetic Local Time
NIPR	National Institute of Polar Research
PACE	Polar Anglo-American Conjugate Experiment
PG	Prince George
PMSE	Polar Mesospheric Summer Echoes
SABRE	Sweden And Britain Radar Experiment
SHERPA	Systeme HF d'Etudes Radar Polaires et Aurorales
STARE	Scandinavian Twin Auroral Radar Experiment
SuperDARN	Super Dual Auroral Radar Network
UHF	Ultra High Frequency
UT	Universal Time
VHF	Very High Frequency

Chapter 1

Introduction

1.1 Solar-Terrestrial Environment

In this thesis we study the small-scale structures in the Earth's ionosphere, the weakly ionized plasma that envelops the Earth. When studying the physics of the Earth's ionosphere one should always have in mind that the ionosphere is just one part of a more global formation called the *solar-terrestrial environment*, which is generally considered to consist of the solar wind, magnetosphere and ionosphere, as shown in Figure 1.1.

Hot charged particles from the Sun's outermost region, corona, form the flow of fully-ionized plasma streaming radially in every direction. This flow, known as the *solar wind*, is highly conductive and carries the so called *Interplanetary Magnetic Field* (IMF), whose origin is in the inner layers of the Sun. It is said that the IMF is "frozen" into the solar wind plasma.

When the solar wind is about to reach the Earth, the IMF and the Earth's magnetic field, begin to interact. The latter distorts from its almost dipole shape and

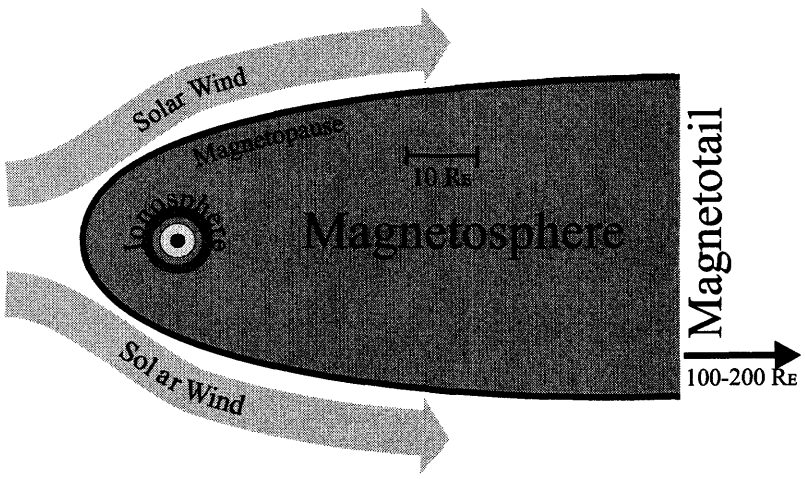

Figure 1.1: Solar-terrestrial environment (equatorial cross-section). Adapted from *Sahr* [1990].

forms a comet-shaped cavity around the Earth called the *magnetosphere.* By definition, the magnetosphere is the region of the solar-terrestrial environment which is mainly governed by the magnetic field of the Earth [e.g., *Hargreaves*, 1992]. The outer boundary of the magnetosphere is called the *magnetopause.* On the dayside, the magnetopause is compressed to the point where the Earth's magnetic field pressure is balanced by the solar wind pressure. It is located at $\sim$ 10 Earth radii (R_E). On the nightside, the magnetic field lines are distorted much more severely, but instead of compression they are stretched back away from the Sun. The region of the nightside magnetosphere, in the tail of the comet-shaped cavity, where the field lines are highly stretched is called the *magnetotail.* It can extend up to 200 R_E. Highly energetic particles from the solar wind still can penetrate to the magnetosphere through the so called *cusp* region (not shown), essentially a "hole" in the magnetopause, leading to the magnetic pole. Depending on the kinetic energy, particles can either reach the Earth's atmosphere or drift back to the magnetotail, accumulating there. Under certain conditions the particles from the magnetotail can precipitate into the Earth's

atmosphere.

Solar illumination as well as the precipitation of particles from the solar wind and magnetosphere causes the ionization of the neutral atoms and molecules in the lower atmosphere and forms the layer of the weakly-ionized plasma around the Earth which is called the *ionosphere*.

Because of the interaction between the magnetosphere and the solar wind, the magnetosphere acts as a huge magneto-hydrodynamic generator of electric fields, which are carried along the highly conducting magnetic field lines down to the ionosphere. These electric fields result in plasma convection both in the magnetosphere and in the ionosphere.

1.2 Ionosphere

The Earth's ionosphere is a very complex medium because it is formed through a variety of processes both internal and external, the latter arising in other parts of the solar-terrestrial environment. Consider, for example, the vertical distribution of the charged particles or the *number density* (number of charged particles per unit volume) profiles. Figure 1.2 gives examples of the electron density profiles measured with the European Incoherent Scatter (EISCAT) radar over Tromso (Northern Scandinavia, geographic latitude $\sim 69°$) on 12 February, 1999 over three successive 10-min intervals during relatively quiet magnetospheric conditions. In all profiles one can recognize three local maxima in the electron density at $\sim$ 95, 120, and 270 km. These maxima correspond to three separate and physically different layers or regions of the Earth's ionosphere, namely the D, E, and F regions. The D region (below 95 km) is not always pronounced (e.g., 1220 UT profile); often it is considered to be simply the lowest portion of the ionosphere. The middle layer from 95 to 150 km is called the

E region; this is usually a well defined feature of the high-latitude density profiles. The upper part of the ionosphere from 150 km and above is called the F region. The F-region densities are usually several times larger than those in the E region. Figure 1.2 demonstrates that the electron density in the ionosphere can vary considerably over a period of 30 min even during quiet conditions. One can see a doubling in the maximum density of the D layer and $\sim$ 15% variations in the maximum density of the E and F layers. Much faster and larger changes are typical for disturbed conditions when strong particle precipitation occurs. It is well known that the density profiles change significantly with the time of the day, season and solar cycle phase. The density distribution depends on the latitude interval as well.

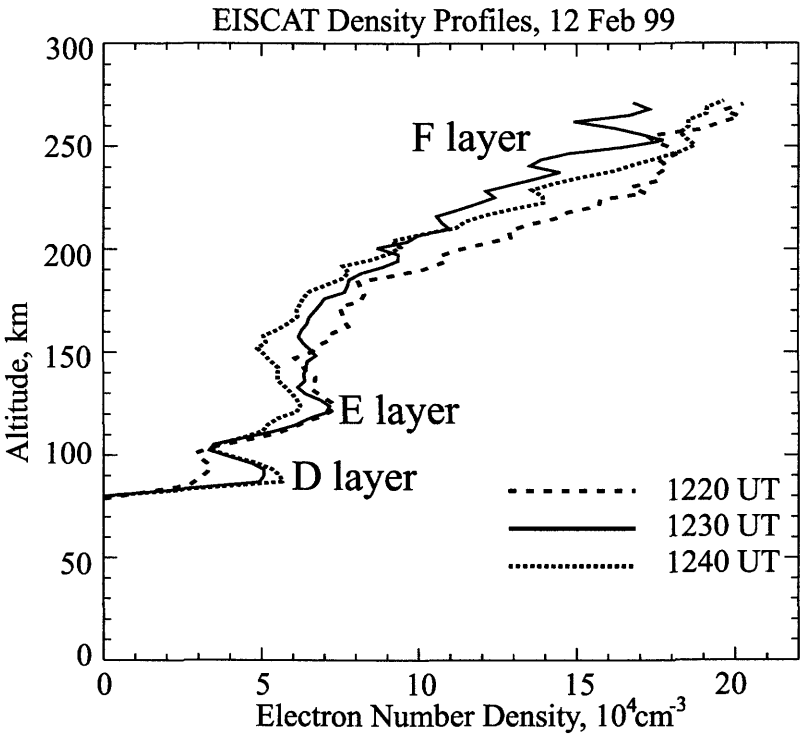

Figure 1.2: Examples of density profiles measured with the EISCAT radar.

In this thesis, processes in the high-latitude E region are considered. An important feature that distinguishes the lower E region (below 120 km) is the existence of significant relative flow between ions and electrons. The reasons are as follows. In the lower part of the E region, the number of the neutral particles is still high enough for the collision frequency of ions with neutrals ν_{in} to be larger than the ion gyro frequency ($\Omega_i \cong 150\ s^{-1}$). To illustrate this point, Figure 1.3 presents altitude profiles of the ion and electron collision frequencies for the lower part of the E region, calculated using the expressions given by *Schunk and Walker* [1973] and *Schunk and Nagy* [1978].

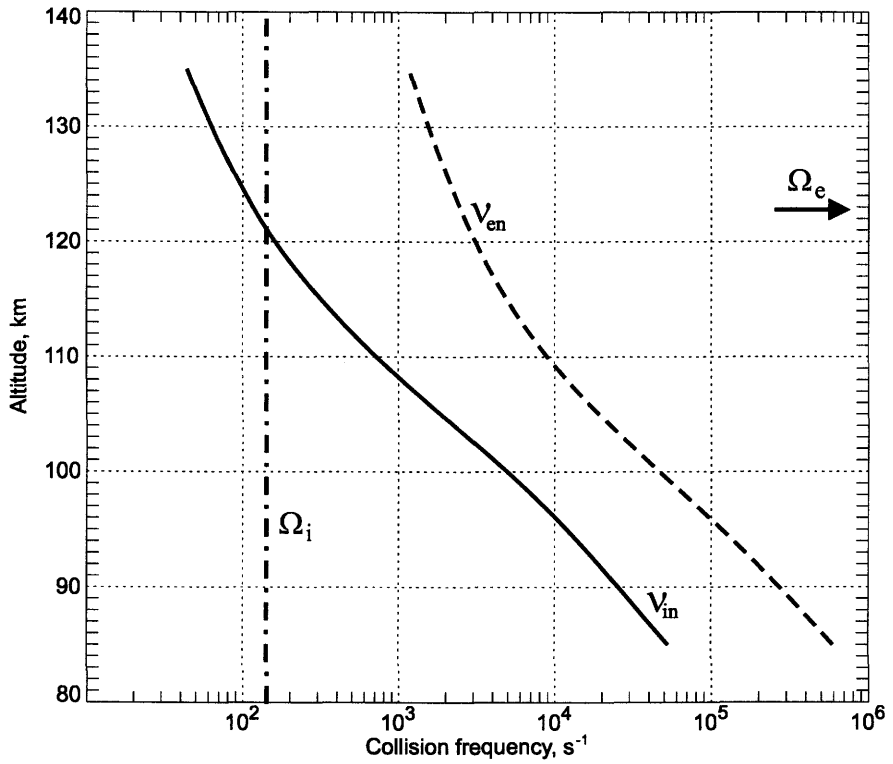

Figure 1.3: Collision frequencies of the ions and electrons with neutrals (ν_{in}, ν_{en}) in the Earth's ionosphere. The gyro frequency of ions is shown by the vertical dash-dotted line, the gyro frequency of electrons $\Omega_e = 10^7 s^{-1}$ is beyond the scale of this diagram.

Under such conditions, the ion motion is strongly controlled by collisions with neutral particles. It is said that ions in the lower E region are not magnetized. In the presence of a neutral wind (which is typical for the E region), ions move with the streaming velocity of neutral particles. For the electrons, on the other hand, the gyro frequency is much larger than the collision frequency with neutrals ν_{en} (dashed curve in Figure 1.3), so that they are magnetically controlled; electrons rotate around the magnetic field lines rarely colliding with neutrals. The neutral wind does not affect the electron motion. This means that the neutral wind provides relative motion between electrons and ions. The effect can be significantly enhanced if an external electric field is applied to the ionosphere in addition to the neutral wind. In the presence of a strong electric field, as it happens at high latitudes, electrons experience, on average, $\mathbf{E} \times \mathbf{B}$ drift while ions have only very slow drift along the electric field direction (the ion drift in an external electric field is of the order of the drift provided by neutral winds and both are much smaller than the $\mathbf{E} \times \mathbf{B}$ drift).

The relative flow between plasma species is manifesting itself in the presence of the electric current in the ionosphere. The currents are significantly enhanced at high latitudes (due to the electric field of magnetospheric origin) where they are often called *convective electrojets.* To characterize the convective electrojets, it is customary to consider plasma flow (plasma convection) at F-region heights where both electrons and ions experience $\mathbf{E} \times \mathbf{B}$ drift. Plasma convection thus is of opposite polarity with respect to the electrojet direction. Figure 1.4 shows the two-cell convection pattern typical for the high latitudes [e.g., *Clauer and Kamide*, 1985]. The digits indicate the Magnetic Local Time (MLT) with the Sun at 12. Dotted circles depict the magnetic parallels. The convection flow is antisunward at high latitudes over the magnetic pole (polar cap, inner circles) and sunward at lower latitudes (auroral zone, outer circles). Such plasma circulation can be characterized by the electric field $\mathbf{E}$ in the auroral zone and polar cap being oriented as shown by the black arrows. In the evening

(morning) sector of the auroral zone the electric field is poleward (equatorward). The direction of convection can be obtained by applying the simple $\mathbf{E} \times \mathbf{B}$ rule for the electric field and the Earth's magnetic field. For convenience, the orientation of the Earth's magnetic field $\mathbf{B}$ (down in the northern hemisphere) is indicated in Figure 1.4 by the circle with the cross. Also showed in Figure 1.4 are the *convection reversal boundaries*, the areas where the direction of convection changes from antisunward to sunward and vice versa. Real convection patterns, of course, are not so simple; they are distorted, sometimes very severely, and more than two individual cells can often be seen.

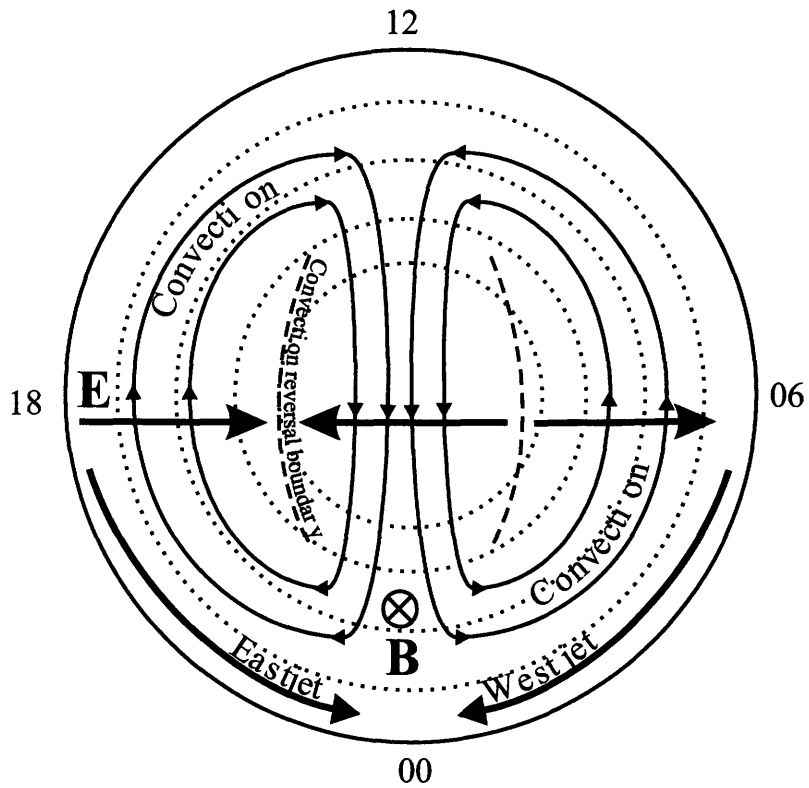

Figure 1.4: Schematic two-cell convection pattern.

Since in the E region only electrons are free to move with the $\mathbf{E} \times \mathbf{B}$ drift (ions

are at rest to a first approximation), the convection pattern presented in Figure 1.4 stipulates the existence of the westward electric current (westjet) in the dawn sector and the eastward current (eastjet) in the dusk sector as shown by the solid curved arrows. Because of existence of the electrojets, the lower E region is sometimes referred to as the *electrojet region.*

1.3 Plasma Instabilities and Ionospheric Irregularities

The relative drift between electrons and ions in the lower E region creates favorable conditions for the amplification of the random thermal fluctuations or, in other words, for the development of plasma instability. Because there are two mismatched flows of electrons and ions involved, the instability in the crossed electric and magnetic fields driving the electrons is sometimes referred to as the *modified* (by the magnetic field) *two-stream instability.* In space physics, the instability is also well known as the *Farley-Buneman* (F-B) *instability* after the names of its discoverers. Another potentially important factor for the amplification of the E-region thermal fluctuations is the background gradient of the electron density perpendicular to the Earth's magnetic field, and the instability associated with this factor is called the *gradient drift* (G-D) *instability.* Theories of the F-B and G-D plasma instabilities are considered in detail in Chapters 2 and 3.

The result of the F-B and G-D instability development is that electrons in the E region form themselves into the alternating regions of density enhancements and depletions, or *irregularities.* The electrojet irregularities thus reflect the micro-structure of the E region, and for this reason understanding the processes of their formation is

a fundamental question in the physics of the ionosphere.

In the past, several methods for studying the electrojet irregularities have been employed [*Fejer and Kelley*, 1980]. Over the years, coherent backscatter radars have proven to be one of the best instruments in such studies [*Fejer and Kelley*, 1980]. Coherent radar measurements of the radio waves backscattered from ionospheric irregularities can be used to study the nature of the irregularities. Despite the weakness of the signal from each irregularity wave front, there are many of them so that signals from parallel structures can add up coherently to a signal strong enough to be detected. An important point is also that a radar transmits a probing wave of a certain frequency and "selects" from plasma waves of a huge variety of scales/wavelengths (from centimeters to kilometers) only waves of one specific wavelength (see Chapter 4). It is important to realize that because the electrons in the ionosphere are free to move parallel to the magnetic field, the electrojet irregularities are aligned with the magnetic field lines. Since the Earth's magnetic field is almost vertical in the auroral zone, the radar beam will reach orthogonality with the magnetic field at the E-region heights only if the coherent radar is positioned several hundred kilometers equatorward from the region of interest. It is clear that the geometry of observations is a very important factor for coherent backscatter measurements.

Figure 1.5 shows the typical geometry for E-region plasma wave observations by the coherent radar method. For backscatter from $\sim$ 110 km, the radar launches a probing wave at an angle of $\delta \sim 10^{\circ}$ (the *elevation angle*) and measures the phase velocity of the moving plasma structures. The range to the echo region r is evaluated by measuring the travel time for radio waves **to** the irregularities and **back** to the radar, along the beam. This range (often called *slant range*) is typically several hundred kilometers.

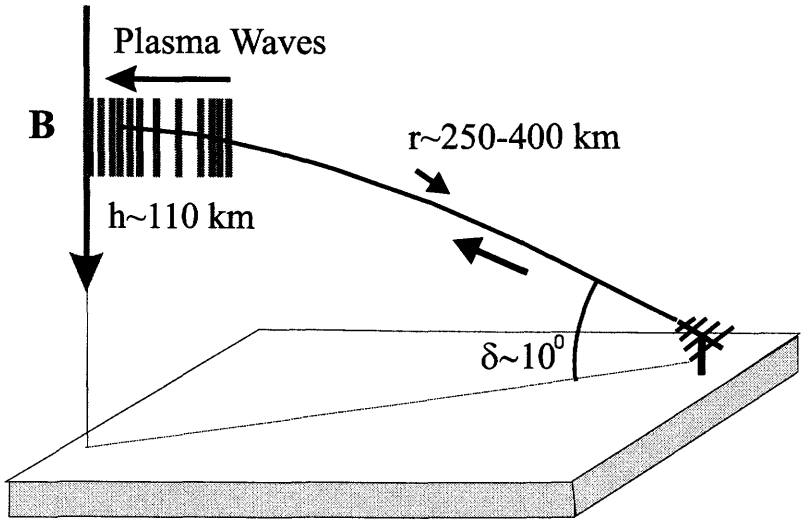

Figure 1.5: Coherent radar observations of the E-region plasma waves.

1.4 Super Dual Auroral Radar Network

Important contributions to the current knowledge on E-region irregularities have been made through Very High Frequency (VHF) radar observations (50–150 MHz) [see review papers by *Fejer and Kelley*, 1980; *Haldoupis*, 1989; *Schlegel*, 1996; *Sahr and Fejer*, 1996]. Such radars are sensitive to meter-scale irregularities (λ = 1–3 m). Over the years, the theory of E-region irregularities has been evaluated through the experimental data on meter-scale irregularities. Only a few E-region experiments involved High Frequency (HF) radars (8–20 MHz) [*Villain et al.*, 1987; 1990; *Hanuise et al.*, 1991; *Bourdillion et al.*, 1995; *Haldoupis et al.*, 1996; 1998; *Hussey et al.*, 1997] and most of these experiments were performed at mid-latitudes. The recent deployment of the Super Dual Auroral Radar Network (SuperDARN) system of coherent HF radars at high latitudes has provided opportunities for the study of the auroral electrojet irregularities in the decameter band (λ = 10–20 m) [*Milan and Lester*,

1998; 1999; 2001; *Milan et al.*, 2001; 2002; *Jayachandran et al.*, 2000; *Koustov et al.*, 2001; 2002; *Makarevitch et al.*, 2001; 2002a; 2002b; *Uspensky et al.*, 2001; 2002; *Ogawa et al.*, 2001]. These recent studies have concentrated on identifying differences between the HF and VHF echo characteristics and attempting to reveal the specifics of electrojet instability development at longer wavelengths.

Since SuperDARN radars will be major instruments used in this thesis, we give a short introduction to the philosophy of the experiment. More details relevant to this thesis will be presented later in Section 5.1. Also a very detailed description of the radars can be found in *Greenwald et al.* [1995].

The SuperDARN experiment is a network of identical HF coherent radars located at various places across the globe. Most of the radars are paired to have a common field of view with radar beam intersections at 256 points. Each radar scans through 16 successive beam positions in $\sim 3.25°$ steps, covering a $\sim 52°$ range of azimuths. The sounding frequency is usually fixed somewhere between 9 and 18 MHz. Most of the time the radars operate in the so called *common* or *normal mode*. One full scan in this mode through the radar Field of View (FOV) lasts 2 min. Recently, 1-min scans are gaining popularity.

Figure 1.6a shows the coverage of the SuperDARN radars in the northern hemisphere. The solid thick lines are lines of equal magnetic latitudes ($\Lambda = 60°$, $70°$, and $80°$) obtained using the Polar Anglo-American Conjugate Experiment (PACE) magnetic field model [*Baker and Wing*, 1989]. The dotted lines are geographic latitudes and longitudes. Figure 1.6b shows the location and field of view of the SuperDARN radars in the southern hemisphere.

The main goal behind the creation of the SuperDARN network was to achieve a capability for global monitoring of the F-region convection patterns at high latitudes. The SuperDARN radars use the Doppler velocity of the coherent scatter from the F-region irregularities to obtain information on plasma motion. It is assumed that

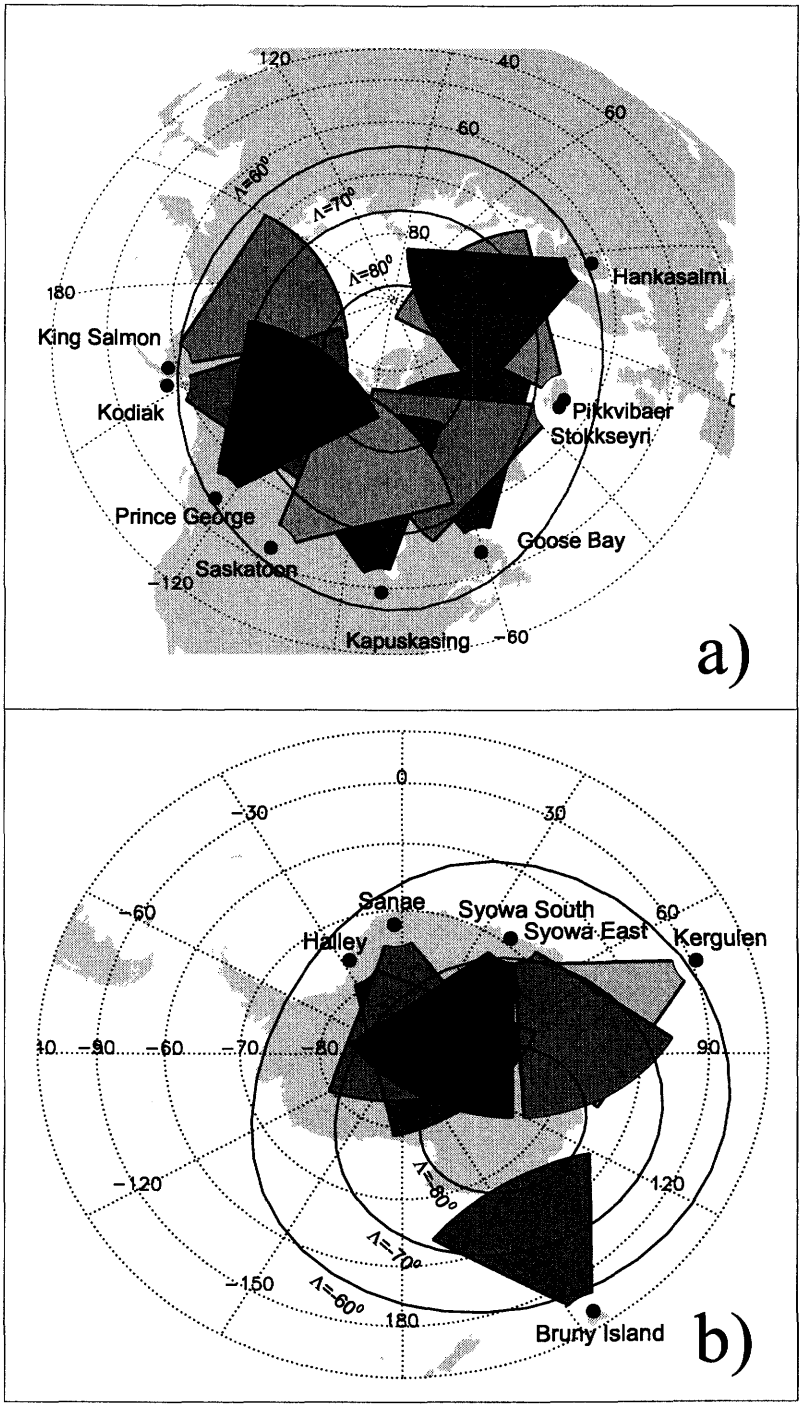

Figure 1.6: SuperDARN radars in the (a) northern and (b) southern hemispheres.

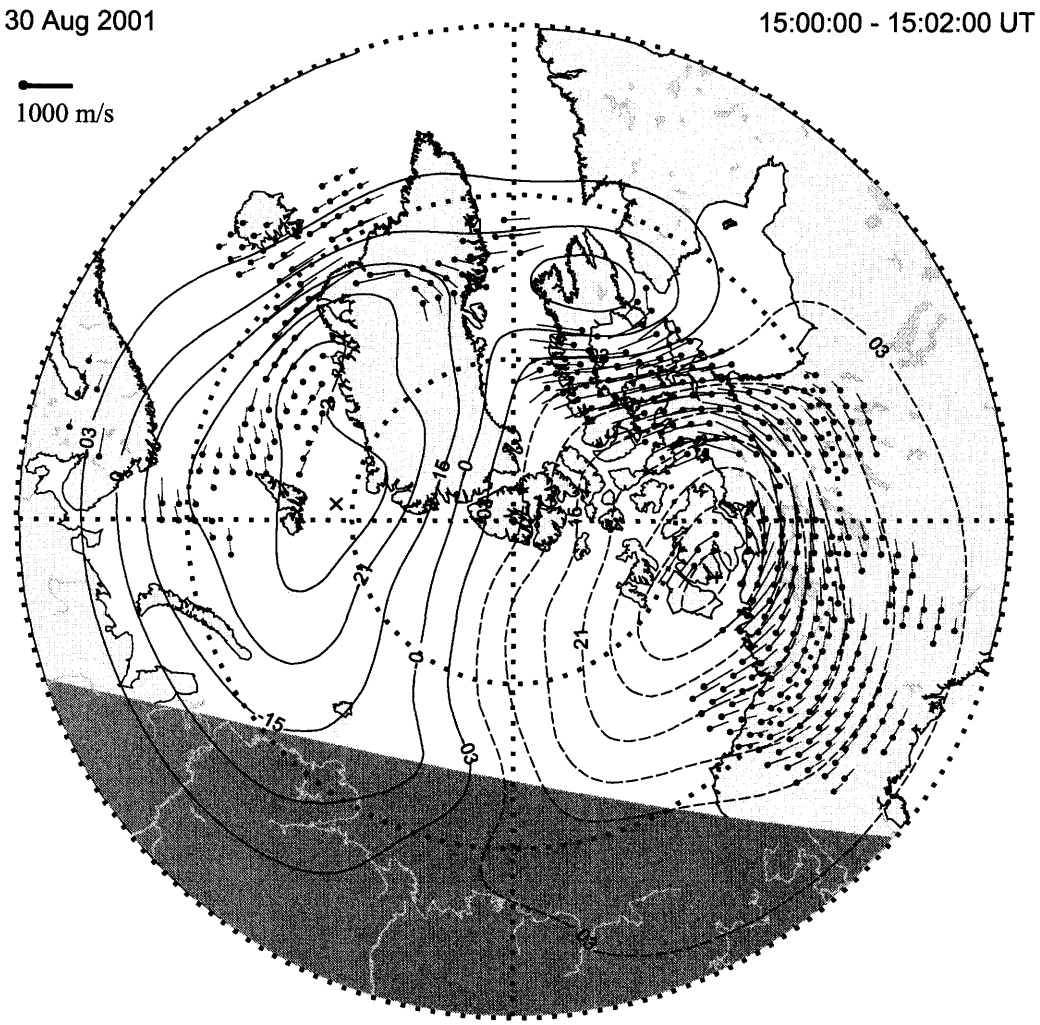

Figure 1.7: SuperDARN fit convection map for the northern hemisphere.

plasma irregularities of decameter scale move with the $\mathbf{E} \times \mathbf{B}$ drift velocity. Having a component of plasma convection in one direction, one can combine it with another component obtained from a different direction by simple merging [*Greenwald et al.*, 1995] or one can use the velocity to fit the expected convection pattern as prescribed in a recently developed fit technique [*Ruohoniemi and Baker*, 1998].

In Figure 1.7 we present an example of a convection map in the northern hemisphere obtained with the SuperDARN radars based on the *Ruohoniemi and Baker* [1998] fit technique. The large dots with directed lines whose length is proportional to the speed, show the convection velocities at the F-region heights. The scale for the speed is shown in the top-left corner of the diagram. Also shown are the equipotential contours (solid and dashed lines) from the fit model and the magnetic parallels (dotted circles) and meridians (dotted lines). The map covers magnetic latitudes of 60°–90°. The digits on the solid and dashed contours indicate the value of the electrostatic potential in kV. The shaded area is the part of the auroral ionosphere not illuminated by the Sun.

In Figure 1.7, the raw data coverage is better for the right cell (more dots in the morning sector), but two convection cells are clearly discernible. One can see that (similar to the simplified model of Figure 1.4) the flow is mostly along magnetic parallels in the evening and morning sectors, and it deviates from the direction of magnetic parallels for MLT near midnight and noon, which is typical for southward IMF (corresponding to the period of measurement).

Though the SuperDARN radars were primarily designed to monitor the F-region plasma convection, studying E-region irregularities with them is also possible. Indeed, the largest possible slant range for each SuperDARN radar is about 3500 km, whereas the E-region echoes occur mostly at ranges shorter than the E-region radio horizon range of $r \sim 1200$ km. In this thesis we consider echoes detected at ranges shorter than 810 km.

An important difference between HF and VHF observations is that HF radio waves, while propagating to the scattering volume and back to the radar, experience much more significant refraction. Depending on the density distribution with altitude, there can be several typical trajectories of the HF radio wave propagation through the ionosphere. Figure 1.8 illustrates schematically different propagation modes for HF radio waves. If the amount of radar ray bending is such that the radio wave can reach orthogonality with the magnetic field in the E region, then it is said that one has direct scatter from the E region, case a) in Figure 1.8. In the auroral zone, where the magnetic field is almost vertical (slightly tilted black arrows in Figure 1.8), HF radars, unlike VHF radars, are capable of reaching the orthogonality condition for the F-region heights as well, simply because radar ray bends more at HF. The direct scatter from the F region is then possible for significantly higher ionospheric densities, case b) in Figure 1.8. If, on the other hand, the density is too high then the radio waves can be reflected by the ionosphere to the ground and then be scattered back towards the radar, case c), *ground scatter*. Radio waves can also be reflected by the ground towards farther ranges and irregularities and then scattered back. It is said in this case that there is a *one and a half hop* propagation mode for F-region scatter, case d). Obviously, there can be also $1^{1/2}$ hop E-region scatter (not shown in Figure 1.8). In the D region echoes can occur because of the scatter on ionization trails associated with the meteors, case e). During summer months in the polar D region, coherent radars also detect *polar mesospheric summer echoes (PMSE)* (not shown) that are thought to be generated by instabilities associated with large aerosols and ice particles [see the recent review by *Cho and Röttger*, 1997]. The mechanisms that govern the production of D-region irregularities are quite different from the ones in the E and F regions. However, when dealing with the scatter from the nearest range gates, one should be aware of the possibility of D-region contamination. This issue will be addressed specifically in Chapter 7.

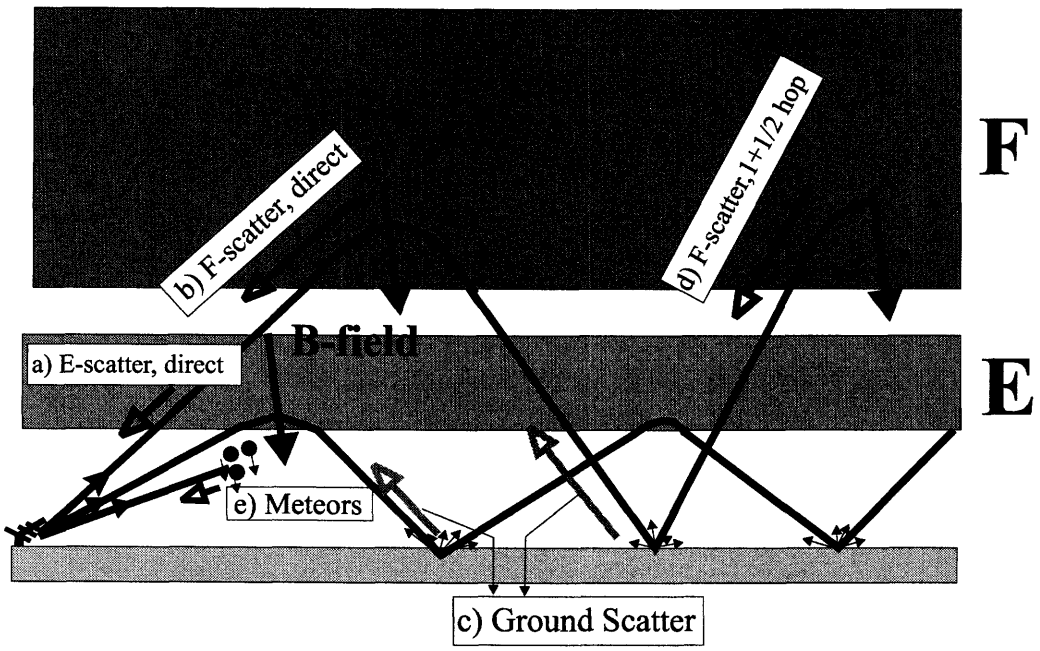

Figure 1.8: Propagation modes for an HF backscatter radar.

1.5 Objectives and Thesis Outline

One of the ways to learn more about the physics of E-region irregularity formation is to study the irregularity phase velocity. Numerous previous publications have shown that the situation, in this regard, is very complicated [see review papers by *Fejer and Kelley*, 1980; *Haldoupis*, 1989; *Sahr and Fejer*, 1996; *Moorcroft*, 2002]. The phase velocity of E-region irregularities is known to depend on the electric field magnitude and direction, the electron and ion temperatures (for certain types of echoes), the angle of propagation with the magnetic field, and the irregularity wavelength. Current knowledge on the wavelength/radar frequency effects in the irregularity phase velocity is scarce. The years of research have also revealed quite significant inconsistencies between measurements of the Doppler velocity and theoretical predictions [*Sahr and Fejer*, 1996; *Moorcroft*, 2002]. It turned out that velocity of echoes is a

crucial parameter that allows us to distinguish various nonlinear effects influencing the evolution of the F-B and G-D instabilities.

The main goal of this thesis is to study the phase velocity of the meter and decameter waves in the auroral E region in order to reveal the specifics of the irregularity production at decameter scales. We follow the traditional approach in the field, namely we combine theoretical reasoning and data analysis.

Progressively more specific, the objectives of the thesis can be formulated as follows:

(1) Attempt to identify the instabilities that are responsible for the decameter irregularity generation in the auroral E region.

(2) Within the existing instability theories, find the factors that determine the properties of the irregularity phase velocity.

(3) Among various factors, study the dependence of the irregularity phase velocity on the direction of wave propagation.

(4) By taking into account the propagation direction dependence, compare the irregularity phase velocity at different wavelengths/radar frequencies.

(5) Using the results of the latter comparison, infer the mechanisms of irregularity production.

The outline of the thesis is as follows. After introductory Chapter 1, Chapter 2 reviews the theories of E-region irregularities. We derive the general 2-D linear dispersion equation for the Farley-Buneman and gradient drift instabilities and analyze it, focusing on the properties of the irregularity phase velocity. We also formulate conclusions of other theories on this issue.

In Chapter 3 we consider in more detail one extremely important mechanism of the F-B instability saturation, the mode coupling processes. We demonstrate how to obtain a nonlinear equation which describes the interaction between the waves of different scales. We then study the stability of the turbulent background of the F-B

waves with respect to long-wavelength secondary perturbations propagating along the electrojet flow. Subsequent analysis of the derived dispersion equation for the secondary waves provides new insights into the properties of the F-B waves.

A brief review of the experimental results on the phase velocity of E-region irregularities is given in Chapter 4. We present a classification of the auroral E-region echoes based on measurements of the spectral power, mean Doppler velocity, and spectral width and concentrate on the dependencies of the Doppler velocity upon the flow angle, aspect angle, and wavelength (radar frequency) of the irregularities.

Chapter 5 presents results of E-region irregularity observations at two significantly different radar frequencies of 50 and 12 MHz (3-m and 12-m plasma waves). We reveal the existence of two separate classes of HF echoes and study in detail the dependence of Doppler velocity upon the flow angle/azimuth at both frequencies separately for each class. We also study the difference between HF and VHF echo characteristics by considering the echo power-velocity relationship.

Chapter 6 considers multifrequency measurements of the Doppler velocity at 5 very close HF frequencies. We study the scale dependence of the Doppler velocity for strong electric field conditions at radar directions almost perpendicular to the plasma flow.

Chapter 7 contains the discussion of the experimental results. We attempt to look at the data gathered in two independent experiments from a unifying point of view. We discuss various plasma instabilities that can potentially produce echoes with different characteristics at different radar frequencies. We also consider the role of refraction in observed velocities of HF echoes.

Finally, in Chapter 8 we list major conclusions of this study and present suggestions for future research.

Chapter 2

The Theory of E-region Irregularities: A Brief Review

This chapter outlines the hierarchy of the theories of the F-B and G-D plasma instabilities. The purpose of this presentation is, first of all, to give a background for nonlinear consideration of the next chapter and, secondly, to give general ideas on properties of unstable waves in the auroral E region. In the course of presentation we focus on the velocity of the plasma waves. We start (Section 2.1) with the derivation of a general 2-D linear dispersion equation and then analyze this equation for two different cases: wave propagation vector parallel and perpendicular to the background electron density gradient. Section 2.2 describes qualitatively quasi-linear theories of the F-B and G-D instability saturation. Finally, Section 2.3 reviews nonlinear theories of these instabilities and their numerical (fluid and particle) simulations.

2.1 Linear Fluid Theory of the F-B and G-D Instabilities

The linear theory of the F-B instability was first formulated independently by *Farley* [1963], who adopted a kinetic approach, and by *Buneman* [1963], who used fluid equations. The conclusions of kinetic and fluid theories are in fairly good agreement for irregularities with wavelengths greater than a few meters [see review papers by *Fejer and Kelley*, 1980; *Farley*, 1985; *Haldoupis*, 1989]. At shorter wavelengths the predictions of the two theories diverge due to the increase of Landau damping, which can only be accounted for by the kinetic theory [*Schmidt and Gary*, 1973]. However, in spite of its limitations, the fluid theory is widely used for the interpretation of experimental data at HF and even at VHF radar frequencies. For this reason, we give a detailed description of the linear theory of the F-B instability. We focus on the fluid approach but add the impact of kinetic effects where appropriate.

The F-B instability is considered for a uniform plasma. The E-region ionosphere, however, is highly inhomogeneous, especially in the auroral zone where the precipitation of energetic particles creates strong plasma gradients. In the presence of such gradients, another instability, namely the G-D instability, can be excited. This instability was originally studied by *Simon* [1963] and *Hoh* [1963] for laboratory plasma applications. Besides the plasma density gradient, the instability requires relative electron-ion drift perpendicular to the gradient.

2.1.1 Momentum and Continuity Equations

To demonstrate how to derive and analyze the dispersion equation for the F-B and G-D waves we consider simple fluid theory. In the framework of this approach, the

ionospheric plasma consisting of three types of particles (ions, electrons and neutrals) is described as a two-particle fluid (electrons and ions) with the effects of the neutrals taken into account through friction forces (collisions of charged particles with neutrals) in the momentum equation:

$$m_\alpha \frac{d\mathbf{V}_\alpha}{dt} = e_\alpha(\mathbf{E} + \mathbf{V}_\alpha \times \mathbf{B}) - \nu_\alpha m_\alpha(\mathbf{V}_\alpha - \mathbf{U}) - \frac{\nabla(n_\alpha T_\alpha)}{n_\alpha}, \tag{2.1}$$

while the continuity equation is given by:

$$\frac{\partial n_\alpha}{\partial t} + \nabla \cdot (n_\alpha \mathbf{V}_\alpha) = 0. \tag{2.2}$$

Here $e_\alpha, m_\alpha, \mathbf{V}_\alpha, n_\alpha, \nu_\alpha$, and T_α denote charge, mass, velocity, number density, collision frequency with neutrals, and temperature (in energy units) of species α ($\alpha = i, e$), $\mathbf{E}$ and $\mathbf{B}$ are the electric and magnetic fields, and $\mathbf{U}$ is the neutral wind velocity.

Each unknown variable $(\mathbf{V}_\alpha, n_\alpha, \mathbf{E})$ in (2.1) and (2.2) can be represented as a sum of background level and perturbation (for example, $n_\alpha \equiv n_{\alpha 0} + \delta n_\alpha$). Within linear theory one assumes that all perturbations are small compared to the background values (e.g., $\delta n_\alpha \ll n_{\alpha 0}$). Generally, when considering an equation of n-th order in perturbations ($n = 0, 1, \ldots$) one needs to include all terms that are proportional to perturbations to the n-th degree while all other terms can be omitted. Linear theory deals with the first order equations, $n = 1$.

From heretofore we adopt the following geometry (Figure 2.1). The magnetic field $\mathbf{B}$ (which is considered to be constant $\mathbf{B} = \mathbf{B}_0$) is antiparallel to the z axis, background electric field $\mathbf{E}_0$ is assumed to be in the $x - y$ plane. The neutral wind vector $\mathbf{U}$ and the background electron density gradient vector ∇n_0 are also assumed to be in the $x - y$ plane (n_0 here signifies both electron and ion background densities; we assume that the plasma is quasineutral, that is that $n_{i0} = n_{e0} \equiv n_0$, and $\delta n_i = \delta n_e \equiv \delta n$). Introducing unit vectors $\mathbf{e}_x, \mathbf{e}_y, \mathbf{e}_z$ along the x, y, and z axes, respectively, one can write $\mathbf{B}_0 = -B_0 \mathbf{e}_z$, $\mathbf{E}_0 = E_{0x}\mathbf{e}_x + E_{0y}\mathbf{e}_y$.

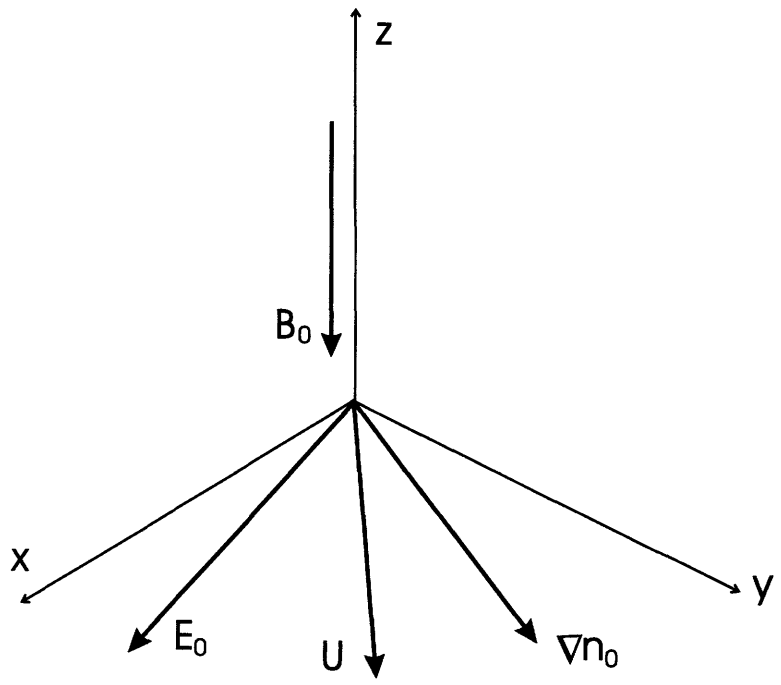

Figure 2.1: Mutual orientation of magnetic and electric field, gradient of electron density, and neutral wind velocity.

2.1.2 Background Plasma Motions

Expressions for the background electron and ion drift velocities $\mathbf{V}_{e0}$ and $\mathbf{V}_{i0}$ can be readily obtained from (2.1). Since all derivatives are zero for the background, the momentum equation (2.1) becomes

$$0 = e_\alpha(\mathbf{E}_0 + \mathbf{V}_{\alpha 0} \times \mathbf{B}) - \nu_\alpha m_\alpha(\mathbf{V}_{\alpha 0} - \mathbf{U}). \tag{2.3}$$

In equation (2.3) one more term should be included, since the last term in (2.1) is not zero due to the background electron density gradient ∇n_0. For simplicity we consider here the case of cold plasma, $T_\alpha = 0$. This is a good approximation for the ionospheric E region [*Kelley*, 1989]. Then, dividing (2.3) by $e_\alpha B$ we obtain

$$\frac{\mathbf{E}_0}{B} - \mathbf{V}_{\alpha 0} \times \mathbf{e}_z - r_\alpha(\mathbf{V}_{\alpha 0} - \mathbf{U}) = 0, \tag{2.4}$$

where Ω_i (Ω_e) is the gyro frequency of ions (electrons), $\Omega_\alpha \equiv e_\alpha B/m_\alpha$ and $r_\alpha \equiv \nu_\alpha/\Omega_\alpha$ are the ratios of collision and gyro frequencies. From (2.4) the background drifts are

$$\mathbf{V}_{\alpha 0} = s_\alpha(r_\alpha \mathbf{V}'_\alpha - \mathbf{V}'_\alpha \times \mathbf{e}_z), \tag{2.5}$$

where we introduced the notation $s_\alpha \equiv 1/(1+r_\alpha^2)$ and $\mathbf{V}'_\alpha \equiv \mathbf{E}_0/B + r_\alpha \mathbf{U}$.

One should note that expression (2.5) for the background drifts of electrons and ions is valid for a large range of ionospheric heights, both for the E and lower F regions.

Background Plasma Motions in the E region

In the lower E region, the collision frequency of ions (electrons) with neutrals is much larger (smaller) than the ion (electron) gyro frequency $\nu_i \gg \Omega_i$ ($\nu_e \ll \Omega_e$) or in terms of r_α

$$r_i \gg 1, \quad r_e \ll 1\ . \tag{2.6}$$

Then we have

$$\mathbf{V}_{e0} \cong r_e \mathbf{E}_0/B - \mathbf{E}_0/B \times \mathbf{e}_z + r_e^2 \mathbf{U} - r_e \mathbf{U} \times \mathbf{e}_z\ , \tag{2.7}$$

$$\mathbf{V}_{i0} \cong r_i^{-1} \mathbf{E}_0/B - r_i^{-2} \mathbf{E}_0/B \times \mathbf{e}_z + \mathbf{U} - r_i^{-1} \mathbf{U} \times \mathbf{e}_z. \tag{2.8}$$

Equations (2.7) and (2.8) under the conditions (2.6) indicate that the electron background drift is determined almost entirely by the Hall drift (perpendicular to the electric and magnetic fields, term 2 in (2.7)), while the ion background drift is determined mostly by the Pedersen drift of ions (parallel to the electric field, term 1 in (2.8)) with some contribution from the neutral motions (term 3 in (2.8)). All other terms are generally very small, so that one can approximate (2.7) and (2.8) as

$$\mathbf{V}_{e0} \simeq -\mathbf{E}_0/B \times \mathbf{e}_z, \tag{2.9}$$

$$\mathbf{V}_{i0} \simeq r_i^{-1} \mathbf{E}_0/B + \mathbf{U}. \tag{2.10}$$

One should use (2.9) and (2.10), however, very carefully, since the relative contribution of different terms in (2.7) and (2.8) depends on the directions of the electric field and neutral wind.

2.1.3 Equations for Perturbations

So far we considered zeroth order equations and obtained expressions for the background velocities. The next step is to analyze equations for perturbations.

The general first order equations (including temperature and background gradient effects) derived from (2.1) and (2.2) are as follows

$$\frac{\partial \delta \mathbf{V}_\alpha}{\partial t} + (\mathbf{V}_{\alpha 0} \cdot \nabla)\delta \mathbf{V}_\alpha = \Omega_\alpha (\frac{\delta \mathbf{E}}{B} - \delta \mathbf{V}_\alpha \times \mathbf{e}_z) - \nu_\alpha \delta \mathbf{V}_\alpha - u_\alpha^2 (\frac{\nabla \delta n}{n_0} - \frac{\delta n}{n_0}\mathbf{G}), \quad (2.11)$$

$$\frac{1}{n_0}\frac{\partial \delta n}{\partial t} + \nabla \cdot \delta \mathbf{V}_\alpha + \mathbf{V}_{\alpha 0} \cdot \frac{\nabla \delta n}{n_0} + \delta \mathbf{V}_\alpha \cdot \mathbf{G} + \delta \mathbf{V}_\alpha \cdot \frac{\nabla \delta n}{n_0} = 0, \quad (2.12)$$

where $\mathbf{G} \equiv \nabla n_0 / n_0$ is the "normalized" gradient of background electron density, and $u_\alpha \equiv \sqrt{T_\alpha / m_\alpha}$ is the thermal velocity of species α; we neglected here the effects of the plasma nonisothermality assuming $T_\alpha = const$.

In (2.12) we retained all linear terms and included the nonlinear term 5. When dealing with the continuity equation, it is customary to neglect the nonlinear term for ions, assuming that $V_{i0} \gg \delta V_i$, thus retaining only one nonlinear term, namely $\delta \mathbf{V}_e \cdot \nabla \delta n / n_0$, in the electron continuity equation [e.g., *Sudan*, 1983; *Sharma and Kaw*, 1986; *Sahr*, 1990]. In addition, we neglect the inertia terms for electrons (terms 1 and 2 on the left-hand-side of (2.11), $\alpha = e$), assuming low-frequency waves $\omega - \mathbf{k} \cdot \mathbf{V}_{e0} \ll \nu_e$. We also neglect the effects of ion background drift $\mathbf{k} \cdot \mathbf{V}_{i0} \ll \nu_i$, and the effects of ion magnetization $\Omega_i \delta \mathbf{V}_i \times \mathbf{e}_z \ll \nu_i \delta \mathbf{V}_i$. Under the above simplifications, (2.11) and (2.12) can be rewritten as

$$\frac{\partial \delta \mathbf{V}_i}{\partial t} = \Omega_i \frac{\delta \mathbf{E}}{B} - \nu_i \delta \mathbf{V}_i - u_i^2 (\frac{\nabla \delta n}{n_0} - \frac{\delta n}{n_0}\mathbf{G}), \quad (2.13)$$

$$0 = \Omega_e(\frac{\delta \mathbf{E}}{B} - \delta \mathbf{V}_e \times \mathbf{e}_z) - \nu_e \delta \mathbf{V}_e - u_e^2(\frac{\nabla \delta n}{n_0} - \frac{\delta n}{n_0}\mathbf{G}), \tag{2.14}$$

$$\frac{1}{n_0}\frac{\partial \delta n}{\partial t} + \nabla \cdot \delta \mathbf{V}_i + \delta \mathbf{V}_i \cdot \mathbf{G} = 0, \tag{2.15}$$

$$\frac{1}{n_0}\frac{\partial \delta n}{\partial t} + \nabla \cdot \delta \mathbf{V}_e + \mathbf{V}_{e0} \cdot \frac{\nabla \delta n}{n_0} + \delta \mathbf{V}_e \cdot \mathbf{G} + \delta \mathbf{V}_e \cdot \frac{\nabla \delta n}{n_0} = 0, \tag{2.16}$$

or dividing (2.13) and (2.14) by Ω_i and Ω_e, respectively, and using the identity

$$\nabla \frac{\delta n}{n_0} = \frac{\nabla \delta n}{n_0} - \frac{\delta n}{n_0}\frac{\nabla n_0}{n_0} \equiv \frac{\nabla \delta n}{n_0} - \frac{\delta n}{n_0}\mathbf{G}, \tag{2.17}$$

we have

$$\left(\frac{1}{\Omega_i}\frac{\partial}{\partial t} + r_i\right)\delta \mathbf{V}_i = \frac{\delta \mathbf{E}}{B} - C_i \nabla \frac{\delta n}{n_0}, \tag{2.18}$$

$$r_e \delta \mathbf{V}_e = \frac{\delta \mathbf{E}}{B} - \delta \mathbf{V}_e \times \mathbf{e}_z - C_e \nabla \frac{\delta n}{n_0}, \tag{2.19}$$

where

$$C_\alpha \equiv \frac{u_\alpha^2}{\Omega_\alpha}\,. \tag{2.20}$$

The continuity equations (2.15) and (2.16) we rewrite as

$$\frac{\partial}{\partial t}\frac{\delta n}{n_0} + (\nabla + \mathbf{G}) \cdot \delta \mathbf{V}_i = 0\,, \tag{2.21}$$

$$\frac{\partial}{\partial t}\frac{\delta n}{n_0} + (\nabla + \mathbf{G}) \cdot \delta \mathbf{V}_e + (\mathbf{V}_{e0} + \delta \mathbf{V}_e) \cdot (\nabla + \mathbf{G})\frac{\delta n}{n_0} = 0. \tag{2.22}$$

Ion Equation

We combine the momentum and continuity equations for the ions into one single equation. Applying to (2.18) $(\nabla + \mathbf{G})\cdot$,

$$\left(\frac{1}{\Omega_i}\frac{\partial}{\partial t} + r_i\right)(\nabla + \mathbf{G}) \cdot \delta \mathbf{V}_i = (\nabla + \mathbf{G}) \cdot \frac{\delta \mathbf{E}}{B} - C_i(\nabla + \mathbf{G}) \cdot \nabla \frac{\delta n}{n_0}, \tag{2.23}$$

then expressing $(\nabla + \mathbf{G}) \cdot \delta \mathbf{V}_i$ from (2.21)

$$(\nabla + \mathbf{G}) \cdot \delta \mathbf{V}_i = -\frac{\partial}{\partial t}\frac{\delta n}{n_0}, \tag{2.24}$$

and substituting into (2.23), we obtain an equation for ions, containing two variables $\delta\mathbf{E}/B$ and $\delta n/n_0$:

$$\left(\frac{1}{\Omega_i}\frac{\partial}{\partial t}+r_i\right)\frac{\partial}{\partial t}\frac{\delta n}{n_0}+(\nabla+\mathbf{G})\cdot\frac{\delta\mathbf{E}}{B}-C_i(\nabla+\mathbf{G})\cdot\nabla\frac{\delta n}{n_0}=0. \tag{2.25}$$

Electron Equation

A single equation for electrons is obtained from (2.19) and (2.22). From (2.19) one can find that

$$\delta\mathbf{V}_e=r_e\frac{\delta\mathbf{E}}{B}-\frac{\delta\mathbf{E}}{B}\times\mathbf{e}_z-C_e\left(r_e\nabla\frac{\delta n}{n_0}-\nabla\frac{\delta n}{n_0}\times\mathbf{e}_z\right) \tag{2.26}$$

and hence

$$\begin{aligned}(\nabla+\mathbf{G})\cdot\delta\mathbf{V}_e &= r_e(\nabla+\mathbf{G})\cdot\frac{\delta\mathbf{E}}{B}-(\nabla+\mathbf{G})\cdot\frac{\delta\mathbf{E}}{B}\times\mathbf{e}_z- \\ &- r_eC_e(\nabla+\mathbf{G})\cdot\nabla\frac{\delta n}{n_0}+C_e(\nabla+\mathbf{G})\cdot\nabla\frac{\delta n}{n_0}\times\mathbf{e}_z,\end{aligned} \tag{2.27}$$

or taking into account the fact that the perturbations of the electric field are electrostatic ($\nabla\times\delta\mathbf{E}\equiv 0 \quad\Rightarrow\quad \nabla\cdot\frac{\delta\mathbf{E}}{B}\times\mathbf{e}_z\equiv 0$)

$$\begin{aligned}(\nabla+\mathbf{G})\cdot\delta\mathbf{V}_e &= r_e(\nabla+\mathbf{G})\cdot\frac{\delta\mathbf{E}}{B}-\mathbf{G}\cdot\frac{\delta\mathbf{E}}{B}\times\mathbf{e}_z- \\ &- r_eC_e(\nabla+\mathbf{G})\cdot\nabla\frac{\delta n}{n_0}+C_e\mathbf{G}\cdot\nabla\frac{\delta n}{n_0}\times\mathbf{e}_z.\end{aligned} \tag{2.28}$$

Substituting (2.28) into (2.22) we obtain

$$\begin{aligned}\frac{\partial}{\partial t}\frac{\delta n}{n_0}+\mathbf{V}_{e0}\cdot(\nabla+\mathbf{G})\frac{\delta n}{n_0}+\delta\mathbf{V}_e\cdot(\nabla+\mathbf{G})\frac{\delta n}{n_0} &- \\ -r_eC_e(\nabla+\mathbf{G})\cdot\nabla\frac{\delta n}{n_0}+C_e\mathbf{G}\cdot\nabla\frac{\delta n}{n_0}\times\mathbf{e}_z &+ \\ +r_e(\nabla+\mathbf{G})\cdot\frac{\delta\mathbf{E}}{B}+\mathbf{G}\times\mathbf{e}_z\cdot\frac{\delta\mathbf{E}}{B} &= 0.\end{aligned} \tag{2.29}$$

2.1.4 Linear Equations for Fourier Transforms

From now on in this chapter we will not consider nonlinear term 3 in the electron equation (2.29). This term, however, will be used later in Chapter 3, where we formulate nonlinear theory of the F-B instability. Perturbations we consider to be plane waves (for example, $\delta n/n_0 = n_{\mathbf{k}} \exp(i\mathbf{k}\cdot\mathbf{r} - i\omega_{\mathbf{k}}t)$), with wave propagation vector $\mathbf{k}$ (in the $x-y$ plane, $k_{\|} \equiv 0$) and wave frequency $\omega_{\mathbf{k}}$. For Fourier transforms, (2.25) and (2.29) become

$$\left[\left(\frac{-i\omega_{\mathbf{k}}}{\Omega_i} + r_i\right)(-i\omega_{\mathbf{k}}) - C_i(i\mathbf{k}+\mathbf{G})\cdot i\mathbf{k}\right] n_{\mathbf{k}} - (i\mathbf{k}+\mathbf{G})\cdot i\mathbf{k}\frac{\phi_{\mathbf{k}}}{B} = 0, \tag{2.30}$$

$$\begin{aligned}[-i\omega_{\mathbf{k}} + \mathbf{V}_{e0}\cdot(i\mathbf{k}+\mathbf{G}) - r_e C_e(i\mathbf{k}+\mathbf{G})\cdot i\mathbf{k} - C_e\mathbf{G}\times\mathbf{e}_z\cdot i\mathbf{k}]\, n_{\mathbf{k}} - \\ - [r_e(i\mathbf{k}+\mathbf{G})\cdot i\mathbf{k} + \mathbf{G}\times\mathbf{e}_z\cdot i\mathbf{k}]\frac{\phi_{\mathbf{k}}}{B} = 0,\end{aligned} \tag{2.31}$$

where we introduced Fourier transform of the perturbation of electric potential $\phi_{\mathbf{k}}$ through $\delta\mathbf{E} \equiv -\nabla\delta\phi = -i\mathbf{k}\phi_{\mathbf{k}}$.

Introducing notations

$$a \equiv \mathbf{G}\cdot\mathbf{k}, \qquad b \equiv \mathbf{G}\cdot\mathbf{k}\times\mathbf{e}_z, \tag{2.32}$$

and rewriting, we have

$$\left\{\left(\frac{-i\omega_{\mathbf{k}}}{\Omega_i} + r_i\right)(-i\omega_{\mathbf{k}}) + C_i(k^2 - ia)\right\} n_{\mathbf{k}} + (k^2 - ia)\frac{\phi_{\mathbf{k}}}{B} = 0, \tag{2.33}$$

$$\begin{aligned}\left\{-i\omega_{\mathbf{k}} + \mathbf{V}_{e0}\cdot(i\mathbf{k}+\mathbf{G}) + C_e\left[r_e(k^2 - ia) + ib\right]\right\} n_{\mathbf{k}} + \\ + \left[r_e(k^2 - ia) + ib\right]\frac{\phi_{\mathbf{k}}}{B} = 0.\end{aligned} \tag{2.34}$$

2.1.5 Linear Dispersion Equation

The linear system (2.33)–(2.34) has a nonzero solution if the determinant is equal to zero, which gives us the dispersion equation:

$$\left\{\left(\frac{-i\omega_{\mathbf{k}}}{\Omega_i} + r_i\right)(-i\omega_{\mathbf{k}}) + C_i(k^2 - ia)\right\}\left[r_e(k^2 - ia) + ib\right] =$$

$$= \left\{-i\omega_{\mathbf{k}} + \mathbf{V}_{e0}\cdot(i\mathbf{k}+\mathbf{G}) + C_e\left[r_e(k^2-ia)+ib\right]\right\}(k^2-ia). \tag{2.35}$$

Reorganizing (2.35) and noticing that

$$C_i - C_e = \frac{U_i^2}{\Omega_i} - \frac{U_e^2}{\Omega_e} = \frac{T_i}{m_i}\frac{m_i}{eB} - \frac{T_e}{m_e}\frac{m_e}{-eB} = \frac{T_i+T_e}{eB} = \frac{T_i+T_e}{m_i}\frac{m_i}{eB} \equiv \frac{C_s^2}{\Omega_i}, \tag{2.36}$$

where C_s is the ion acoustic speed in the medium, we obtain

$$\left\{\omega_{\mathbf{k}}(i\omega_{\mathbf{k}}-\nu_i) - (ik^2+a)C_s^2\right\}\left(k^2 - ia + ibr_e^{-1}\right) = \frac{\nu_i}{\psi}\left(\omega_{\mathbf{k}} - \mathbf{k}\cdot\mathbf{V}_{e0}\right)(k^2-ia). \tag{2.37}$$

Here we introduced the anisotropy parameter ψ [*Sahr and Fejer*, 1996]:

$$\psi \equiv -r_e r_i = -\frac{\nu_e\nu_i}{\Omega_e\Omega_i} = \frac{\nu_e\nu_i}{|\Omega_e|\Omega_i}. \tag{2.38}$$

The dispersion equation (2.37) can be analyzed for arbitrary directions of the background density gradient. Consider solutions of (2.37) for two extreme cases, $a = 0$ and $b = 0$.

Case 1. Wave Vector Parallel to the Gradient Vector. b=0

For the case $b = 0$, (2.37) becomes

$$\omega_{\mathbf{k}}(i\omega_{\mathbf{k}}-\nu_i) - (ik^2+a)C_s^2 = \frac{\nu_i}{\psi}(\omega_{\mathbf{k}} - \mathbf{k}\cdot\mathbf{V}_{e0}). \tag{2.39}$$

By introducing the real and imaginary parts of the wave frequency (oscillation frequency and growth rate) $\omega_{\mathbf{k}} \equiv \omega_{\mathbf{k}r} + i\gamma_{\mathbf{k}}$ and considering wave-like perturbations $\gamma_{\mathbf{k}} \ll \omega_{\mathbf{k}r}$ we obtain simple expressions for the oscillation frequency and growth rate:

$$\omega_{\mathbf{k}r} = \frac{1}{1+\psi}\left[\mathbf{k}\cdot\mathbf{V}_{e0} - \mathbf{k}\cdot\mathbf{G}\,\frac{C_s^2\,\psi}{\nu_i}\right], \tag{2.40}$$

$$\gamma_{\mathbf{k}} = \frac{1}{1+\psi}\frac{\psi}{\nu_i}\left[\omega_{\mathbf{k}r}^2 - k^2C_s^2\right]. \tag{2.41}$$

Hereafter, unless specifically indicated, we use for various estimates the following values for ionospheric parameters: $C_s = 400$ ms^{-1}, $G = 10^{-4}$ m^{-1}, $\nu_i = 1500$ s^{-1},

$\nu_e = 5 \cdot 10^4$ s^{-1}, $\Omega_i = 150$ s^{-1}, and $\Omega_e = 10^7$ s^{-1}. Using these values, let us estimate the second term in (2.40):

$$\mathbf{k} \cdot \mathbf{G} \frac{C_s^2 \psi}{k \nu_i} \simeq \frac{\mathbf{k} \cdot \mathbf{G}}{kG} \; 5 \cdot 10^{-4} \text{ ms}^{-1}. \tag{2.42}$$

Thus, one can conclude that the contribution of the background gradient parallel to the wave vector of interest to the oscillation frequency and hence to the phase velocity of waves is negligible compared to the dominating $\mathbf{E} \times \mathbf{B}$ velocity:

$$\omega_{\mathbf{k}r} \cong \frac{\mathbf{k} \cdot \mathbf{V}_{e0}}{1 + \psi}. \tag{2.43}$$

Case 2. Wave Vector Perpendicular to the Gradient Vector. a=0

If one divides equation (2.37) by k^2 and assumes $a = 0$, it becomes

$$\left[\omega_{\mathbf{k}}(i\omega_{\mathbf{k}} - \nu_i) - ik^2 C_s^2\right](1 + ibr_e^{-1}/k^2) = \frac{\nu_i}{\psi}(\omega_{\mathbf{k}} - \mathbf{k} \cdot \mathbf{V}_{e0}). \tag{2.44}$$

This a dispersion equation that was derived by several authors [e.g., *Sudan et al.*, 1973].

We again take real and imaginary parts of (2.44) and write two equations with two unknown variables, oscillation frequency and growth rate:

$$-\left[\omega_{\mathbf{k}r}^2 - k^2 C_s^2 - \gamma_{\mathbf{k}} \nu_i\right] r_e^{-1} \frac{b}{k^2} - \nu_i \omega_{\mathbf{k}r} = \frac{\nu_i}{\psi}(\omega_{\mathbf{k}r} - \mathbf{k} \cdot \mathbf{V}_{e0}), \tag{2.45}$$

$$\omega_{\mathbf{k}r}^2 - k^2 C_s^2 - \gamma_{\mathbf{k}} \nu_i - \nu_i \omega_{\mathbf{k}r} r_e^{-1} \frac{b}{k^2} = \frac{\nu_i}{\psi} \gamma_{\mathbf{k}}. \tag{2.46}$$

From (2.46) it immediately follows that

$$\gamma_{\mathbf{k}} = \frac{\psi}{1 + \psi}\left[\frac{1}{\nu_i}(\omega_{\mathbf{k}r}^2 - k^2 C_s^2) - \omega_{\mathbf{k}r} r_e^{-1} \frac{b}{k^2}\right]. \tag{2.47}$$

To find the oscillation frequency one has to substitute (2.47) into (2.45) and solve the resultant quadratic equation

$$\eta \omega_{\mathbf{k}r}^2 - \omega_{\mathbf{k}r}(1 + \psi) + \mathbf{k} \cdot \mathbf{V}_{e0} - \eta k^2 C_s^2 = 0. \tag{2.48}$$

Here we introduced the notation

$$\eta \equiv -\frac{\psi}{1+\psi}\frac{1}{\nu_i}\frac{b}{k^2}r_e^{-1} = \frac{1}{1+\psi}\frac{1}{\Omega_i}\frac{b}{k^2} \tag{2.49}$$

and neglected the terms proportional to b^2 utilizing the so called local approximation, namely that the typical scale of the background gradient is much larger than the wavelength, $1/G \gg \lambda$ or $G \ll k$.

The two solutions are:

$$\omega_{\mathbf{k}r} = \frac{1}{2\eta}\left\{(1+\psi) \pm \left[(1+\psi)^2 - 4\eta(\mathbf{k}\cdot\mathbf{V}_{e0} - \eta k^2 C_s^2)\right]^{1/2}\right\}. \tag{2.50}$$

Since

$$\eta k = \mathbf{G}\cdot\mathbf{k}\times\mathbf{e}_z/k\frac{1}{1+\psi}\Omega_i^{-1} \simeq \frac{\mathbf{G}\cdot\mathbf{k}\times\mathbf{e}_z}{kG}10^{-4}\mathrm{m}^{-1}\ 150^{-1}\mathrm{s} \simeq 10^{-6}\mathrm{m}^{-1}\mathrm{s}, \tag{2.51}$$

the second term in the square root is much smaller than the first term and we can expand the square root using $(1+x)^{1/2} \simeq 1 + x/2$:

$$\omega_{\mathbf{k}r} \cong \frac{1}{1+\psi}\left(\mathbf{k}\cdot\mathbf{V}_{e0} - \eta k^2 C_s^2\right) = \frac{1}{1+\psi}\left(\mathbf{k}\cdot\mathbf{V}_{e0} - \frac{1}{1+\psi}\frac{C_s^2}{\Omega_i}\,\mathbf{G}\cdot\mathbf{k}\times\mathbf{e}_z\right). \tag{2.52}$$

As in Case 1, the second term is small as compared with the $\mathbf{E}\times\mathbf{B}$ drift:

$$\frac{\eta k^2 C_s^2}{\mathbf{k}\cdot\mathbf{V}_{e0}} = \eta k\frac{kC_s^2}{\mathbf{k}\cdot\mathbf{V}_{e0}} \simeq \frac{\mathbf{G}\cdot\mathbf{k}\times\mathbf{e}_z}{kG}\ 10^{-6}\ \mathrm{m}^{-1}\mathrm{s}\ \frac{16\cdot 10^4}{10^3}\mathrm{m\ s}^{-1} \simeq 10^{-4}. \tag{2.53}$$

Nearly the same expression for the oscillation frequency was derived by *Janhunen* [1995]. The difference is that our expression is valid for an arbitrary direction of the wave vector $\mathbf{k}$ and we obtained the additional multiplier $(1+\psi)^{-1}$ for the second term in (2.52), though for the typical E-region heights ψ is small and $1+\psi \cong 1$. Also (2.52) is valid not only for marginally stable waves $\gamma_{\mathbf{k}} = 0$ as in *Janhunen* [1995], but for all $\gamma_{\mathbf{k}} \ll \omega_{\mathbf{k}r}$.

For estimation (2.53) we used the electron drift of 10^3 m s^{-1}. For smaller electric fields, however, the second term in (2.52) may become important since

$$\frac{1}{k}\frac{1}{1+\psi}\frac{C_s^2}{\Omega_i}\,\mathbf{G}\cdot\mathbf{k}\times\mathbf{e}_z \cong \frac{\mathbf{G}\cdot\mathbf{k}\times\mathbf{e}_z}{kG}\frac{16\cdot 10^4\ \mathrm{m^2 s^{-2}}}{150\ \mathrm{s}^{-1}}10^{-4}\ \mathrm{m}^{-1} \sim \frac{\mathbf{G}\cdot\mathbf{k}\times\mathbf{e}_z}{kG}10^{-1}\mathrm{m\ s}^{-1}. \tag{2.54}$$

and if one assumes strong gradients, say $G = 100$ m, [*St.-Maurice et al.*, 1994] and somewhat elevated ion acoustic speed C_s (see Section 2.2.3) then the contribution of the gradient term in the expression for the oscillation frequency (2.52) can be as large as some tens of meters per second.

If we now compare the contributions of the gradient term from Case 1 and Case 2, one can conclude that it is stronger in Case 2, that is when the wave vector of interest is perpendicular to the gradient, the assumption which is commonly made from the very beginning of the theoretical consideration [e.g., *Sudan et al.*, 1973; *Fejer et al.*, 1984b; *Hamza and St.-Maurice*, 1993a,b].

The Effects of the Ion Motions and $k_{\parallel} \neq 0$

In the previous sections we considered the linear fluid theory of the F-B and G-D instabilities for the arbitrary direction of the background gradient of electron density $\mathbf{G}$ in the plane perpendicular to the magnetic field. For simplicity we neglected the ion background drift ($\mathbf{k} \cdot \mathbf{V}_{i0} \ll \nu_i$) and considered 2-D case ($k_{\parallel} = 0$).

The expressions for $\omega_{\mathbf{k}r}$ and $\gamma_{\mathbf{k}}$ with nonzero ion drift, a parallel component of the wave vector and recombination, but with a fixed direction of the background gradient (perpendicular to the wave vector), as derived by several authors [e.g., *Rogister and D'Angelo*, 1970; *Sudan et al.*, 1973; *Fejer et al.*, 1975] are:

$$\omega_{\mathbf{k}r} = \frac{\mathbf{k} \cdot (\mathbf{V}_{e0} + \Psi \mathbf{V}_{i0})}{1 + \Psi}, \tag{2.55}$$

$$\gamma_{\mathbf{k}} = \frac{1}{1+\Psi} \left\{ \frac{\Psi}{\nu_i} \left[(\omega_{\mathbf{k}r} - \mathbf{k} \cdot \mathbf{V}_{i0})^2 - k^2 C_s^2 \right] + \frac{1}{Lk} \frac{\nu_i}{\Omega_i} (\omega_{\mathbf{k}r} - \mathbf{k} \cdot \mathbf{V}_{i0}) \right\} - 2\alpha_0 n_0. \tag{2.56}$$

Here the characteristic scale of gradient L corresponds to $1/G$ in our notation for the case $a = 0$ ($\mathbf{G} \perp \mathbf{k}$), α_0 is the recombination coefficient, and

$$\Psi \equiv \psi \left(\frac{k_{\perp}^2}{k^2} + \frac{\Omega_e^2}{\nu_e^2} \frac{k_{\parallel}^2}{k^2} \right). \tag{2.57}$$

In terms of the relative electron-ion drift $\mathbf{V}_d = \mathbf{V}_{e0} - \mathbf{V}_{i0}$, equations (2.55)–(2.56) can be rewritten as

$$\omega_{\mathbf{k}r} = \frac{\mathbf{k}\cdot\mathbf{V}_d}{1+\Psi} + \mathbf{k}\cdot\mathbf{V}_{i0}, \tag{2.58}$$

$$\gamma = \frac{1}{1+\Psi}\left\{\frac{\Psi}{\nu_i}\left[\left(\frac{\mathbf{k}\cdot\mathbf{V}_d}{1+\Psi}\right)^2 - k^2C_s^2\right] + \frac{1}{Lk}\frac{\nu_i}{\Omega_i}\frac{\mathbf{k}\cdot\mathbf{V}_d}{1+\Psi}\right\} - 2\alpha_0 n_0. \tag{2.59}$$

2.1.6 Analysis of the Expressions for Growth Rate and Oscillation Frequency

Aspect and Flow Angles

Let us first introduce two useful definitions. Angles α and θ given by

$$\sin\alpha \equiv \frac{k_\parallel}{k} \tag{2.60}$$

and

$$\cos\theta = \frac{\mathbf{k}\cdot\mathbf{V}_d}{kV_d} \tag{2.61}$$

are called *aspect* and *flow angles*, respectively. The former is the angle between the wave vector $\mathbf{k}$ and the perpendicular to the magnetic field $\mathbf{B}$, and the latter is the angle between the wave vector and the relative electron-ion drift in the plane perpendicular to the magnetic field.

Growth Rate: Threshold Condition, Flow and Aspect Angle Cones

Consider the case of a homogeneous plasma $L = \infty$ (F-B instability) and neglect any recombination effects. The threshold condition for the instability $\gamma_{\mathbf{k}} = 0$ means that the first term in (2.59) equals zero, which is equivalent to $\mathbf{k}\cdot\mathbf{V}_d = kC_s(1+\Psi)$, or in terms of flow angle

$$V_d\cos\theta = C_s(1+\Psi). \tag{2.62}$$

Equation (2.62) can be simplified for the case of zero aspect angle $\alpha = 0$. Since $\Psi \equiv \psi[\cos^2\alpha + (\Omega_e^2/\nu_e^2)\sin^2\alpha]$ we have $\Psi(\alpha = 0) = \psi$.

Equation (2.62) means that there is an electric field threshold for the instability ($V_d \propto E_0$, equations for the background drifts (2.9)–(2.10)). For typical ionospheric conditions this threshold electric field is about 20 mV m^{-1}.

Another conclusion from (2.62) is that we have a finite "cone" of flow angles where growth rate is positive, which corresponds to the case of unstable waves. This cone of aperture θ_0 determined through $\cos\theta_0 = C_s(1+\psi)/V_d$ is called the *F-B instability flow angle cone* or simply the *F-B instability cone*. Within the F-B instability cone all waves are unstable independent of wavelength.

For the case of an inhomogeneous plasma $L \neq \infty$, the second, gradient term in (2.59) can have a destabilizing (stabilizing) effect for $L > 0$ ($L < 0$), widening (narrowing) the flow angle cone.

Consider now drifts that are slightly below the F-B instability threshold $V_d < C_s(1+\psi)$. We can still have instability (positive growth rates) if $1/L$ is quite large and positive, but in this case the instability occurs only for certain values of wave number k. The expression for the critical wave number k_{cr} (and corresponding wavelength) can be found from (2.59), and for the typical parameters (we used $V_d \sim 100$ m s^{-1}) it is equal to $\sim 2\pi/40$ m^{-1}. The instability occurs for all $k < k_{cr}$. It is said that in this case we have the gradient drift (G-D) regime.

In homogeneous plasma, a condition for marginally unstable waves in terms of aspect angle can be derived from (2.62). For the case of F-B instability and $\theta = 0$, it is

$$\frac{V_d}{C_s} = 1 + \psi\left(\cos^2\alpha_0 + \sin^2\alpha_0 \frac{\Omega_e^2}{\nu_e^2}\right). \tag{2.63}$$

For the typical E-region parameters (2.63) gives $\alpha_0 \sim 1°$–$2°$, meaning that waves are unstable within a very narrow cone of aspect angles $\alpha < \alpha_0$. One can conclude that

irregularities should be strongly field-aligned with deviations from perpendicularity to the magnetic field lines of not more than one or two degrees.

Strictly speaking, one should not apply the formulas from the linear theory, e.g., equations (2.55)–(2.59), to larger than 1°–2° aspect angles since the waves are damped at these angles. Quite often, however, these formulas are extrapolated to the case of "large" aspect angles, up to 5°–10°, when experimental data are considered. *Dubois* [1989] explored the roots of the dispersion equation at large aspect angles and found that this extrapolation is appropriate for wavelengths of 10 m and greater. In this thesis we study mostly the decameter waves (λ = 8–20 m), and we use these formulas for the interpretation of the measurements at large aspect angles (e.g., Chapter 6).

Phase and Group Velocities

The main thrust of this thesis is on the phase velocity, the velocity with which the wave fronts travel. To judge, however, how the energy in a wave propagates one needs to know the velocity of the finite wave packet propagation, that is the group velocity. An additional reason why we consider here both phase **and** group velocities is that the group velocity will be used in Chapter 3 where we formulate the nonlinear theory of the F-B instability.

To analyze the properties of the phase and group velocity we rewrite the expression for oscillation frequency as

$$\omega_{\mathbf{k}r} = \frac{\mathbf{k} \cdot \mathbf{V}_{e0}}{1 + \psi(\frac{k_\perp^2}{k^2} + \beta\frac{k_\parallel^2}{k^2})}, \tag{2.64}$$

where

$$\beta \equiv \frac{\Omega_e^2}{\nu_e^2} \tag{2.65}$$

and where we neglected ion drift $\mathbf{V}_{i0}$, which is significant only for the bottom of the electrojet and for large flow angles.

By definition

$$\mathbf{V}_{ph} = \frac{\omega_{\mathbf{k}r}}{k^2}\mathbf{k}, \tag{2.66}$$

$$\mathbf{V}_{gr} = \nabla_{\mathbf{k}}\omega_{\mathbf{k}r} \tag{2.67}$$

and hence

$$\mathbf{V}_{ph\perp} = \frac{\mathbf{k}_\perp}{k^2}\frac{\mathbf{k}\cdot\mathbf{V}_{e0}}{1+\Psi}, \tag{2.68}$$

$$\mathbf{V}_{ph\parallel} = \frac{\mathbf{k}_\parallel}{k^2}\frac{\mathbf{k}\cdot\mathbf{V}_{e0}}{1+\Psi}, \tag{2.69}$$

where we used notation for the anisotropy parameter (2.57).

Taking derivatives, we obtain for parallel and perpendicular components of group velocity [e.g., *Lee and Kennel*, 1973; *Moorcroft*, 1984]:

$$\mathbf{V}_{gr\perp} = \frac{\mathbf{V}_{e0}}{1+\Psi} - 2\psi\frac{\mathbf{k}\cdot\mathbf{V}_{e0}}{(1+\Psi)^2}(1-\beta)\frac{k_\parallel^2}{k^2}\frac{\mathbf{k}_\perp}{k^2}, \tag{2.70}$$

$$\mathbf{V}_{gr\parallel} = 2\psi(1-\beta)\frac{k_\perp^2\mathbf{k}_\parallel}{k^4}\frac{\mathbf{k}\cdot\mathbf{V}_{e0}}{(1+\Psi)^2}. \tag{2.71}$$

Figure 2.2 shows parallel and perpendicular components of phase and group velocities normalized to the $\mathbf{E}\times\mathbf{B}$ drift versus aspect angle for typical ionospheric parameters and zero flow angle. One can notice that even perpendicular components of the phase and group velocities are different except for perfect aspect angle $\alpha = 0°$. For parallel components the difference is as large as 10^4.

The parallel component of the phase velocity is much smaller than the perpendicular component for small aspect angles ($\cos\alpha \sim 1$). Therefore, we can rewrite (2.68) in terms of the flow and aspect angles:

$$V_{ph} \cong \frac{V_{e0}\cos\theta}{1+\Psi} \cong \frac{V_{e0}\cos\theta}{1+\psi\left(1+\Omega_e^2/\nu_e^2\ \sin^2\alpha\right)}. \tag{2.72}$$

The phase velocity of irregularities is said to obey the "cosine" law, that is phase velocity is proportional to the cosine of the flow angle. Also one can conclude from

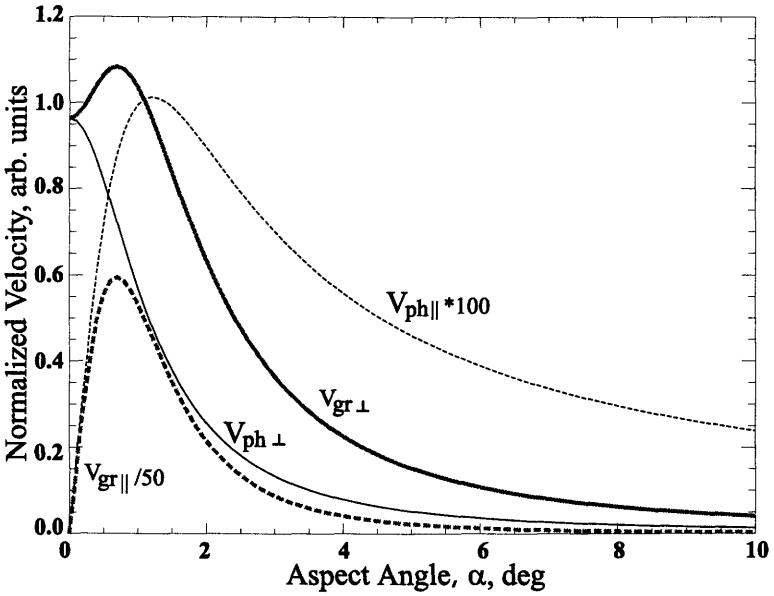

Figure 2.2: Group and phase velocities as functions of aspect angle. Thin (thick) solid line is perpendicular component of the phase (group) velocity. Scaled up (down) parallel component of the phase (group) velocity is shown by the thin (thick) dashed line.

(2.72) that phase velocity does not depend on irregularity wavelength at all. Phase velocity (thin solid line in Figure 2.2) has a maximum at perfect aspect angle $\alpha = 0°$ and decreases rapidly with aspect angle, since the coefficient before $\sin^2\alpha$ in the denominator $(\psi\Omega_e^2/\nu_e^2 = (|\Omega_e|/\nu_e)(\nu_i/\Omega_i))$ is very large for typical E-region heights ($\sim$ 2000). From (2.72) one can also note that $V_{ph}(-\theta) = V_{ph}(\theta)$ and $V_{ph}(-\alpha) = V_{ph}(\alpha)$, which means that the phase velocity is an even function of the aspect and flow angles.

Convective Properties of the F-B Instability

In the previous consideration we tacitly assumed that a medium where the unstable plasma waves are formed is infinite. Observations have shown otherwise, that is, that

the thickness of unstable layer rarely exceeds 20 km in altitude [e.g., *Pfaff et al.*, 1984]. At high latitudes, the group velocity (vertical component, along the magnetic field) can be large enough to take the wave trains out of the region of generation too quickly for them to grow linearly (waves convect by the parallel group velocity faster than grow), so that in principle one should use a nonlocal approach [*St.-Maurice*, 1985; *Drexler et al.*, 2002]. In this thesis, we restricted ourselves to the local theory and did not consider the convective properties of the F-B waves. One should also note that for the equatorial electrojet the local approximation seems to be more appropriate since at the magnetic equator the parallel component of the group velocity is horizontal (along the magnetic field lines) and it does not take the waves out of the thin layer where the instability is excited.

Long Wavelength Limit

Equation (2.59) for the growth rate allows one to determine the long wavelength limit for the unstable F-B waves. It is assumed that gradients of density are small. Then the F-B term in (2.59) should be considered together with the recombination term. Since the first term is proportional to k^2, it decreases with wavelength increase. The second, recombination term in (2.59) is negative, that is stabilizing. Therefore, there exists a critical wavelength (of the order of 100 m) when the first term in (2.59) is exactly compensated by the recombination term. For longer (shorter) wavelengths all waves are stable (unstable). There is no short wavelength limit in the linear fluid theory of the F-B instability. One should keep in mind though that the fluid approach itself is valid only for wavelengths larger than the mean free path of charged particles in the ionosphere, i.e. a few meters, and that for shorter wavelengths the kinetic effects should be considered.

Kinetic Effects: Short Wavelength Limit and Phase Velocity Modification

The linear kinetic dispersion equation for the F-B waves, which takes into account kinetic effects, has been considered in number of papers [e.g., *Farley,* 1963; *Lee et al.,* 1971; *Schmidt and Gary,* 1973; *Ossakow et al.,* 1975; *Wang and Tsunoda,* 1975; *St.-Maurice et al.,* 1981; *Schlegel,* 1983]. This dispersion equation contains the so called *plasma dispersion function* [*Fried and Conte,* 1961] which generally can not be treated analytically, and therefore in most cases the dispersion equation was solved numerically for the phase velocity and growth rate of the F-B waves. Parameters in such computations usually are the collision frequencies ν_α, background densities $n_{\alpha 0}$, temperatures of electrons and ions T_α, and electric field (background drift V_d). In addition, one can vary wave number, flow angle, and aspect angle ($k = 2\pi/\lambda, \theta, \alpha$), characterizing the wave vector $\mathbf{k}$. By varying one parameter (say, electric field) and assuming that all other are constant one is able to calculate the dependence of the phase velocity and growth rate upon this parameter.

Schlegel and St.-Maurice [1983] presented the growth rate γ as a function of wave number k for different density gradients, background densities and altitudes (see their Figures 1a, 1b, and 3). The main result was that apart from the long wavelength limit for the instability growth rate known to exist from the fluid consideration, kinetic effects stipulated the existence of a short wavelength limit. The critical wavelength was found to be dependent on electric field, background density and density gradients and for typical parameters to be equal to 0.05–0.1 m. In contrast to the long wavelength limit, the growth rate decrease near the short wavelength boundary is very sharp; it drops drastically after reaching its maximum value at $\sim$ 0.2 m, so that instability preferentially occurs in the centimeter range.

The other important conclusion of the kinetic theory is the scale-dependence of the phase velocity. One should note that there exist several approaches to the problem

in the literature. The first approach uses the supposition that waves are propagating with threshold drift velocities, meaning that $\gamma = 0$ and hence the phase velocity is the velocity of the marginally stable waves [e.g., *Balsley and Farley*, 1971]. In this approach Farley's kinetic theory predicts that phase velocity increases somewhat with frequency or in other words decreases with wavelength [*Farley*, 1963; 1985]. The second approach is the "fastest-growing-waves" approach, in which it is assumed that experimentally the waves with the maximum growth rate are observed. *Schlegel* [1983] showed that in this approach the phase velocity increases with wavelength. The rate of increase was found to be dependent on the electric field strength: for larger electric fields the increase was larger. Thus, the phase velocity of the F-B waves is smaller as described by the kinetic theory of *Schlegel* [1983]. We illustrate this point in Figure 2.3 taken from *Schlegel* [1983], where the fluid (f) and kinetic (k) phase velocities (1-m F-B waves) are shown as functions of drift velocity for the height of 105 km. One should note that the validity of the "fastest-growing-waves" assumption has been questioned [e.g., *Kaw*, 1972; *Wang and Tsunoda*, 1975; *Robinson and Honary*, 1990]. The fundamental problem is that the wave amplitude and growth rate do not have to be related. A wave can grow fast to a small amplitude or it can grow slowly to a large amplitude.

2.2 Quasi-Linear Theories of the F-B and G-D Instabilities

According to the linear theory, once a wave starts to grow it continues to grow indefinitely. In reality a wave should reach some state after which its growth rate is essentially zero (the wave amplitude is saturated). For this saturated state, $\gamma^{QL} = 0$,

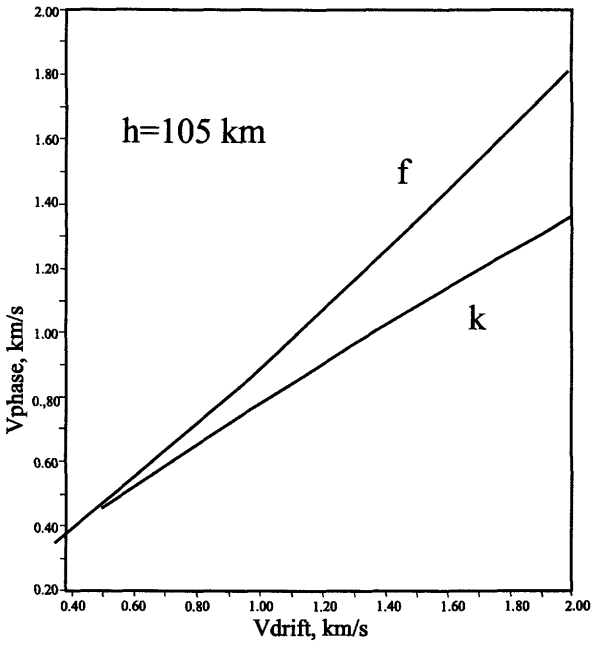

Figure 2.3: Phase velocity of 1-m F-B waves as a function of relative drift velocity.

where index QL is introduced to distinguish between linear growth rate (2.59) and quasi-linear growth rate.

One way of reaching this condition is as follows. Initially a medium has some specific characteristics (for example, background electric field, electron and ion temperatures, collision frequencies with neutrals, background gradients). Immediately after waves start to grow, they modify the medium properties in such a way that growth starts to slow down and eventually stops. The medium modification continues until the growth rate reaches a zero value. The medium and the wave in such state are said to be saturated and the theory that describes this saturated state is called *quasi-linear* [*Sato*, 1976].

The condition $\gamma^{QL} = 0$ means that some parameter in (2.59) ($\mathbf{V}_d$, ∇n_0, C_s^2 or ν_{en}) was changed in such a way that this effectively caused saturation of the wave

amplitude. Symbolically one can write this as $\mathbf{V}_d \rightarrow \mathbf{V}_d^{QL} \equiv \mathbf{V}_d + \mathbf{V}_d^*$, $\nabla n_0 \rightarrow (\nabla n_0)^{QL} \equiv \nabla n_0 + (\nabla n_0)^*$, $C_s^2 \rightarrow C_s^{QL2} \equiv C_s^2 + C_s^{*2}$, $\nu_{en} \rightarrow \nu_{en}^{QL} \equiv \nu_{en} + \nu^*$, where the parameters with stars indicate additional or effective terms due to quasi-linear effects. From (2.59) it is obvious that to slow down the wave growth one would need $V_d^{QL} < V_d$, $(|\nabla n_0|)^{QL} < |\nabla n_0|$, $C_s^{QL2} > C_s^2$, $\nu_{en}^{QL} > \nu_{en}$. Thus there are four main quasi-linear theories. Physical processes that they consider are velocity retardation ("drift velocity becomes smaller"), anti-gradient formation ("gradient becomes smaller"), turbulent heating ("temperatures of species become larger"), and, finally, anomalous collisions ("collision frequencies become larger"). We will briefly describe each of these theories.

2.2.1 Velocity Retardation in a Bounded Jet

The theory of velocity retardation was first formulated by *Sato* [1974]. Qualitatively it can be described as follows.

Figure 2.4 shows a F-B wave propagating in a bounded jet ($0 < x < L$) along the y axis. Since electrons are more mobile than ions, a polarization electric field $\delta\mathbf{E}_y$ is set within the wave. It is directed parallel to the y axis for the crests and antiparallel to the y axis for the troughs of the wave profile. In the course of wave motion, electrons experience $\delta\mathbf{E}_y \times \mathbf{B}_z$ drift along the x axis. Again, the direction of drift is along the x axis for the troughs and antiparallel to the x axis for the crests. However, as *Sato* [1974] showed there is an effective accumulation of electrons at the $x = 0$ boundary and accumulation of ions at the $x = L$ boundary. This causes the appearance of an effective electric field $\mathbf{E}_{eff}$ directed from $x = L$ to $x = 0$, that is opposite to the direction of the initial electric field $\mathbf{E}_0$ (which was along the x axis). $\mathbf{E}_{eff}$ thus partially cancels $\mathbf{E}_0$, causing the retardation of the phase velocity of the wave and decrease of the growth rate (which is proportional to the vector sum of the two electric fields).

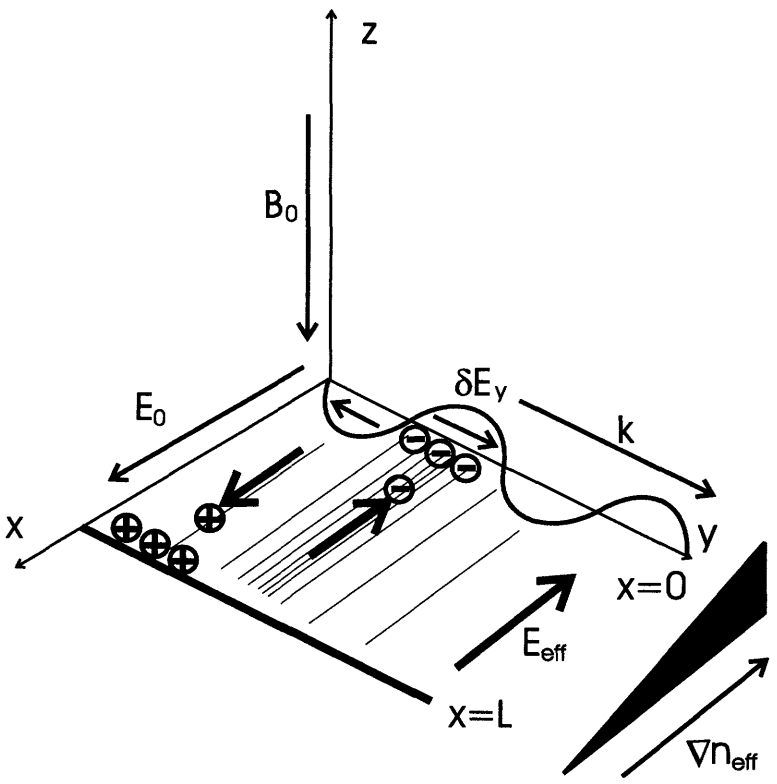

Figure 2.4: F-B wave propagating along a bounded jet.

2.2.2 Anti-Gradient Formation in a Bounded Jet

A similar physical mechanism was proposed later by *Sato* [1976] both for the F-B and G-D waves. Continuing the reasoning described above, on the $x = 0$ border there are more electrons than ions at $x = L$ (since electrons are more mobile than ions). Because of that, immediately after the wave starts to propagate along the y axis, a negative density gradient ∇n_{eff} along the x axis (anti-gradient) starts to form, which decreases the growth of the wave. (For G-D wave excitation along the y axis, the gradient should be positive.)

2.2.3 Turbulent Heating

It is well known that ions are heated when strong electric fields are imposed on the ionosphere due to their collisions with background neutrals [e.g., *Schlegel and St.-Maurice*, 1981]. Electrons at E-region heights can also be heated by the action of electric fields perpendicular to the magnetic field. This heating, however, is not so much due to collisions (collision frequencies of electrons with neutrals are too small) but because of the unstable F-B plasma waves that grow due to the imposed electric field [*St.-Maurice et al.*, 1981; *Robinson*, 1986]. Enhancement of the electron and ion temperatures increases the ion acoustic speed, which in turn, affects the growth of F-B waves. The electron heating was found to be significantly larger than that of the ions and most significant at the center of the electrojet layer.

The observed amplitudes of density fluctuations, on the other hand, are in general too small to account for the heating rates observed if the electrons are driven in the perpendicular direction only. *St.-Maurice and Laher* [1985], therefore, assumed that the electrons are heated mostly by the wave component parallel to the magnetic field, which implies the waves with finite aspect angles. Later *Hamza and St.-Maurice* [1995a,b] using a new nonlinear fluid theory of anomalous transport for the F-B instability concluded that the wave energy can be converted into the parallel electron energy and that the electron heating comes from parallel electrostatic fields.

Existence of waves with nonzero parallel component is also important at high latitudes for another reason. For strong electric field conditions ($E > 50$ mV m^{-1}), the perpendicular mode coupling (Section 2.3) can not account for the damping of energy from the linearly unstable waves propagating along the flow, since most of the modes that could have been produced are linearly unstable (the linear cone becomes quite wide). In this case, the generation of the modes at "large" aspect angles (large parallel components of the electric field) can be invoked in order to channel the

excessive wave energy.

2.2.4 Theory of Diffusion Orbit (Anomalous Collisions)

Sudan [1983] proposed another quasi-linear theory by considering resonance broadening effects, that is the effects of electron scattering by the F-B waves. He established that one can treat these effects by replacing the wave frequency $\omega_{\mathbf{k}}$ in the dispersion equation by $\omega_{\mathbf{k}}+ik_{\perp}^2 D^*$, where $D^* = \nu^* T_e/m_e\Omega_e^2$ is the anomalous diffusion coefficient and ν^* is the anomalous collision frequency. *Sudan* [1983] applied the kinetic theory to the electron motions and adopted the fluid approach for the ion motions. He obtained an essentially fluid-type dispersion relation and showed that the inclusion of D^* requires Ψ to be replaced by $\Psi + \Psi^*$ in the fluid dispersion relation for waves propagating precisely orthogonal to the magnetic field (aspect angle $\alpha = 0°$), where Ψ^* is given by

$$\Psi^* = \frac{\nu^*\nu_i}{|\Omega_e|\Omega_i}. \tag{2.73}$$

This has a formally simple, though physically profound, effect on the fluid dispersion relation, which becomes (without consideration of gradients and ion drifts)

$$\omega_{\mathbf{k}r} = \frac{\mathbf{k}\cdot\mathbf{V}_d}{1+\Psi+\Psi^*}, \tag{2.74}$$

$$\gamma_{\mathbf{k}} = \frac{\Psi+\Psi^*}{1+\Psi+\Psi^*}\frac{\omega_{\mathbf{k}r}^2 - k^2C_s^2}{\nu_i}. \tag{2.75}$$

Sudan interpreted equations (2.74)–(2.75) as follows. When the drift velocity exceeds the threshold value, the wave amplitude grows and D^*, ν^*, and Ψ^* increase from zero. This has the effect of decreasing both the phase velocity and the growth rate of the waves. The wave continues to grow until ν^* reaches a value given by

$$\nu^* = \frac{\Omega_i|\Omega_e|}{\nu_i}\left(\frac{V_d\cos\theta}{C_s} - 1 - \Psi\right), \tag{2.76}$$

at which point the growth rate returns to zero (i.e. the wave amplitude stabilizes) and the phase speed falls to the ion acoustic speed C_s.

The theory of diffusion orbit by *Sudan* [1983] was proposed for the equatorial electrojet. Later *Robinson* [1986] extended this idea to the high latitudes and related the wave-induced diffusion to the anomalous enhancement of the E-region electron temperature. *St.-Maurice* [1987] noted that the anomalous diffusion should take place in the direction perpendicular to the direction where anomalous collisions are the strongest, that is anomalous diffusion should be most effective not along the direction of unstable wave propagation but perpendicular to it. *St.-Maurice* [1987] tried to generalize the idea by assuming a "bath" of anisotropic turbulence in all directions (perpendicular to the magnetic field). He concluded that still anomalous diffusion is not strong enough to support a saturation state consistent with observations, though it can provide up to 4 times enhancement in the electron collision frequency.

Finally, one should note that though the theory of anomalous collisions was originally developed for zero aspect angle, the prediction of the theory on the phase velocity (2.74) has been applied later to the case of nonzero aspect angles, in response to new experimental data on the aspect angle variation of the Doppler velocity (see Section 4.3.2). Under this assumption, because of the electron collision frequency enhanced due to the wave-particle interaction ($\nu_e \rightarrow \nu^* \cong 5 \cdot \nu_e$), the aspect angle dependence of the Doppler velocity becomes much slower than predicted by the linear theory. Unfortunately, very little theoretical work has been done with respect to the plasma waves propagating outside of the linear aspect angle cone, at "large" aspect angles ($\alpha > \alpha_0 = 1°$–$2°$). Therefore, the idea about the substitution of the nominal electron collision frequency by the anomalously large value in the expression for the oscillation frequency can not be regarded as a **theory** but rather represents the **empirical knowledge** derived from the observations of the E-region auroral echoes at large aspect angles.

2.2.5 Phase Velocity: C_s Saturation and Modification by Background Gradients

The condition $\gamma^{QL} = 0$, applied to the F-B waves immediately gives the result

$$V_{ph} = \frac{\omega_{\mathbf{kr}}}{k} = C_s \tag{2.77}$$

for the phase velocity. Therefore, quasi-linear theories (with the only exception of the theory of anti-gradient formation by *Sato* [1976]) predict the exact equality of phase velocity and local ion acoustic speed (C_s saturation). Hence phase velocity of waves in a saturated regime according to these theories does not depend on wavelength, aspect and flow angles.

If one applies the $\gamma^{QL} = 0$ condition to the full expression for the linear growth rate, the gradient term in (2.59) will modify the phase velocity [*Farley and Fejer*, 1975]. Depending on the sign of the gradient, the phase velocity can be either larger or smaller than the ion acoustic speed

$$V_{ph} = C_s \left[(1 + F^2)^{1/2} - F\right] \tag{2.78}$$

with

$$F = \frac{\nu_i \Omega_e}{2\nu_e k^2 L C_s}. \tag{2.79}$$

Notice that the phase velocity in this approach is scale dependent, the amount of deviation from the ion acoustic speed depends on wave number k. For larger wave numbers k (smaller wavelengths) the phase velocity is closer to C_s. The deviation also depends on gradient: the smaller the value of L (typical scale of the gradient), the larger the deviation. If $L = \infty$, we have a homogeneous plasma and the phase velocity is equal to the ion acoustic speed. Thus we recover the case of pure F-B waves, considered in the first paragraph of this section.

2.3 Nonlinear Theories and Numerical Simulations

Both linear and quasi-linear theories are unable to explain the generation of meter-scale irregularities detected experimentally in the equatorial electrojet for the conditions when electric fields were substantially below F-B threshold (the lowest possible wavelength in this case was found to be $\sim$ 40 m, see Section 2.1.6).

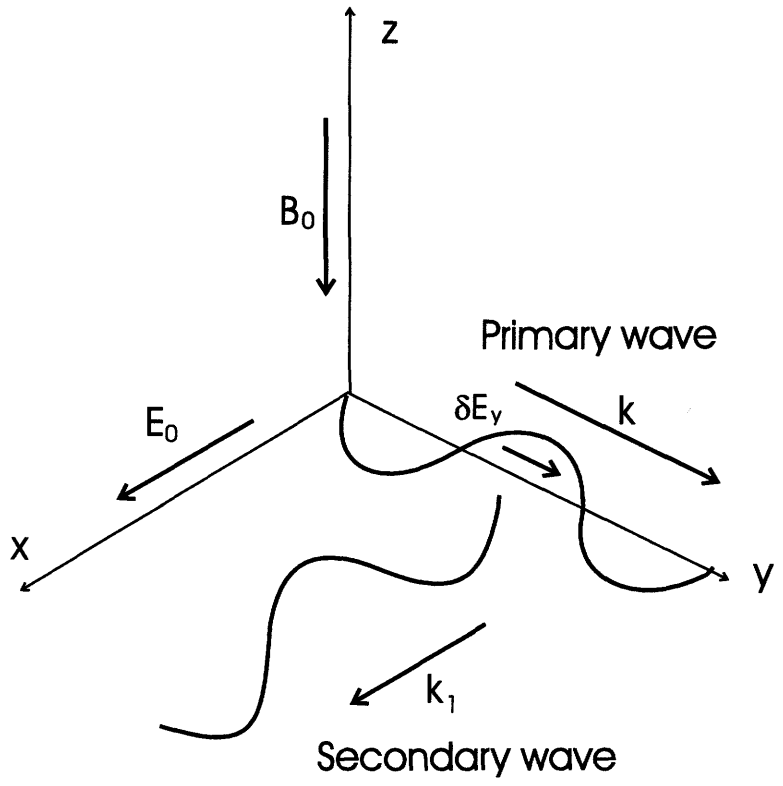

Figure 2.5: Primary and secondary waves.

Sudan et al. [1973] proposed a two-step mechanism for generation of meter-scale irregularities for subcritical electric fields. The qualitative idea can be formulated as follows. Consider a G-D wave propagating along the y axis as shown in Figure 2.5. Similar to the reasoning in Section 2.2.1, the initial perturbation in density with wave vector $\mathbf{k} = k_y \mathbf{e}_y$ and scale of $\sim$ 100 m causes a polarization electric field (δE_y in Figure

2.5) along the y axis. This polarization field can produce waves with wave vectors perpendicular to the initial direction ($\mathbf{k}_1 = k_{1x}\mathbf{e}_x$) once it exceeds the threshold value needed for the instability to occur (this threshold is around zero for the G-D instability and $\sim$ 20 mV m^{-1} for the F-B instability, respectively). The first type of waves is called primary waves (or modes) and the second type, generated by the polarization electric fields, is called secondary waves (modes). The secondary modes in their turn can trigger "the second cascade" of secondary waves that propagate along the initial direction of propagation. It is assumed that secondary waves also have smaller wavelengths, so that during nonlinear processes of secondary wave generation there is an energy transfer from primary to secondary modes or in other words from larger to smaller structures. It is said that in this case we have a "direct" cascade of energy [e.g., *Kadomtsev*, 1965].

All these modes, generally speaking, interact with each other (this process is called *mode coupling*). The primary modes are linearly growing, while the secondaries are strongly damped in the linear regime (their direction of propagation is outside the linear instability cone), but since we have an energy transfer from primaries to secondaries, a saturation level can be achieved. *Sudan et al.* [1973] did not consider the limit on the growth rate of the large-scale irregularities explicitly, but it is quite clear that the direct transfer of energy as described above can easily provide this.

The nonlinear saturation mechanisms for the F-B and G-D instabilities has been considered in a number of papers [e.g., *Kamenetskaya*, 1971; *Rogister*, 1971; *Sato*, 1972; *Sudan and Keskinen*, 1977]. We, however, are mostly interested in results on the phase velocity of irregularities.

In this sense of special interest is the study by *Rogister and Jamin* [1975], who considered the nonlinear 2-D fluid theory of the F-B instability in the equatorial electrojet. It was demonstrated that phase velocity inside the F-B instability cone is not limited by the ion acoustic speed C_s but maximizes at zero flow angle at the

background electron drift velocity V_{e0} (assumed to be larger than C_s) and slowly decreases with flow angle reaching C_s at some angle ($\sim 30°$).

Another important result with respect to velocity was obtained by *Hamza and St.-Maurice* [1993a,b]. According to this theory, the nonlinear growth rate $\gamma_{\mathbf{k}}^{NL}$ can be expressed as

$$\gamma_{\mathbf{k}}^{NL} = \frac{1}{N_{\mathbf{k}}} \sum_{\omega} \left\{ \frac{\psi}{\nu_i(1+\psi)} \left(\omega^2 - k^2 C_s^2\right) + \frac{\mathbf{k}\cdot\mathbf{K}}{k^2(1+\psi)} \frac{\nu_i}{\Omega_i} \omega \right\} |n_{\mathbf{k}\omega}|^2 , \tag{2.80}$$

where

$$\mathbf{K} \equiv \frac{\nabla n_0 \times \mathbf{B}}{n_o B} \tag{2.81}$$

and

$$N_{\mathbf{k}} \equiv \sum_{\omega} |n_{\mathbf{k}\omega}|^2 . \tag{2.82}$$

The frequency spectrum can be characterized in terms of two observables, namely by the average mode frequency $\overline{\omega}_{\mathbf{k}}$ and the average mode frequency spread $\Delta\omega_{\mathbf{k}}$ defined as:

$$\overline{\omega}_{\mathbf{k}} \equiv \frac{1}{N_{\mathbf{k}}} \sum_{\omega} \omega \, |n_{\mathbf{k}\omega}|^2 , \tag{2.83}$$

$$\Delta\omega_{\mathbf{k}}^2 \equiv \frac{1}{N_{\mathbf{k}}} \sum_{\omega} (\omega - \overline{\omega}_{\mathbf{k}})^2 \, |n_{\mathbf{k}\omega}|^2 . \tag{2.84}$$

Using these two variables the nonlinear growth rate (2.80) can be rewritten in the following compact form:

$$\gamma_{\mathbf{k}}^{NL} = \frac{\psi}{\nu_i(1+\psi)} \left(\overline{\omega}_{\mathbf{k}}^2 - k^2 C_s^2 + \Delta\omega_{\mathbf{k}}^2\right) + \frac{\mathbf{k}\cdot\mathbf{K}}{k^2(1+\psi)} \frac{\nu_i}{\Omega_i} \overline{\omega}_{\mathbf{k}} . \tag{2.85}$$

For the steady state the growth rate has to vanish $\gamma_{\mathbf{k}}^{NL} = 0$, which gives the quasi-stationary equation:

$$\frac{\psi}{\nu_i(1+\psi)} \left(\overline{\omega}_{\mathbf{k}}^2 - k^2 C_s^2 + \Delta\omega_{\mathbf{k}}^2\right) + \frac{\mathbf{k}\cdot\mathbf{K}}{k^2(1+\psi)} \frac{\nu_i}{\Omega_i} \overline{\omega}_{\mathbf{k}} = 0. \tag{2.86}$$

Given the above conditions, *Hamza and St.-Maurice* [1993a] considered the gradient-free situation ($\mathbf{K} = 0$) for two extreme cases. First, the average frequency spread

(which is related to the spectral width) was assumed to be small (the case of weak turbulence in their terminology). In this case (2.86) implies that

$$\overline{\omega}_{\mathbf{k}}^2 \cong k^2 C_s^2. \tag{2.87}$$

Second, the average frequency spread was assumed to be comparable with the average frequency (the case of strong turbulence). Then, from (2.86) it follows that

$$\overline{\omega}_{\mathbf{k}}^2 + \Delta\omega_{\mathbf{k}}^2 = k^2 C_s^2. \tag{2.88}$$

One can extend the reasoning above to the case of nonhomogeneous plasma $\mathbf{K} \neq 0$ [*St.-Maurice et al.*, 1994]. Then equation (2.86) is a quadratic equation with the oscillation frequency $\overline{\omega}_{\mathbf{k}}$ as a variable. In terms of solutions for phase velocity, there are two types of situations: phase velocity larger and smaller than the ion acoustic speed. In a case when the spectral width is not zero the phase velocity would be even smaller.

Because of the ever-increasing computational capacities, numerical simulations have proven to be another very useful tool for the study of E-region auroral irregularities. In Table 2.1 we reproduce the expanded list of most relevant works in the field from *Janhunen* [1994].

Numerical studies try to resolve some of the discrepancies between linear and quasi-linear theories and experimental results and in this sense they are similar to nonlinear theories. Some studies [e.g., *Keskinen et al.*, 1979] suggest that mean frequencies (and hence phase velocities) agree well with the linear theory except at short wavelengths, as one would expect on the basis of kinetic theory. *Oppenheim et al.* [1996] explored the nonlinear behavior of the F-B instability and showed that the phase velocity of the saturated waves is below the one predicted by linear theory but above the ion acoustic speed (prediction of quasi-linear theories).

3D	Kinetic	Nonlinear	Nature	Sample References
Yes	No	No	Analytic	*Buneman* [1963]
Yes	Yes	No	Analytic	*Farley* [1963]
No	No	Yes	2D fluid simulations	*McDonald et al.* [1974]; *Ferch and Sudan* [1977]; *Keskinen et al.* [1979]; *Ronchi et al.* [1991]; *Oppenheim et al.* [1995, 1996]
Yes	Yes	No	Analytic/numerical	*Ossakow et al.* [1975]; *Schlegel* [1983]
Yes	No	Yes	3D fluid simulations	*Janhunen* [1992]
No	Yes	Yes	2D particle simulations	*Machida and Goertz* [1988]; *Janhunen* [1994] *Schlegel and Thiemann* [1994] *Otani and Oppenheim* [1998]
Yes	Yes	Yes	3D particle simulations	In the future

Table 2.1: First-principle E-region studies.

2.4 Summary

In this chapter we considered theories of E-region irregularities. In Section 2.1 general expressions for background drifts of ions and electrons, valid in a wide range of ionospheric heights, were derived using standard two-fluid equations. The expressions for background drifts for the E region were then obtained and analyzed. We showed that the motion of ions in the E region is determined by the combined action of the Pedersen drift and the neutral wind, while electrons move with the $\mathbf{E} \times \mathbf{B}$ velocity (Hall drift). A general 2-D dispersion equation for the F-B and G-D instability was then derived and analyzed. It was demonstrated that for small electric fields the strong gradients of the background electron density can modify the properties of the waves. Finally, a summary of theoretical predictions on the properties of the phase velocity of waves was presented.

2.4.1 Phase Velocity and Wave Vector

One of the most fundamental characteristics of E-region waves is the dependence of the phase velocity upon the wave vector $V_{ph} = V_{ph}(\mathbf{k})$. This dependence not only has to do with the scale dependence of the phase velocity (the dependence upon wave number k or wavelength $\lambda_k = 2\pi/k$) but also it provides invaluable information about the dispersive properties of the waves.

A wave vector in general has three components. In radar physics, it is customary to specify $\mathbf{k}$ by the wave number $k = |\mathbf{k}|$ (magnitude of the wave vector) and two angles, the aspect angle α and flow angle θ. One can thus consider three kinds of dependencies by varying one parameter and fixing the other two parameters: phase velocity versus wave number/scale, phase velocity versus aspect angle, and phase velocity versus flow angle.

2.4.2 Aspect Angle Effects

The prediction of linear fluid theory is that the phase velocity of irregularities should maximize at perfect aspect angle $\alpha = 0°$ and decrease rapidly with increasing aspect angle (the thin solid line in Figure 2.2). Phase velocity is a symmetric function of aspect angle: $V_{ph}(-\alpha) = V_{ph}(\alpha)$.

Inclusion of the effects of wave-particle interaction (Section 2.2.4) leads to the prediction of much slower decrease of the phase velocity with aspect angle because of the larger effective collision frequency for the electrons.

2.4.3 Flow Angle Effects

According to linear fluid theory, the phase velocity is proportional to the cosine of the angle between the relative electron-ion drift $\mathbf{V}_d$ and the wave vector $\mathbf{k}$. For very

small electric fields, however, and for either strong gradients of background density or elevated temperatures the phase velocity is also dependent on the direction of the density gradient **G**.

Quasi-linear theories give no dependence of the phase velocity upon the direction of propagation for waves within the instability cone. Nonlinear theory of *Rogister and Jamin* [1975] predicts slow change of the phase velocity of the F-B waves within the instability cone with the maximum equal to the background electron drift velocity at zero flow angle.

2.4.4 Scale Effects

Linear fluid theory predicts no dependence of the phase velocity of the F-B and G-D waves upon the irregularity wavelength.

On the other hand, kinetic effects (that might be important for waves shorter than few meters) effectively increase the phase velocity of the F-B waves under the assumption that phase velocities of the F-B waves are limited to threshold values, so that according to this approach there is a decrease of the phase velocity with the wavelength. The "fastest-growing-waves" approach gives the opposite result, a velocity increase with the wavelength.

Quasi-linear theories predict that, for waves in a saturated state, gradients of the electron density might modify the phase velocity. If for the homogeneous plasma $V_{ph} = C_s$, then in the presence of gradients the phase velocity could deviate from C_s. The amount of deviation depends on the wave and gradient scales. Also, depending on the direction of the gradient vector, the phase velocity is either larger or smaller than C_s, thus either increasing or decreasing with the wavelength.

Chapter 3

Secondary Instability in the Dynamics of the Farley-Buneman Fluctuations

In this chapter the nonlinear theory of the Farley-Buneman instability is considered. In Section 3.2 a nonlinear equation for spatial Fourier transform of electron density perturbations is derived using some results from Chapter 2. Section 3.3 contains the theory of secondary F-B instability in the wave kinetic equation approach. We discuss new nonlinear theory and its predictions in Section 3.4. Results presented in this chapter were published in the paper by *Smolyakov et al.* [2001]. Although the contribution of the candidate has been mostly the analysis of the dispersion equation (Section 3.3.4), we present in more detail the entire content of this study.

3.1 Introduction

In the previous chapter it was demonstrated that the theoretical framework for the linear theory of the F-B instability is well established while there remains a number of issues within the nonlinear theory that are now under investigation.

Traditionally, various researchers studied the mechanisms that provide the energy flow from the larger to smaller plasma structures as described in Section 2.3, that is, direct or forward cascade. For example, *Ronchi et al.* [1991] investigated the evolution of large-scale structures and their role in the dynamics of the meter-scale irregularities for the case of the gradient drift instability. For the pure F-B instability, computer simulations by *Oppenheim et al.* [1996] showed that excitation of the smaller-wavelength secondary waves plays an important role in the nonlinear saturation of this instability.

On the other hand, electric field and plasma density fluctuation measurements made on sounding rockets have shown that the intensity of irregularities increases towards larger scales [e.g., *Pfaff et al.*, 1984]. Figure 3.1 shows one example of such measurements. Indicated in Figure 3.1 is the frequency ω that approximately corresponds to meter-scale waves. As frequency decreases in the region near ω (wavelength increases) the irregularity intensity goes up. This means that the waves with longer wavelength are more intense. Since F-B waves can be excited only at wavelengths shorter than $\sim$ 100 m [*Schlegel and St.-Maurice*, 1983], this implies the possibility of support of significantly larger-scale fluctuations by the energy flow from shorter-wavelength irregularities, i.e., an inverse cascade. *Keskinen* [1981] showed that long-wavelength strong $\mathbf{E} \times \mathbf{B}$ turbulence can stabilize the short-wavelength F-B modes through nonlinear mode coupling processes corresponding to the energy flow towards larger scales. Migration of energy to long-wavelength structures in the process of the electrojet instability evolution has been also noticed by *Ronchi et al.* [1991].

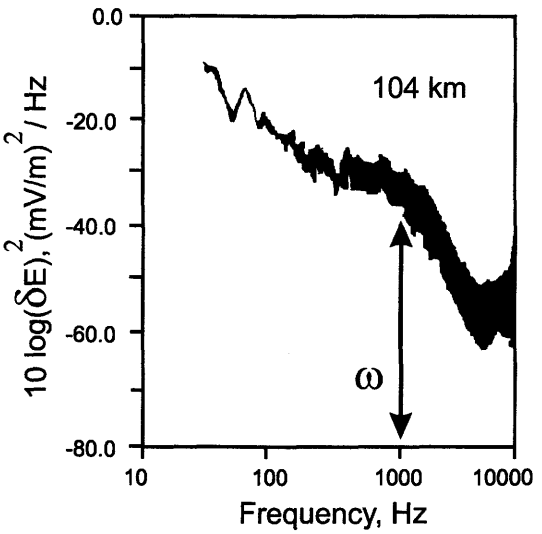

Figure 3.1: Electric field spectrum. Adapted from *Pfaff et al.* [1984]

In this chapter we explore the possibility of energy transfer from smaller to larger structures in the course of the F-B instability development. In this respect, *Sharma and Kaw* [1986] considered modification of the long-wavelength G-D modes in the presence of short-wavelength F-B waves and predicted that the effect can be significant under some conditions. Our goal is somewhat similar: We study the dynamics of long-wavelength perturbations that are coupled to and modified by the primary (short-wavelength) F-B fluctuations. A related problem was also considered by *Sahr and Farley* [1995], who analyzed excitation of secondary waves via the three-wave coupling mechanism.

3.2 Nonlinear Equation for Density Perturbations

In Chapter 2 we derived two equations for density and electric field perturbations. The next step is to derive one single equation for density perturbation. In order to

do that one needs to relate these two variables.

3.2.1 Relationship $\phi_{\mathbf{k}}$ and $n_{\mathbf{k}}$

By neglecting the nonlinear term in (2.34) one can relate the Fourier transforms of perturbations of density and electrostatic potential:

$$n_{\mathbf{k}} = -i\frac{\phi_{\mathbf{k}}}{B}\frac{r_e(k^2 - ia) + ib}{\omega_{\mathbf{k}} - (\mathbf{k} + i\mathbf{G})\cdot\mathbf{V}_{e0} + iC_e\left[r_e(k^2 - ia) + ib\right]}. \tag{3.1}$$

Following *Sudan et al.* [1997], when considering nonlinear effects we will neglect the gradients ($G = 0$, $a = 0$, $b = 0$) and the imaginary part in the denominator:

$$n_{\mathbf{k}} \cong -i\frac{\phi_{\mathbf{k}}}{B}\frac{r_e k^2}{\omega_{\mathbf{k}r} - \mathbf{k}\cdot\mathbf{V}_{e0}}. \tag{3.2}$$

Using (2.43) and (2.38) we obtain

$$\frac{\phi_{\mathbf{k}}}{B} = i\,\frac{\mathbf{k}\cdot\mathbf{V}_{e0}}{k^2}\frac{r_i}{1+\psi}\,n_{\mathbf{k}} = i\,\frac{\omega_{\mathbf{k}r} r_i}{k^2}\,n_{\mathbf{k}}. \tag{3.3}$$

3.2.2 Nonlinear Equation for Density Perturbations

Expressing $(\nabla + \mathbf{G})\cdot\delta\mathbf{E}/B$ from the ion equation (2.25)

$$(\nabla + \mathbf{G})\cdot\frac{\delta\mathbf{E}}{B} = \left[\left(\frac{1}{\Omega_i}\frac{\partial}{\partial t} + r_i\right)\frac{\partial}{\partial t} - C_i(\nabla + \mathbf{G})\cdot\nabla\right]\frac{\delta n}{n_0} \tag{3.4}$$

and substituting into the electron equation (2.29) we have

$$\left\{(1+\psi)\frac{\partial}{\partial t} + \frac{\psi}{\nu_i}\left[\frac{\partial^2}{\partial t^2} - C_s^2(\nabla + \mathbf{G})\cdot\nabla\right] + \mathbf{V}_{e0}\cdot\nabla\right\}\frac{\delta n}{n_0} + \\ + \mathbf{G}\times\mathbf{e}_z\cdot\frac{\delta\mathbf{E}}{B} + \delta\mathbf{V}_e\cdot\nabla\frac{\delta n}{n_0} = 0. \tag{3.5}$$

The last term in (3.5) contains perturbations of both electron drift velocity and electron density and hence is nonlinear. Using (2.26), it can be approximately written

as

$$\delta \mathbf{V}_e \cdot \nabla \frac{\delta n}{n_0} \cong -\frac{\delta \mathbf{E}}{B} \times \mathbf{e}_z \cdot \nabla \frac{\delta n}{n_0} = \frac{\nabla \delta\phi}{B} \times \mathbf{e}_z \cdot \nabla \frac{\delta n}{n_0} = -\frac{\nabla \delta\phi}{B} \times \nabla \frac{\delta n}{n_0} \cdot \mathbf{e}_z. \tag{3.6}$$

Finally, similar to *Hamza and St.-Maurice* [1993b] we consider Case 2 in our terminology, $a = 0$. Then (3.5) becomes

$$\left\{ \frac{\partial}{\partial t} + \frac{\psi}{1+\psi} \frac{1}{\nu_i} \left[\frac{\partial^2}{\partial t^2} - C_s^2 \nabla^2 \right] + \frac{\mathbf{V}_{e0} \cdot \nabla}{1+\psi} \right\} \frac{\delta n}{n_0} -$$
$$- \frac{1}{1+\psi} \mathbf{G} \times \mathbf{e}_z \cdot \frac{\nabla \delta\phi}{B} - \frac{1}{1+\psi} \frac{\nabla \delta\phi}{B} \times \nabla \frac{\delta n}{n_0} \cdot \mathbf{e}_z = 0. \tag{3.7}$$

3.2.3 Linear Dispersion Equation

Let us demonstrate that (3.7) gives the same result for the oscillation frequency and growth rate as the result obtained in Section 2.1. Dropping the last nonlinear term in (3.7) and using (3.3) we obtain for Fourier transform of density perturbations $\delta n/n_0 \sim n_{\mathbf{k}} \exp(i\mathbf{k} \cdot \mathbf{r} - i\omega_{\mathbf{k}} t)$

$$\frac{\psi}{\nu_i} \left[\omega_{\mathbf{k}r}^2 - k^2 C_s^2 \right] + i(1+\psi)(\omega_{\mathbf{k}r} + i\gamma_{\mathbf{k}}) - i\mathbf{k} \cdot \mathbf{V}_{e0} - \omega_{\mathbf{k}r} r_i \frac{b}{k^2} = 0. \tag{3.8}$$

To find $\omega_{\mathbf{k}r}$ and $\gamma_{\mathbf{k}}$ we take the real and imaginary parts of (3.8):

$$\frac{\psi}{\nu_i} \left[\omega_{\mathbf{k}r}^2 - k^2 C_s^2 \right] - (1+\psi)\gamma_{\mathbf{k}} - \omega_{\mathbf{k}r} r_i \frac{b}{k^2} = 0, \tag{3.9}$$

$$(1+\psi)\ \omega_{\mathbf{k}r} - \mathbf{k} \cdot \mathbf{V}_{e0} = 0. \tag{3.10}$$

From (3.9)–(3.10) it immediately follows that

$$\gamma_{\mathbf{k}} = \frac{\psi}{1+\psi} \left\{ \frac{1}{\nu_i} \left[\omega_{\mathbf{k}r}^2 - k^2 C_s^2 \right] - \omega_{\mathbf{k}r}\ r_e^{-1}\ \frac{b}{k^2} \right\}, \tag{3.11}$$

$$\omega_{\mathbf{k}r} = \frac{\mathbf{k} \cdot \mathbf{V}_{e0}}{1+\psi}. \tag{3.12}$$

One should note, however, that dispersion equation (3.8) is not the exact linear dispersion equation (2.37), but rather an approximation. One can easily show that if, instead of (3.2), (3.1) would be used, then the resultant dispersion equation would be the same as (2.37).

3.2.4 Nonlinear Equation for Fourier Transforms

To obtain a nonlinear equation in terms of Fourier components one needs to apply a somewhat different procedure than the one that was used before when we just made substitutions $\partial/\partial t(\delta n/n_0) \rightarrow -i\omega_{\mathbf{k}}\delta n/n_0$, $\nabla(\delta n/n_0) \rightarrow i\mathbf{k}\delta n/n_0$.

First, we introduce the Fourier transforms perturbations of density and potential in space only:

$$\frac{\delta n}{n_0}(\mathbf{r},t) \equiv \int n_{\mathbf{k}}(t)e^{i\mathbf{k}\cdot\mathbf{r}}d\mathbf{k}, \tag{3.13}$$

$$\delta\phi(\mathbf{r},t) \equiv \int \phi_{\mathbf{k}'}(t)e^{i\mathbf{k}'\cdot\mathbf{r}}d\mathbf{k}'. \tag{3.14}$$

Next, we substitute (3.13) and (3.14) into nonlinear equation (3.7)

$$\int\left\{\frac{\partial}{\partial t}+\frac{\psi}{1+\psi}\frac{1}{\nu_i}\left[\frac{\partial^2}{\partial t^2}+C_s^2k^2\right]+\frac{\mathbf{V}_{e0}\cdot i\mathbf{k}}{1+\psi}\right\}n_{\mathbf{k}}(t)e^{i\mathbf{k}\cdot\mathbf{r}}d\mathbf{k}-$$
$$-\frac{1}{(1+\psi)B}\int \mathbf{G}\times\mathbf{e}_z\cdot i\mathbf{k}\;\;\phi_{\mathbf{k}}(t)e^{i\mathbf{k}\cdot\mathbf{r}}d\mathbf{k}-$$
$$-\frac{1}{(1+\psi)B}\int\int i\mathbf{k}'\times i\mathbf{k}''\cdot\mathbf{e}_z\;\;n_{\mathbf{k}'}(t)\phi_{\mathbf{k}''}(t)e^{i(\mathbf{k}'+\mathbf{k}'')\cdot\mathbf{r}}d\mathbf{k}'d\mathbf{k}''=0. \tag{3.15}$$

The last term in (3.15) describes the nonlinear interaction of all kinds of modes with wave vectors $\mathbf{k}'$ and $\mathbf{k}''$. For momentum to be conserved in such interactions, the condition

$$\mathbf{k}'+\mathbf{k}''=\mathbf{k} \tag{3.16}$$

should hold. Then $d\mathbf{k}''=d(\mathbf{k}-\mathbf{k}')\rightarrow d\mathbf{k}$ and (3.15) can be rewritten as

$$\int\left\{\frac{\partial}{\partial t}+\frac{\psi}{1+\psi}\frac{1}{\nu_i}\left[\frac{\partial^2}{\partial t^2}+C_s^2k^2\right]+i\omega_{\mathbf{k}r}\right\}n_{\mathbf{k}}(t)e^{i\mathbf{k}\cdot\mathbf{r}}d\mathbf{k}-$$
$$-\frac{1}{(1+\psi)B}\int \mathbf{G}\times\mathbf{e}_z\cdot i\mathbf{k}\;\;\phi_{\mathbf{k}}(t)e^{i\mathbf{k}\cdot\mathbf{r}}d\mathbf{k}+$$
$$+\frac{1}{(1+\psi)B}\int\int \mathbf{k}'\times(\mathbf{k}-\mathbf{k}')\cdot\mathbf{e}_z\;\;n_{\mathbf{k}'}(t)\phi_{\mathbf{k}-\mathbf{k}'}(t)e^{i\mathbf{k}\cdot\mathbf{r}}d\mathbf{k}'d\mathbf{k}=0 \tag{3.17}$$

or for each mode $\mathbf{k}$ using definition of b (2.32)

$$\left\{\frac{\partial}{\partial t}+\frac{\psi}{1+\psi}\frac{1}{\nu_i}\left[\frac{\partial^2}{\partial t^2}+C_s^2k^2\right]+i\omega_{\mathbf{k}r}\right\}n_{\mathbf{k}}(t)-\frac{ib}{(1+\psi)B}\;\;\phi_{\mathbf{k}}(t)-$$

$$-\frac{1}{(1+\psi)B}\int \mathbf{k}'\times(\mathbf{k}-\mathbf{k}')\cdot\mathbf{e}_z\ n_{\mathbf{k}'}(t)\ \phi_{\mathbf{k}-\mathbf{k}'}(t)\ d\mathbf{k}'=0. \tag{3.18}$$

And finally, using the relationship between $n_{\mathbf{k}}$ and $\phi_{\mathbf{k}}$ (3.3), we obtain

$$\left\{\frac{\partial}{\partial t}+\frac{\psi}{1+\psi}\frac{1}{\nu_i}\left[\frac{\partial^2}{\partial t^2}+C_s^2k^2\right]+i\omega_{\mathbf{k}r}+\frac{r_i\ b}{1+\psi}\frac{\omega_{\mathbf{k}r}}{k^2}\right\}n_{\mathbf{k}}(t)+$$
$$+\frac{ir_i}{(1+\psi)^2}\int \mathbf{k}'\times(\mathbf{k}-\mathbf{k}')\cdot\mathbf{e}_z\ \frac{(\mathbf{k}-\mathbf{k}')\cdot\mathbf{V}_{e0}}{|\mathbf{k}-\mathbf{k}'|^2}\ n_{\mathbf{k}'}(t)\ n_{\mathbf{k}-\mathbf{k}'}(t)\ d\mathbf{k}'=0 \tag{3.19}$$

or

$$\left\{\frac{\partial}{\partial t}+i\omega_{\mathbf{k}r}+\frac{\psi}{1+\psi}\left[\frac{1}{\nu_i}\left(\frac{\partial^2}{\partial t^2}+C_s^2k^2\right)+\omega_{\mathbf{k}r}r_e^{-1}\frac{b}{k^2}\right]\right\}n_{\mathbf{k}}(t)+$$
$$+\int M_{\mathbf{k}',\mathbf{k}-\mathbf{k}'}\ n_{\mathbf{k}'}(t)\ n_{\mathbf{k}-\mathbf{k}'}(t)\ d\mathbf{k}'=0, \tag{3.20}$$

where we introduced the symmetrized coupling coefficient $M_{\mathbf{k}',\mathbf{k}-\mathbf{k}'}$ as

$$M_{\mathbf{k}',\mathbf{k}-\mathbf{k}'}\equiv\frac{i}{2}\frac{r_i}{(1+\psi)^2}\ (\mathbf{k}-\mathbf{k}')\times\mathbf{k}'\cdot\mathbf{e}_z\left\{\frac{\mathbf{k}'\cdot\mathbf{V}_{e0}}{k'^2}-\frac{(\mathbf{k}-\mathbf{k}')\cdot\mathbf{V}_{e0}}{|\mathbf{k}-\mathbf{k}'|^2}\right\}. \tag{3.21}$$

We then approximate time derivative in the second term by $-i\omega_{\mathbf{k}r}$ [e.g., *Sahr and Farley*, 1995], recall (3.11), and obtain the final nonlinear equation that will be used in the further analysis:

$$\left[\frac{\partial}{\partial t}+i(\omega_{\mathbf{k}r}+\gamma_{\mathbf{k}})\right]n_{\mathbf{k}}(t)+\int M_{\mathbf{k}',\mathbf{k}-\mathbf{k}'}\ n_{\mathbf{k}'}(t)\ n_{\mathbf{k}-\mathbf{k}'}(t)\ d\mathbf{k}'=0. \tag{3.22}$$

3.3 Wave Kinetic Equation Approach

The set of nonlinear equations (3.22) for an infinite number of wave vectors $\mathbf{k}$ has been obtained in the past by several authors [*Sudan*, 1983; *Sahr*, 1990; *Hamza and St.-Maurice*, 1993a]. *Sudan* [1983] then used this set to obtain the estimates of power spectra in the "weak turbulence" regime [*Kadomtsev*, 1965], which is equivalent to the *direct interaction approximation* (DIA) of *Kraichnan* [1959]. *Sahr* [1990] assumed that

one can truncate the infinite set of equations (3.22) to only three modes and derived a set of three quadratically coupled first-order equations. An analysis of the latter system has shown that linearly stable waves generated through three-wave interaction mechanism at large flow angles should propagate with approximately half of the ion acoustic speed. An eddy-damped quasi-normal Markovian (EDQMM) model [*Orszag*, 1970] for spectral density closure was employed later by *Hamza and St.-Maurice* [1993a,b] to relate mean Doppler shifts, spectral widths, and wave amplitude levels. In this thesis we use a different approach, namely, the multiple-scale expansion in space and time, in order to obtain the wave kinetic equation for the evolution of the wave action.

3.3.1 Nonlinear Equation in Configuration Space

In this section we consider a case of pure Farley-Buneman instability $G = 0$ with the background electron flow along the y axis $\mathbf{V}_{e0} \equiv V_0 \mathbf{e}_y$, Figure 3.2. For this case, the nonlinear equation for density and potential perturbations (3.7) becomes

$$\left\{ \frac{\partial}{\partial t} + \frac{\psi}{1+\psi} \frac{1}{\nu_i} \left[\frac{\partial^2}{\partial t^2} - C_s^2 \nabla^2 \right] + \frac{\mathbf{V}_{e0} \cdot \nabla}{1+\psi} + \frac{1}{1+\psi} \frac{\nabla \delta\phi}{B} \times \mathbf{e}_z \cdot \nabla \right\} \frac{\delta n}{n_0} = 0. \quad (3.23)$$

It is convenient to write the nonlinear equation (3.23) by using a new variable F introduced by the relation:

$$\frac{\partial F}{\partial y} = \phi, \quad (3.24)$$

where ϕ is electrostatic potential [*Sudan et al.*, 1997]. To derive the nonlinear equation for density perturbations only we use the real space analog of (3.3):

$$-\frac{\nabla^2 \phi}{B} = r_i \frac{\mathbf{V}_{e0} \cdot \nabla}{1+\psi} \frac{\delta n}{n_0} \quad (3.25)$$

rewritten in terms of F

$$-\frac{\nabla^2 F}{B} = r_i \frac{V_0}{1+\psi} \frac{\delta n}{n_0}. \quad (3.26)$$

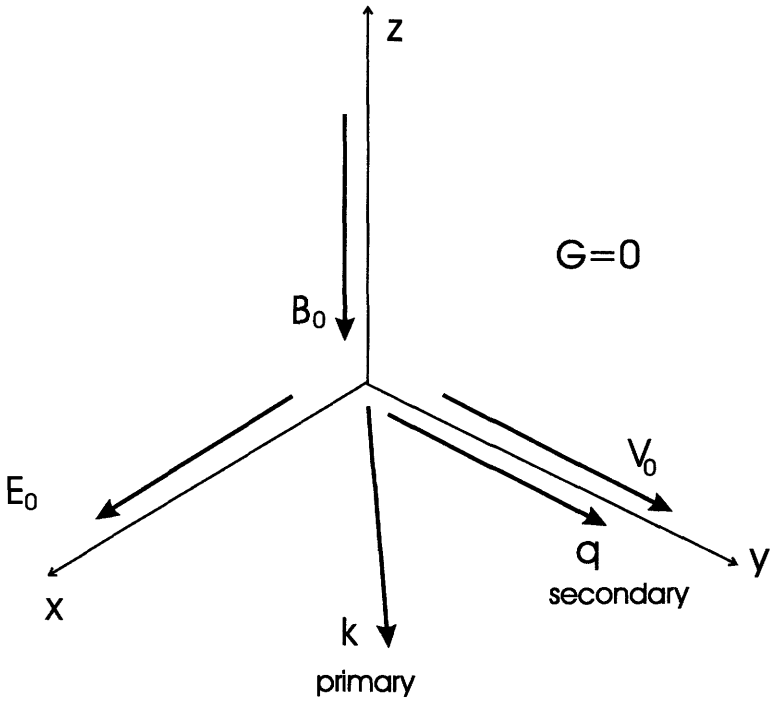

Figure 3.2: Mutual orientation of electric and magnetic fields, background electron flow, primary and secondary wave vectors.

With this new variable the nonlinear equation (3.23) can be written as

$$\frac{\partial}{\partial t}\nabla^2 F + \widehat{L}\nabla^2 F + \frac{1}{B(1+\psi)}\nabla\frac{\partial F}{\partial y} \times \mathbf{e}_z \cdot \nabla\nabla^2 F = 0. \tag{3.27}$$

The linear operator $\widehat{L}$ describes the real part of the wave frequency and the growth rate. In Fourier representation this operator takes the form

$$\widehat{L} \rightarrow i\left(\omega_{\mathbf{k}r} + i\gamma_{\mathbf{k}}\right). \tag{3.28}$$

3.3.2 Multiple-Scale Separation

We assume that the background primary fluctuations have reached their steady state. We do not consider in detail how the saturation was achieved. In general, the steady

Waves	Primary	Secondary
Wave Number	k large	q small
Wavelength	λ_k short	λ_q long
Spatial Scale	Small	Large
Time Scale	Fast	Slow

Table 3.1: Scale separation for primary and secondary waves.

state is established as a result of competition between the linear instability and nonlinear damping due to mode interaction [*Hamza and St.-Maurice,* 1993b].

We now consider a perturbation of the background equilibrium primary short-wavelength turbulence due to the secondary long-wavelength modes. Thus we assume the scale separation between the background fluctuations and the secondary waves. Table 3.1 summarizes the scale separation information. This approach allows us to use averaging over the short-wavelength fluctuations.

We present fluctuations as a sum of fast and slow parts:

$$F = \widetilde{F} + \overline{F}. \tag{3.29}$$

The fast part $\widetilde{F} = \widetilde{F}(\mathbf{x}, t, \mathbf{X}, T)$ depends on fast $(\mathbf{x}, t)$ and slow $(\mathbf{X}, T)$ variables, while the slow part $\overline{F} = \overline{F}(\mathbf{X}, T)$ is a function of slow variables $(\mathbf{X}, T)$ only; the slow variables are formally introduced by $\mathbf{X} = \varepsilon\mathbf{x}$ and $T = \varepsilon t$, where $\varepsilon \ll 1$ is the small parameter of the scale separation.

Equations for $\overline{F}$ and $\widetilde{F}$ are derived from the nonlinear equation (3.27). The equation for the evolution of the "mean" function $\overline{F}$ is obtained from (3.27) by averaging over short-wavelength fluctuations

$$\frac{\partial}{\partial t}\nabla^2\overline{F} + \hat{L}\nabla^2\overline{F} + \frac{1}{B(1+\psi)}\frac{\partial}{\partial \mathbf{X}} \cdot \overline{\left(\nabla\frac{\partial\widetilde{F}}{\partial y} \times \mathbf{e}_z\nabla^2\widetilde{F}\right)} = 0. \tag{3.30}$$

The equation for the short-wavelength component is

$$\frac{\partial}{\partial t}\nabla^2\widetilde{F} + \hat{L}\nabla^2\widetilde{F} + \frac{1}{B(1+\psi)}\nabla\frac{\partial\overline{F}}{\partial Y} \times \mathbf{e}_z \cdot \nabla\nabla^2\widetilde{F} \; +$$

$$+\frac{1}{B(1+\psi)}\nabla\frac{\partial\widetilde{F}}{\partial y}\times\mathbf{e}_z\cdot\nabla\nabla^2\widetilde{F}=0 \tag{3.31}$$

The last term in this formula describes the self-interaction of short-wavelength perturbations. This self-interaction is important to establish the equilibrium steady state.

The interaction of short-wavelength fluctuations with the mean flow is described by the third term in (3.31). In general, the coupling of short-wavelength fluctuations to the mean flow can be described by the kinetic equation for wave packets, which is the conservation law for the wave action invariant $N_{\mathbf{k}}$. The standard form [*Kadomtsev*, 1965; *Vedenov et al.*, 1967] for such an equation is

$$\frac{\partial N_{\mathbf{k}}}{\partial T}+\frac{\partial\omega'_{\mathbf{k}r}}{\partial\mathbf{k}}\cdot\frac{\partial N_{\mathbf{k}}}{\partial\mathbf{X}}-\frac{\partial\omega'_{\mathbf{k}r}}{\partial\mathbf{X}}\cdot\frac{\partial N_{\mathbf{k}}}{\partial\mathbf{k}}=S_{\mathbf{k}}, \tag{3.32}$$

where $\omega_{\mathbf{k}r}$ is the real part of the wave eigenfrequency and $N_{\mathbf{k}}=N_{\mathbf{k}}(\mathbf{X},T)$ is the generalized wave action density, which is a slow function in time and space.

The coupling of the intensity of short-wavelength fluctuations $N_{\mathbf{k}}$ with the slow component $\overline{F}$ is provided via the variations of the wave eigenfrequency by the slow component of the electric field, $\omega'_{\mathbf{k}r}=\omega'_{\mathbf{k}r}(\mathbf{X},T)$, where $\omega'_{\mathbf{k}r}$ is the wave frequency taking into account the contribution of the slow component. From (3.31) one can easily find that

$$\omega'_{\mathbf{k}r}=\omega_{\mathbf{k}r}+\frac{1}{B(1+\psi)}\nabla\frac{\partial\overline{F}}{\partial Y}\times\mathbf{e}_z\cdot\mathbf{k}, \tag{3.33}$$

where $\omega_{\mathbf{k}r}$ is the wave eigenfrequency in the stationary plasma.

As shown in Appendix A, the generalized wave action, $N_{\mathbf{k}}$ in our case, is given by the expression $N_{\mathbf{k}}=k^4|\widetilde{F}_{\mathbf{k}}|^2$, so that the wave kinetic equation for the wave packets in the presence of a slow, long-wavelength component takes the form

$$\begin{aligned}&\frac{\partial}{\partial T}\left(k^4\left|\widetilde{F}_{\mathbf{k}}\right|^2\right)+\\&+\frac{\partial}{\partial\mathbf{k}}\left(\omega_{\mathbf{k}r}+\frac{1}{B(1+\psi)}\nabla\frac{\partial\overline{F}}{\partial Y}\times\mathbf{e}_z\cdot\mathbf{k}\right)\cdot\frac{\partial}{\partial\mathbf{X}}\left(k^4\left|\widetilde{F}_{\mathbf{k}}\right|^2\right)-\\&-\frac{\partial}{\partial\mathbf{X}}\left(\omega_{\mathbf{k}r}+\frac{1}{B(1+\psi)}\nabla\frac{\partial\overline{F}}{\partial Y}\times\mathbf{e}_z\cdot\mathbf{k}\right)\cdot\frac{\partial}{\partial\mathbf{k}}\left(k^4\left|\widetilde{F}_{\mathbf{k}}\right|^2\right)=S_{\mathbf{k}}.\end{aligned} \tag{3.34}$$

The right-hand side of (3.34) describes the wave growth due to the linear instability and the nonlinear wave damping due to the self-interaction of short-wavelength waves. In the stationary state, $S_{\mathbf{k}} \to 0$.

3.3.3 Dispersion Equation for Secondary Instability

Equations (3.30) and (3.34) describe coupled dynamics of the slow varying field $\overline{F}(\mathbf{X}, T)$ and the wave action density $N_{\mathbf{k}}(\mathbf{X}, T)$. Now we can investigate the stability of this system with respect to slow deviations from the stationary turbulent state. We assume that the steady state fluctuation spectrum $N_{\mathbf{k}}^0$ is maintained through competition of the linear growth and nonlinear damping because of interactions among small scales (this balance is described by the last term in (3.34), which is thus zero in the equilibrium, $S_{\mathbf{k}} = 0$). We assume that there is a small deviation $\delta N_{\mathbf{k}}$ from this equilibrium, $N_{\mathbf{k}} = N_{\mathbf{k}}^0 + \delta N_{\mathbf{k}}$. This deviation is related to the slow perturbation in the F field which is thus a slow field $\overline{F}$. The system is linear with respect to $\delta N_{\mathbf{k}}$ and $\overline{F}$; one can use the Fourier representation to analyze it:

$$\left(\delta N_{\mathbf{k}},\ \overline{F}\right) \propto \exp\left(-i\Omega_{\mathbf{q}} T + i\mathbf{q}\cdot\mathbf{X}\right). \tag{3.35}$$

We consider small perturbations with a wave vector $\mathbf{q}$ along the equilibrium flow $\mathbf{V}_0 = V_0\mathbf{e}_y$ and $\mathbf{q} = q\mathbf{e}_y$, where q is the wave number, Figure 3.2. Linearizing (3.34) with respect to $\delta N_{\mathbf{k}}$, we obtain

$$-i\left(\Omega_{\mathbf{q}} - qV_{gr}\right)\delta N_{\mathbf{k}} + iq^3 \frac{1}{B(1+\psi)} \overline{F} k_x \frac{\partial N_{\mathbf{k}}^0}{\partial k_y} = 0, \tag{3.36}$$

where $V_{gr} = \partial\omega_{\mathbf{k}r}/\partial k_y$ is the group velocity of the primary (short-wavelength) F-B waves. From (3.30) we find

$$i\Omega_{\mathbf{q}} q^2 \overline{F} - \frac{1}{B(1+\psi)} iq \sum k_x k_y k^2 \left|\widetilde{F}_{\mathbf{k}}\right|^2 = 0. \tag{3.37}$$

Perturbations of the spectrum $|\widetilde{F}_{\mathbf{k}}|^2$ can be related to the wave action perturbations by the relation

$$k_x k_y k^2 \left|\widetilde{F}_{\mathbf{k}}\right|^2 = \frac{k_x k_y}{k^2} \delta N_{\mathbf{k}}. \tag{3.38}$$

The sum in (3.37) is taken over the spectrum of short-wavelength fluctuations. It occurs as a result of averaging the last term in (3.30).

Excluding $\overline{F}$ and $\delta N_{\mathbf{k}}$ from (3.36) and (3.37), we obtain the dispersion relation

$$\Omega_{\mathbf{q}} \left(\Omega_{\mathbf{q}} - q V_{gr}\right) + \Gamma_0^2 = 0. \tag{3.39}$$

The nonlinear growth rate Γ_0 is defined by

$$\Gamma_0^2 = -\left[\frac{1}{B(1+\psi)}\right]^2 q^2 \sum \frac{k_x^2 k_y}{k^2} \frac{\partial N_{\mathbf{k}}^0}{\partial k_y}. \tag{3.40}$$

As follows from the analysis below, the parameter Γ_0^2 defines the growth rate of the long-wavelength instability. To evaluate the magnitude of this parameter, we use an estimate from (3.26):

$$k^2 \frac{F}{B} \simeq r_i \, V_0 \frac{\delta n}{n_0}. \tag{3.41}$$

Also using $N_{\mathbf{k}} = k^4 |\widetilde{F}_{\mathbf{k}}|^2$ and assuming a roughly isotropic spectrum of the turbulence, we obtain for Γ_0^2 the following order of magnitude estimate in terms of density fluctuations:

$$\Gamma_0^2 = q^2 r_i^2 V_0^2 \left(\frac{\delta n}{n_0}\right)^2. \tag{3.42}$$

Note that $\partial N_{\mathbf{k}}^0 / \partial k_y < 0$ is required for the instability. This is a typical condition for the saturated turbulence.

3.3.4 Analysis of the Nonlinear Dispersion Equation

As a matter of fact, in (3.39) we have neglected the linear dynamics of the secondary mode that is given by the linear operator $\widehat{L}$ in (3.30). Restoring these effects, we

obtain for the general case

$$(\Omega_{\mathbf{q}} - \omega_{\mathbf{q}r} - i\gamma_{\mathbf{q}})(\Omega_{\mathbf{q}} - qV_{gr}) + \Gamma_0^2 = 0, \tag{3.43}$$

where $\omega_{\mathbf{q}r} + i\gamma_{\mathbf{q}}$ is the oscillation frequency and growth rate of the F-B fluctuations with the wave vector number $\mathbf{q}$. They are given by (3.11) and (3.12) with the wave vector $\mathbf{q}$ substituted for $\mathbf{k}$.

The nonlinear dispersion equation (3.43) describes two branches of fluctuations: the regular F-B mode with a wave vector $\mathbf{q}$ and $\Omega_{\mathbf{q}} = \omega_{\mathbf{q}r} + i\gamma_{\mathbf{q}}$ and the modes with $\Omega_{\mathbf{q}} = qV_{gr}$ that correspond to the long-wavelength modulations of the background turbulence moving with the group velocity of the F-B mode. In the presence of nonlinear effects these two modes are coupled via the nonlinear interaction described by the Γ_0^2 term. The result is the nonlinear instability that produces long-wavelength perturbations.

A simple analysis can be made taking into account that $\omega_{\mathbf{q}r} \simeq qV_{gr}$. Then, the dispersion equation (3.43) can be rewritten as

$$\left(\Omega'_{\mathbf{q}} - i\gamma_{\mathbf{q}}\right)\Omega'_{\mathbf{q}} + \Gamma_0^2 = 0, \tag{3.44}$$

where $\Omega'_{\mathbf{q}} \equiv \Omega_{\mathbf{q}} - qV_{gr}$ is the mode frequency in the reference frame moving with the group velocity. The dispersion equation (3.44) yields

$$\Omega'_{\mathbf{q}} = \frac{i\gamma_{\mathbf{q}}}{2} \pm \sqrt{-\frac{\gamma_{\mathbf{q}}^2}{4} - \Gamma_0^2}. \tag{3.45}$$

One remarkable property of this expression is that the instability occurs for any sign of $\gamma_{\mathbf{q}}$. This means that (because of nonlinear effects for the longer wavelengths) there is no ion acoustic threshold for the secondary instability development contrary to what is known for the primary F-B instability. This conclusion also holds in a more general case where $\omega_{\mathbf{q}r} \neq qV_{gr}$. In the latter case we have

$$\Omega_{\mathbf{q}} = \frac{qV_{gr} + \omega_{\mathbf{q}r}}{2} + \frac{i\gamma_{\mathbf{q}}}{2} \pm \frac{1}{2}\sqrt{D_{\mathbf{q}}}, \tag{3.46}$$

where

$$D_{\mathbf{q}} \equiv a_{\mathbf{q}} + ib_{\mathbf{q}}, \tag{3.47}$$

$$a_{\mathbf{q}} \equiv (qV_{gr} - \omega_{\mathbf{qr}})^2 - \gamma_{\mathbf{q}}^2 - 4\Gamma_0^2, \tag{3.48}$$

$$b_{\mathbf{q}} \equiv -2\gamma_{\mathbf{q}}(qV_{gr} - \omega_{\mathbf{qr}}). \tag{3.49}$$

The real and imaginary parts of the wave frequency $\Omega_{\mathbf{q}}$ are then given by the following expressions:

$$\text{Re}\ \Omega_{\mathbf{q}} = \frac{qV_{gr} + \omega_{\mathbf{qr}}}{2} \pm \frac{1}{2}\sqrt{\frac{b_{\mathbf{q}}^2}{2(r_{\mathbf{q}} - a_{\mathbf{q}})}}\ , \tag{3.50}$$

$$\text{Im}\ \Omega_{\mathbf{q}} = \frac{\gamma_{\mathbf{q}}}{2} \pm \frac{1}{2}\sqrt{\frac{r_{\mathbf{q}} - a_{\mathbf{q}}}{2}}\ . \tag{3.51}$$

Here

$$r_{\mathbf{q}}^2 = a_{\mathbf{q}}^2 + b_{\mathbf{q}}^2.$$

After simple algebra one can show that

$$r_{\mathbf{q}} > \gamma_{\mathbf{q}}^2 + (qV_{gr} - \omega_{\mathbf{qr}})^2 - 4\Gamma_0^2, \tag{3.52}$$

and hence

$$(r_{\mathbf{q}} - a_{\mathbf{q}})/2 > \gamma_{\mathbf{q}}^2.$$

The latter inequality means that for any sign of $\gamma_{\mathbf{q}}$, one of the two roots of (3.51) is positive that corresponds to the instability. For stable F-B modes with $\gamma_{\mathbf{q}} < 0$ the growth rate is proportional to the amplitude of the background turbulence.

The numerical estimates of $\gamma_{\mathbf{q}}$ showed that for wavelengths of $\sim$ 500 m it is of the order of 1–10 s^{-1}. The question whether the growth rate of the secondary waves is small enough for the convective effects (Section 2.1.6) to be significant for the secondary instability, was not under consideration in this thesis. It is worth mentioning though that the new theory can also be applied to the equatorial electrojet where the effects of wave convection with the parallel group velocity are less important.

Phase Velocity of the Secondary Waves

Once the imaginary part of the wave frequency is found (3.51), it is easy to calculate the phase velocity of the secondary waves:

$$V_{NL}^{\mathbf{q}} = \frac{1}{2}\left(V_{gr}^{\mathbf{k}} + V_{ph}^{\mathbf{q}}\right) \pm \frac{1}{2}\left|V_{gr}^{\mathbf{k}} - V_{ph}^{\mathbf{q}}\right| \sqrt{\frac{2\gamma_{\mathbf{q}}^2}{r_{\mathbf{q}} - a_{\mathbf{q}}}}. \tag{3.53}$$

Here we introduced the following definitions:

$$V_{NL}^{\mathbf{q}} \equiv \frac{\mathrm{Re}\ \Omega_{\mathbf{q}}}{q}, \tag{3.54}$$

$$V_{ph}^{\mathbf{q}} \equiv \frac{\omega_{\mathbf{q}r}}{q}, \tag{3.55}$$

$$V_{gr}^{\mathbf{k}} \equiv \frac{\partial \omega_{\mathbf{k}r}}{\partial k_y}, \tag{3.56}$$

where index NL indicates that we consider **secondary** waves, the development of which is governed by nonlinear mechanisms.

For the case $\omega_{\mathbf{q}r} = qV_{gr}$

$$V_{gr}^{\mathbf{k}} = V_{ph}^{\mathbf{q}}, \tag{3.57}$$

the second term in (3.53) is equal to zero and

$$V_{NL}^{\mathbf{q}} = V_{ph}^{\mathbf{q}}. \tag{3.58}$$

If, however, $\omega_{\mathbf{q}r} \neq qV_{gr}$, the second term in (3.53) is not zero and the phase velocity of secondary waves "splits" into two components. We are interested in dependence of the phase velocity upon wave vector. In our theory we assumed that the aspect conditions are perfect ($k_{\|} = 0$, $\alpha = 0$). Also we assumed that the secondary wave propagates along the $\mathbf{E} \times \mathbf{B}$ drift, and hence the flow angle is zero as well ($\theta = 0$). The only dependence which can be studied in this approach is the scale dependence of the phase velocity. The condition $\omega_{\mathbf{q}r} \neq qV_{gr}$ means that there is some nonzero dispersion; phase velocity is not equal to the group velocity. One of the possible

reasons for that is the condition of nonorthogonality ($\alpha \neq 0$). Then (see Section 2.1.6) the group velocity differs from the phase velocity, and therefore $V_{NL}^{\mathbf{q}}$ should depend on the wave number q. Our estimations show that such dependence does exist, but it is very weak. For reasonable differences between $V_{gr}^{\mathbf{k}}$ and $V_{ph}^{\mathbf{q}}$ the change of the phase velocity with scale is of the order of 10 m s^{-1} for a drift of 1000 m s^{-1}. One can hence conclude that to a first approximation $V_{NL}^{\mathbf{q}}$ does not depend on the wave number q.

3.4 Discussion

In this chapter we have considered the dynamics of the long-wavelength perturbations of the turbulent background made up by short-wavelength F-B (primary) waves. We have shown that the F-B waves that reached the equilibrium state are unstable with respect to the long-wavelength perturbations propagating along the background plasma flow with the velocity approximately equal to the group velocity of the F-B modes. The growth of the long-wavelength structures can be interpreted as the inverse energy cascade with the energy flow from short toward long wavelengths.

The mechanism of the secondary instability considered in this study is related to the wave coupling between the short-wavelength fluctuations and the long-wavelength modes (a parametric process somewhat similar to that considered by *Sharma and Kaw* [1986]). The secondary mode generation is related to the nonlinear terms in the electron continuity equation.

We used the wave kinetic equation to describe the modulations of the background short-wavelength turbulence. It should be noted that the primary short-wavelength fluctuations must be excited before the secondary instability takes place. We did not consider the mechanism for the primary F-B wave saturation. It was assumed that

primary waves reach their saturated state and that then they interact with secondary long-wavelength modes. An interesting feature of the secondary instability considered is that it does not have the ion acoustic threshold typical for the primary F-B modes. The growth rate of secondary long-wavelength modes is determined by the intensity of the primary fluctuations. Certainly, the growth of the secondary instability will eventually be slowed down, and the saturation of the whole primary-secondary wave system will be reached because of the influence of the long-wavelength modes on the short-wavelength waves and the nonlinear interaction between the secondary modes. Quantitative analysis of these processes requires a nonlinear theory for the secondary modes that is beyond the scope of the present study.

Our approach to the analysis of the F-B instability differs from previous studies in several aspects. The major difference is that we assume the energy transfer to the longer perturbations. Traditionally, the energy transfer to shorter scales was considered, starting with the work by *Sudan et al.* [1973]. Our analysis is closely related to the work by *Sharma and Kaw* [1986], who have suggested that the dynamics of secondary G-D waves can be strongly modified in the presence of short-wavelength F-B fluctuations. *Sharma and Kaw* [1986] have also anticipated a possibility of nonlinear instability supported by the primary fluctuations. Contrary to these authors, we considered perturbations propagating along the background flow to be the most favorable direction for the F-B instability. Though technically different, our analysis is somewhat similar to that of *Sahr and Farley* [1995]. Analogous to that work, the long wavelength modes in our model originate from three-wave coupling processes. These long-wavelength modes are excited by "beating" of short-wavelength fluctuations.

Implication of our scenario of the F-B instability evolution is that the long-wavelength secondary waves (at scales that cannot be excited linearly, namely, more than $\sim$ 100 m) should be observed along the electrojet. Since the group velocity of

the F-B fluctuations is close to their phase velocity, the nonlinearly generated long-wavelength modes should move with the velocity of the background fluctuations. These predictions seem to agree with radar observations at equatorial latitudes [*Farley et al.*, 1994].

Chapter 4

Experimental Data on the Velocity of E-region Irregularities

This chapter briefly describes the coherent radar method and experimental data on auroral E-region irregularities with a focus on the Doppler velocity dependence upon wavelength/radar frequency, flow and aspect angles.

4.1 Coherent Radar Measurements

The physical principle of operation of coherent radars is based on momentum conservation applied to the wave vectors for incident and scattered waves and the wave vector of the irregularities, from which follows the Bragg condition for wavelengths of radar waves and irregularities under study, namely, $\lambda_{Radar} = 2\lambda_{irr}$ [see the reviews by *Fejer and Kelley*, 1980; *Haldoupis*, 1989; *Schlegel*, 1996]. Coherent radars are

hence sensitive only to one specific scale of irregularities. Mostly, radars with wavelengths between ~0.3 and 15 m (500 MHz–10 MHz) are used in the study of E-region plasma irregularities [*Fejer and Kelley*, 1980; *Schlegel*, 1996]. Similar to conservation of momentum, the conservation of energy applied to a scattering problem gives $\omega_i = \omega_s + \omega_m$, where subscripts i, s, and m stand for incident, scattered, and medium, respectively. The difference between transmitted and received frequencies ω_i and ω_s is the Doppler shift measured by the radar system $\omega_m = 2\pi\Delta f$. This Doppler shift is related to the phase velocity of the irregularities through $V_{ph} = (c/2)(\Delta f / f_{Radar})$, where c is the speed of light. It is customary in radar physics to use Doppler velocity instead of Doppler frequency when describing the spectra, to make the comparison of the results obtained using different radar frequencies more convenient [*Schlegel*, 1996]. Historically, the velocity of waves propagating toward (away from) the radar is considered to be positive (negative).

Ideally, due to the Bragg condition, one would expect that the returned signal spectrum is almost a delta function at the Doppler velocity corresponding to $\lambda_{Radar}/2$. In reality, the wave travels through the irregular plasma filled with irregularities. In this case, instead of a singular delta-function-like spectral peak at some specific velocity, the medium is characterized by a spectrum of some finite width centered around this velocity and instead of one amplitude we have a spectrum. Symbolically this spectrum can be written as $F = F(V)$. F here denotes irregularity wave amplitude and V denotes Doppler velocity. One can naturally construct a moment of n-th order using this given distribution function. The first three moments are called spectral power, mean velocity, and spectral width:

$$P \equiv \int F(V)dV; \quad \overline{V} \equiv \int VF(V)dV; \quad W \equiv 2\sqrt{1/P \int (V-\overline{V})^2 F(V)dV} \quad (4.1)$$

A pulsed coherent radar can measure spectral power ("irregularity wave amplitude") and mean Doppler shift (phase velocity) of irregularities. Radars that use a

multi-pulse technique can also measure spectral width. Technically, spectral width is a measure of the "narrowness" of the power spectrum. Spectral power (P), mean Doppler velocity ($\overline{V}$), and spectral width (W) are properties that can be studied with coherent radars and in general are functions of the medium characteristics. The focus of this thesis is on the irregularity phase velocity, but we also consider other echo characteristics such as echo occurrence, spectral power, and spectral width that are pertinent to the main issue, velocity.

4.2 Types of Echoes: Morphology and Generation Mechanisms

Before considering the experimental data on irregularity Doppler velocity one more question should be addressed. Radar observations revealed that there are various classes of auroral E-region echoes and that the echoes belonging to different classes exhibit completely different properties. For example, the phase velocity varies in a different fashion with the flow angle, depending on the type of echoes that radar detects, so it is important to know what type of echoes one deals with.

A number of different types of E-region auroral echoes have been identified over the years of research. In this review we follow the traditional classification scheme based on VHF observations that includes four echo types [e.g., *Haldoupis*, 1989; *Schlegel*, 1996; *Sahr and Fejer*, 1996; *Moorcroft*, 2002]. Since the echo types have been studied most systematically with VHF radars, we use VHF studies as a "base" and compare them with UHF and HF studies.

Figure 4.1 illustrates schematically all four types. Type 1 echoes exhibit relatively narrow ($W < C_s$) and powerful spectra, centered around C_s (Figure 4.1a). Type 2

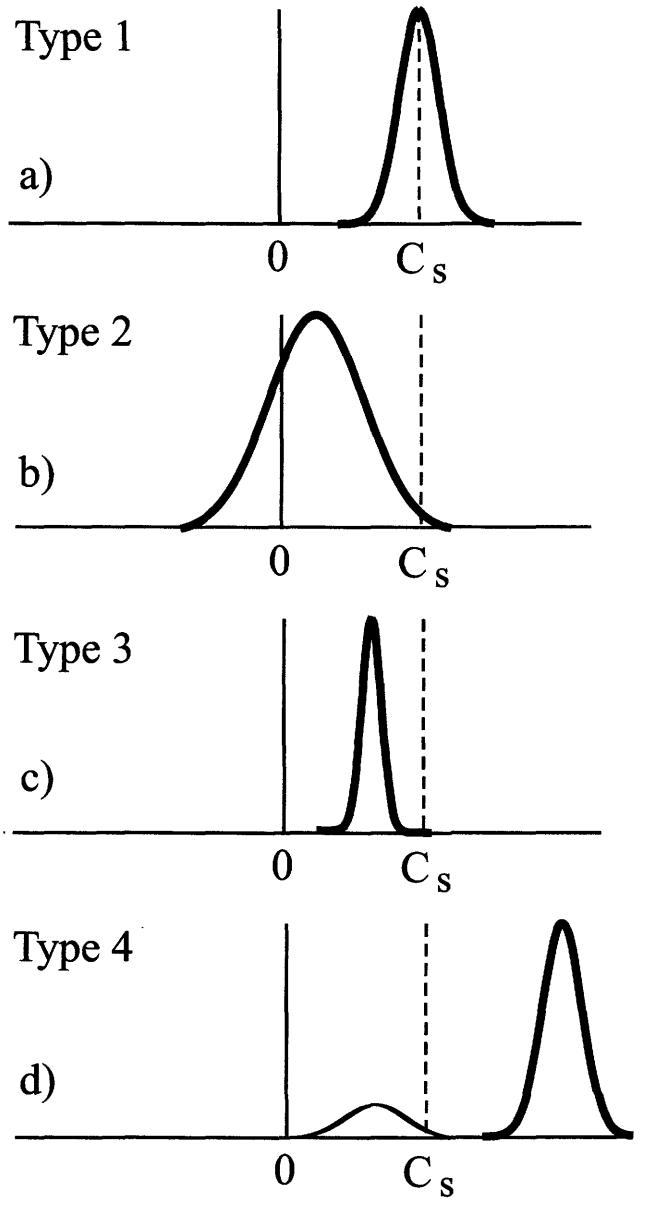

Figure 4.1: Types of auroral coherent echoes

spectra are wide ($W \geq C_s$), with lower power and are centered near zero velocity (Figure 4.1b). Type 1 echoes are observed at directions close to the $\mathbf{E} \times \mathbf{B}$ drift direction; while type 2 echoes can be observed at any direction. Type 3 and 4 spectra (Figures 4.1c and 4.1d) are narrow and their mean velocity is about 200 and 1000 m s^{-1} for type 3 and type 4, respectively [e.g., *Haldoupis et al.*, 1995].

In total type 1 and type 2 constitute the majority of echoes while type 3 and 4 echoes occur significantly less frequently [*Moorcroft*, 2002]. A strong type 4 peak is very often accompanied by a weak, type 3 peak [*St.-Maurice et al.*, 1994].

Several explanations of the observed types of echoes have been offered. Type 1 echoes are thought to originate from the F-B instability. The general understanding [see, for example, the recent review by *Moorcroft*, 2002] is that type 1 waves are waves in a saturated state ($\gamma = 0$) that propagate at threshold velocities given by the linear theory, namely a phase velocity that is close to the ion acoustic speed. The final steady state is reached by the action of some nonlinear processes. One of the possible mechanisms is mode coupling, the detailed theory of which was developed by *Hamza and St.-Maurice* [1993a] (see Section 2.3). Type 2 echoes are usually believed to be secondary waves generated through nonlinear cascade from long-wavelength structures [*Sudan*, 1983]. The theory of *Hamza and St.-Maurice* [1993a] can be applied for interpretation of both type 1 **and** type 2 echoes. If one considers the quasi-stationary state equation (2.86), the width of type 1 spectra is small, meaning that we have the weak turbulence regime (2.87) and the phase velocity is close to the ion acoustic speed. For the strong turbulence situation we have to use (2.88); the spectral width is relatively large and the phase velocity is below the ion acoustic speed, suggesting that type 2 echoes can be regarded as echoes generated by the F-B instability in the strong turbulence regime. The larger the second term in (2.88) the larger the deviation from the ion acoustic speed.

As for the origin of type 3 and 4 echoes, there is no general agreement [*Sahr et*

al., 1991; *Sahr and Fejer*, 1996; *Haldoupis et al.*, 1992; 1995]. In the past, researchers tried to explain type 3 echoes using the Electrostatic Ion Cyclotron (EIC) instability [e.g., *Fejer et al.*, 1984a; *Haldoupis et al.*, 1985; *Villain et al.*, 1987]. This instability is operational at the top of the electrojet layer (130–140 km heights) and requires significant electron drifts parallel to the magnetic field [see, for example, a comprehensive theoretical study by *Fejer et al.*, 1984b]. Recent experimental data [*Sahr et al.*, 1991; *Haldoupis et al.*, 1992], however, disproved the EIC hypothesis. For example, *Sahr et al.* [1991] showed that type 3 echoes originate from typical electrojet heights (100–120 km). Three other propositions (among others) have been put forward. *Haldoupis et al.* [1992] proposed that type 3 echoes are simply type 1 echoes generated at much lower thresholds by the action of large destabilizing plasma density gradients. Later *Haldoupis et al.* [1995] in his extensive review of type-3 auroral research concluded that the existing evidence in favor of this mechanism "is necessary but not sufficient". *Shalimov and Haldoupis* [1995] postulated that another plasma instability, namely the electron thermal diffusion instability may be appropriate for the generation of type 3 echoes in the lower auroral E region. One should note that *Shalimov and Haldoupis* [1995] neglected the ion inertia effects and that this assumption was questioned later by *St.-Maurice and Kissack* [2000]. *Sahr and Farley* [1995], by considering three-wave coupling processes, showed that driven waves; that is, those that are stable in the linear regime but can be generated through the energy cascading from the linear unstable waves, could be responsible for type 3 echoes.

Two major hypotheses have been offered in an attempt to explain the properties of type 4 echoes. The first one takes into account the elevation of the ion acoustic speed with the increase of the electric field (see Section 2.2.3). The phase velocity of these echoes is still equal to the ion acoustic speed, but since the latter is enhanced due to the heating, the phase velocity is larger than the nominal value of 350–400 m s^{-1}. The second explanation is based on the theory of the phase velocity modification

by strong gradients of electron density, from which the original type 1 spectra with mean velocity C_s are "split" by the strong gradients into two type-3- and type-4-like spectra, the mean velocities of which are less and larger than C_s, respectively [*St.-Maurice et al.*, 1994]. This idea is similar to that of *Haldoupis et al.* [1992] except for the fact that *St.-Maurice et al.* [1994] considered the effect of sharp gradients for type 3 **and** type 4 echoes simultaneously.

Most radar studies have concentrated on type 1 and type 2 echoes since they constitute the vast majority of all echoes. The two "new" types (3 and 4) have only been observed only at VHF and mostly with 50-MHz radars [*Moorcroft*, 2002]. It has been noticed, however, that the distinction between echo types varies from one frequency band to another. At UHF, the difference between the properties of type 1 and type 2 echoes was found to be significantly smaller than at VHF [*Moorcroft*, 1996]. The powers of type 1 and 2 echoes at UHF are almost the same, contrary to the VHF observations [*Nielsen et al.*, 1984]. The widths do not significantly differ either (30% difference at UHF versus a factor of 2 at VHF). Recent studies have shown that at HF the situation is even more complicated. *Milan and Lester* [1999] introduced a new extended classification of HF echoes that included not only classic type 1 and type 2 echoes but also several additional types that did not have VHF analogs.

One might conclude then that the number of different echo types seems to increase with wavelength and in this sense the interesting problem for study might be to check the conclusions of *Milan and Lester* [1999] and find out how many different classes of echoes exist at HF and what are their properties.

4.3 Experimental Data on Doppler Velocity

4.3.1 Flow Angle Effects

One of the most important issues that traditionally was under study is the flow angle dependence of the Doppler velocity. The general question here is whether the phase velocity variation with the flow angle obeys the "cosine" law (Section 2.1.6). The answer up to now seems to be uncertain and to depend on the radar frequency and whether one deals with type 1 or type 2 echoes.

It was thought for a long time that type 1 echoes, observed mostly along the flow direction at small flow angles and associated with primary F-B waves, do not exhibit any velocity variation with the flow angle [e.g., *Nielsen and Schlegel*, 1983]. In this and a subsequent study by *Kofman and Nielsen* [1990], the electric fields and flow angles derived from the European Incoherent Scatter (EISCAT) radar measurements and VHF Doppler velocities from the Scandinavian Twin Auroral Radar Experiment (STARE) radar system at 140 MHz were used. The major conclusion was that at small flow angles the Doppler velocity tends to be limited by the local ion acoustic speed (C_s saturation). Essentially the same result was obtained in a three-radar VHF experiment in which the data from two STARE radars were complemented by the Sweden And Britain Radar Experiment (SABRE) radar data at 142 MHz [*Nielsen et al.*, 1983; *Reinleitner and Nielsen*, 1985]. Evidence of C_s saturation were presented for UHF observations at 440 MHz at Millstone Hill [*St.-Maurice et al.*, 1989; *del Pozo et al.*, 1993] and at 398 MHz with the Homer radar in Alaska [e.g., *Moorcroft and Tsunoda*, 1978; *Moorcroft*, 1996]. At HF *Milan and Lester* [1998] used 10-MHz radar observations from Pykkvibaer, Iceland to show that the Doppler velocity saturates at the local ion acoustic speed for small flow angles.

Studies at 140 MHz (1-m waves) have shown that for echoes observed at large flow

angles (presumably type 2 echoes), the phase velocity does closely follow the "cosine" law [*Nielsen and Schlegel*, 1983; *Nielsen et al.*, 1983; *Reinleitner and Nielsen*, 1985]. In other words, the phase velocity is the line-of-sight component of the $\mathbf{E} \times \mathbf{B}$ drift velocity. Strong evidence of the "cosine" law has been reported in the lower VHF band (50 MHz, 3-m waves) [*Ecklund et al.*, 1977]. Later *St.-Maurice et al.* [1989] and *del Pozo et al.* [1993] substantiated the cosine law at UHF (440 MHz, 34-cm waves). In other UHF studies [e.g., *Hall and Moorcroft*, 1988; *Moorcroft*, 1996], which used data from the Homer radar (398 MHz, 38-cm waves), it was demonstrated that the average rate of decrease of the Doppler velocity at large flow angles is too rapid to be consistent with the cosine law. On the other hand at HF, *Villain et al.* [1987] and *Jayachandran et al.* [2000], using Goose Bay and Saskatoon HF radars, respectively, presented evidence that measurements at large flow angles were consistent with the cosine law.

Recently *Nielsen et al.* [2002] showed that the STARE Doppler velocity is maximized at zero flow angle and slowly decreases up to a flow angle of $\sim 40°$ where it is equal to the ion acoustic speed. Doppler velocity decreases away from the direction of flow and the rate of decrease is slower than predicted by the cosine law. The change of the Doppler velocity with the flow angle/radar direction for observations within the F-B instability cone was also noticed at HF by *Uspensky et al.* [2001].

Table 4.1 lists relevant studies on flow angle dependence of the phase velocity. One can conclude that the question of the dependence of the Doppler velocity upon the flow angle still remains unresolved.

Reference	Radar	f_{radar}	λ_{irr}	C_s	Cos
St.-Maurice et al. [1989]	Millstone Hill	440 MHz	34 cm	Yes	Yes
del Pozo et al. [1993]	Millstone Hill	440 MHz	34 cm	Yes	Yes
Moorcroft and Tsunoda [1978]	Homer	398 MHz	38 cm	Yes	
Hall and Moorcroft [1988]	Homer	398 MHz	38 cm		No
Moorcroft [1996]	Homer	398 MHz	38 cm	Yes	No
Nielsen and Schlegel [1983]	STARE	140 MHz	1 m	Yes	Yes
Nielsen et al. [1983]	STARE	140 MHz	1 m	Yes	Yes
Reinleitner and Nielsen [1985]	STARE	140 MHz	1 m	Yes	Yes
Kofman and Nielsen [1990]	STARE	140 MHz	1 m	Yes	
Nielsen et al. [2002]	STARE	140 MHz	1 m	No	No
Ecklund et al. [1977]	Aniak	50 MHz	3 m		Yes
Villain et al. [1987]	Goose Bay HF	12 MHz	12 m		Yes
Jayachandran et al. [2000]	Saskatoon HF	12 MHz	12 m		Yes
Milan and Lester [1998]	Iceland East HF	10 MHz	15 m	Yes	
Uspensky et al. [2001]	Iceland East HF	10 MHz	15 m	No	

Table 4.1: Studies on flow angle dependence of the phase velocity.

4.3.2 Aspect Angle Effects

The E-region irregularities are known to align with the magnetic field lines, which means that the spectral power of the backscatter signal decreases rapidly with deviation from orthogonality [e.g., review by *Haldoupis*, 1989, and references therein], so that, following the idea of Section 2.4.1, one more type of dependence could be studied using radar Doppler velocity data, namely how the irregularity phase velocity varies with the angle between the wave vector and the magnetic field.

Ogawa et al. [1982] presented 50-MHz velocity measurements in the range of aspect angles between 2° and 7°. These data showed that velocity decrease over this aspect angle range was about 3 times. *Nielsen* [1986] examined data from the STARE radar at 140 MHz and found that the aspect angle attenuation of the normalized phase velocity for small aspect angles (0°–1.5°) was about 25%. Both studies are in disagreement with the linear fluid theory of electrojet instabilities which predicts much larger aspect angle attenuation of the phase velocity. Both *Ogawa et al.* [1982]

and *Nielsen* [1986] used anomalously large collision frequencies $\nu^* \cong 6 \cdot \nu_e$ resulting from wave-particle interaction, Section 2.2.4, though the validity of such substitution in the expression for the phase velocity is questionable [*Foster et al.*, 1992]. Another complicating factor is that in both VHF studies cited above, no strict sorting according to echo types was performed. *Haldoupis et al.* [1987] gathered a large database for aspect angles between 1° and 14°, and both for type 1 and type 2 echoes, for several 50-MHz experiments performed by the University of Saskatchewan radar group using high-resolution Continuous Wave (CW) Doppler systems. Their data showed that for type 1 observations the rate of velocity decrease with the aspect angle was even slower, of the order of $\sim$ 10% only. For type 2 the results were inconclusive; velocity was changing in the range between -100 m s^{-1} and +100 m s^{-1} in seemingly random fashion with the aspect angle.

One might relate the discrepancies between the predictions of the linear fluid theory and VHF experiments to the fact that the geometric aspect angle was used, while at 50 MHz and even sometimes at 140 MHz refraction effects can be important. Doppler velocity attenuation with aspect angle, corrected for refraction, was studied by *Hall and Moorcroft* [1992] and *Kustov et al.* [1994]. In both *Hall and Moorcroft* [1992] and *Kustov et al.* [1994], however, it was demonstrated that the phase velocity decrease is still slower than one would expect on the basis of linear fluid theory.

Refraction effects are negligible for radio frequencies larger than 300 MHz; therefore, of special importance is the UHF study by *Moorcroft and Schlegel* [1988]. These authors used 933 MHz data from the EISCAT radar which was operated in a special mode looking at low elevation angles and detecting E-region 16-cm waves at large aspect angles ($\sim$ 6°), while simultaneously measuring F-region electric fields. The results of *Moorcroft and Schlegel* [1988] indicated that the velocity of the E-region coherent echoes correlated remarkably well with the $\mathbf{E} \times \mathbf{B}$ drift, but were about 2–3 times smaller, suggesting a rather strong velocity attenuation with aspect angle.

Even stronger velocity attenuation was reported in another UHF study by *Foster et al.* [1992] where the aspect angle variation of the phase velocity for 34-cm E-region waves was investigated using the data from the Millstone Hill 440-MHz radar. When the $\mathbf{E} \times \mathbf{B}$ drift exceeded 1000 m s^{-1} or, in other words, when the maximum E-region velocities observed were in excess of 600 m s^{-1}, the phase velocity was around zero in the range of aspect angles between 4° and 6° (see their Figure 10).

All of the studies cited above used measurements at radar frequencies greater than 50 MHz. At HF (8–20 MHz), the amount of refraction and hence the difference between geometric and actual aspect angles could be much more significant than at VHF, so it would be useful to check whether the velocity attenuation with aspect angle is the same at smaller radar frequencies/longer wavelengths. Another important question is whether there is a difference in aspect angle dependencies at small and large flow angles; or, if to put it differently, for observations of type 1 and type 2 echoes.

The results of the recent double-frequency (12 and 50 MHz) study by *Koustov et al.* [2001] based on a 30-min event observed at the Syowa Antarctic station suggested that the dependence of the Doppler velocity upon the aspect angle is approximately the same along the flow direction at HF and VHF. One should note that *Koustov et al.* [2001] considered variations of Doppler velocities with slant range together with the model calculations of the aspect angle for each slant range (see their Figure 2, we use similar aspect angle calculations in Chapter 5), but did not compare the aspect angle dependencies of the Doppler velocity directly, so that our conclusion about similarity in aspect angle dependencies at 12 and 50 MHz can be considered only as a very rough estimate.

One of the objectives of this thesis is to consider the aspect angle dependence of phase velocity for different frequencies in more detail and to check whether the preliminary results of *Koustov et al.* [2001] are true on a statistical basis. No less

important is a study of the velocity dependence upon the aspect angle at large flow angles.

4.3.3 Scale Effects

Besides aspect and flow angles, the phase velocity can also depend on the wave number/irregularity wavelength/radar frequency. Similar to the case of flow angle dependence, observations have shown that the phase velocity behaves differently for type 1 and type 2 echoes.

Over the years, there have been only a few double- and multi-frequency measurements of Doppler velocity of type 1 echoes observed at radar directions close to the direction of the flow. *Balsley and Farley* [1971] reported that at the magnetic equator, the Doppler velocity of type 1 echoes increased with radar frequency: the reported velocity ratios between frequencies at 16 MHz, 50 MHz, and 146 MHz were 0.9:1.0:1.1. In the statistical study by *Hanuise et al.* [1991], which used the Systeme HF d'Etudes Radar Polaires et Aurorales (SHERPA) radar operated in Schefferville, northern Quebec in Canada, it was shown that Doppler velocity increased slightly with the radar frequency. The ratio of the velocity at the lowest (9.3 MHz) to the largest (18.5 MHz) frequency was found to be about 0.9. A much slower (about 5%) increase was observed by *Koehler et al.* [1997] for 50- and 144-MHz type 1 echoes observed at mid-latitudes. The data from the same experiment have been revisited by *Haldoupis et al.* [2002], who found velocity increase with frequency in the range from 5% to 14% with an overall average of 10%. The recent analysis performed in the auroral zone by *Koustov et al.* [2001] did not reveal a significant difference between velocities at 12 and 50 MHz in the directions presumably along the flow, though the VHF and HF data were not simultaneous in this study.

Another question is: What should be the phase velocity for type 2 echoes at different radar frequencies? *Balsley and Farley* [1971] compared 16- and 50-MHz equatorial electrojet echoes and did not find significant differences between the velocities of type 2 echoes observed presumably perpendicular to the flow. Also, no variation of the phase velocity was found for multifrequency observations at HF in the equatorial electrojet [*Crochet*, 1977; *Hanuise and Crochet*, 1977]. *Koehler et al.* [1997] worked with 50-MHz and 144-MHz radars at mid-latitudes and reported that velocity of 50-MHz type 2 echoes can be both smaller and larger than the velocity of 144-MHz type 2 echoes (see their Figure 4). Comparisons of 12- and 50-MHz velocities at high latitudes by *Koustov et al.* [2001] showed that the situation is more complicated there. At large flow angles, the 12-MHz velocities were often much smaller than the 50-MHz velocities.

Eglitis et al. [1995] considered velocity statistics for VHF and HF radars, but their analysis of the velocity ratio was inconclusive because data were gathered for different observational conditions. *Hanuise et al.* [1991] presented simultaneous HF data for 6 frequencies between 9 and 18 MHz. Their main thrust was the study of high-velocity type 1 echoes. With respect to low-velocity, type 2 like echoes, these authors expected that velocities at lower HF radar frequencies should be slightly smaller than velocities at larger frequencies, but the results presented were inconclusive. Data shown later by *Uspensky et al.* [1994] confirmed this expectation to some extent (see their Figure 7), but the effect was not obvious for all measurements. More recently, *Jayachandran et al.* [2000] gathered significant velocity statistics at several HF frequencies that showed a velocity increase with the radar frequency, but the magnitude of the increase observed in this study was greater than would be expected on the basis of the predictions by *Hanuise et al.* [1991] (for some frequencies, the increase was as high as 2–3). The results of *Jayachandran et al.* [2000] are in apparent contradiction with data of *Haldoupis et al.* [1996] and *Haldoupis et al.* [1998], who

considered mid-latitude HF measurements at radar frequencies between 9 and 16 MHz and found only a minor (of the order of 5%) difference in the velocities of echoes observed from directions almost perpendicular to the magnetic L shell.

It is clear from this brief review that the issue of the frequency dependence of HF and VHF Doppler velocities requires further investigation as well, especially for type 2 echoes, for observations at large flow angles.

4.4 Summary

In this chapter we reviewed the experimental database on E-region irregularities. We considered in detail the phase velocity dependence upon three variables: flow angle, aspect angle, and wavelength of the irregularities. It was demonstrated that despite the significant progress, there still are gaps in our knowledge of irregularity phase velocity properties. We pointed out that it would be very useful to concentrate efforts on studying the phase velocity properties for HF observations at large angles with respect to the background plasma flow.

Chapter 5

Double-Frequency HF/VHF Observations

So far in this thesis we have demonstrated that the irregularity phase velocity in the auroral E region is dependent on the scale of the waves involved. We showed, however, that the character of this dependence is far from being clear either from theoretical or experimental point of view (Chapters 2 and 4, respectively), especially at large flow angles.

The main objective of this chapter is to compare the irregularity phase velocities at two significantly different wavelengths of 12 and 3 m. We consider here data from the Syowa SuperDARN HF radars in Antarctica. We selected these radars because of the large azimuthal coverage (see Figure 1.6b for the relative location and FOVs of the Syowa SuperDARN radars). The fields of view of the Syowa radars are side by side (in fact, they slightly overlapped during the period under study) so that one can detect echoes at both small and large flow angles. Another very important

reason for the selection of the Syowa SuperDARN radars is that their data have been complemented by VHF radar data. Finally, the E-region geometric aspect angle conditions are exceptionally good at Syowa. Most of the material of this chapter was recently published by *Makarevitch et al.* [2001, 2002b].

5.1 Brief Description of the Syowa Radars

The VHF radar observations at the Syowa Antarctic station (69°00′S, 39°35′E geographic, $\sim 67°$ magnetic latitude) have been carried out, from time to time, for over 35 years [*Ogawa*, 1996]. The recent construction of two SuperDARN HF radars at Syowa created experimental opportunities for studying irregularities in a new range of wavelengths (8–20 m).

5.1.1 SuperDARN HF Radars

The first SuperDARN radar, Syowa East, was installed at Syowa by the National Institute of Polar Research (NIPR) and began operation in February 1995. This radar was originally constructed to constitute a pair with the Halley Bay radar, Figure 1.6b. In October 1995 the second SuperDARN radar (Syowa South) began operation.

The Syowa HF radars are analogous to all other SuperDARN radars in the network [*Villain et al.*, 1987; *Greenwald et al.*, 1995; *Huber*, 1999]. Each radar scans through 16 successive beam positions in 3.33° steps, covering a $\sim 53°$ range of azimuths. The radar forms and steers its beam by the phasing of the 16 antennas in a linear antenna array.

The basic radar operation consists of the following steps: (1) selection of a beam position (0–15), (2) search for the quietest 5-kHz channel about the assigned transmitting frequency (8–20 MHz), (3) repeated transmission of a 7-pulse sequence over

the selected integration period and reception of backscattered signal with gating in range (0–75), and (4) calculation of the Auto-Correlation Functions (ACFs). These operations are usually carried out in sequence for the 16 beam positions, which collectively constitute 1 scan. The beam integration period is typically around 7 s, and the scan repeat time is 60 s (fast mode) or 120 s (normal mode). Within a scan, beam 0 corresponds to the most westward beam position and beam 15 to the most eastward.

Through direct analysis in real time of the 18-lag complex ACF, the spectral power, mean Doppler velocity and spectral width are determined for each direction (beam = 0–15) and range cell (bin = 0–75). The range cells start at a range of 180 km and step by 45 km. Range bin n thus corresponds to the range gate from $180 + 45 * n$ to $180 + 45 * (n + 1)$ in kilometers.

To obtain the ACF as a function of time (lag number) for each beam and for each range cell, a 7-pulse sequence is used, Figure 5.1. The pulse length is 300 μs, corresponding to 45-km range resolution, and the basic lag separation is 2400 μs. An 18-lag ACF is generated by sampling and processing the backscattered signals from the pulse sequence. The ACF consists of the zeroth lag and 17 other unique lags, all integers of the basic lag separation τ, as shown in Figure 5.1. A radar transmits, integrates and averages 70 multipulse sequences for each beam to increase the signal to noise ratio.

The complex ACFs consisting of the real (R) and imaginary (I) parts are further processed in order to obtain the estimates of the spectral moments (spectral power, mean Doppler shift, and spectral width). Figure 5.2 shows schematically two signal processing techniques that can be used in the SuperDARN experiment. It is illustrated that the real (imaginary) part of the ACF is a damped cosine (sine) function of lag number, Figure 5.2a. The first technique is the Fourier analysis of the spectral power. The Fast Fourier Transform (FFT) of the ACF is shown in Figure 5.2b as a

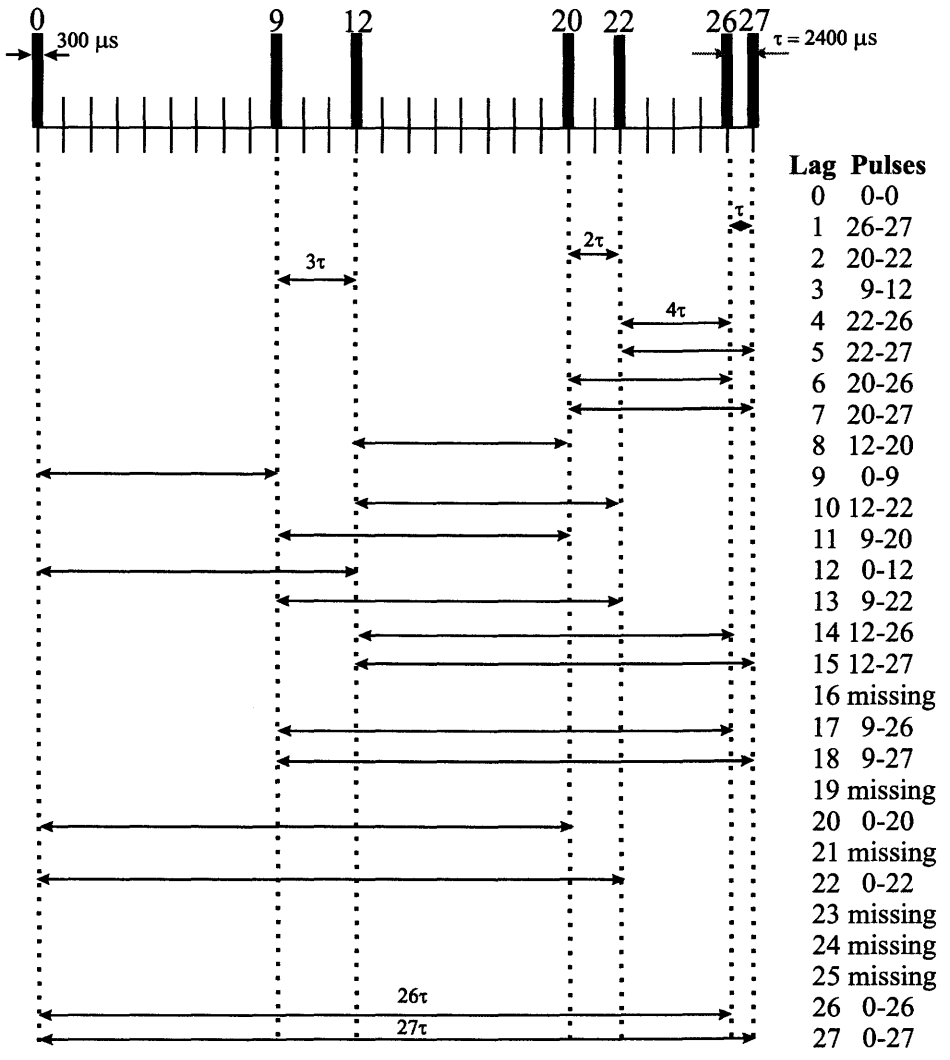

Figure 5.1: The 7-pulse sequence currently in use in the SuperDARN experiment. The pulse length is 300 μs. The basic lag separation τ is 2400 μs.

32-point Doppler spectrum. This method is generally more time consuming and thus less convenient.

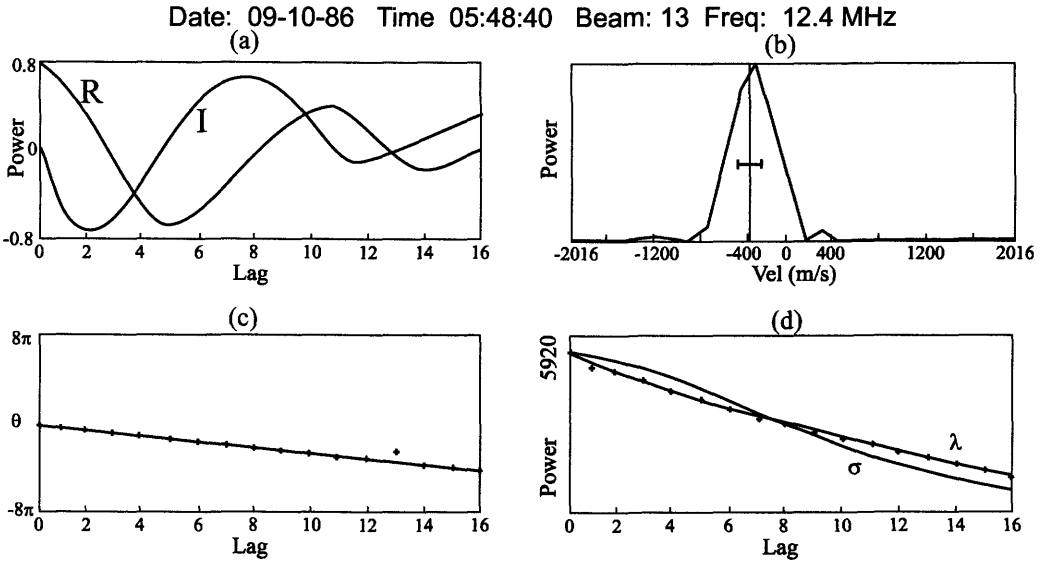

Figure 5.2: Radar signal processing technique. (a) Real and imaginary part of an ACF. (b) Doppler spectrum obtained through fast Fourier transform of the ACF. (c) Phase angle θ as a function of lag and its linear least squares fit. (d) Power variation of the ACF as a function of lag with exponential λ and Gaussian σ least squares fits. The vertical line shows the mean Doppler velocity deduced from Figure 5.2c, and the horizontal bar shows the width computed from λ in Figure 5.2d. Adapted from *Villain et al.* [1987].

A second signal processing approach, the FITACF method, is currently a standard technique in the SuperDARN experiment [*Greenwald el al.*, 1995]. It derives the line of sight Doppler velocity (FITACF velocity) by performing a least squares fit to the phase angle as a function of lag number. The phase angle $\theta = \tan^{-1}(I/R)$ variation with lag number is shown in Figure 5.2c by the pluses and its least squares linear fit is shown by the solid line. Typically, the phase angle variation is an almost perfect straight line [*Villain et al.*, 1987], which results in the high accuracy of the mean Doppler velocity estimate.

To determine the echo power and spectral width, one has to analyze the ACF amplitude $P(t) = (R^2 + I^2)^{1/2}$ variation with lag number shown in Figure 5.2d by pluses. One can assume that the ACF amplitude decorrelates with time (lag number) either exponentially (Lorentzian function, $P_\lambda(t) = C_\lambda e^{i\omega t} e^{-\lambda t}$, the least squares fit curve marked by λ in Figure 5.2d) or as a Gaussian function ($P_\sigma(t) = C_\sigma e^{i\omega t} e^{-\sigma^2 t^2}$, σ-curve in Figure 5.2d), which provides estimates of the spectral power (C_λ or C_σ) and half-power width (2λ or 3.3σ). The question which model (Lorentzian, Gaussian, or intermediate) is better to use for fitting (from which the estimates of the spectral power and width are derived) is quite complex [*Villain et al.*, 1987; *Hanuise et al.*, 1993; *Villain et al.*, 1996]. *Villain et al.* [1987] concluded that $\sim$ 80% of the ACFs are better described as exponentially decaying (Lorentzian) functions. In this thesis, we used the spectral power and width obtained from the Lorentzian fit. However, the main focus of this thesis is on the phase (Doppler) velocity, whose estimates do not require any assumptions about the shape of the ACF amplitude.

5.1.2 Scanning-Beam VHF Radar

Another coherent radar, namely a scanning-beam Communications Research Laboratory (CRL) 50-MHz Doppler radar capable of observing a wide area of the high-latitude ionosphere, was installed in February 1995 at Syowa [*Igarashi et al.*, 1995; 1998; *Ogawa*, 1996] almost simultaneously with the SuperDARN Syowa East HF radar. Table 5.1 lists some specifications of the CRL radar.

This radar measures the echo power and Doppler velocity (15-km range resolution starting from 120 km) using the double-pulse technique. Five transmitting antennas with an azimuthal beam width of $\sim$ 30° cover a wide area of $\sim$ 160° in azimuth. The receiving beam direction is scanned in 5° steps by using two sets of phased-array antennas with 5°-wide beams covering about $\sim$ 160° in azimuth. One scan through

Location	Syowa Station (69°00′S, 39°35′E geographic)
Transmitting frequency	50.0 MHz
Peak transmitting power	20kW
Pulse width	10–190 μs every 10 μs
Transmitting pulse pattern	Double pulse
Transmitting antenna	5 sets of 8 element Yagi antennas
Receiving antenna	Two sets of sixteen Yagi antennas
Receiving beam width	5 degrees
Beam cover region	$\pm$ 80 degrees in azimuth, 0° $\equiv$ geomagnetic south

Table 5.1: Specifications of scanning-beam VHF auroral radar. Adapted from *Igarashi et al.* [1995].

the FOV is accomplished in 4 min. Below we refer to the beams of the 50-MHz radar by their geomagnetic azimuth (e.g., beam 40 has a geomagnetic azimuth of 40° and a geographic azimuth of 83.7°).

5.2 Experiment Setup and Statistical Characteristics of Echoes

5.2.1 Observations

Figure 5.3 shows the experiment setup with the near (slant ranges r less than 900 km) FOV of the Syowa East (light gray sector) and Syowa South (dark gray sector) radars. The FOV of the CRL radar for $r < 1000$ km is shown by the black sector. The solid white curve represents the line of zero off-perpendicular (aspect) angle ($\alpha = 0°$) at 110-km altitude, assuming no refraction for the radio waves, and the circular dashed white lines are the slant range marks (r = 400, 600, and 800 km). Also shown by black dashed lines are several beam positions of the CRL radar (the data from these radar directions are considered in Section 5.4). The number by every 50-MHz

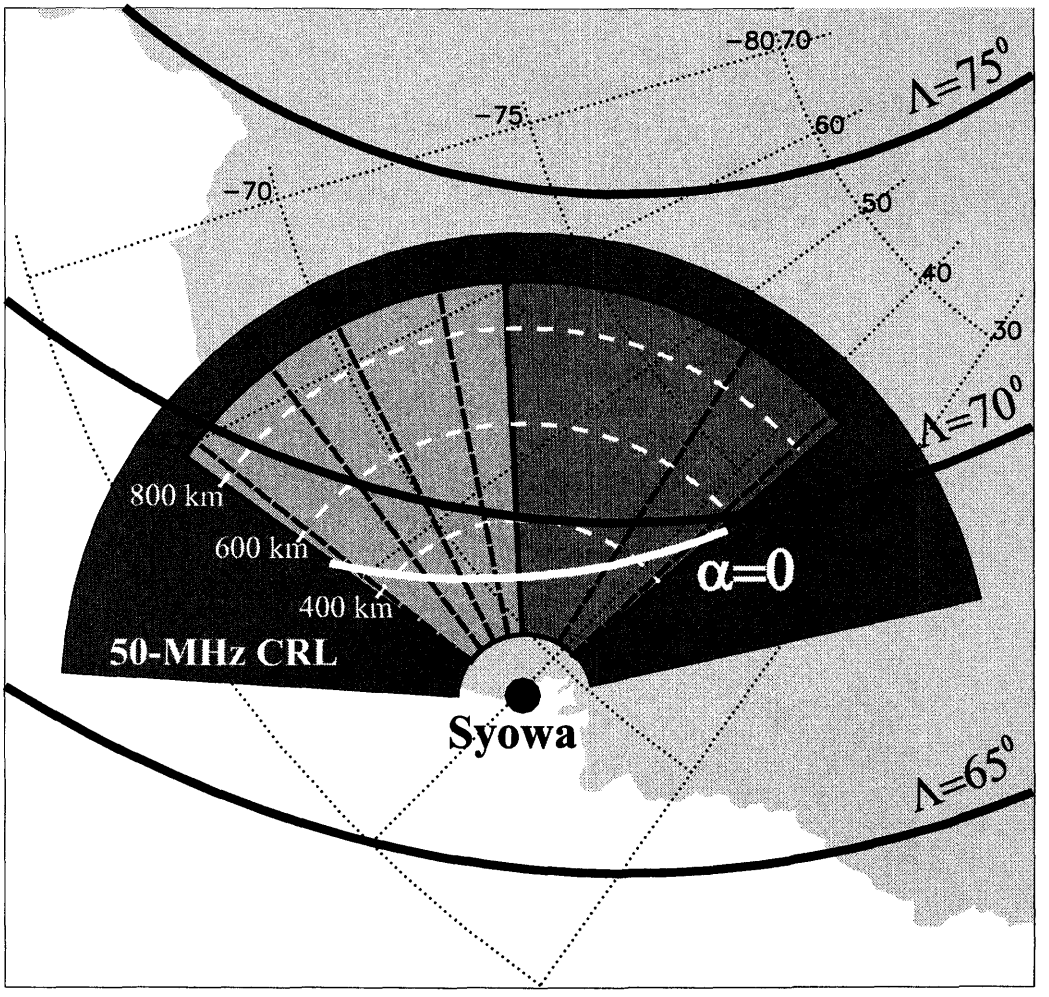

Figure 5.3: Near field of view of the Syowa East (light gray sector) and Syowa South (dark gray sector) SuperDARN (Super Dual Auroral Radar Network) HF radars. The black sector corresponds to the field of view of the Communications Research Laboratory VHF radar. Also shown are PACE (Polar Anglo-American Conjugate Experiment) lines of equal magnetic latitudes $\Lambda = 65°$, 70°, and 75°. The thick white curve is the zero off-orthogonal (aspect) angle line ($\alpha = 0°$). The white dashed circular lines are range marks of 400, 600, and 800 km.

direction denotes its geographic azimuth, measured clockwise from geographic north. The thick black lines in Figure 5.3 are the PACE magnetic parallels [*Baker and Wing*, 1989].

In this study we formulate results in terms of L-shell angle ϕ defined as the angle between the direction of the radar wave vector $\mathbf{k}$ and the magnetic L shell. One must note here that the lines of equal magnetic latitude, as calculated from the PACE magnetic model, were found to be approximately the same as the L shells (lines of equal L value [*McIlwain*, 1961]) from *Ogawa* [1996] and for this reason we use PACE magnetic parallels and L shells interchangeably. The L-shell angles within Syowa East and Syowa South FOVs are positive and change continuously from $\phi \cong 20°$ (eastern edge of HF FOV, Syowa East beam 15, azimuth of $\sim 83.7°$, Figure 5.3) to $\phi \cong 140°$ (southern edge of HF FOV, Syowa South beam 0, azimuth of $\sim 183.7°$). The azimuth corresponding to an L-shell angle of 90° is located close to the eastern edge of the Syowa South FOV, and we will call the radar directions close to this azimuth "perpendicular directions" or "directions perpendicular to the flow". The radar directions close to the edges of the common FOV (Syowa East beam 15 and Syowa South beam 0) will be called "parallel directions" or "directions along the flow", even though the L-shell angle is not exactly zero or 180°. In this terminology we assume that the flow is predominantly along the L shells.

In this study we used data from the normal mode of SuperDARN operation (2-min temporal resolution). No interferometer measurements for angle of echo arrival (or echo height) were available. During HF data postprocessing, ground-scattered signals were removed from the records by applying the standard criteria that such signals have low (< 50 m s^{-1}) velocity and low (< 20 m s^{-1}) spectral width. For the analysis, the echo power of all the radars was corrected for slant range using an r^{-3} power decrease with range r under the assumption that irregularities are neither "hard", non-beam-filling ($P \propto r^{-4}$) nor "soft", beam-filling ($P \propto r^{-2}$) targets [*Hunsucker*,

1991].

To obtain a data set unbiased by event selection and with the maximum possible number of records, we decided to consider one month of joint (HF and VHF) measurements. The CRL VHF radar observations were only carried out during austral winter and equinox seasons of 1995–1997, and this was one of the factors limiting our choice. Analysis of the HF and VHF data sets showed that VHF echoes were rarer than HF echoes. Because of that we selected for the analysis the month of March 1997, for which 50-MHz echo occurrence was the highest.

For the 31 days in March of 1997, the SuperDARN radars worked in the normal mode of operation only during 23 days and we selected these days. To exclude possible F-region echoes we restricted the slant ranges of all radars to values less than 810 km. Finally, HF echoes with unusually large spectral width (> 500 m s^{-1}) and HF and VHF echoes with low uncorrected power (< 3 dB at HF and < 1 dB at VHF) were excluded from the database.

5.2.2 Echo Occurrence

Diurnal Variation

We first assess the echo occurrence for all three systems during the selected period. Figure 5.4 shows the total number of echoes as a function of universal time at 12 MHz (upper panel) and 50 MHz (bottom panel). Here we marked data obtained by Syowa East and Syowa South as 12 MHz though the radars used slightly different frequencies to avoid interference ($\sim$ 12 MHz for Syowa East and $\sim$ 11 MHz for Syowa South; we will neglect this difference below for simplicity of presentation).

The number of echoes in Figure 5.4 was computed as follows. Since the FOV of the VHF radar is broader than the combined FOVs of the two HF radars, we considered

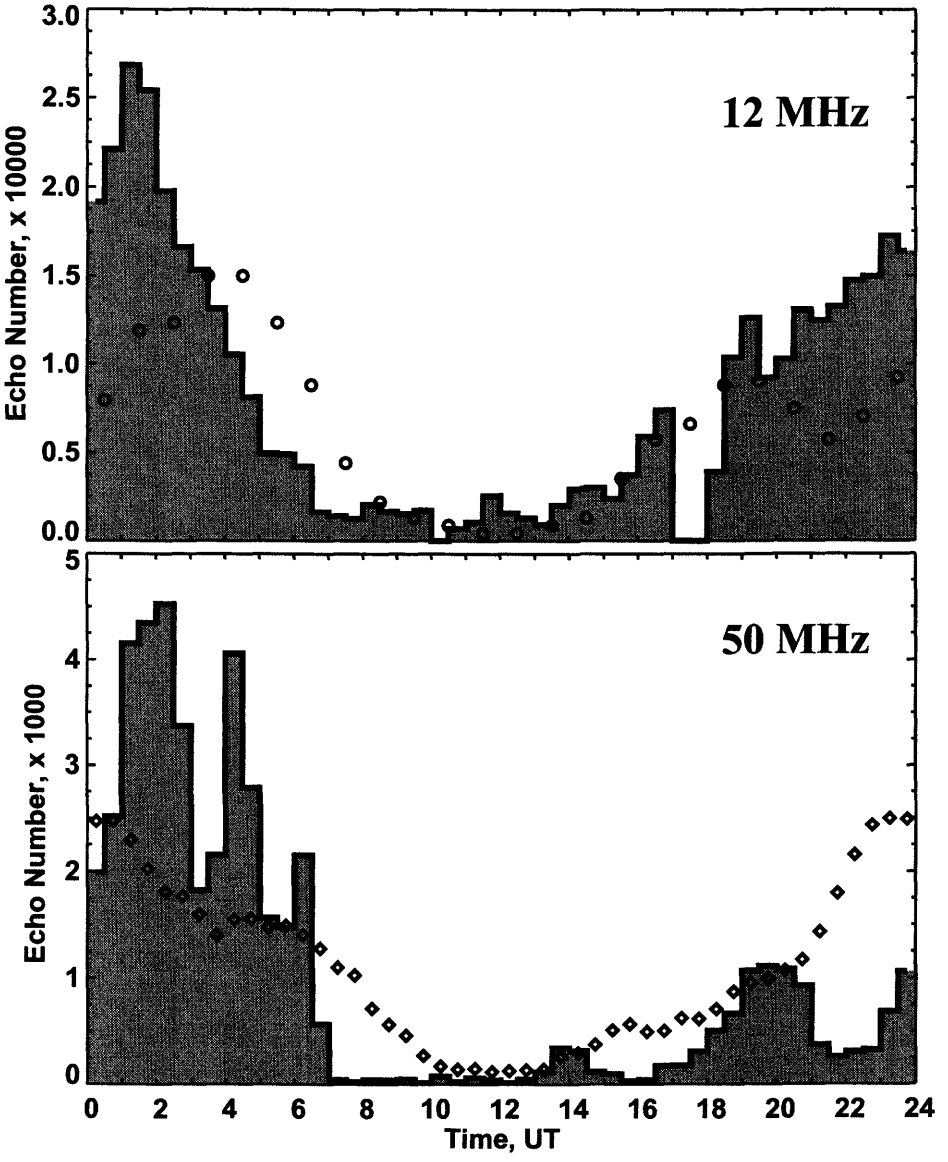

Figure 5.4: Number of echoes in the near field of view detected in all available beams as a function of universal time at 12 MHz (upper panel) and 50 MHz (bottom panel). The open circles in the upper panel represent data of *Hanuise et al.* [1991] for their HF observations (the scale is arbitrary), and the diamonds in the bottom panel show number of 50-MHz echoes versus time from *McNamara* [1972].

only those VHF radar directions that were within this combined HF FOV. Then we computed the total number of echoes for all directions and for all near slant ranges ($r < 810$ km for all radars) for each 30-min period of time. The universal time is approximately equal to the magnetic local time (MLT) for the near FOV of the Syowa radars (UT $\cong$ MLT), therefore Figure 5.4 essentially presents the number of echoes for both frequencies as a function of MLT. For comparison we provide the results from *Hanuise et al.* [1991] for the radar frequency of 12 MHz (open circles) and data from the Saskatoon International Geophysical Year (IGY) auroral radar [*McNamara*, 1972] at 50 MHz (diamonds) in arbitrary scale. For these radars the universal time differs significantly from the magnetic local time so that we shifted their data to account for this difference.

One can see that the number of echoes at 12 MHz exhibits a clear maximum around 0100 UT and that there are significantly fewer echoes during the daytime (7–19 UT). This result is in reasonable agreement with the data of *Hanuise et al.* [1991], except for a slight shift in the time of the maximum ($\sim$ 5 MLT vs $\sim$ 1 MLT).

A similar maximum can be seen at 50 MHz (bottom panel of Figure 5.4). The maximum is broader here (1–4 UT), the number of echoes during the evening (18–24 UT) is much less than that at 12 MHz, and there are almost no echoes between 7 and 17 UT. The data of *McNamara* [1972] show smoother variation with time, and the maximum is shifted ($\sim$ 0 MLT vs ours $\sim$ 3 MLT), but, overall, the shape of the curve is similar.

The absence of echoes during some specific times (1000–1030 UT and 1700–1800 UT in the upper panel) at HF is due to the fact that the HF radars simply were not operational during these periods. The reasons for the existence of the local minima at VHF (0300–0400 and 0500–0600 UT in the bottom panel) are not clear. We believe that this is most likely because of the smaller data set at VHF (the number of echoes at HF is several times larger than that at VHF).

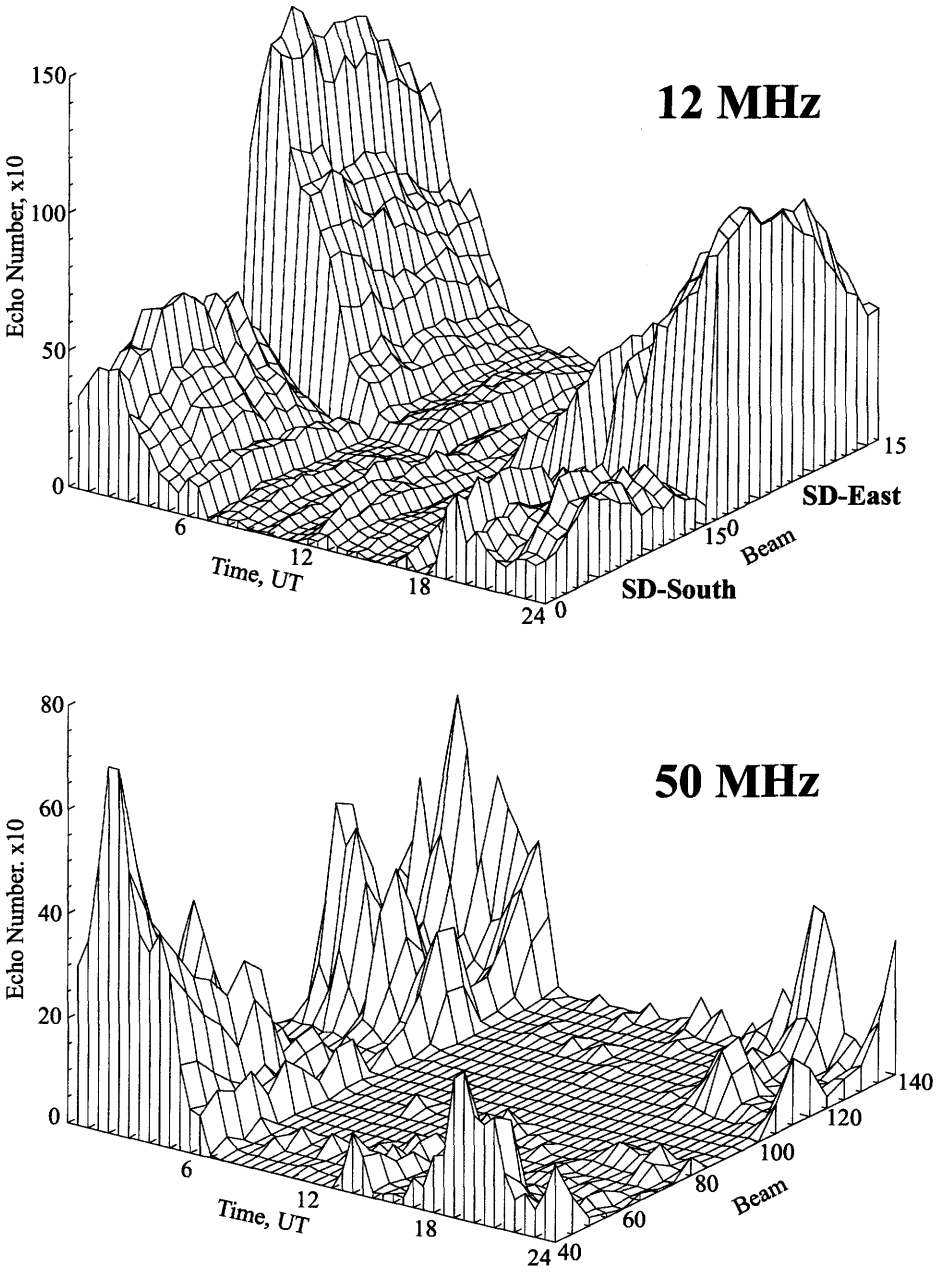

Figure 5.5: Variation of number of echoes in the near field of view with radar beam number and universal time at 12 MHz (upper panel) and 50 MHz (bottom panel).

Figure 5.4 gives the overall occurrence in the common FOV. In Figure 5.5 we present more detailed information. Here we plotted the number of echoes as a function of the time of the day and radar direction, for 12 and 50 MHz (upper and bottom panels, respectively). Notice that the number of echoes for Syowa East is 2–3 times larger than that for Syowa South. However, there is no significant difference between various beams for individual radars; the azimuthal distribution of echoes is more or less homogeneous for each HF radar. One can notice that for every UT sector the number of echoes is slightly larger for the central beams of each HF radar.

At 50 MHz the situation is completely different. The number of echoes varies with azimuth of observations/beam number. There are almost no echoes for beams 80–100 and the number of echoes is at maximum at the edges of the common FOV (50-MHz beams 40 and 140).

Details of Echo Occurrence Within FOV

Our next step is to include into analysis the slant range information. We consider here HF and VHF echo occurrence versus range and azimuth for the morning observations between 02 and 06 UT when the echo occurrence is at maximum (see previous section). We also expect that for this interval the plasma flow is mostly L-shell aligned, Figure 1.4.

Figure 5.6 is a contour plot of number of echoes (azimuth of observations horizontally, slant range vertically) for the near FOVs (180–765 km) of the 12-MHz (upper panel) and 50-MHz (bottom panel) radars. The white curve on these plots is the line of perfect aspect angle ($\alpha = 0°$) at the height of 110 km, calculated for each radar by assuming the ionospheric electron density profile from the International Reference Ionosphere-95 (IRI-95) model [*Bilitza*, 1997]. The dashed black lines in Figure 5.6 are contours of equal L-shell angle ϕ (contour step is 20°), computed using the PACE

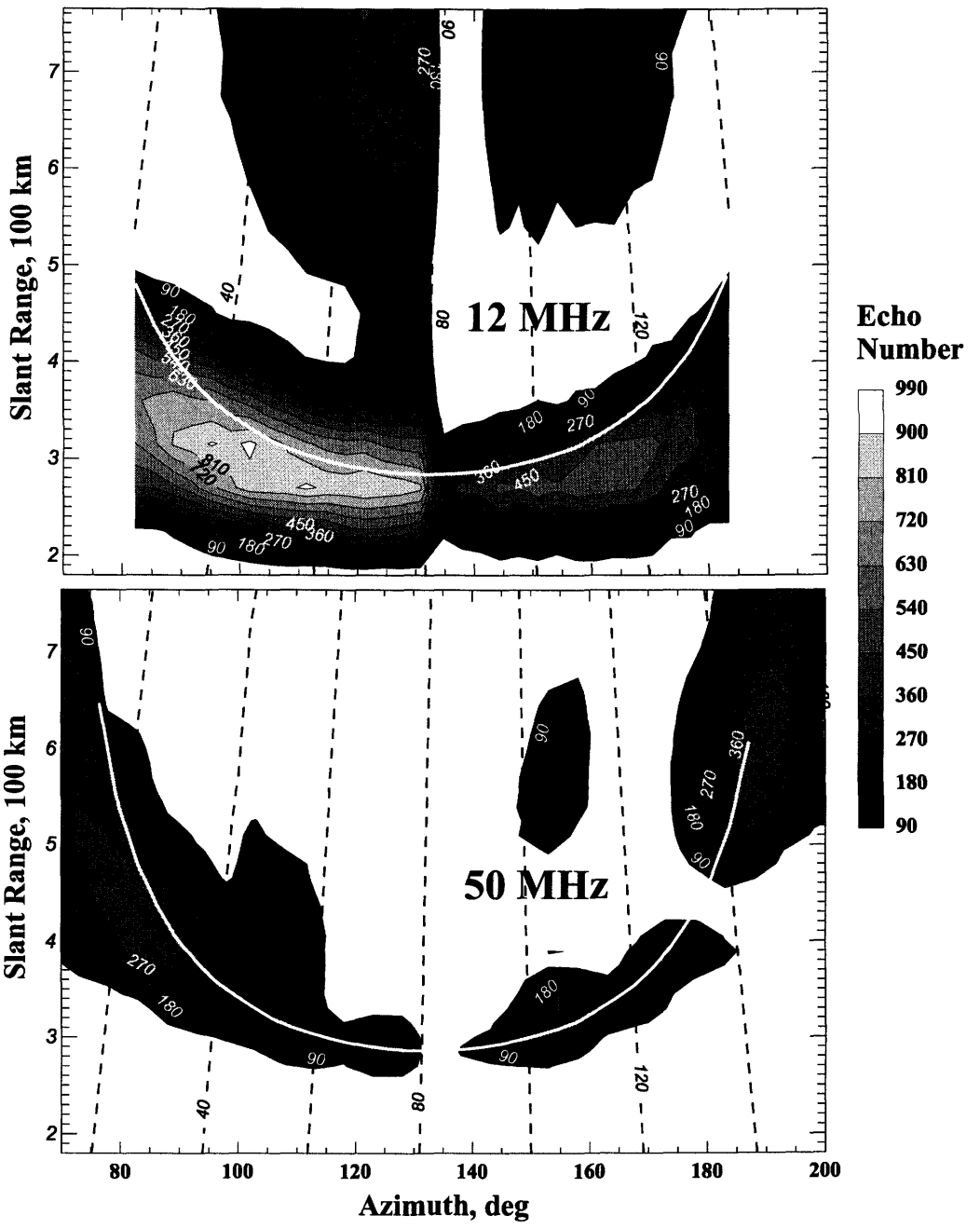

Figure 5.6: Number of echoes for various azimuths of observations and slant ranges for 12- (upper panel) and 50-MHz (bottom panel) radars, during the time interval 02–06 UT.

magnetic field model. Data from both SuperDARN radars are combined in the upper panel of Figure 5.6; the transition between two adjacent SuperDARN FOVs occurs at an azimuth of $\sim 135°$ ($\phi \sim 85°$), with the apparent minimum in echo occurrence existing simply because the echo occurrence contours change drastically in this area of the plot. The FOV of the 50-MHz radar is about 160°-wide, Figure 5.3; we show 50-MHz data for only those directions that are close to the SuperDARN radar directions.

In the 12-MHz part of the diagram one can recognize two distinct areas: close slant ranges (200–500 km), where the distribution of echo occurrence is almost homogeneous with azimuth (except for the noted earlier difference in number of echoes between the two SuperDARN radars) and farther ranges (500–765 km) where echoes tend to occur close to the perpendicular directions. There is a clear gap between echoes at closer and farther ranges. For the perpendicular directions, the gap is located at $\sim$ 480 km and it is quite narrow while for the edges of the HF FOV (azimuths of 82° and 184°) it is much wider (there are no echoes detected for r = 500–765 km). The location of the radar cells with maximum number of echoes "follows" closely the perfect aspect line, except for the fact that they are shifted slightly to closer ranges. The shift seems to increase towards the edges of the FOV. Interestingly, for the eastern sector (Syowa East) there is a broad global maximum (ϕ = 40°–60°, azimuth= 95°–115°) with some local peaks (white spots). For the southern sector the maximum is smaller ($\sim$ 500 echoes versus $\sim$ 1000) and its azimuthal location is ϕ = 100°–120°, azimuth = 150°–170°. Thus the maxima of echo occurrence are somewhere between the parallel and perpendicular directions. In our opinion, the echoes from the nearest ranges ($r < 500$ km) originate from E-region heights (aspect angles at the electrojet heights of 110 km are around zero for this area), while the echoes from farther ranges most probably originate from the bottom/central part of the F region. The far range echoes can also be obtained through the one and a half hop propagation mode, Chapter 1.

At 50 MHz (bottom panel) the echo occurrence distribution is quite different. There are no echoes for slant ranges greater than 650 km for perpendicular directions and the shift between the perfect aspect angle line and the location (in slant range) of maxima in echo occurrence is smaller than that at 12 MHz, especially for the perpendicular directions. But the most striking feature in the 50-MHz diagram is that the distribution of echo occurrence with azimuth is not as homogeneous as at 12 MHz. The number of echoes maximizes at L-shell angles of 20° and 150° for the eastern and southern sectors of the VHF radar FOV, respectively. Away from these directions, echo occurrence drops by a factor of 3 or more.

5.2.3 Spectral Power

The echo occurrence diagram of Figure 5.6 reflects only the fact of echo presence and does indicate the echo strength. We address this issue in this section.

In Figure 5.7 we show the average power in a format similar to Figure 5.6. To produce this diagram, we averaged the range-corrected power in each radar cell and plotted it as a function of azimuth and slant range. As with the echo occurrence diagram, here and in the next section we consider only observations between 02–06 UT to limit ourselves to the period of maximum echo occurrence.

One can see that the distribution of 12-MHz power is essentially the same as the distribution of number of echoes. One can see the stripe of E-region echoes at short ranges and the F-region echoes at farther ranges. Within the stripe of E-region echoes, power decreases gradually by 2–4 dB from maximum at the edges to the center of FOV. The difference between average power for the Syowa East and the Syowa South radars is $\sim$ 6 dB. Interestingly, the power maxima along any radar direction (for each specific azimuth) are located at ranges where the aspect angle is zero (at perfect aspect angle line marked by solid white curve) or a little closer to the radar. The

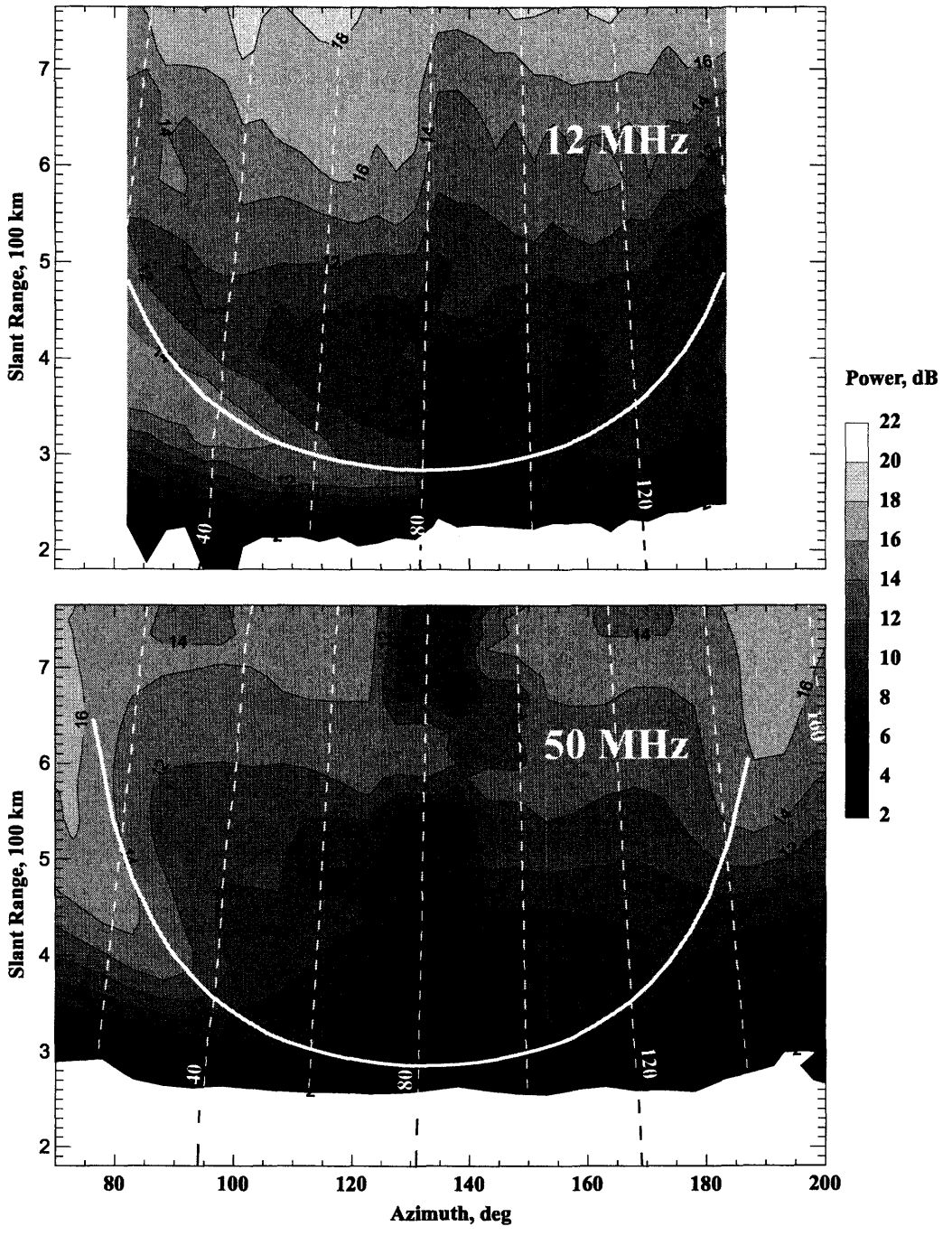

Figure 5.7: The same as Figure 5.6, but for the average power.

effect is more obvious if one uses power not corrected for slant range (not shown).

At 50 MHz, there is a substantial variation of power with azimuth; the difference in power between parallel and perpendicular directions is $\sim$ 10 dB, and power maximizes at L-shell angles of $\sim 20°$ and $\sim 150°$.

5.2.4 Doppler Velocity

Our next step is to consider variations of the Doppler velocity with range and azimuth, Figure 5.8. One can see that along the band of E-region echoes, the velocity changes from -400 m s^{-1} on the eastern edge of the HF radar FOV to +300 m s^{-1} on the southern edge. The change of the velocity polarity occurs at the azimuth of $\sim$ 130–140°, close to the perpendicular directions. The average velocities along and perpendicular to the L shells are consistent with much larger data set for Syowa East beams 15 and 0 considered by *Ogawa et al.* [2001]. One can also notice that the HF velocity is maximized for ranges slightly farther than the ranges of perfect aspect angle (r = 450–500 km, azimuth = 82°–90°); thus in the range profiles of echo power and velocity there is a shift in the location of their maxima (see also Section 5.4). The VHF radar data have a velocity distribution similar to the HF data except that the velocity maxima are located closer to the ranges of perfect aspect angle.

The HF radar measurements show larger velocities at farther ranges (r = 600–700 km, azimuth = 82°–90° and $r \cong$ 550 km, azimuth = 170°–180°). The VHF radar echoes also have large average velocities at far ranges (r = 600–765 km, azimuth = 170°–180°). We think, however, that these measurements may not reflect the general tendencies since the number of echoes for these areas is very low (Figure 5.6).

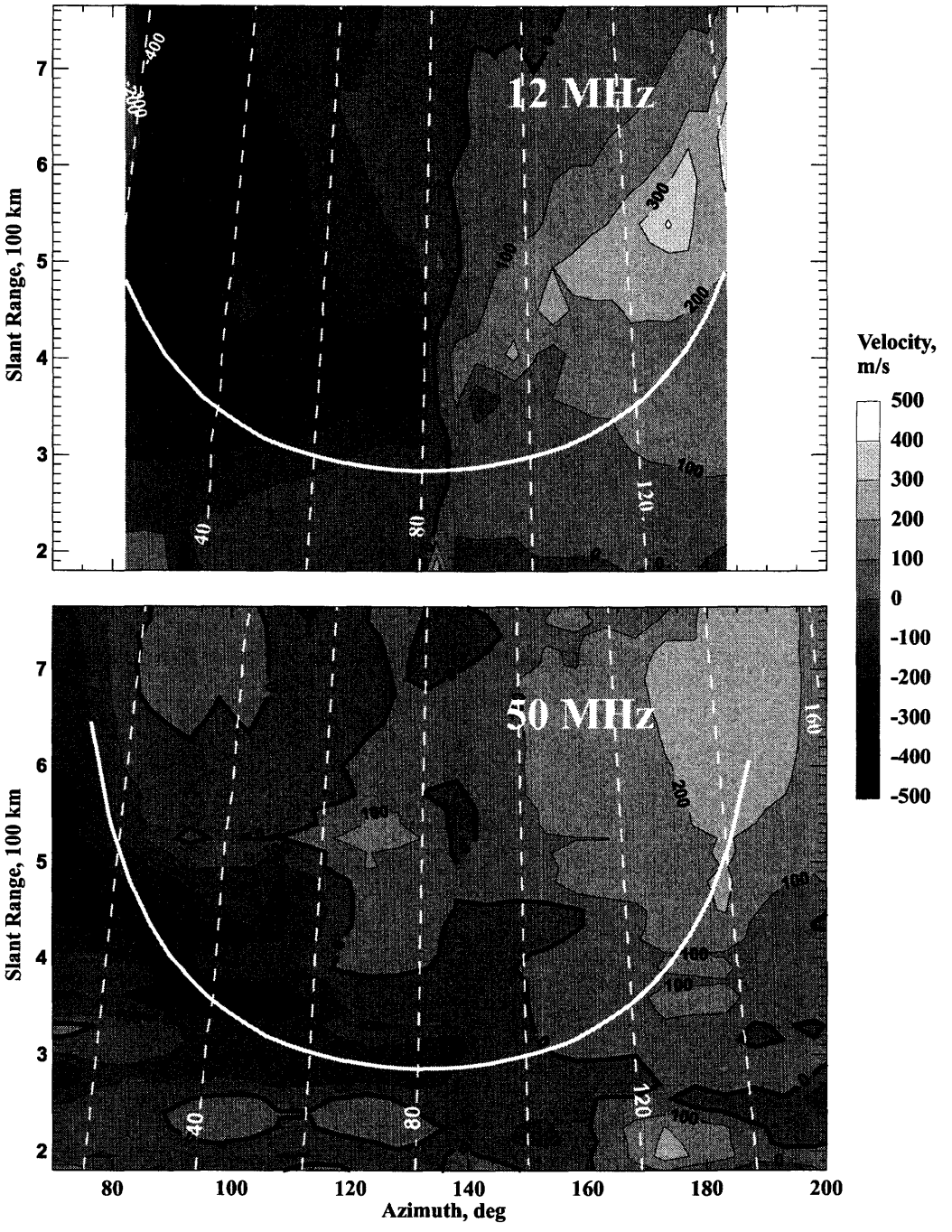

Figure 5.8: The same as Figure 5.6, but for the average Doppler velocity.

5.2.5 Spectral Width

For completeness of presentation we show in Figure 5.9 the average spectral width within the FOV. The format of the diagram is the same as for the three previous diagrams, with the only exception that now we have only the 12-MHz portion of the figure. The information on spectral width of the 50-MHz echoes was not available in this experiment (50-MHz radar used double-pulse technique). One can see that the average width maximizes for directions perpendicular to the flow. Another feature is that the width has maxima farther from the ranges of the perfect aspect angle (solid white curve in Figure 5.9), meaning that the spectral width maximizes at farther slant ranges than the spectral power (Figure 5.7).

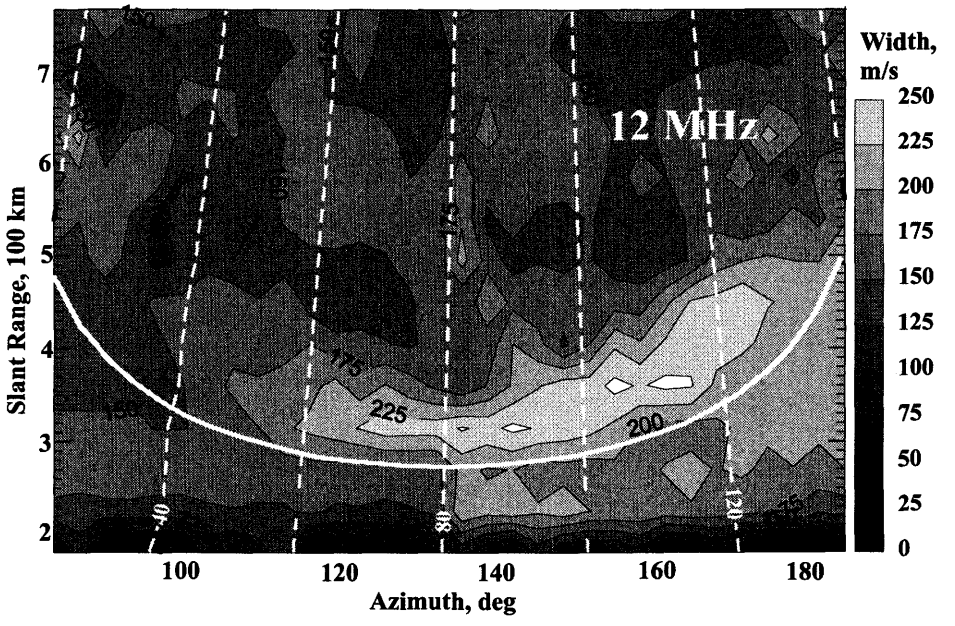

Figure 5.9: The same as Figure 5.6, but for the average spectral width at 12 MHz.

5.3 Detailed Comparison of HF and VHF Velocities

From the statistics for the HF and VHF velocities presented in the previous section one can conclude that HF and VHF velocities are comparable, to a first approximation. Such a conclusion, however, needs to be refined since the comparison revealed some differences in details. Also, for VHF measurements, several types of E-region echoes are known and they have different mean Doppler shifts and variations of the Doppler velocity with the L-shell (flow) angle [*Fejer and Kelley*, 1980; *Haldoupis*, 1989; *Moorcroft*, 2002]. It is interesting to find out if some of these features are identifiable in the common HF/VHF data set.

5.3.1 High- and Low-Velocity HF Echoes

In this section we produce a scatter plot of HF velocities versus VHF velocities for 6 azimuths of observations over a period of 00–24 UT for all 23 days of observations, Figure 5.10. Here we consider so called "nearly simultaneous" points. By definition, some measurement at 12 MHz for the azimuth az_{12}, slant range r_{12}, and time t_{12} was considered to be "nearly simultaneous" with a measurement at 50 MHz at az_{50}, r_{50}, t_{50} if $|az_{12} - az_{50}| < 5°$, $|r_{12} - r_{50}| < 15$ km, and $|t_{12} - t_{50}| < 60$ s. In total, 552 hours of observations were considered.

The considered radar directions (Syowa East beams 15, 10, 7, and 2 and Syowa South beams 0 and 6) cover the entire area of joint observations. Indicated in the top left corner of each panel of Figure 5.10 is the mean L-shell angle ϕ for each specific radar direction (it was shown earlier in Figures 5.6–5.9 that ϕ changes with range). Angle ϕ progressively increases as one moves from the easternmost Syowa East beam

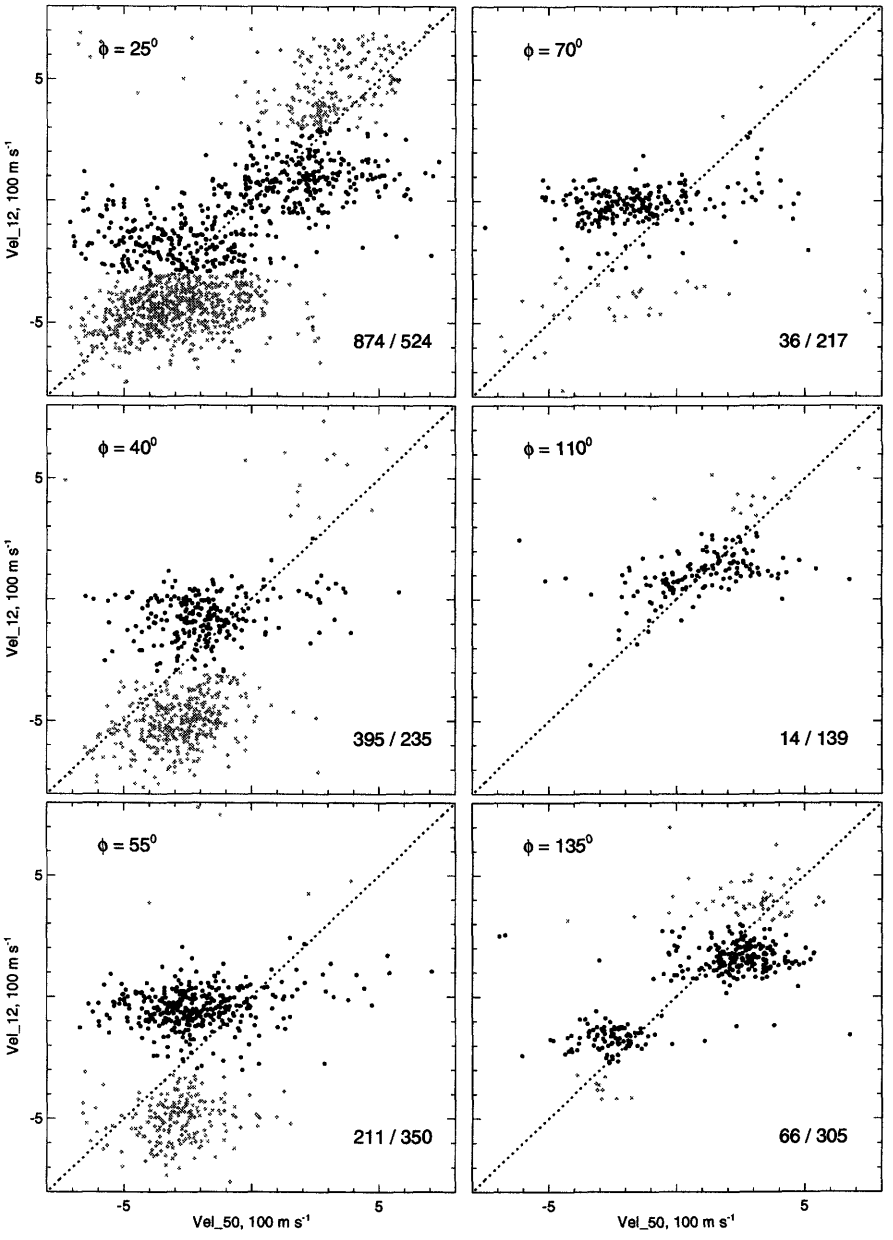

Figure 5.10: Velocity of 12-MHz echoes versus velocity of 50-MHz echoes for 6 azimuths. Average value for the L-shell angle ϕ is shown in the top left corner of each panel. For each azimuth, nearly simultaneous measurements at all distances are considered. Gray (black) dots correspond to those echoes whose velocity magnitudes were larger (smaller) than the critical velocity of 320 ms^{-1}. Number of gray dots/number of black dots is shown in the right bottom corner of each panel.

15 ($\phi \cong 25°$) to the westernmost Syowa South beam 0 ($\phi \cong 135°$).

One can clearly see the existence of two echo populations: the high- and low-velocity points. We divided all echoes according to the magnitude of the 12-MHz Doppler velocity: gray (black) dots are echoes with $V > V_{crit}$ ($V < V_{crit}$), $V_{crit} = 320$ m s^{-1}. The number of gray/black points is shown in the right bottom corner of each panel. The difference (vertical distance) between the two clouds of points appears to be increasing with ϕ for the first four panels. Two echo types are obvious for both negative and positive HF velocities (morning and evening sectors of observations for the first 4 panels, respectively). There is a drastic change in the number of high- and low-velocity points as angle ϕ increases. While the low-velocity echoes occur for all directions, the high-velocity echoes are rare for the perpendicular directions (the smallest numbers of high-velocity echoes of 36 and 14 are at $\phi = 70°$ and 110°).

The ratio of 12- to 50-MHz velocity magnitudes depends strongly on whether one deals with low- or high-velocity 12-MHz echoes. For the black dots the velocity magnitude at 50 MHz is almost always larger than that at 12 MHz ($V^{50} \gg V^{12}_{low}$, where index "low" indicates low-velocity 12-MHz echoes). For the gray dots the situation seems to be the opposite ($V^{50} < V^{12}_{high}$, gray cloud for negative (positive) velocities is shifted to the right (left) from the dotted line of ideal coincidence, index "high" indicates high-velocity 12-MHz echoes).

5.3.2 Velocity Versus L-Shell Angle

In this section we study high- and low-velocity echoes using a different approach, namely we make scatter plots of HF and VHF velocities versus L-shell angle. Thus for each radar cell (slant range-azimuth) we consider all available data points rather than present one averaged value as in Figure 5.8.

Figure 5.11 shows a scatter plot of velocity versus L-shell angle for a 30-min

event on March 17, 1997, 0100–0130 UT. This event was studied by *Koustov et al.* [2001], who considered the variation of the average power and velocity with range. Panel (a) represents data for HF measurements and panel (c) shows data for VHF measurements. The scale for the L-shell angle is given at the bottom of the panel (e). For each echo the aspect angle was calculated by assuming one generic electron density profile as explained in Section 5.2.2, and we indicate the magnitude of the aspect angle by the color of the point. The color scheme is given in panel (a). Panels (b) and (d) show the histograms of velocity distribution for 12 and 50 MHz, respectively. The total number of points is indicated in the bottom right corner of panels (b) and (d). The scale for panels (b) and (d) is given at the bottom of panel (d).

The most prominent feature in (a) is the existence of two populations of echoes, high- and low-velocity 12-MHz echoes. The low-velocity echoes have relatively small Doppler velocity magnitudes (< 200 m s^{-1}) and they are present at all L-shell angles ϕ. High-velocity points have relatively large velocity magnitudes ($>\sim 300$ m s^{-1}) and they exist only for $\phi <\sim 60°$. The presence of two echo types is obvious not only from panel (a), but also from the histogram (b), where two maxima can be seen, one at ~ -500 m s^{-1} and another one at ~ 0 m s^{-1}.

We believe that these two populations or species correspond to 2 different mechanisms of echo formation, and for this reason we consider data separately for echoes with velocity magnitudes larger and smaller than $V_{crit} = 320$ m s^{-1}. The value of V_{crit} is indicated by the dashed line in panel (a).

In addition to the just described separation according to the velocity magnitude, the velocities of the two echo species have different Doppler velocity variations with L-shell angle ϕ. The high-velocity HF echoes first increase in velocity magnitude with ϕ and then decrease, exhibiting a "cosine-like" variation for $\phi = 20°$–$60°$ with the maximum at $\phi \cong 35°$. The Doppler velocity of the low-velocity 12-MHz echoes, on the other hand, increases with ϕ for all directions, also exhibiting a "cosine-like"

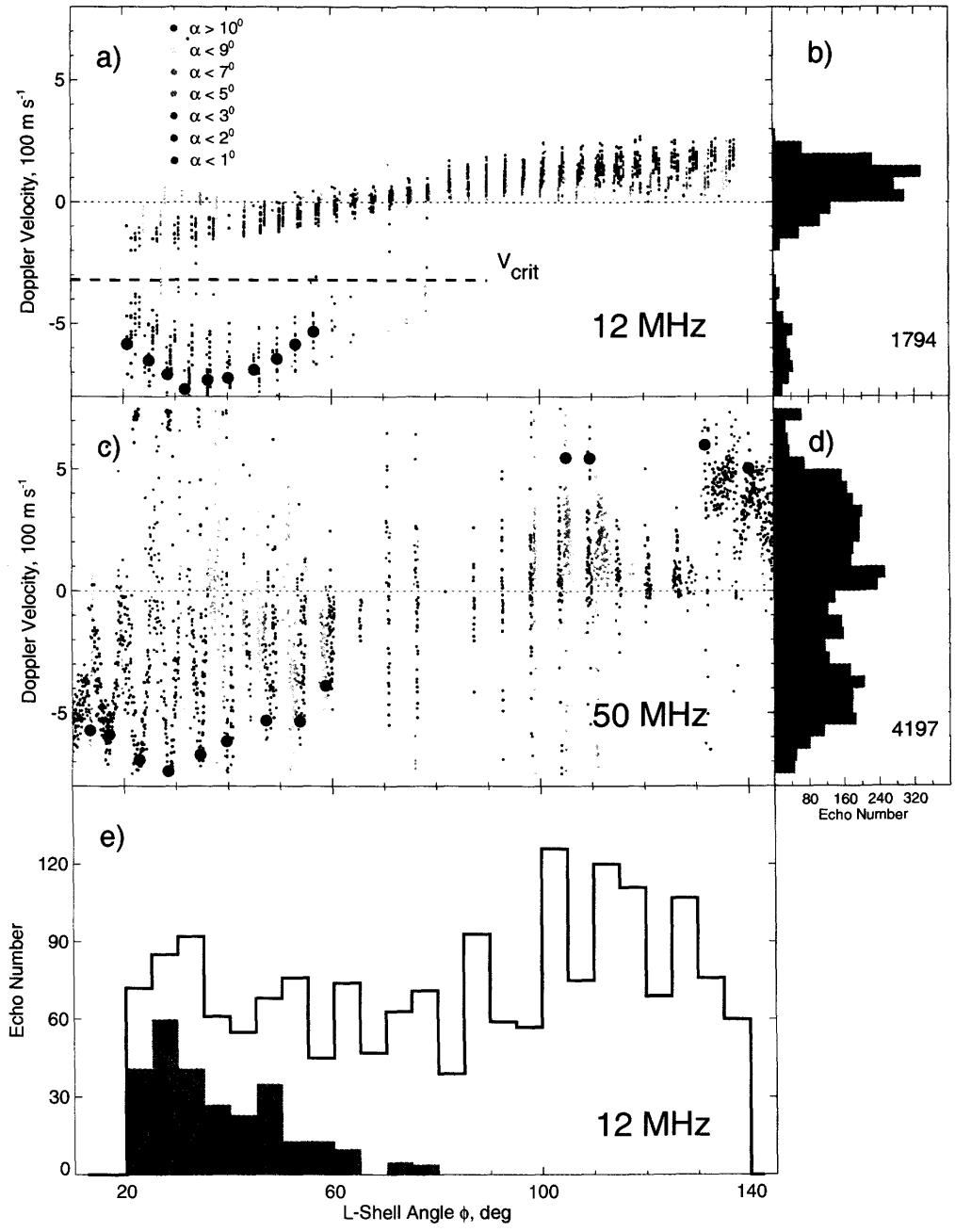

Figure 5.11: Doppler velocity versus L-shell angle at (a) 12 and (c) 50 MHz for March 17, 1997, 0100-0130 UT. Right panels are histograms of velocity distribution for (b) 12- and (d) 50-MHz radars. Panel (e) is the histogram of number of echoes (in 5°-wide bins) versus the L-shell angle at 12 MHz.

variation, but with the maxima at the edges of HF FOV ($\phi \sim 20°$ and $\sim 140°$). Interestingly, the reversal of the velocity sign occurs not perpendicular to the L shells at $\phi = 90°$ but rather at $\phi \sim 75°$. The "amplitude" of "cosine" variation is much smaller for the low-velocity HF echoes than that for high-velocity echoes (~ 150 m s^{-1} versus ~ 750 m s^{-1}).

If one concentrates on the 50-MHz part of the diagram, panels (c) and (d), no distinct echo populations can be identified. The histogram (d) shows a rather homogeneous distribution: one can find any specific velocity magnitude with approximately equal probability, except for at the very large velocities $V > 600$ m s^{-1}. There are some kind of V-structures both for small ($\phi < 60°$) and large ($\phi > 120°$) L-shell angles. For $\phi < 60°$, echoes with small aspect angles (black and dark blue dots) tend to have large velocity magnitudes; they are generally located at the bottom of V-structures.

The V-like structures in Figure 5.11 are no doubt associated with the velocity attenuation with aspect angle known for VHF echoes [*Ogawa et al.*, 1982; *Nielsen*, 1986; *Kustov et al.*, 1994]. Each V-structure is in fact the data from one of the radar beams. As the range and L-shell angle changes along the beam, so does the aspect angle, reaching at some point the perfect aspect angle condition ($\alpha = 0°$). Since the phase velocity of the plasma waves is expected to have a maximum at a perfect aspect angle, the V-structures in Figure 5.11 are simply a different form of representation of the velocity variation with aspect angle. V-structures for $\phi \sim 90°$ are not well seen because here the L-shell angle does not change much as one goes along individual radar beams. One can conclude that all "VHF low-velocity points" in (c) are actually echoes with poor aspect angles. Thus Figure 5.11 indicates that there is no special "low-velocity" kind of echoes at VHF.

One must bear in mind that values of the aspect angle in Figure 5.11 are calculated from the density distribution model. The actual aspect angle conditions might be

different from the ones given by the model. With this in mind, only maximum velocities should be considered for the comparison at HF and VHF since others are significantly affected by the aspect angle attenuation.

Because there is a substantial data spread for each radar cell, to obtain statistically meaningful estimates of the maximum velocity, we performed one more type of analysis. For each radar beam, we considered all points with Doppler velocity magnitudes larger than the critical value V_{crit} (for 12 MHz, points below the dashed line in (a)). We found the average of these points for each slant range (thus we obtained one point for each vertical line in (a) and (c)) so that the maximum average velocity of high-velocity echoes in each radar beam was calculated. The obtained velocities are plotted in panels (a) and (c) as large black circles. These circles should correspond to zero aspect angle measurements since velocity magnitude maximizes at perfect aspect angle.

Now we can compare directly the L-shell dependencies for high-velocity HF echoes and VHF echoes, large black circles in panels (a) and (c). One can see that, overall, the two trends (if one connects the large black circles) are similar. The only distinguishable difference between the two curves is that the 12-MHz curve appears to be shifted with respect to that at 50 MHz. The latter maximizes at $\phi \cong 30°$ and the former at $\phi \cong 35°$. Because of this shift, the velocity magnitudes at HF are slightly larger (smaller) than that at VHF for $\phi > 30°$ ($\phi < 30°$) if one compares velocities for the same value of ϕ (by drawing a vertical line through (a) and (c)). If one compares 50-MHz echoes with low-velocity 12-MHz echoes, it is evident that the velocity magnitude at 50 MHz is always larger than that at 12 MHz. Thus symbolically we can write for magnitudes $V^{50} \gg V^{12}_{low}$ for all ϕ, $V^{50} > V^{12}_{high}$ for $\phi < 30°$, and $V^{50} < V^{12}_{high}$ for $\phi > 30°$.

In panel (e) we present the histogram of number of 12-MHz echoes at various L-shell angles ϕ. We indicated the total number of echoes for 5°-wide L-shell angle bins

by the solid line and the number of high-velocity echoes (with velocity magnitudes larger than V_{crit}) by the shaded area. The difference or the vertical distance between the curve and shaded area thus represents the number of low-velocity echoes. Total number of points for this particular event is approximately the same for all directions of the FOV. The number of high-velocity points decreases steadily from $\phi = 20°$ to $\phi = 90°$. For $\phi > 90°$ there are no high-velocity echoes. Notice also that the number of low-velocity points (the vertical difference) slightly increases with ϕ.

In Figure 5.12 we present data for the expanded period of 23 days (02–06 UT). Here we used only "nearly simultaneous" measurements (as defined in the previous section) to make the diagram readable. One can notice that in Figure 5.12 the relative number of points with large aspect angles is lower than in Figure 5.11, and that the two peaks in the distribution of velocities, corresponding to the two species of 12-MHz echoes, are more distinct. The distribution of the 50-MHz velocities also becomes "smoother", with a maximum at ~ 0 m s^{-1}. The fact that the VHF radar sees some echoes with low velocities is entirely due to the poor aspect angle conditions for these echoes. The peaks in Figure 5.11 are less prominent (two at 12 MHz and one at 50 MHz) than in Figure 5.12 because of the larger relative number of echoes with poor aspect angles. In Figure 5.11e one can also observe that the number of high-velocity echoes decreases with ϕ and the number of low-velocity echoes is almost the same for all ϕ, except for some differences between the east and west sectors.

Finally, one important feature should be emphasized. In both Figures 5.11 and 5.12 a significant number of HF echoes has quite large Doppler velocities. Thus, a peak in the echo number distribution in Figure 5.12b is located at 475–500 m s^{-1} and there are points with considerably larger velocities (700–800 m s^{-1}). We will return to this question later in Section 7.2.1.

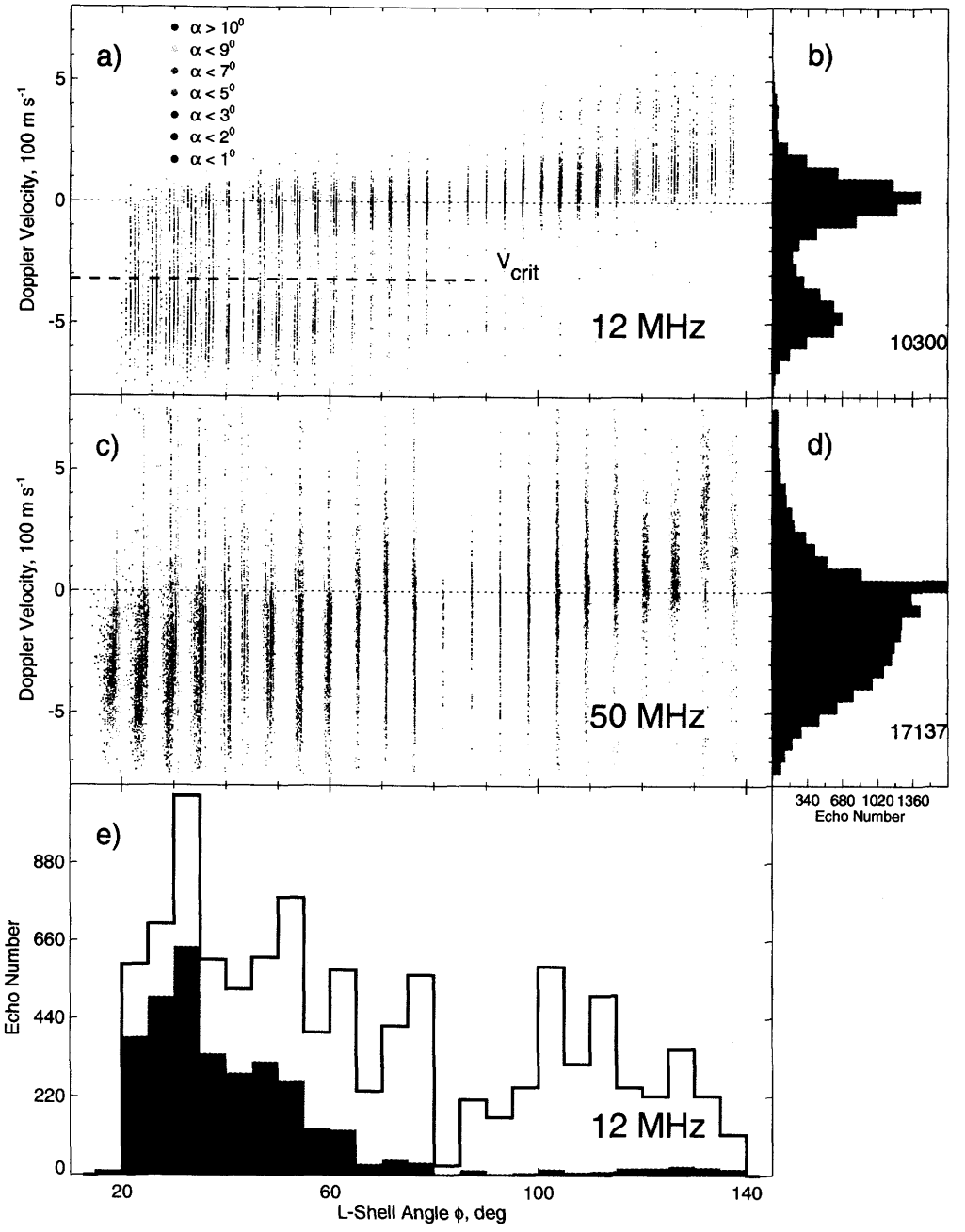

Figure 5.12: The same as Figure 5.11, but for 23 days in March 1997, 0200–0600 UT, nearly simultaneous points (see description in the text).

5.3.3 High- and Low-Velocity Echoes: Power and Width Versus L-Shell Angle

Since HF echoes can be of two classes, we decided to look more carefully at the L-shell variation for the echo power of each class, and, in addition, we studied whether there was any difference between spectral widths of these two HF echo classes.

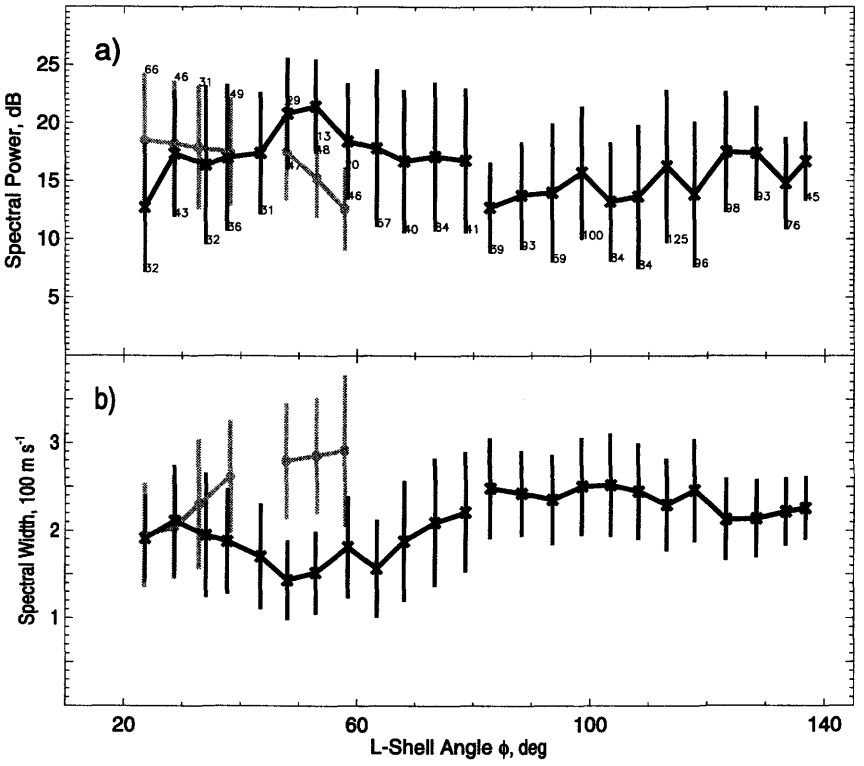

Figure 5.13: Spectral power at HF versus L-shell angle for 0100–0130 UT on March 17, 1997, panel (a). Averaged (for 5°-wide bins in L-shell angle) values, standard deviations and numbers of points are indicated for high- and low-velocity HF echoes (gray circles and black crosses, respectively). The spectral width at HF versus L-shell angle is shown in panel (b).

Figure 5.13 shows the L-shell angle variation of the spectral (a) power and (b) width. We used again the small 30-min database for all, not joint points. Gray dots

and black crosses in Figure 5.13 are averaged values of the spectral power and width calculated using 5°-wide L-shell angle bins for high- and low-velocity HF echoes, respectively. Also in Figure 5.13 we show the standard deviations and the number of points used for averaging for each bin and each type of echoes. The average value was not plotted if the number of points in a bin was too small (less than 11). The direction corresponding to the boundary between the two HF radars is at $\phi \cong 80°$, and we connected the average values for each radar separately.

One can notice in Figure 5.13 that high-velocity echoes tend to have larger power than low-velocity echoes and that there is a tendency for the power to decrease with L-shell angle. The power of low-velocity echoes is approximately the same for all ϕ though one can recognize a peak at $\phi \cong 50°$.

The high-velocity echoes have the same widths as the low-velocity echoes for $\phi <\sim 30°$. For $30° < \phi < 60°$, the high-velocity echoes have larger widths. For high-velocity echoes, width appears to increase with ϕ. For low-velocity echoes, width varies with ϕ in an apparently random fashion.

In Figure 5.14 we present results for the entire database of joint points (23 days for 02–06 UT). One can more clearly see here that the power of HF high-velocity echoes is stronger than the power of low-velocity echoes, and that the Syowa East echoes are typically stronger than Syowa South ones, in agreement with the data presented in Figure 5.7. We can state that a quasi-homogeneous power-azimuth distribution of HF echoes discussed by *Koustov et al.* [2001] is rather an exception. One can also see that high-velocity HF echoes have smaller widths than low-velocity echoes and that the width of low-velocity echoes is about the same at all L-shell angles, the results being in contrast with Figure 5.13. We believe, however, that these disagreements are because of the lack of statistics in Figure 5.13.

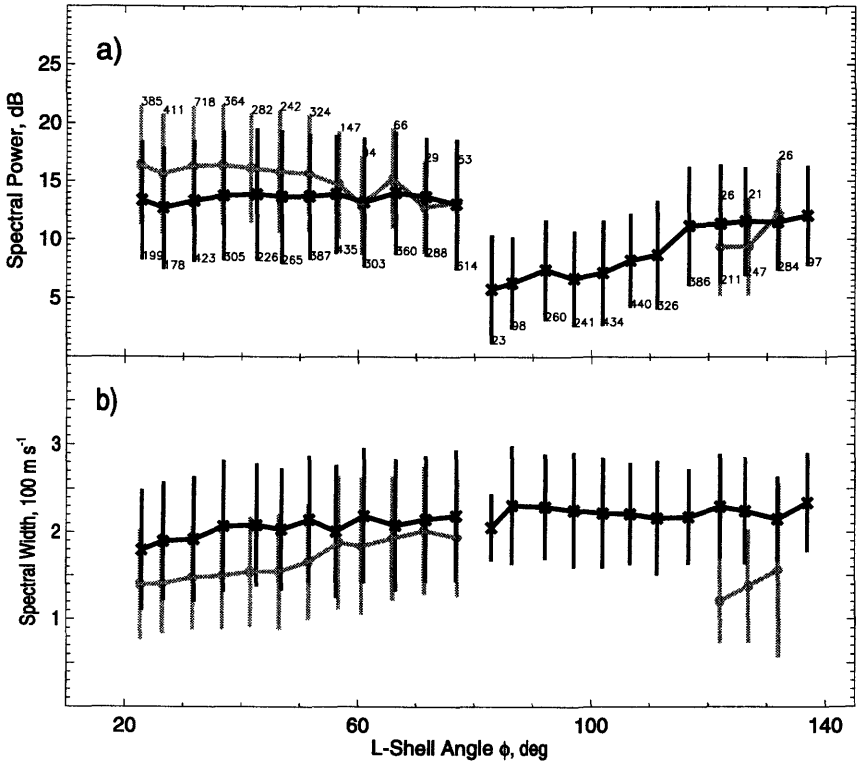

Figure 5.14: The same as Figure 5.13, but for 23 days of nearly simultaneous measurements in March 1997, 0200–0600 UT.

5.4 Power-Velocity Relationship at HF and VHF

The general statistical assessment of the data from the Syowa radars and their more detailed comparison have demonstrated that the properties of HF and VHF echoes are significantly different. In this section we demonstrate one more difference between HF and VHF echoes, namely we show that they exhibit different power–Doppler velocity relationships.

This aspect of the observations is important for understanding the major issue of this thesis, the properties of phase velocity of meter and decameter irregularities. Materials presented in this section have been published by *Makarevitch et al.* [2001].

Date, in 1997	Start Time, UT	End Time, UT
March 6	0000	0600
March 13	0000	0200
March 14	0000	0200
March 16	0000	0400
March 17	0000	0400
March 18	0000	0600
March 26	0000	0400
March 29	0000	0500
March 30	0000	0400

Table 5.2: Selected periods of Syowa observations.

5.4.1 Database Selection

In this study we consider data only for some directions of the CRL radar shown in Figure 5.3. These directions correspond to Syowa East beams 15, 10, 7, and 2 and Syowa South beams 6 and 0. One can see that we cover all typical directions ranging from almost along the magnetic L shells (assumed direction of the electrojet) to perpendicular to the L shells. These specific beam positions were selected because of the large amount of common data for them.

In this study we used a subset of the database used in previous sections. We limited ourselves only to the periods when the 50-MHz echo bands were centered around 450–500 km. Also we preferred those events for which there were periods of fairly large Doppler velocities, up to 500 m s^{-1}, as viewed through the standard SuperDARN software. Table 1 lists the selected events.

Besides these restrictions, the additional data "cleaning" was performed as follows. For every radar beam position, data in any specific range bin were entered into a database only if (1) there was another echo in at least one adjacent bin (at shorter or farther slant range), (2) in this bin there were echoes either immediately prior to or after the specific time, and (3) the echo velocity was either increasing or decreasing monotonically in three consecutive (in time) bins or the velocity change in an

adjacent range was $< 50\%$. In our opinion, this procedure removed, as much as possible, contributions due to meteors and strong and quick changes of the ionospheric parameters or noise.

5.4.2 Range Profiles Comparison

First we consider power and velocity slant range profiles of 12- and 50-MHz echoes for observations roughly along the L shells, geographic azimuth 83.7°. Figures 5.15a and 5.15b show averaged (over all nine events) power and Doppler velocity versus slant range. Here the bar around every point represents the standard deviation for each bin of measurements. We indicate the total number of points available for individual bins. Dotted curves in these diagrams show the geometrical aspect angle at various slant ranges. The scale for the aspect angle in degrees is indicated on the right-hand side of each panel. The presentation of Figure 5.15 is analogous to that of Figures 5.7 and 5.8 except that in Figure 5.15 data from one radar direction only are presented. Also the database is different from the one used in Figures 5.7 and 5.8; here we used more rigid data selection criteria and the data cleaning procedure as described in the text above.

Figures 5.15a and 5.15b show data for observations along the magnetic L shells (azimuth of 83.7°). The 50-MHz power profile, Figure 5.15a, exhibits a broad maximum centered at a slant range of $\sim$ 450 km. This maximum is 20–30 km equatorward of the slant range of zero aspect angles at 110 km (480 km). The 12-MHz echoes also show a broad maximum in power, but it was centered at shorter distances of $\sim$ 400 km. One should note that no absolute calibrations of the power have been performed for both radars, so that only relative variations of power with range or azimuth can be discussed.

Figure 5.15b shows slant range variations of the Doppler velocity. One can see

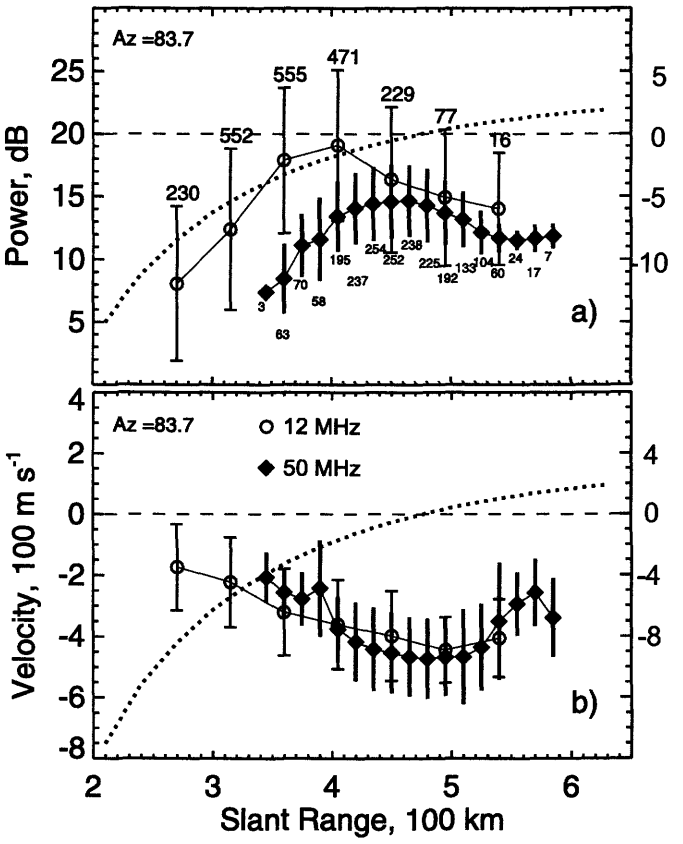

Figure 5.15: (a) Power and (b) Doppler velocity versus slant range for 12- and 50-MHz radar observations at an azimuth of 83.7°, approximately along the magnetic L shell direction, averaged over nine events. Dotted curves represent the geometrical aspect angle. The scale for the aspect angle is indicated at right.

that both 50- and 12-MHz velocity magnitudes are small at short distances and they increase with range, reaching magnitudes of $\sim$ 450 m s^{-1} at ranges of $\sim$ 500 km. There is a tendency for 12-MHz velocity magnitudes, on average, to be slightly larger by 50–100 m s^{-1} than 50-MHz velocity magnitudes for ranges $<$ 400 km and to be slightly smaller for ranges $>$ 400 km, though these differences are within the standard deviations. One can also notice that the maximum velocity magnitudes are at ranges of 450–500 km, corresponding to ranges of near-zero aspect angles. For slant ranges

of $>$ 500 km, the 50-MHz velocity magnitude decreases to values of $\sim$ 250 m s^{-1}. The 12-MHz curve shows only a slight decrease at a range of 540 km, and there are no points at farther slant ranges.

5.4.3 Power-Velocity Relationship From Slant Range Profiles

The power and velocity slant range profiles presented in Figure 5.15 are used to plot a power-velocity diagram, Figure 5.16.

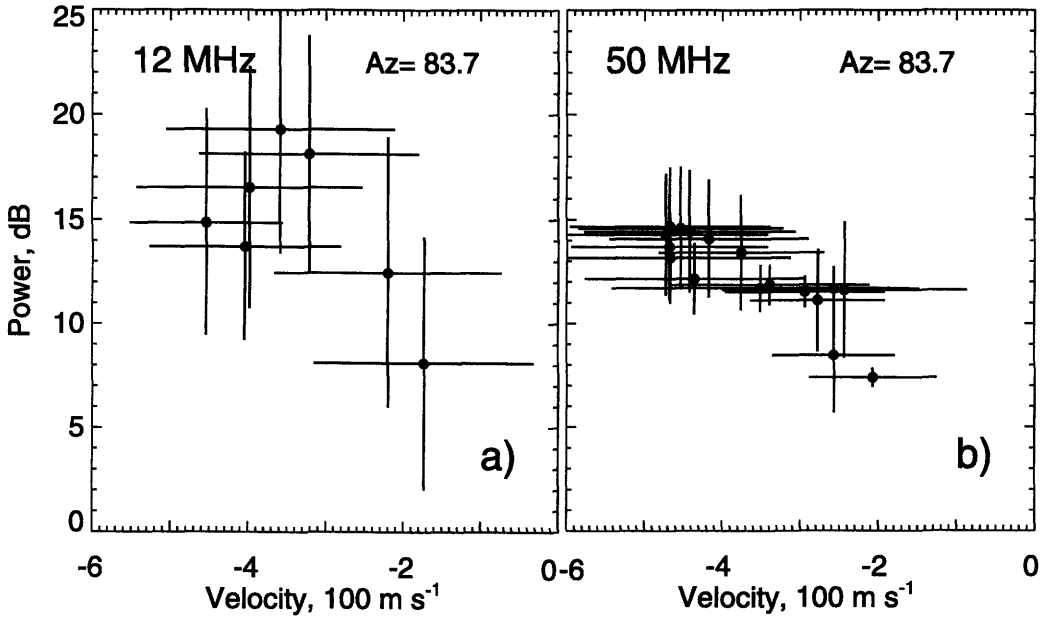

Figure 5.16: Power versus Doppler velocity at slant ranges of 200–500 km for (a) 12- and (b) 50-MHz radar at an azimuth of 83.7°.

One can see that there is a difference between the P-V relationships at 12 and 50 MHz, though we cannot precisely say what functional dependencies there are for the different radar frequencies because of the small number of available points. At 50 MHz, Figure 5.16b, there is an increase of echo power with Doppler velocity

(magnitude) in a range of velocities 200–500 m s^{-1}. At 12 MHz, Figure 5.16a, there are two entirely different parts of the P-V diagram, depending on the velocity magnitude. For velocities in the velocity magnitude range of 150–350 m s^{-1}, there is a constant increase of power. At larger velocities, power clearly saturates; one can even say that power decreases with velocity.

5.4.4 Power-Velocity Relationship From Scatterplots

We showed in Section 5.4.3 that the character of the 12-MHz power-velocity relationship changes at velocities around 350 m s^{-1}. In this section we consider the power-velocity relationship on a point-by-point basis. Note that for joint points there was still some time difference ($<$ 1 min) between 12- and 50-MHz records because the radar beam positions were not synchronized in time.

Figure 5.17 shows power-velocity diagrams for various azimuths of observations at 12 MHz (left) and 50 MHz (right). For each azimuth of measurements we consider data obtained in all bins. Here 50-MHz data are averaged over 45-km range intervals to match them with the range bins of the 12-MHz measurements. We introduce two types of symbols, solid and open circles. Solid circles correspond to those measurements for which the 12-MHz velocity was smaller than 360 m s^{-1}, the nominal ion acoustic velocity in the E layer and the threshold for the F-B instability. As in Section 5.3 we call these echoes the "low-velocity 12-MHz echoes". Open circles then correspond to those measurements for which the 12-MHz velocity magnitude was larger than 360 m s^{-1}. These echoes are called the "high-velocity 12-MHz echoes".

For 12-MHz echoes one can see that low-velocity and high-velocity echoes exhibit different power-velocity relationships. For low-velocity echoes there is an increase of power with velocity. This effect is seen more clearly at azimuths of 98.7°, 163.7°, and 183.7°. The high-velocity echoes do not show obvious trends, though one can see that

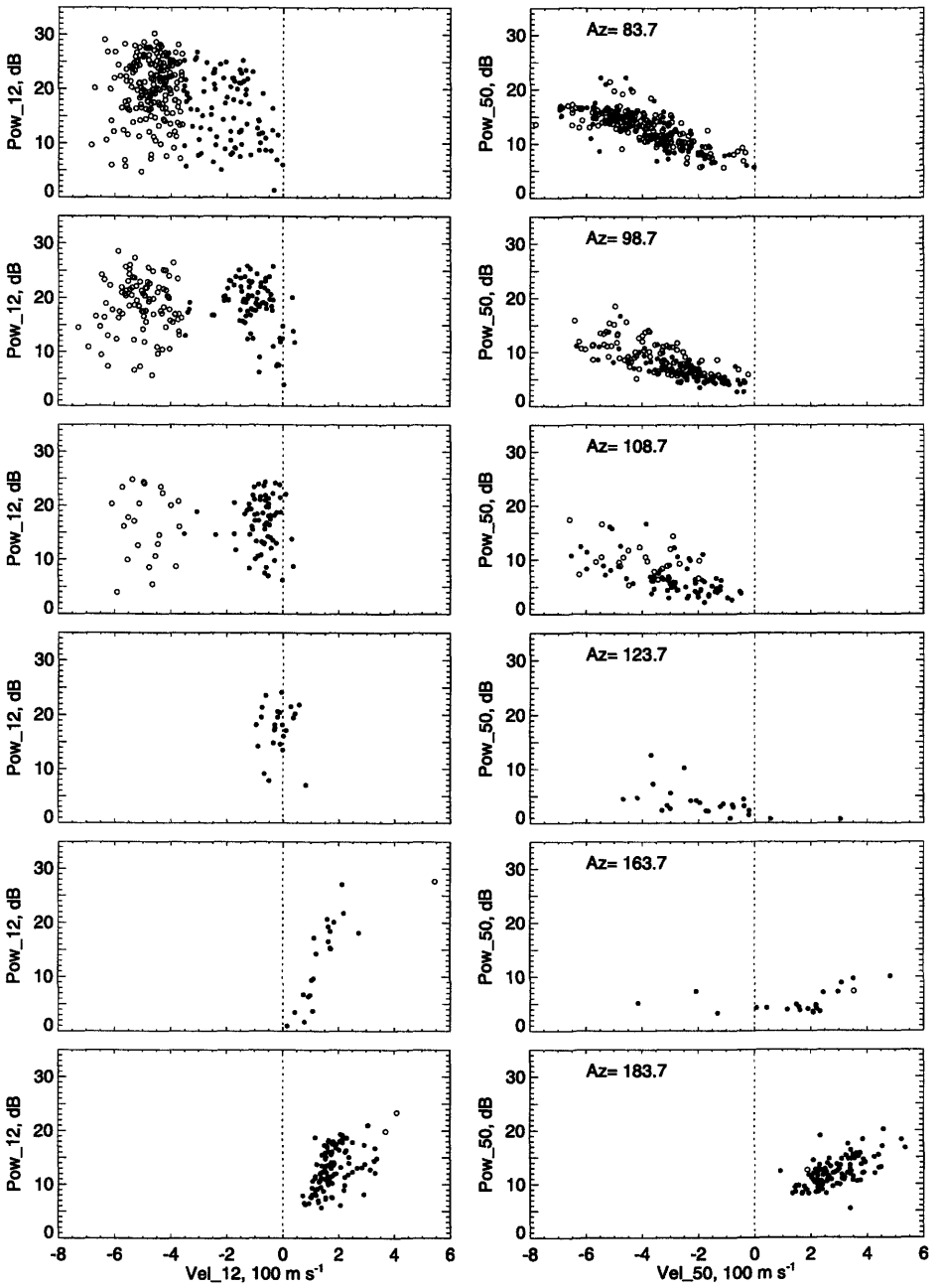

Figure 5.17: Power versus velocity for (left) 12- and (right) 50-MHz echoes at several azimuths.

most points at larger velocities have less power for an azimuth of 98.7°. We can state that there is at least a saturation in the power increase. One can also clearly see a tendency for the high-velocity echo cloud to be "split" from the low-velocity cloud.

Remarkably, 50-MHz echoes (Figure 5.17, right) exhibit a monotonic increase of power with velocity at all azimuths. The strongest power increase is at an azimuth of 83.7°.

5.5 Summary

In this chapter a comparison of echo characteristics at two significantly different radar frequencies (12 and 50 MHz) has been performed.

In Sections 5.2–5.3 we considered one month of nearly simultaneous double-frequency measurements in a broad range of flow and aspect angles. We concentrated on the azimuth/L-shell variation for such echo parameters as echo occurrence, spectral power, mean Doppler shift, and spectral width (12 MHz only).

We showed that overall echo occurrence within the common FOV of the radars varied with the time of the day in a similar manner at both radar frequencies and had maxima at post-midnight hours. However, when specific radar directions were compared, it was found that the echo occurrence depended on the azimuth/L-shell angle of measurements. We explored the nature of this difference using two approaches.

First, we considered data for the morning sector, for which the echo occurrence was the highest, and found that while VHF echoes were more frequently detected at small L-shell angles, HF echoes were observed at all L-shell angles with some broad maximum at angles around 45° and 115°. The azimuthal distribution of the power was found to have a strong maximum along L shells at VHF and to be more or less homogenous at HF.

We then turned our attention to the velocities of echoes at various L-shell angles. We showed that HF echoes can be divided into two populations, the high- and low-velocity echoes, while VHF echoes are of only one kind, the high-velocity echoes and their aspect-attenuated counterparts. We also explored the behavior of the HF power and spectral width with L-shell angle for these two echo populations and showed that the high-velocity echoes are stronger and narrower that the low-velocity ones.

In Section 5.4 we studied the power-velocity relationship for 12- and 50-MHz auroral coherent echoes using two different approaches. First, we considered the slant range profiles for the power and velocity. These measurements, presented as a power-velocity plot, showed the effect of strong power saturation and even some decrease with velocity at large velocity magnitudes of $>\sim 350$ m s^{-1} for 12-MHz echoes and a steady power increase for all velocities for 50-MHz echoes, the latter being in agreement with previous studies. We then studied the power-velocity relationship by considering only those measurements that were recorded almost simultaneously. We found that this much more restrictive database still showed similar tendencies in echo parameter variations with slant range. The 12-MHz power-velocity plots also showed the effect of power saturation at large velocities, contrary to the power increase at 50 MHz.

Chapter 6

Multifrequency HF Observations

In the previous chapter we considered the data from the radar observations of meter and decameter E-region irregularities. We concentrated on the properties of the irregularity phase velocity. In this chapter we continue focusing on the phase velocity but consider decameter irregularities of very close scales. We study the velocity variation with the wavelength/radar frequency, flow and aspect angles. For this purpose we consider data gathered by another SuperDARN HF radar, recently installed in Prince George, British Columbia, Canada. The radar was run by the University of Saskatchewan SuperDARN team in a special multifrequency mode. The results of this chapter were reported in the recent paper by *Makarevitch et al.* [2002a].

6.1 Experiment Setup and Event Description

6.1.1 Prince George Coherent HF Radar

The Prince George (PG) SuperDARN radar was installed for cooperative observations with the Kodiak radar operated by the University of Alaska. The PG radar is located at geographic coordinates 122.58°E, 53.97°N, with the field of view centered in the direction 5°W of N (geographic), see Figure 1.6a for relative (with respect to other SuperDARN radars) location and beam orientation of the PG radar.

We consider here data for a special mode of PG radar operation, the multifrequency mode. In this mode the radar frequency is changed after the radar completes one 2-minute scan at a fixed frequency. The typical frequencies used were 9.3, 10.5, 12.0, 13.5, and 15.7 MHz though exact values varied slightly in response to changing noise conditions. One sequence through the five radar frequencies was thus completed in 10 min. The pulse length was 300 μs, corresponding to 45-km slant range resolution. We concentrate in this study on echoes from slant ranges between 180 and 765 km (bin numbers of 0–13) which very likely correspond to E-region echoes. To ensure that received echoes were indeed coming from the E region, we employed the elevation angle data obtained from the radar interferometer.

Figure 6.1 shows the location of the PG radar site, the radar field of view for short ranges (shaded area), the actual positions (thin solid lines) of the radar beams (separated by 3.25°), and slant range marks of 300, 600, and 900 km (circular dashed lines). The PACE magnetic parallels [*Baker and Wing*, 1989] are indicated in Figure 6.1 by a thick curve. We also show, by white thick curves, the lines of equal magnetic aspect angle at 110-km altitude (-5°, 0°, and +5°), assuming that the radar rays undergo refraction in the ionosphere with the electron density profile as described by the

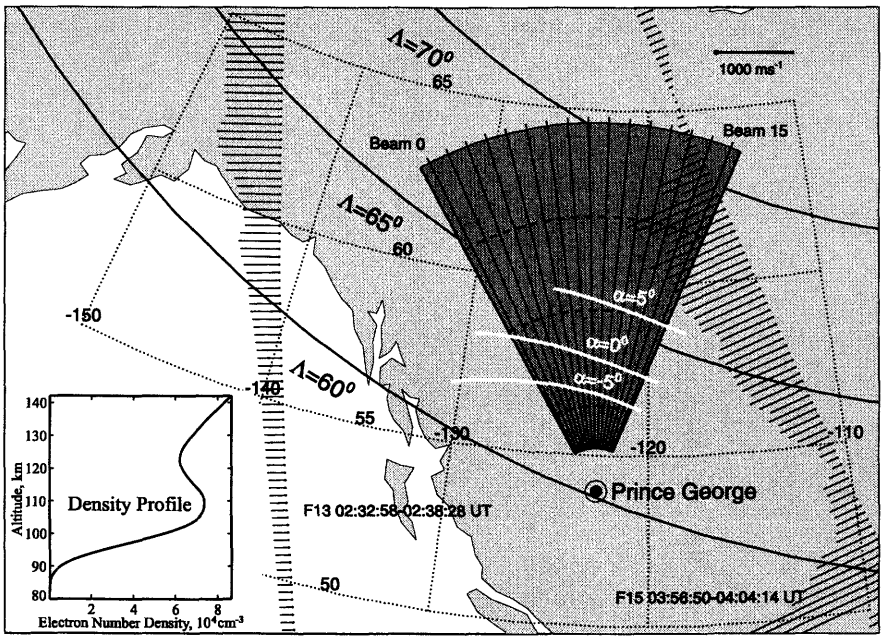

Figure 6.1: Field of view of the Prince George SuperDARN HF radar. Nominal directions of the SuperDARN beams (from 0 to 15) are indicated by the thin solid lines. Also shown are PACE lines of equal magnetic latitudes $\Lambda = 60°$, 65°, and 70°. Thick white solid curves denote the off-perpendicular (aspect) angle lines (-5°, 0°, and 5°). Circular black dashed lines are 300-, 600-, and 900-km slant range marks. Two DMSP passes with the measured perpendicular ion velocities are indicated by black thin vectors. The scale for the ion velocities is shown in the top right corner of the diagram. The electron density profile used for calculations is shown in the left bottom corner.

IRI-95 model. We show the selected density profile in the left bottom corner of Figure 6.1. The aspect angles were computed for the radar frequency of 12 MHz using a simple geometric optics approach [*Uspensky et al.*, 1994]. The line for +5° terminates in the western part of the FOV; this angle cannot be reached west of the termination point due to total reflection of radio waves at smaller ranges. For higher/lower radar frequencies, the aspect angle lines are shifted poleward/equatorward (up to 150 km). With an electron density decrease/increase, the aspect angle lines in Figure 6.1 would

be shifted poleward/equatorward.

In addition, Figure 6.1 exhibits convection data for two Defense Meteorologic Satellite Program (DMSP) passes near the observational area. The vector length at each point of the path corresponds to the measured ion velocity component perpendicular to the path. The scale for the ion velocity is indicated in the top right corner of the diagram. Data from the DMSP altitude of 800 km were projected to the E-region height of 110 km along the magnetic field lines. Fairly uniform and strong electron flows up to 700–800 m s^{-1} are evident, indicating that the F-B plasma instability was operational.

6.1.2 Event Selection

We consider in this study one short event on 6 August, 2000, from 0200 to 0400 UT. During this period, E-region echoes were observed continuously and at all five radar frequencies. In addition, the azimuthal distribution of echoes was fairly stable and unique for each radar frequency. This resulted in appearance of quite remarkable regular patterns in the range-time-intensity plots, with the period of repetition of 10 min, corresponding to the five-frequency sequence period. Inspection of the range-time-intensity (velocity) data plots (not shown) shows that the whole echo region was observed at greater ranges for higher radar frequencies, and that there was a very consistent and gradual decrease in the velocity magnitude from beam 0 to beam 15. In many cells there were up to 12 records of measurements, the maximum possible number for the 2-hour period given the 10-min frequency sequence period. All these features suggest that the electric field and electron density distributions across the entire PG radar FOV at short distances were fairly stable in time.

To demonstrate the latter stability we plotted in Figure 6.2 spectral power (left) and Doppler velocity (right) range profiles for the frequency of 15.7 MHz and beam

5 for 12 successive individual scans in time. Echoes were present in all 12 scans at all slant ranges from 2 to 13 (except of scan 0220–0230 UT). The spectral power distribution was very stable. Velocity changes from scan to scan were more significant, but, overall, the profiles were similar. Only for 3 scans of the 12 (0230–0300 UT) was the velocity maximum shifted significantly (2–3 range bins) from the average position of bin 6. For these scans, power profiles were also shifted the same way (2–3 bins) but the maximum power values were the same (40–45 dB), which indicates that these shifts in the velocity and power maxima are most probably due to a local (in time) change in the electron density and not due to a change in the electric field.

As in the previous chapter, signals due to ground scatter were removed from the database and the standard power-range correction was performed by assuming a r^{-3} power decrease with range r; echoes that had uncorrected power of < 3 dB were not considered at all.

To be certain that we consider the E-region echoes, we restricted ourselves to those measurements for which the scatter height was less than 140 km, as inferred from the elevation angle measurements. To exclude contributions from the side and back lobes of the antenna pattern we did not consider echoes with a velocity larger than 800 m s^{-1} bearing in mind that echoes with such a high Doppler shift are traditionally attributed to small flow angles inside the F-B instability cone.

To eliminate possible contamination from meteor trails and interference, additional criteria have been set. For every beam, data in any specific range bin were entered into a database only if (1) there was another echo in at least one adjacent slant range bin, (2) in this bin there were echoes either immediately prior to or after the specific time, and (3) the echo Doppler velocity was either increasing or decreasing monotonically in three consecutive (both in time and range) bins or the velocity difference between adjacent bins was $< 100\%$.

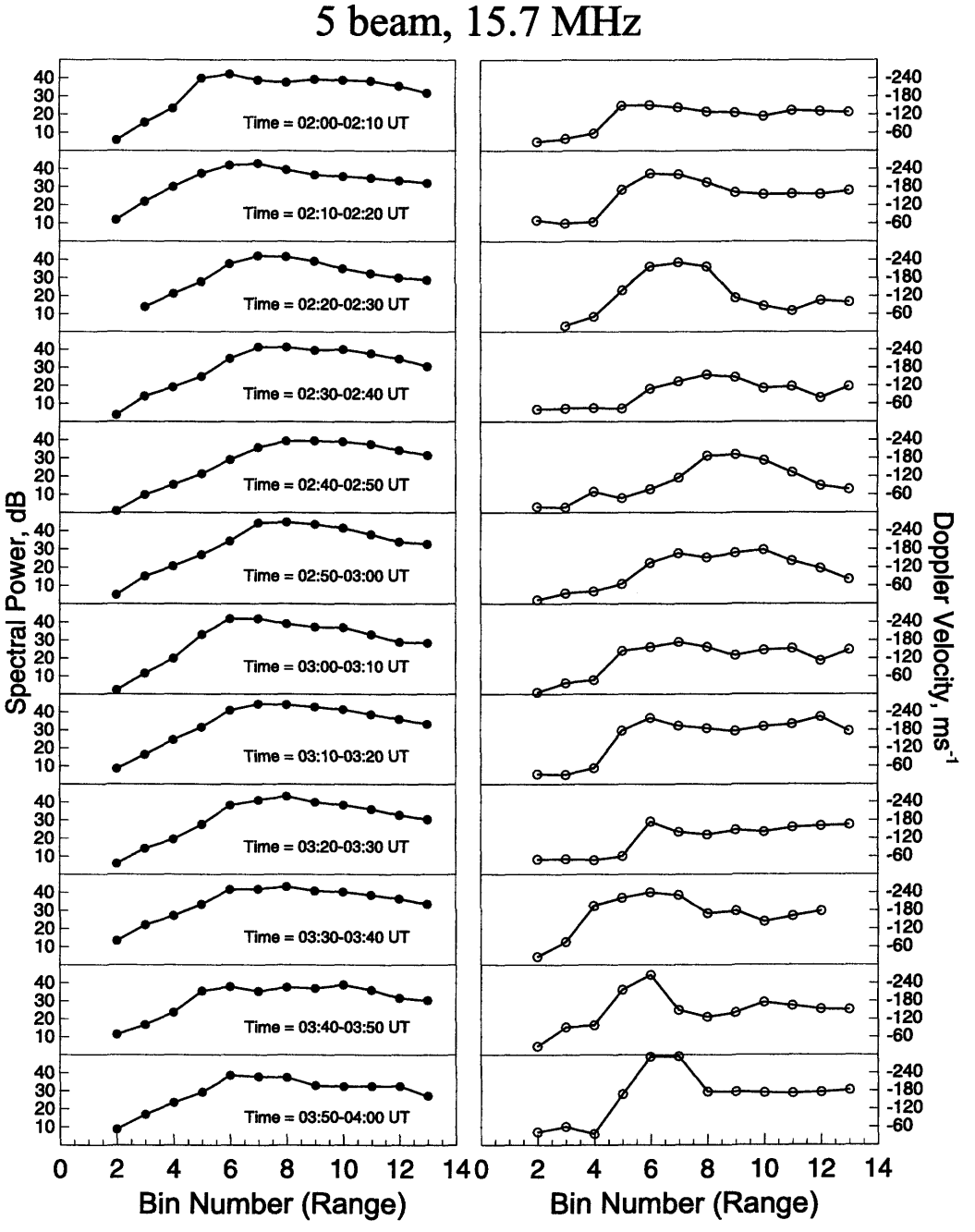

Figure 6.2: Stackplots of echo power (left) and Doppler velocity (right) slant range profiles for beam 5, frequency 15.7 MHz, and 12 successive individual scans.

6.1.3 Flow and Aspect Angle Calculations

In this study, we describe echo characteristics in terms of the flow angle and the aspect angle. Unfortunately, both of them cannot be specified with high precision for each radar cell and each moment of time. To determine the flow angle one needs to know exactly the plasma convection pattern within the field of view. For the event under study, although there were good short-range E-region echoes seen by the PG radar, the number of F-region echoes seen by all northern-hemisphere SuperDARN radars was too low to give an accurate global convection pattern based on *Ruohoniemi and Baker*'s [1998] technique. In part, this was due to special experiments being carried out by some of the radars of the SuperDARN network.

We can nevertheless estimate the convection pattern. The period of observations roughly corresponds to 1700–1900 MLT for the PG radar location. Since the IMF B_z component was strongly negative, on average around -10 nT, and the IMF B_y component was positive, slowly varying between 0 and +5 nT, one would expect that the convection pattern consists of 2 global cells and, to a first approximation, one can assume that the flow is L-shell aligned for the evening sector of the magnetosphere. Therefore the flow angle θ (angle between the component of the wave vector perpendicular to the magnetic field line $\mathbf{k}$ and the flow velocity) is assumed to be the L-shell angle ϕ (angle between $\mathbf{k}$ and the L shell). We applied the PACE magnetic model to each specific cell to determine the L-shell angle. All angles were measured counterclockwise from geographic north and the L-shell angle was defined as the difference between the azimuth of western sector of the L shell (assumed direction of the electron flow) and the azimuth of observations. Thus L-shell angle is always positive and it changes continuously from $\phi \cong 45°$ (beam 0, western edge of FOV, Figure 6.1) to $\phi \cong 100°$ (beam 15, eastern edge of FOV). With respect to the definition of the L-shell angle described above, one needs to keep in mind that it is customary in

radar physics to consider flow angles to be less than 90° even if the angle between the radar wave vector and flow direction is more than 90°, by simply selecting the complementary angle. We, however, will formulate all our results in terms of the L-shell angle as defined above.

The aspect angle for each cell of the HF radar measurements depends strongly on the amount of ionospheric refraction, which is controlled by the electron density variation with height. Since no direct measurements of the electron density were available anywhere within the radar FOV, we used the IRI-95 model density profile selected for the central time of the observational period, for a point at the center of the FOV. The selected profile (shown in the left bottom corner of Figure 6.1) has a broad maximum at the electrojet heights around 110 km with an electron density of $\sim 7.4 \times 10^4$ cm^{-3}. This profile was used to calculate the aspect angle for each cell by a simple geometric optics method, similar to that used by *Uspensky et al.* [1994].

6.2 Velocity Versus Aspect Angle

The main goal of this section is to study Doppler velocity variation with aspect angle for 5 radar frequencies. In order to do this we first consider the slant range profiles of the spectral power and Doppler velocity, along with the aspect and elevation angles.

6.2.1 Averaged Echo Range Profiles

Figure 6.3 shows the averaged slant range profiles of spectral power (thin solid line), mean Doppler velocity (thick solid line), elevation angle (dash-dotted line), and aspect angle (dotted line, height is 110 km) at 12.0 (left) and 13.5 MHz (right) for several radar directions. The scale for the aspect angle is given on the middle vertical axis with the tick marks $\pm 10, \pm 5, 0$ corresponding to $\pm 10°, \pm 5°, 0°$ of aspect angle. The

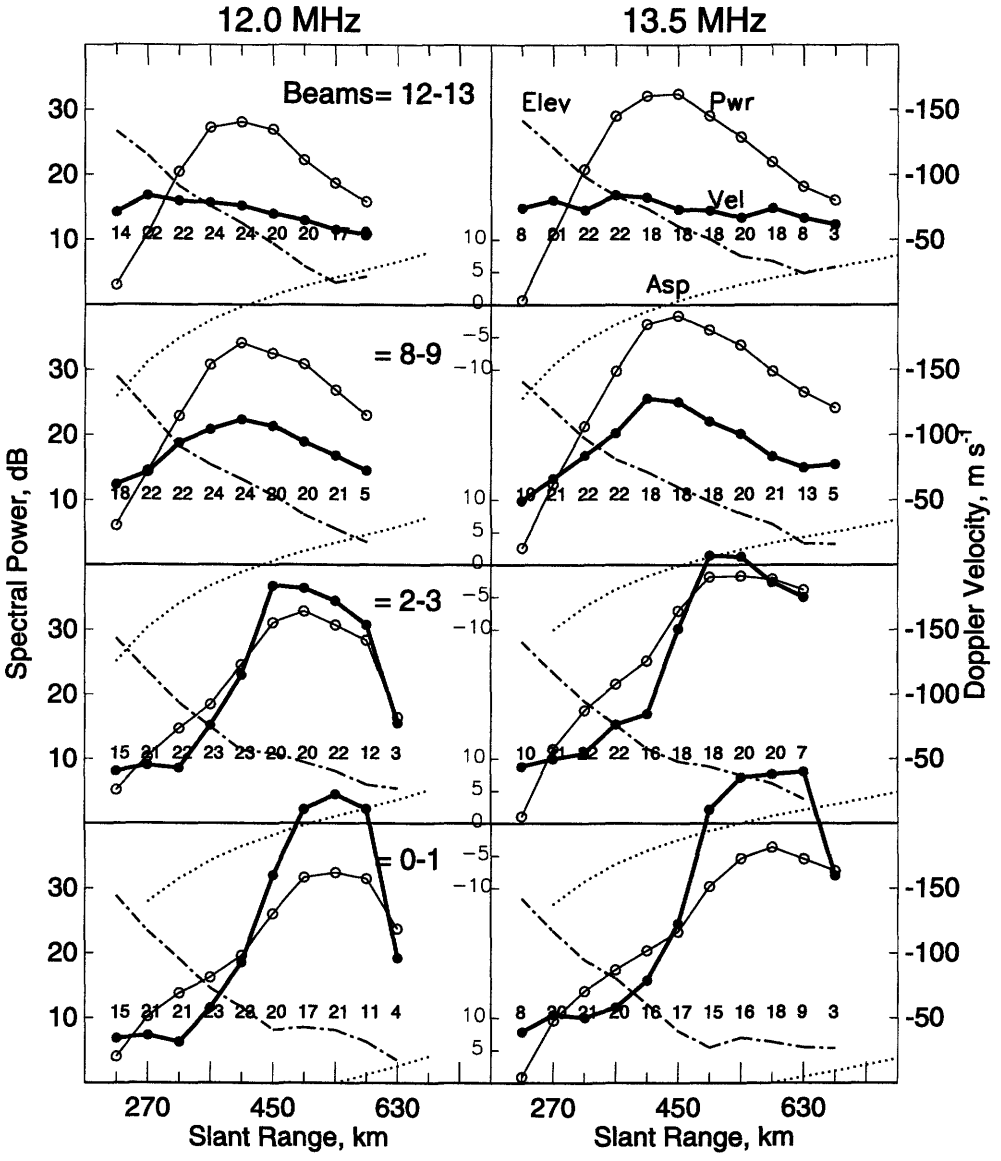

Figure 6.3: Slant range profiles of echo power (thin solid line), Doppler velocity (thick solid line), elevation angle (dash-dotted line) and aspect angle (dotted line), at (left) 12.0 MHz and (right) 13.5 MHz for several radar beams. For each radar range bin, the number of points (used for averaging) is shown. The scale for aspect angle is indicated on the middle vertical axis with zero aspect corresponding to horizontal lines at the bottom of each of 8 panels. The scale for elevation angle is the same as the scale for power.

scale for elevation angle (in degrees) is the same as the scale for spectral power (left axis). In Figure 6.3 we illustrate the frequency effects in the Doppler velocity, although for simplicity of presentation we show data for two frequencies only. In each panel, data were averaged over two neighboring radar beams to improve the data statistics (the differences in echo characteristics between any two adjacent beams were found to be insignificant). For example, in the bottom panel we present data for beams 0 and 1 for which the L-shell angle $\phi \cong 45°$ (we will denote this direction as 0–1) while in the top panel we present data from beams 12 and 13 for which the L-shell angle $\phi \cong 90°$. Beams 0 and 1 are oriented closer to the L-shell direction while beams 12 and 13 are oriented almost perpendicular to the flow. Digits on the diagram indicate the number of records for each radar cell (range). The standard deviations for the echo parameters are not given in Figure 6.3 because the figure would be too "cluttered". Typical standard deviations are 4–5 dB for power, 30–40 m s^{-1} for velocity and 1°–2° for elevation angle.

One can see in Figure 6.3 that for each direction the power and velocity have clear maxima at certain ranges; also, the velocity and power maxima are located at about the same distances (the only exceptions are the velocity profiles for the direction 12-13). Remarkably, the positions of the velocity and power maxima match well with ranges of zero aspect angle. There is a slightly poorer agreement between the echo velocity/power maxima and ranges of zero aspect angles at 13.5 MHz than at 12 MHz, but one should keep in mind that the aspect angle depends strongly on the electron density. The actual density might differ from the model used, so that the location of the zero aspect line may well be at closer ranges. In Figure 6.3 there is a clear correlation in the power and velocity changes with range, similar to that reported in Section 5.4.

One can also notice that the power/velocity maxima are progressively shifted to closer ranges as the direction shifts eastward from the beams 0–1 to beams 12–13.

The effect is very clear at all other radar frequencies (data are not presented here) and this feature is no doubt associated with the eastward decrease in range of the position of the angle $\alpha = 0°$ at which the best aspect sensitivity for scattering occurs. This is clearly shown in Figure 6.1 where the line of $\alpha = 0°$ is located at closer ranges for the high-number beams on the east side of the FOV.

If one considers only one radar frequency, the maximum power values are about the same for all beam directions meaning that, on average, the power distribution is flow angle independent, consistent with recent measurements of *Koustov et al.* [2001] and the results of Chapter 5. If one compares values of the velocity maxima at 12.0 and 13.5 MHz in Figure 6.3, one can clearly see that the velocity magnitude is larger at 13.5 MHz (exceptions are data for beams 12–13), especially for the low-numbered beams, whose directions are more parallel to the L shells, i.e. to the assumed electrojet flow.

Two more features should be noted. First, the span of echo ranges increases slightly with frequency for every beam direction. Secondly, the elevation angle decreases with range, consistent with the expectation that the echoes come from the E region. One can notice that the rate of the decrease is faster at lower frequencies.

The velocity profiles in beams 12–13, corresponding to the largest flow angles, do not show a significant variation with range, and the velocities are about the same at both radar frequencies. This is in contrast to the accompanying power profiles that show maxima at ranges with near zero aspect angles.

6.2.2 Power and Velocity Versus Aspect Angle

One of the most fundamental properties of VHF backscatter is the aspect angle attenuation of the power [see review by *Haldoupis*, 1989, and references therein]. Coincidence between the power maximum and the range of zero aspect angle is obvious

in Figure 6.3. From Figure 6.3, roughly the power attenuation with aspect angle α is of the order of 2 dB/deg at both radar frequencies. We will not discuss this issue in greater detail because it is a topic of special study by *André et al.* [2001]. The more rigorous approach by *André et al.* [2001] shows that there is also a frequency dependence of the aspect angle effect in power.

The velocity decrease with increasing α is also a well established property of VHF echoes (see the review in Section 4.3.2). To check whether this effect exists at HF, the Doppler velocity was plotted against the aspect angle, using the data from Figure 6.3. The result is shown in Figure 6.4. For completeness, we present here the power variation with the aspect angle (thin line); these plots illustrate more clearly the attenuation of the power with the aspect angle at a rate of ~ 2 dB/deg at both radar frequencies.

In the bottom four panels of Figure 6.4 we show predictions for the phase velocity, based on the formulation of the linear fluid theory (see Chapter 2). We assume that, in the linear expression for the phase velocity, the normal electron-neutral collision frequency ν_{en} of $5 \cdot 10^4$ s^{-1} increases by a factor of 5 in the direction 0–1. One can notice a reasonable agreement between the predictions and experiment. To match experimental data with the predictions in other directions one has to assume somewhat larger factors. For completeness of presentation we show the curve with a factor of 10 for direction 2–3, though we realize that such large factors are rather unusual (factors of 5–6 have been reported in the past, see Section 4.3.2).

One can see once again that there is almost no dependence of Doppler velocity upon the aspect angle for the direction perpendicular to the flow (beams 12–13). For this direction, the spectral power, on the other hand, demonstrates the aspect attenuation very clearly.

Inspection of the aspect attenuation for the velocity at various HF frequencies reveals a slight weakening of the effect at lower frequencies. In Figure 6.5 we present

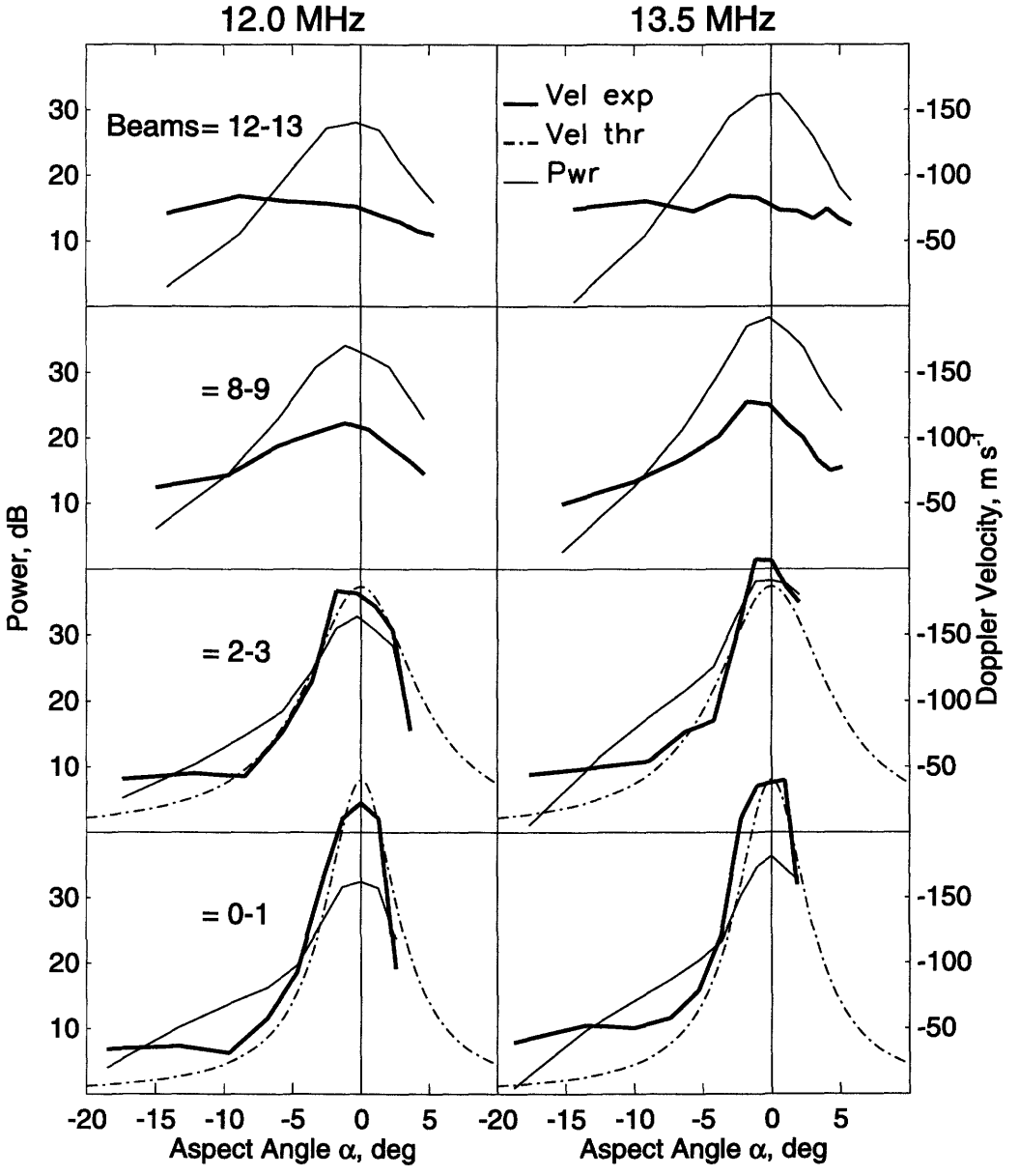

Figure 6.4: Doppler velocity (thick solid lines) and spectral power (thin solid lines) versus aspect angle at 12.0 (left) and 13.5 MHz (right) for several radar beams. Predictions for the Doppler velocity with $\nu^* = 5\nu_{en}$ (beams 0–1) and $\nu^* = 10\nu_{en}$ (beams 2–3) are shown by dash-dotted lines.

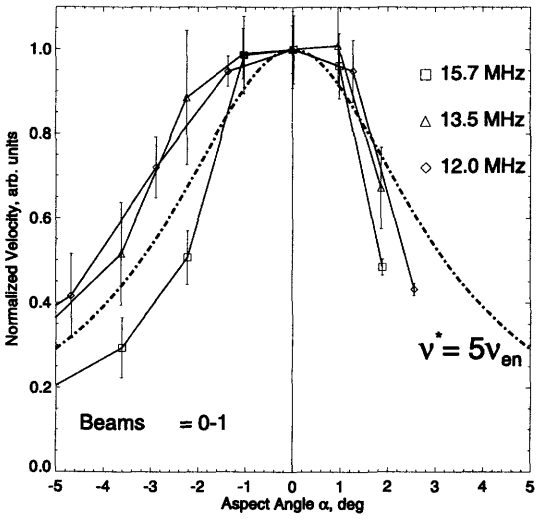

Figure 6.5: Normalized Doppler velocities as a function of aspect angle for several radar frequencies for beams 0–1. Dash-dotted line is the prediction for the phase velocity with $\nu^* = 5\nu_{en}$.

normalized velocities in direction 0–1 versus aspect angle for 3 radar frequencies, together with the curve for $\nu^* = 5\nu_{en}$. Here data were taken from diagrams similar to Figure 6.4. Standard deviations were scaled down by 4 times to provide a more clear picture.

6.2.3 Velocity Maxima Versus Radar Frequency

Since the Doppler velocity is expected to be at maximum for regions with zero (of course, if it is achievable) real aspect angle, a velocity maximum variation with radar frequency should represent a scale effect (dependence on wavelength or frequency), if the electric field is constant. This is the starting point for the velocity scale effect estimate.

For each radar frequency and for each radar direction we considered the value of Doppler velocity at its maximum in a slant range profile. Altogether we had a 5×8

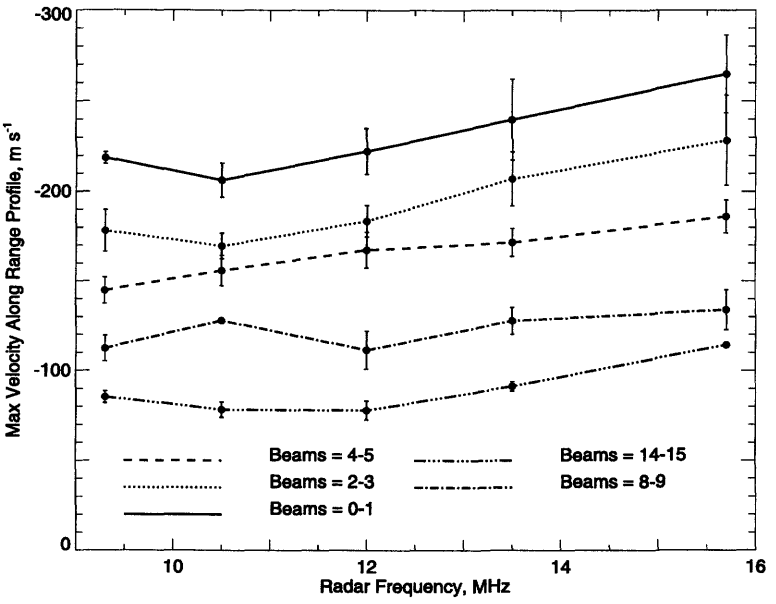

Figure 6.6: Maximum Doppler velocities as measured at various radar frequencies.

(number of frequencies×number of radar beams, remember that we merged data for every pair of beams) matrix of velocity values and a 5×8 matrix of bin numbers, where velocity was at the maximum. Figure 6.6 shows the typical variations of maximum velocity with radar frequency for some directions. Again standard deviations were scaled down here four times to provide a more readable picture. Overall, one can see that Doppler velocities at low-number beams (say, 0–1) are much larger than at high-number beams (velocity at large L-shell angles is much smaller) as one would expect for L-shell aligned flow. With respect to the radar frequency effect, one can clearly see that there is a Doppler velocity increase with frequency for each particular beam, though for some beams (e.g., 0–1) the dependence is within the statistical error of measurements. A velocity increase with HF radar frequency has been reported by *Jayachandran et al.* [2000], but the rate of increase is much smaller in our case.

6.2.4 Details of Velocity Variations With Range

So far in our analysis we have considered the phase velocity variation due to various plasma physical effects; for example, because of the change in aspect angle conditions. Previous studies have shown, however, that at HF the refraction is also a potential factor that could affect the properties of the phase velocity observed experimentally [e.g., *Uspensky et al.*, 1994]. For our experiment, since the amount of refraction is frequency dependent, one might expect different velocities for various HF radar frequencies in the same range of the high-latitude ionosphere. To estimate how strong this effect is in our event, we plotted the velocity ratio, lower frequency velocity to higher frequency velocity, versus slant range in Figure 6.7. For this presentation, in addition to combining beam pairs, we split the data into 2 groups, the low radar frequency group data for 9 and 10 MHz, and the high radar frequency group data for 13 and 15 MHz. Data at 12 MHz were used as a base to be compared with. We then applied the standard averaging procedure to obtain mean values of the Doppler velocity ratio in each range bin, 8 pairs of beams, and for 2 groups of frequencies. Then two ratios of low- and high-frequency echoes: velocity at 9 and 10 MHz divided by velocity at 12 (circles in Figure 6.7), and velocity at 12 divided by velocity at 13 and 15 MHz (squares in Figure 6.7) were plotted. Figure 6.7 shows such ratios for four beam pairs only.

Let us start with the beams 12–13 data. One can see that $V_{9,10}/V_{12}$ ratio is around 1 but overall there is a negative slope of the curve. This effect is much more obvious for the ratio $V_{12}/V_{13,15}$ that has additional values for farther ranges. Data for beams 8–9 show similar tendencies. For beams 2–3 and 0–1 there is also a general tendency for the velocity ratios to decrease with range, and the effect is very obvious for distances of 450–650 km.

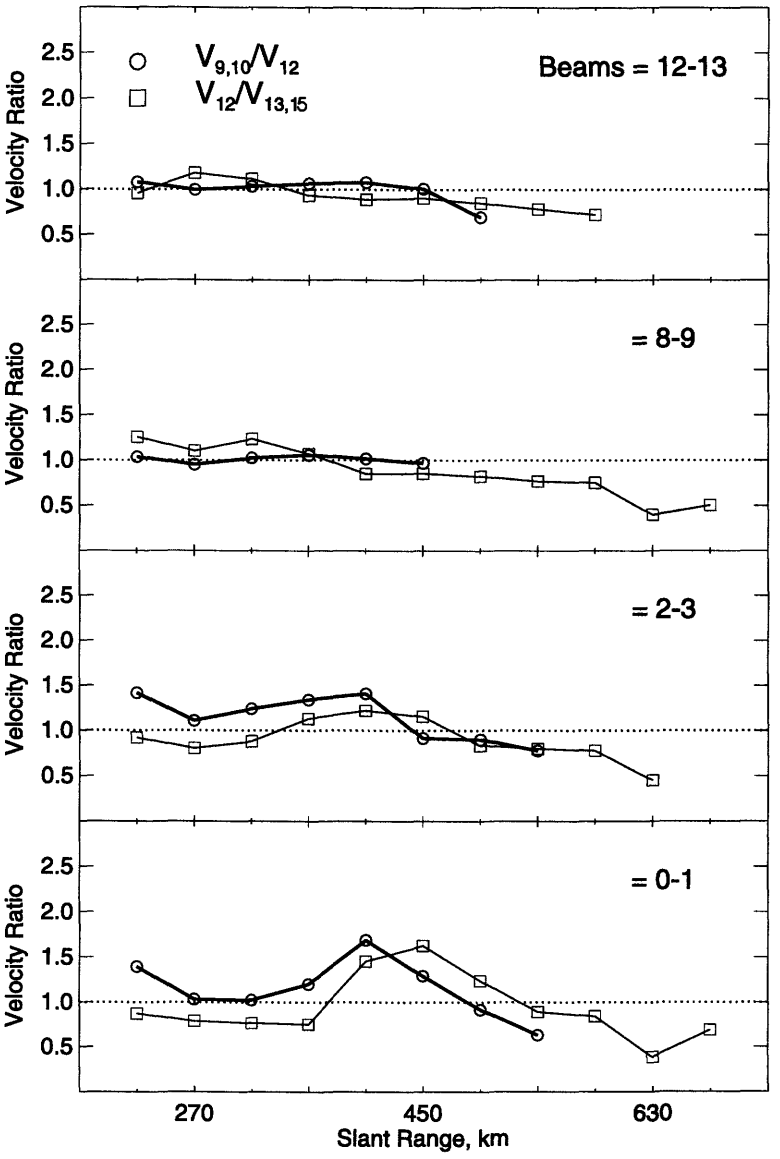

Figure 6.7: Averaged ratios of Doppler velocity for lower- to higher radar frequency as a function of slant range for several radar beams.

6.3 Velocity Versus L-Shell Angle

In this section we study the velocity flow angle variation, using two different approaches. First, we consider velocity maxima versus L-shell angle inferred from averaged range profiles of Doppler velocity. Second, we use a scatter plot approach, analogous to that used in Section 5.3.2 and consider all available points without averaging over the slant range or beam.

6.3.1 Velocity Maxima Versus L-Shell Angle

The logical continuation of the previous section is to plot velocity maxima (obtained as described above) versus azimuth of measurements or, for convenience of comparison with theory, versus L-shell/flow angle, at various frequencies. To make such a plot, we calculated the L-shell angle for the bin with the maximum velocity for every radar beam and every radar frequency. The reasoning here is the same as in the previous section: since there appears to be an approximately constant electric field in the near FOV, any change of the velocity maximum reflects the flow angle effect, for each of the 5 radar frequencies/irregularity scales.

Figure 6.8 shows the velocity maxima at various L-shell angles. The range of L-shell angles is 40°–95°, and the range of velocities is -70 to - 300 m s^{-1}.

Though the data spread is significant, several important features can be noticed immediately. The Doppler shift magnitude for all frequencies decreases with L-shell angle increase, as expected, but the shape of this dependence is not the expected "cosine" variation. To make this point clearly we show in Figure 6.8 an example of a cosine variation curve (solid line) for a modest value of the electron drift of 600 m s^{-1}. As for the frequency dependence of the velocity variation there is a trend in the data for L-shell angles $\phi < 75°$, namely that the Doppler velocity is greater

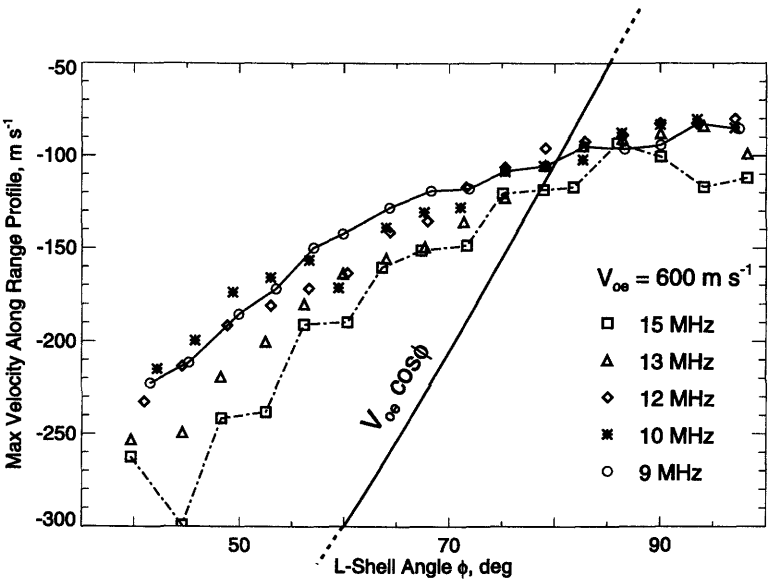

Figure 6.8: Maximum Doppler velocities in the range profiles as measured at various azimuths/L-shell angles.

at larger frequencies. The difference in maximum velocity between the highest and lowest frequencies seems to increase as the L-shell angle decreases.

6.3.2 Velocity Versus L-shell Angle: Scatter Plot Approach

In this section we use a different method of data analysis. For each bin where the ionospheric echo was registered, we computed the L-shell angle as described in Section 6.1.3 and then the measured Doppler velocity was plotted against this angle. In Figure 6.9 (upper panel) each point (both white and black) represents an individual record at two radar frequencies, 12 MHz in left upper panel and 13 MHz in the right upper panel. Total number of records is indicated in the left corner of each panel. Here two sorts of points describe two different echo populations; white dots correspond to those measurements for which the aspect angles were poor $|\alpha| > 3°$, while black

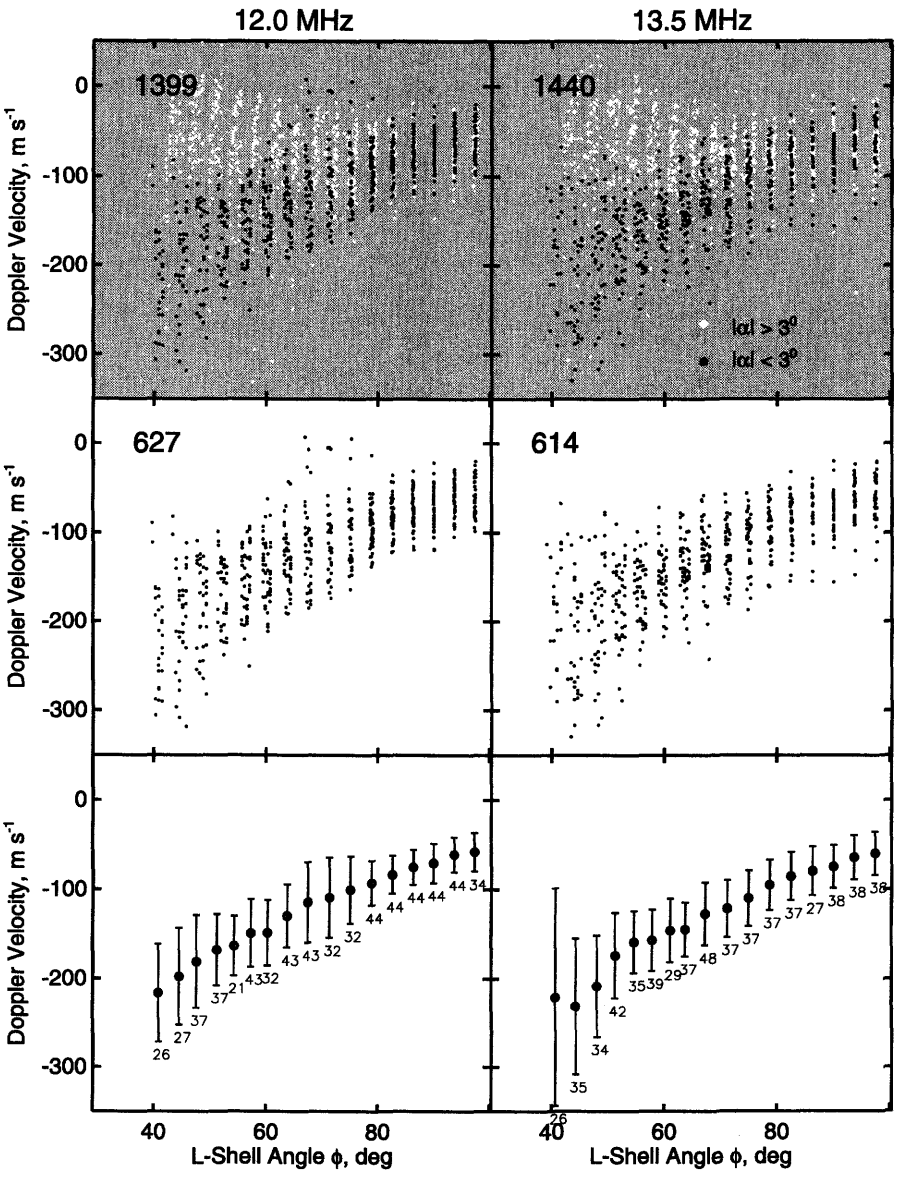

Figure 6.9: Doppler velocity versus L-shell angle at 12.0 (left) and 13.5 MHz (right). Upper two panels show scatter plots for all measurements. White (black) dots denote measurements with aspect angles larger (smaller) than 3°. Also indicated is the number of points for each radar frequency. The middle two panels show data for measurements with aspect angles smaller than 3°. The bottom two panels show averaged velocity versus L-shell angle; 3.5° L-shell angle bins have been used. Mean value of velocity, standard deviation, and number of points are shown for each bin.

dots correspond to good aspect angle measurements with $|\alpha| < 3°$. Additional reason for such a data separation is quite obvious from Figure 6.9; the population of white dots shows a distinctly different flow angle variation as compared to the black dot population; the white dots exhibit a velocity magnitude increase with L-shell angle increase, while the black dots show just the opposite tendency, a velocity magnitude decrease.

In the middle panel of Figure 6.9 we show only points measured at good aspect angles, and again we indicate the total number of points in the top left corner. We have about 50–60% of the original points. There is a clear velocity variation with L-shell angle here. To show it more explicitly we binned velocity with L-shell angle bins of 3.5°. The resultant mean values, standard deviations, and total number of points for each bin are shown in the bottom panel of Figure 6.9.

Diagrams similar to Figure 6.9 were obtained for all radar frequencies and data from the bottom panels of these diagrams were gathered together in Figure 6.10 in order to reveal any frequency effect in velocity variation with L-shell angle. Overall, this diagram looks very similar to Figure 6.8. Notice that data for Figure 6.8 were averaged with respect to the range while the Figure 6.10 data were averaged over L-shell angle, which is perhaps more appropriate for the study of flow angle effects. Another significant difference from the Figure 6.8 data is that Figure 6.10 is based upon a number of data points obtained at small aspect angles, not just one point at presumably perfect aspect angle. One can also notice that the velocity variations in Figure 6.10 are smoother than those shown in Figure 6.8.

Despite the difference in approach, the results of Figure 6.8 and 6.10 are essentially the same. For all frequencies, the velocity magnitude increases with flow angle decrease and all curves depart significantly from the expected "cosine" variation. In Figure 6.10, we emphasize the data at 9 MHz by a solid line and at 15 MHz by a dash-dotted line. At large L-shell angles, between 75° and 100° (right part of the

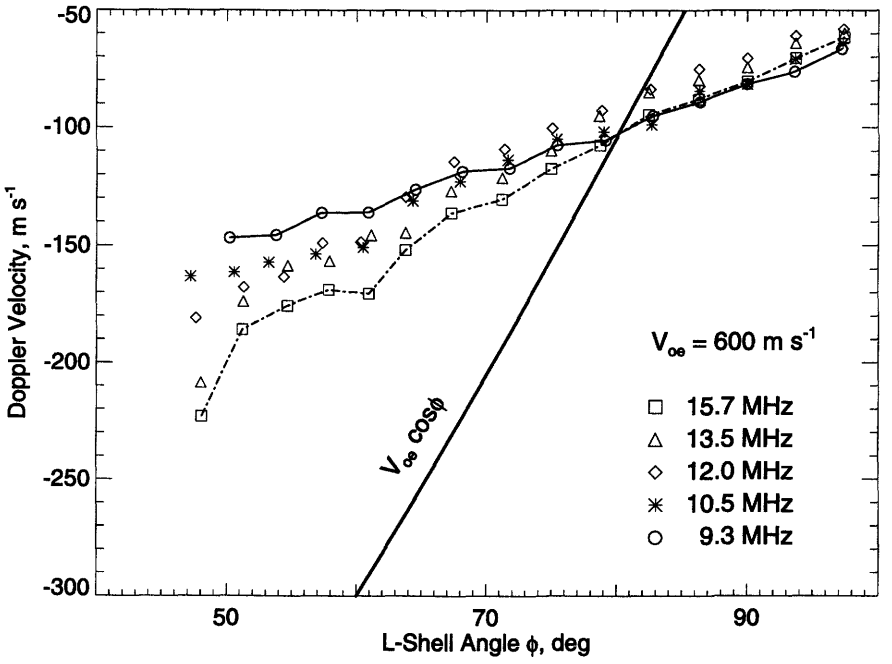

Figure 6.10: Average Doppler velocity versus L-shell angle at all radar frequencies.

diagram), the rate of velocity change is about the same at all radar frequencies. At smaller L-shell angles ($\phi < 75°$, left part of the diagram) the rate of the increase in velocity magnitude with decreasing ϕ is greater at higher radar frequencies (the dash-dotted line is at velocities that are more negative than the solid line).

6.4 Summary

In this chapter, we considered the HF radar observations of E-region coherent echoes at frequencies from 9.3 to 15.7 MHz at Prince George for an event characterized by an extremely consistent pattern of echo parameter variations with range over the period of two hours. Averaged profiles of echo power, Doppler velocity and elevation angle were presented. Elevation angle measurements clearly demonstrated that the

observed echoes came from the E region. Profiles of the power versus range showed clear maxima at all radar frequencies, with consistent shifts of the power maximum towards the radar site with frequency decrease and L-shell angle increase. The ranges of echo power maxima were consistent with the ranges of nearly zero aspect angles at the center of the electrojet layer. Velocity range profiles also demonstrated maxima; for most cases, the velocity maxima occurred at the same ranges as the power maxima. However, observations made in directions perpendicular to the L shells showed very little change in the velocity with range. We estimated the rate of power and velocity decrease with aspect angle and found the HF values to be in agreement with those at VHF. It was found that the velocity decrease with aspect angle can be described by the fluid theory if the nominal electron collision frequencies are replaced by anomalous collision frequencies that are about 5 times larger. We also showed that there was an effect of change with range in the ratio of the velocity at low frequency to that at high frequency. At short distances, the ratio is slightly more than 1 while at farther distances, the ratio is less than 1.

The velocity variation with L-shell angle have been explored using two methods. First, we considered the variation of the maximum velocity with L-shell angle and found this variation to be very similar at all radar frequencies and not obeying the expected cosine law. In the second approach, measurements in all beams were merged and sorted in accordance with both the L-shell angle and the aspect angle. Only points with aspect angles less than 3° were then considered. The flow angle variation was also found to be very similar to the maximum velocity variation, again not in agreement with the expected cosine law.

Chapter 7

Discussion

7.1 General Remarks

In this thesis we considered several aspects of meter and decameter irregularity excitation in the high-latitude ionosphere. Our major focus was on the irregularity phase velocity.

In the theoretical part (Chapter 2) we first reviewed existing theories of the electrojet plasma instabilities and showed that the irregularity phase velocity is expected to depend on several factors such as the plasma parameters (including ionospheric electric field), the scale of the wave and the direction of its propagation. For strong electric fields, when the F-B plasma instability is the main source of irregularities, fundamentally different velocities are predicted for the propagation along and perpendicular to the electron drift. The fact that various theories co-exist so that one cannot give preference to one specific theory (for various reasons) tells us that more theoretical work is needed. Another way to look at the issue is to compare theoretical predictions with observations. Both approaches have been tried in this thesis.

In Chapter 3 we proposed a new theory of the F-B instability evolution addressing the question on what would happen after the plasma turbulent state was reached through mode coupling. We considered the modification of secondary, long-wavelength fluctuations ($\sim$ 500 m in size) by the primary, short-wavelength ($\sim$ 1 m) perturbations. We showed that the secondary waves can grow under typical conditions implying that the long wave perturbations in the auroral ionosphere can be supported not only by direct excitation through the G-D instability but also by nonlinear generation with the energy supply from the smaller scale perturbations. Even though this theory was developed for long wavelengths of $\sim$ 500 m, one can expect similar processes to occur at shorter wavelengths with the energy of $\sim$10-m waves being transferred from the linearly unstable waves in the centimeter range. The new theory predicts that the long-wavelength irregularities move with the velocity corresponding to the linear regime (line-of-sight component of the electron drift). This means that the irregularity phase velocity inside the unstable cone is not limited to the local ion acoustic speed C_s. Whether this prediction corresponds to the experimental data needs to be seen. As was mentioned in Chapter 4, there is evidence that the velocity of decameter irregularities does show some saturation at 400–500 m s^{-1}; however, we presented in Chapter 5 cases for which the HF velocity was 700–800 m s^{-1}, which is above typical values of the ion acoustic speed.

On the experimental side of the thesis, we first reviewed publications with respect to velocity (Chapter 4) and demonstrated that the data themselves show quite a variability in their trends meaning that further research is required. Also, major differences between theoretical predictions and experimental data were identified. We showed that these differences appear to be more pronounced for the observations at HF. This was one of the reasons why HF radars were selected for experimental work. As far as HF echoes are concerned, the following questions were found to be interesting and important.

(1) How many types of E-region echoes exist at HF and what is the relationship between these types and the ones at VHF and UHF?

(2) Is there phase velocity saturation at C_s for observations along the flow and does the velocity outside the F-B instability cone follow the cosine law?

(3) Is the velocity variation with aspect angle along the flow similar to the ones reported in the past for VHF? How does it change with the frequency? What is the velocity variation with aspect angle perpendicular to the flow?

(4) How does the phase velocity of E-region irregularities depend on the radar frequency/wavelength?

These are the main issues that we will discuss in this chapter. We will also show how our observations fit into the general picture described in Chapter 4. In our presentation, we follow two different comparisons that were undertaken in this thesis, the velocity comparison at significantly different wavelengths, 12 m versus 3 m (Chapter 5) and at 5 closely spaced wavelengths, between 9.6 and 16.1 m (Chapter 6).

7.2 What Did We Learn From the HF/VHF Comparison?

First of all, we would like to note that we will refrain from using the term "type" with respect to our observations, unless we establish that the echoes we observed are indeed classical types 1, 2, 3, or 4 as described in the reviews [e.g., *Haldoupis*, 1989; *Sahr and Fejer*, 1996; *Moorcroft*, 2002]. Part of the reason is that identification of HF echo types in terms of well accepted VHF terminology is difficult. As we showed, the spectral width parameter often does not tell much. Also, one can not estimate

the instability cone due to the lack of electric field/particle temperature information.

7.2.1 High- and Low-Velocity HF Echoes Versus Classical Types 1 and 2

Our major finding of Chapter 5 is that HF echoes appear to belong to two distinct populations of 12-MHz echoes, the high- and low-velocity echoes, Section 5.3. The existence of two echo groups is obvious not only from the scatter plots (say Figure 5.10) but also from the distribution diagrams (Figures 5.11b and 5.12b).

In splitting the overall data set into two HF groups our criterion was whether the velocity of the observed echo is below or above the critical value. It is customary to identify echoes with Doppler velocities around the ion acoustic speed (350–400 m s^{-1}) and around zero with traditional types 1 and 2, respectively. But what should be the velocity that can be used as a "boundary" between echoes of different types? The simplest answer is of course the ion acoustic speed C_s, the threshold velocity for the F-B instability [see, for example, the recent review by *Moorcroft*, 2002]. In the original study by *Makarevitch et al.* [2001] the value of the typical ion acoustic speed in the E region, $V_{crit} = 360$ m s^{-1}, was adopted. This selection was also obvious from the scatter plots that were analyzed. In this thesis (Chapter 5) we considered an expanded data set and found (Figure 5.10) that echo separation is more pronounced for $V_{crit} \cong 320$ m s^{-1}. Interestingly, a velocity of 320 m s^{-1} was also obtained by *Villain et al.* [1987] as a "lower boundary" for their high Doppler shift HF echoes. We then used this value in Section 5.3, keeping in mind that it is approximate. If, for example, one follows the presentation of Figure 5.12b, it can be seen that the high-velocity HF echoes are most frequently observed with the velocities of 450–525 m s^{-1} and that the least frequent echoes have velocities of 200–250 m s^{-1}. Summarizing,

we have to note that the exact value for V_{crit} is not crucial for the present study; the result would be about the same if one would take any value between 300 and 400 m s^{-1}.

Before making comparisons between our echo groups and type 1/type 2 echoes we would like to restate the most salient properties of high- and low-velocity HF echoes. We showed that their power is comparable at large flow angles while along the flow the high-velocity HF echoes are stronger than the low-velocity HF echoes, on average by $\sim$ 7 dB (Figure 5.14). High-velocity echoes are also narrower, on average, though the difference in spectral width is not large (70–100 m s^{-1}, Figure 5.14). The difference in velocity is, however, very significant; for low-velocity echoes the mean Doppler velocity does not exceed $\sim$ 150 m s^{-1}, contrary to high-velocity echoes for which it is typically above $\sim$ 350 m s^{-1}.

The two echo populations exhibited completely different dependencies of their Doppler velocity upon the L-shell angle. Low-velocity 12-MHz echoes were observed for all radar directions and their Doppler velocity variation with the L-shell angle, Figures 5.11 and 5.12, approximately follows the cosine law. High-velocity HF echoes were observed only for the radar beam directions close to the L shells. Their Doppler velocities were not constant and can be approximated by cosine-like variation with much larger amplitude, above the typical ion acoustic speed. For both small and large data sets the direction with the largest velocity magnitude measured was at an angle $\sim$ 30°, contrary to the low-velocity HF echoes, whose velocity was maximized at the edges of the HF FOV, at L-shell angles of $\sim$ 20° and $\sim$ 140°. The VHF echoes showed properties similar to the high-velocity HF echoes.

The majority of HF echoes, both low- and high-velocity, considered in this study exhibited aspect angle sensitivity (Figure 5.11). The effect, of course, was very pronounced at VHF. This fact strongly supports the notion that the majority of observed HF echoes were of the electrojet origin rather than associated with the meteor trails

in the D/lower E regions. Unfortunately, a quantitative assessment of HF and VHF velocity variation versus aspect angle in a fashion similar to Chapter 6 was not successful; for a fixed electron density profile we did not find correspondence in ranges between echo power maxima/velocity maxima and zero aspect angle for all radar directions. This means that the assumption of the same density distribution within the entire FOV is not appropriate.

Bearing in mind the above-listed properties of high-velocity echoes, we have little doubt that they are related to the Farley-Buneman plasma instability. Such echoes had velocities above the instability threshold, were observed mostly along the L shells, their power was generally larger than that of low-velocity echoes, and power was decreasing with the L-shell angle. Also the high-velocity echoes were narrower and they were aspect sensitive.

We believe that the low-velocity HF echoes originate from secondary F-B or G-D instabilities. *Bourdillion et al.* [1995] and *Haldoupis et al.* [1996] argued that some HF mid-latitude echoes may be associated with the primary G-D instability. The main point was as follows. At mid-latitudes extremely sharp gradients of electron density of the order of 1 km could lower the short wavelength limit for the G-D instability up to the point where the primary G-D waves could be seen by an HF radar. The "overwhelmingly narrow power spectra" with the Doppler velocities well below the ion acoustic speed observed by *Haldoupis et al.* [1996] seem to support this idea. We do not have enough information to address this possibility.

The above hypothesis on the nature of low- and high-velocity echoes implies that the echoes could be associated with the classical type 1 and type 2 echoes, respectively, at least in terms of the mechanism of their production. We should say that we do not think that the correspondence is exact, and we will comment on some differences later. To make a certain conclusion on the issue one would need to compare spectra for high- and low-velocity echoes, which requires better spectral resolution than the

one currently in use in the SuperDARN experiment. We should note also that our analysis did not reveal additional classes of HF echoes that would be entirely different from the two major populations. For example, we did not find signatures analogous to type 3 VHF echoes.

In the case of high-velocity HF echoes, there are several complications that prevent us from direct identification of high-velocity HF echoes as the classical type 1. First, velocities of these echoes were quite high. In Figure 5.12b the peak in the velocity distribution is at 475–500 m s^{-1} and there are many points with even larger velocities, up to 800 m s^{-1}, whereas the typical ion acoustic speed is 350–400 m s^{-1} [*Fejer and Kelley*, 1980; *Haldoupis*, 1989]. Observed velocities are in excellent agreement with the statistical HF study by *Hanuise et al.* [1991] in which the peak in the velocity distribution function was observed at 425–500 m s^{-1}. Second, for small flow angles, the velocity of high-velocity HF echoes varies in a cosine-like fashion. Similar features, reported previously at 140 MHz by *Nielsen et al.* [2002] and at 10 MHz by *Uspensky et al.* [2001] does not fit the idea of C_s saturation for the phase velocity of type 1 echoes. Finally, we found that 12-MHz velocities were somewhat larger than the 50-MHz velocities (Figure 5.10), while previous measurements showed the opposite variation [*Balsley and Farley*, 1971; *Hanuise et al.*, 1991]. We return to the question about the ratio between velocities at 12 and 50 MHz later, in Section 7.2.6.

With respect to the notion of C_s saturation, one should keep in mind two important observations. First, during electron heating events (when the electron temperature is enhanced in the presence of strong electric fields due to the wave-particle interaction, Section 2.2.3) the nominal value of the ion acoustic speed of 350–400 m s^{-1} [*Fejer and Kelley*, 1980] can be significantly increased, up to 700 m s^{-1} [*Schlegel and St.-Maurice*, 1981]. Second, C_s is usually calculated under the assumption of the plasma isothermality. If, on the other hand, one assumes that ions are not isothermal but rather adiabatic (with one degree of freedom), it would also effectively increase

the ion acoustic speed. Both ideas do lend some support to the C_s interpretation of the considered data, since the observed velocities of more than 700 m s^{-1} can be still regarded as the ion acoustic echoes with "larger than typical" C_s. We, however, believe that both effects do not work on a regular basis. For the amount of the electron heating to be large enough in order to explain the Doppler shifts of 500–600 m s^{-1} with the C_s idea, the electric field should be larger than 45 mV m^{-1} [*St.-Maurice et al.*, 1981], while HF radars observe E-region echoes with Doppler shifts of more than 700 m s^{-1} **on a routine basis** (see Figures 5.11–5.12). Also, the question about the E-region plasma isothermality/nonisothermality is rather complex and controversial [see, for example, the recent paper by *Haldoupis et al.*, 2002, and references therein]. For example, *Farley and Providakes* [1989] argued that the electrons for most of situations should be treated as adiabatic with three degrees of freedom, meaning that C_s should be even smaller than in case of the isothermal electrons. *Stubbe* [1989] concluded that ions are isothermal for the case of low-frequency waves ($\omega \ll \nu_i$).

There are three features that are somewhat at odds with the "low-velocity = type 2" identity as well. First is that if the low-velocity HF echoes were indeed classical type 2 echoes then one would expect a VHF counterpart in the scatter plot of Figures 5.11–5.12. We did not find any substantial evidence for this. Second is that, consistent with *Hanuise et al.* [1991] who concluded that HF widths are smaller than VHF ones, the width of the low-velocity echoes ($\sim$ 200 m s^{-1}) is small compared to typical widths of type 2 echoes. The third and the most striking feature of low-velocity 12-MHz echoes is their unusually small, typically less then 100–150 m s^{-1}, velocities. These values are suspiciously close to the neutral wind velocities observed at auroral latitudes [e.g., *Tsunoda*, 1988]. The irregularities generated by the G-D instability (type 2 echoes) are expected to move with a component of the $\mathbf{E} \times \mathbf{B}$ drift velocity that could be anywhere in the range from zero to C_s [e.g., *Moorcroft*, 2002].

One can state thus that, to a first approximation, one can associate high- and

low-velocity 12-MHz echoes with the classical type 1 and 2 echoes, respectively, but the question requires further investigation.

7.2.2 Low-Velocity HF Echoes: Other Sources/Instabilities

The fact that the velocities of low-velocity HF echoes are below or very close to the neutral wind speeds observed in the auroral zone suggests that the low-velocity echoes are associated with electrojet instabilities that are affected in a significant way by the neutral wind and neutral turbulence. These processes are more efficient for the electrojet bottom side, at 90–100 km heights [*Kagan and Kelley*, 1998, 2000; *Gurevitch et al.*, 1997, *Ogawa et al.*, 2001]

Another observation that lends some support to the importance of the lower ionosphere for the low-velocity echoes is their occurrence at all azimuths with some preferential directions $\phi \sim 45°$, contrary to the higher occurrence of high-velocity echoes along the flow (Figure 5.12e). We processed the data set by considering only low-velocity echoes and did confirm their preferential occurrence at azimuths of 110° and 170°. One can also look at Figures 5.12e where only simultaneously occurring echoes are considered. One can recognize here that low-velocity echoes for the Syowa South radar have local maxima at $\phi \sim 100°$ and $\phi \sim 110°$. Data for the Syowa East radar show 4 local maxima. We should note here that Figure 5.12e contains information about echoes at all slant ranges/aspect angles.

One can offer several explanations of the preferential direction of HF echo generation neither parallel nor perpendicular to the flow. From one side, numerical simulations of *Janhunen* [1994] showed that the power of the F-B waves maximizes not along the flow but at an angle of $\sim 45°$. The nonlinear theory by *St.-Maurice and Hamza* [2001] gives essentially the same result. But on the other hand, why the effect is important at decameter scales and not at meter scales is unclear.

Now, there are two ways to argue why this result would suggest the importance of the lower ionosphere. *Dimant and Sudan* [1995a, b, c; 1997] developed the theory of a new instability operational at the electrojet bottom side. This instability, sometimes called the *Pedersen conductivity instability* [*Robinson*, 1998; *St.-Maurice and Kissack*, 2000], belongs to a separate class of electrojet instabilities, namely the thermal instabilities where the plasma nonisothermal effects are taken into account. It is more easily excited at an angle of $\sim 45°$ with respect to the flow. Thus it could effectively provide a shift of the echo occurrence maximum both at VHF and HF. However, since this instability is more efficient at decameter scales, the effect can only be seen in the occurrence of HF echoes. *Dimant and Sudan* [1997] do not directly address the phase velocity of irregularities; however, this instability is a close analog of the electron thermal diffusion instability developed by *Gurevich and Karashtin* [1984] and advanced and applied to type 3 observations by *Shalimov and Haldoupis* [1995]. *Shalimov and Haldoupis* [1995] concluded that the phase velocity of unstable waves is a fraction of the $\mathbf{E} \times \mathbf{B}$ drift under the assumption that the waves propagate at threshold velocities.

The other possible explanation is that the irregularities produced through the neutral wind-related instabilities are controlled by neutral wind that might provide some preferential direction for the echo detection, though this question requires further investigation.

One can think of a different explanation for the rotation of preferential detection of HF echoes with respect to VHF echoes. As discussed later in Section 7.2.6, the echoes for different radar frequencies might come from different heights within the electrojet layer. In this case, since both the F-B and G-D instabilities are easier to excite along the vector of the relative electron-ion drift $\mathbf{V}_d$, one might have slightly different preferential directions for the instabilities to occur at various heights.

Figure 7.1 illustrates this point showing the electron and ion background

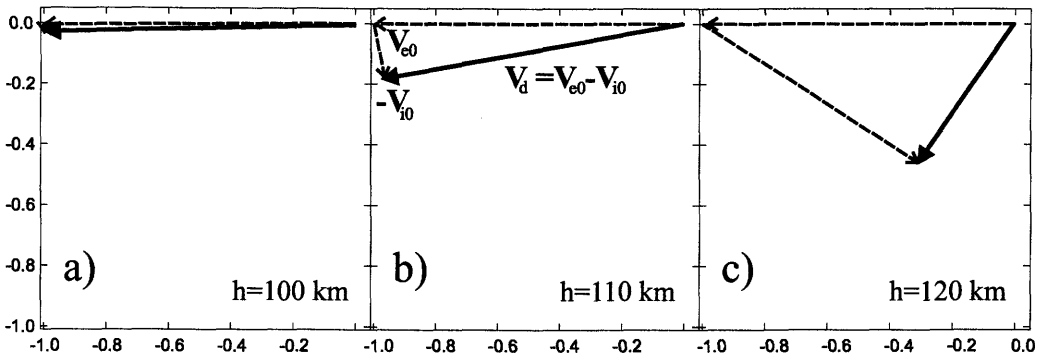

Figure 7.1: The electron, ion, and relative electron-ion drifts for (a) 100 km, (b) 110 km, and (c) 120 km. The vector denotation is shown in panel (b).

($\mathbf{V}_{e0}$ and $\mathbf{V}_{i0}$) and relative electron-ion drift $\mathbf{V}_d$, calculated for three different heights. The y (x) axis is northward (eastward), electric field $\mathbf{E}$ in the evening sector is poleward (see Figure 1.4) that is along the y axis (for the morning sector the directions would be changed). For calculation we used the estimates for collision frequencies from Figure 1.3. One can see that the direction of the relative drift vector $\mathbf{V}_d$ is rotating with the altitude and since, according to (2.59), the growth rate $\gamma_{\mathbf{k}}$ should be at maximum for the wave vector $\mathbf{k}$ parallel to $\mathbf{V}_d$, one can expect then that the directions at which instabilities are easier to excite would be different for different radar frequencies and that the maxima of echo occurrence would be shifted by some angle with respect to one another.

St.-Maurice and Schlegel [1983] considered the effects in backscatter power associated with the electrojet direction rotation in a kinetic approach under the assumption that the unstable plasma waves spend most of their lifetime in a linear growth phase. They showed that the power maximum for the scatter at 115 km is located at $\sim 20°$ with respect to the $\mathbf{E} \times \mathbf{B}$ direction versus several degrees for the scatter at 105 km (see their Figure 3).

The proposed explanation is satisfactory for the Syowa East observations, but,

unfortunately, it can not be accepted for the Syowa South observations, for which the direction of current rotation is opposite to the required one.

For this reason, we believe that the preferential detection of HF echoes at $\sim$ 45°/115° directions occurs due to neutral turbulence and temperature contributions to the electrojet instabilities.

7.2.3 Low-Velocity Echoes: Collisional Depression and Neutral Wind Effects

If one assumes that the low-velocity 12-MHz echoes are generated at the bottom side of the electrojet layer then one would expect their velocity to be strongly depressed. From equation (2.55) it follows that the larger the ψ term in the denominator the smaller the oscillation frequency and hence the phase velocity. At the bottom of the electrojet, the ψ term is increased due to strong collisions. The decrease of the phase velocity with ψ increase we call *collisional depression* since ψ is proportional to the collision frequencies. The coefficient $1/(1+\psi)$ is called the *depression coefficient.*

Let us estimate the amount of collisional depression at the electrojet bottom side (height of 95 km). For calculation of the depression coefficient at $h = 95$ km we used the estimates for collision frequencies from Figure 1.3: $\nu_e = 10^5$ s^{-1} and $\nu_i = 1.5 \cdot 10^4$ s^{-1}. Given these collision frequencies, the anisotropy factor ψ simply equals to 1. Also for this height the equations for background plasma drifts (2.7)–(2.8) give that ion background drift is very small ($\sim 0.01 V_{e0}$) in the absence of a neutral wind, while electron background velocity V_{e0} is close to the $\mathbf{E} \times \mathbf{B}$ drift velocity, so that phase velocity is determined mainly by the electron drift V_{e0}. However, since $V_{ph} \cong V_{e0}/(1+\psi)$ and $\psi = 1$ the phase velocity is two times smaller than the $\mathbf{E} \times \mathbf{B}$ drift. Thus, one can explain small velocity values of the low-velocity HF echoes using

the collisional depression at the bottom of electrojet.

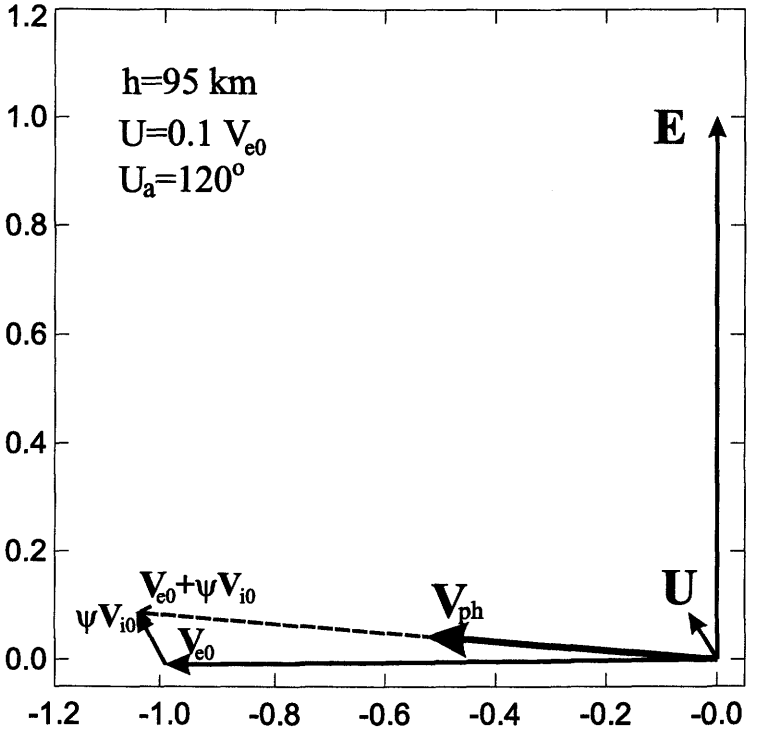

Figure 7.2: The effects of neutral wind on the phase velocity at the bottom of electrojet $h = 95$ km. The depression coefficient is $1/(1+\psi) = 1/2$.

For the bottom of the electrojet layer the effects of neutral winds can also be very important. We illustrate this in Figure 7.2 which shows the effect of a nonzero neutral wind on the phase velocity of the F-B waves at the bottom of the electrojet, $h = 95$ km. The format of the diagram is the same as for Figure 7.1. The neutral wind vector $\mathbf{U}$ is at an angle 120° counterclockwise from the x axis and the magnitude of the neutral wind speed is 10 times smaller than the $\mathbf{E} \times \mathbf{B}$ drift velocity.

One can see that, despite the fact that the ion background drift due to the electric field is negligible ($\sim 0.01 V_{e0}$), even a modest value of neutral wind velocity of 1/10 of V_{e0} gives a significant magnitude for the ion background velocity, which causes

the direction of the phase velocity to be changed significantly as compared to the background drift of the electrons $\mathbf{V}_{e0}$.

The proposed above mechanism of the phase velocity direction change by combined action of the collisional depression and neutral wind is similar to the one in the recent study by *Uspensky et al.* [2002] who considered the change of the phase velocity due to the possible contribution from the top of the electrojet layer, where the Pedersen drift of ions, first term in (2.10), become extremely important. The major difference between *Uspensky et al.* [2002] and this study is that our mechanism does not require finite aspect angles.

One can then use this hypothesis to explain the fact that the reversal in the sign of HF velocities in Figure 5.11a occurs at $\phi \cong 75°$ and not exactly perpendicular to the assumed direction of the flow, at $\phi = 90°$.

7.2.4 High-Velocity Echoes: Velocity Variation Within the Instability Cone

With respect to the high-velocity echoes, one important conclusion of this study is that their velocity changes with the flow/L-shell angle. The effect is well seen at both HF and VHF, Figures 5.11–5.12. This contrasts with the long time notion that type 1 echoes observed at small flow angles, inside the F-B instability cone, do not exhibit any significant velocity variation with the flow angle [e.g., *Nielsen and Schlegel*, 1983]. The obtained results agree well with the recent paper by *Nielsen et al.* [2002] that showed that the phase velocity of VHF (140 MHz) echoes is maximized at zero flow angle and slowly decreases up to a flow angle of 40° where it is equal to the ion acoustic speed. This result was predicted theoretically by *Rogister and Jamin* [1975]. A similar feature at HF was discussed recently by *Uspensky et al.* [2001]. In another

study by *Milan and Lester* [2001] it was shown that some HF echoes (type 3 and 4 in their notation) exhibit quite peculiar dependence of the Doppler velocity upon the L-shell angle. Velocity magnitudes of such echoes maximized at L-shell angles of 25°–35°, neither along nor perpendicular to the flow. We found, Figure 5.11, that both VHF and HF velocity magnitudes are largest at the L-shell angles of $\sim$ 30°, and, in this sense, our results support the results of *Milan and Lester* [2001].

One may ask why high-velocity echoes have largest magnitudes at certain angle (about 30°) with the L shells? This feature can be explained by departure, on average, of the flow from the L-shell direction. Indeed, in the morning sector of the auroral zone one might expect additional "curving" of the flow towards the magnetic pole for the two-cell convection pattern, Figure 1.4. If the amount of flow curving for the eastern part of the FOV was of the order of 30° then our results are in good agreement with the results of *Nielsen et al.* [2002].

If the current "curving" was indeed occurring then the low-velocity HF echoes should also show larger velocities for the L-shell angles about 30°. This did not happen, and the reason, in our opinion, is that these echoes are related not only to the F-B and G-D instabilities but also to other instabilities as discussed above. Acceptance of the electrojet curving by 30° would mean that the departure of the maximum echo occurrence for HF echoes from the electrojet direction would be smaller.

The results somewhat similar to the present study were reported by *Villain et al.* [1987, 1990] using the data from the Goose Bay HF radar. Their data analysis has revealed the existence of three separate types of HF echoes. The main thrust was on high-velocity echoes ($V >\sim 350$ m s^{-1}) that were divided into two separate categories. First class of echoes (320 m s^{-1} $< V <$ 550 m s^{-1}) has been identified as the classical ion acoustic echoes and the second class of echoes with larger Doppler shifts (550 m s^{-1} $< V <$ 650 m s^{-1}) has been associated with the EIC instability. From the point of view of the present study of special interest are the low-velocity

echoes of *Villain et al.* [1987, 1990] that showed the features similar to the ones reported in the present study. The low-velocity echoes of *Villain et al.* [1987, 1990] had relatively small Doppler velocities ($V < 200$ m s^{-1}), they followed the cosine law and have been interpreted as the echoes generated through the G-D instability. A shift of 15°–20° (from the perpendicular direction $\phi = 90°$) in the angle at which velocity sign reversal occurred has been also reported and discussed in terms of not exactly L-shell aligned flow. Contrary to *Villain et al.* [1987, 1990], in the present study the echoes at all available slant ranges (aspect angles) were considered. Another important difference is that *Villain et al.* [1987, 1990] interpreted the low Doppler shift echoes as the tracers of the plasma drift at the top E region, while we believe that the low-velocity HF echoes originate from the bottom part of the electrojet layer.

7.2.5 Is Low-Velocity Echoes Scatter From Meteor Trails?

Hall et al. [1997] and *Hussey et al.* [2000] reported on the correlation of SuperDARN HF Doppler velocities at short ranges and neutral winds measured independently by a Medium Frequency (MF) radar. These authors assumed that the majority of the detected echoes were meteor scatter. A natural question is whether the low-velocity echoes were in fact simply the scatter from the meteor trails in our measurements.

It was established that meteor contribution to echo detection at the Syowa station was not negligible [e.g., *Ogawa et al.*, 1985; 2001]. In the previous studies by *Fukumoto et al.* [1999, 2000] and *Ogawa et al.* [2001] attempts have been made to exclude meteor echoes from the data base. Such an approach is certainly successful in eliminating isolated in time and space reflections (that are more likely to be truly meteor echoes), but not reflections occurring simultaneously with the auroral ionospheric scatter. Contrary to this approach, in Chapter 5, while performing general assessment of the data, we considered all available echoes at short ranges. We expect, consequently,

that some of the low-velocity VHF and especially HF echoes were, in fact, meteor scatter.

We believe, however, that the meteor contribution was not a significant factor in the observed HF echoes. This opinion is supported by several facts. First, Syowa echoes were more frequent at 1–2 UT and not in the late morning hours (UT $\cong$ MLT at Syowa). Second, when HF echoes occurred, they typically had quite an extensive spatial and temporal coverage. Third, we also analyzed HF/VHF data in the evening sector and found results similar to the ones presented in this thesis for the morning sector. Additional support comes from the revealed features of echo characteristics, for example, velocities were quite often large, > 100 m s^{-1}, more than typical meteor echo velocities, and the HF spectra were broader than typical meteor-associated spectra. We do believe, however, that low-velocity echoes were strongly affected by neutral particle motions, and in this sense our results are in agreement with *Hall et al.* [1997] and *Hussey et al.* [2000].

Elimination of "meteor" echoes by employing a modified approach of *Fukumoto et al.* [1999] in *Makarevitch et al.* [2001] and in Section 5.4 showed that all reported results in this thesis for the low-velocity echoes are in effect. An additional argument that the echoes associated with the scatter from the meteor trails do not constitute the majority of E-region echoes (in our study) is the fact that Figure 5.10 from Chapter 5 looks exactly like Figure 5 from *Makarevitch et al.* [2001] with the only exception that the number of points is different.

7.2.6 High-Velocity Echoes: Importance of Refraction

As mentioned in Section 7.2.1, our measurements indicate that the velocity magnitude at 12 MHz was generally larger than that at 50 MHz for observations along the flow and for the conditions when the F-B instability was very likely operational. This

finding contradicts previous experimental results [*Balsley and Farley*, 1971; *Hanuise et al.*, 1991; *Koehler et al.*, 1997]. This also disagrees with the kinetic theory of the F-B plasma instability [*Farley*, 1963; 1985] and the theory of type 1 velocity modification by plasma gradients [*Farley and Fejer*, 1975].

In this section we look at the problem of scale-dependence of the irregularity phase velocity from other than a plasma physics perspective. We attempt to explain the velocity differences at HF and VHF by the fact that refraction is more significant at HF, so that 12- and 50-MHz echoes can be received from different ionospheric heights where the local ion acoustic speed is different.

One clear conclusion of our measurements along the flow (Syowa East beam 15) was that 12-MHz power of short-distance Syowa echoes has a distinct maximum near 350–400 km, Figures 5.15. This was obtained by averaging over a significant data set containing 35 hours of measurements. A similar result was obtained for 92 hours of data in Figure 5.7. The statistical position of the maximum agrees well with the data over the short (half an hour) interval considered by *Koustov et al.* [2001]. These authors explained that the power maximum occurs at ranges of an optimal HF signal reception. At short distances, radar waves are scattered more efficiently at low heights of 95–100 km (the heights of near-zero aspect angles), where, first, the intensity of electrojet irregularities is low [*Fejer and Kelley*, 1980; *Haldoupis*, 1989] and, second, the electron density is decreased. At distances around 400 km, radar waves are scattered at the heights around the center of the electrojet layer, where both the irregularity intensity and electron density reach their maxima. At larger slant ranges, with radar waves being focused onto the top of the electrojet layer, echo power is decreased because the irregularity intensity is smaller here [*Fejer and Kelley*, 1980; *Haldoupis*, 1989]. In addition, the electron density might go down as well [*Kelley*, 1989]. The shift of the 50-MHz echo power maximum to farther ranges (to $\sim$ 450 km) can be explained by smaller radar wave refraction at this frequency.

Modeling of the power distribution versus slant range by employing the *Uspensky et al.*'s [1994] model indicates a reasonable agreement with measurements [*Koustov et al.*, 2001].

We showed in this study that, on average, both 50- and 12-MHz Doppler velocities along L shells increased with slant range, up to distances of 500 km, Figures 5.8 and 5.15b. This result agrees well with more extensive data statistics (11 months) for Syowa HF radar beam 15 considered by *Ogawa et al.* [2000]. Similar velocity variations for 50-MHz observations at the Antarctic Siple station (similar geometry of measurements) were reported by *Ogawa et al.* [1980]. Remarkably, the 12-MHz velocities were, to a first approximation, close to the 50-MHz velocities, substantiating the conclusion of *Koustov et al.* [2001]. Quantitatively, according to Figure 5.15b, velocity ratio $V_{12\text{MHz}}/V_{50\text{MHz}}$ was slightly more than 1 at distances < 400 km and slightly < 1 at farther distances. We confirmed this result later in Chapter 6 (Figure 6.7), where we showed that there was a general tendency for the ratio of the velocity at lower radar frequencies to the velocity at higher radar frequencies to be more than 1 at short ranges and to be less than 1 at far radar ranges. This finding is in agreement with the expectations of *Uspensky et al.* [1994]. Because of the velocity ratio variation with distance, if one would like to use typical velocities at various HF frequencies to infer the mechanisms of plasma irregularity formation, one cannot simply average data over certain ranges, especially for small flow angles of measurements. The effect is azimuth dependent, and we believe this is, at least partially, the reason for the different velocity ratios reported by *Haldoupis et al.* [1998] and *Jayachandran et al.* [2000] in their multifrequency measurements.

In Section 5.3 we studied the relationship between velocities at 12 and 50 MHz using scatter plot approach, Figures 5.10. We showed that it was convenient to split the points into two groups, according to the velocity of 12-MHz echoes being either smaller or larger than the critical velocity of ~ 320 m s^{-1}. Overall, the low-velocity

12-MHz echoes have smaller velocity magnitudes than 50-MHz echoes, while high-velocity 12-MHz echoes have larger velocity magnitudes.

To understand these features of 12- and 50-MHz velocities, we consider the aspect angle conditions of observations, since, generally, 12-MHz radio waves are known to refract much more than 50-MHz waves. We consider here the aspect angle variation with distance for observations along the L shells (azimuth of 83.7°).

Figure 7.3a shows several possible electron density profiles, the IRI-95 electron density profile selected for the time and location of the Syowa measurements (case 1), as well as increased densities by 4 times (case 2) and 7 times (case 3), to explore the effects if the electron density is actually enhanced. Similar profiles have been adopted by *Koustov et al.* [2001]. For calculations of the real aspect angle, a simple geometrical optics approach was adopted, similar to that of *Uspensky et al.* [1994].

Figure 7.3b shows the heights of the 12-MHz zero aspect angle at various slant ranges without considering refraction (dashed line, case 0) and with refraction taken into account according to the above electron density profiles: cases 1, 2, and 3. The range of possible heights at 50 MHz is shown by the stippled area. One can infer from Figure 7.3b that at short distances of 370 km, one would expect HF echoes to come mostly from the bottom of the electrojet layer. At distances $\sim$ 420 km the typical altitudes would be 105 km, while at large distances of $\sim$ 500 km one would expect HF echoes to come from the top of the electrojet layer, 115–120 km. Thus it is expected that the mean altitude of E region scatter increases with the slant range.

The next question, of course, is what would be a typical velocity of echoes received from various heights. Surely, there is some uncertainty here, since the "Doppler velocity–echo height" relationship is not well established experimentally or theoretically. Experimentally, *Unwin and Johnston* [1981] reported that 53-MHz echoes can come from two layers centered around 106 and 112 km, with larger velocities (often by several hundred meters per second) at the top layer. Theoretically, if one assumes

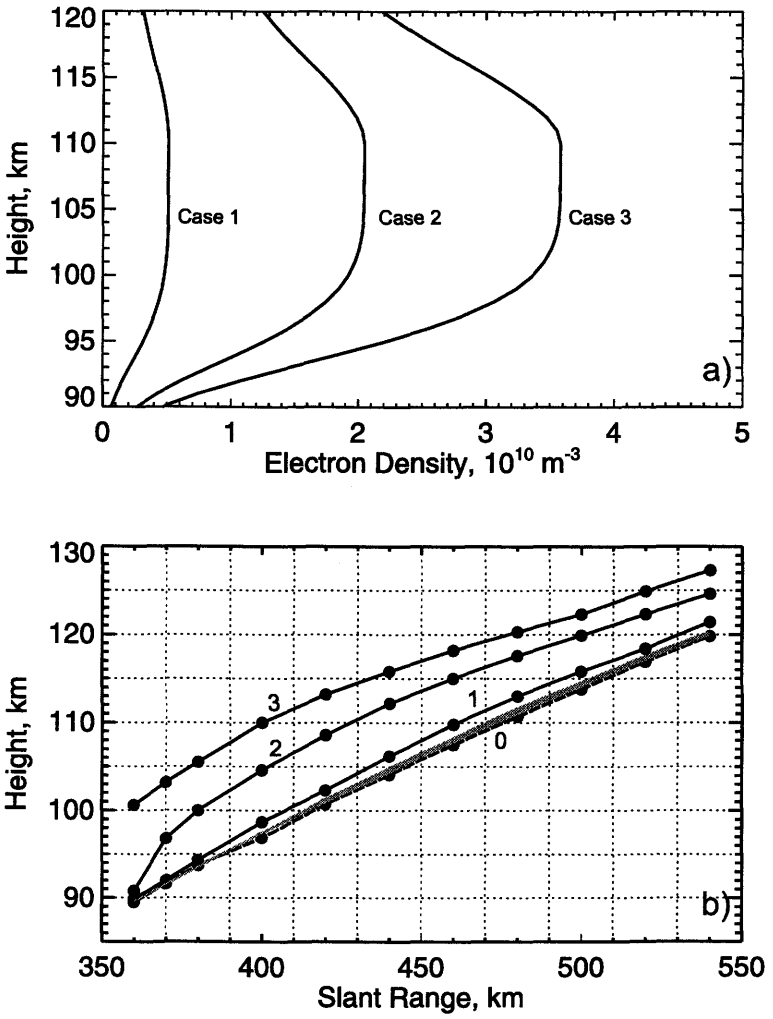

Figure 7.3: (a) Electron density profiles used for calculations and (b) height of zero aspect angle at 12 MHz versus slant range in the absence of refraction (case 0, dashed line) and with refraction taken into account for three different electron density profiles (see text). Stippled line indicates the range of possible heights at 50 MHz.

that high-velocity 12-MHz echoes are generated through the F-B and G-D instabilities, as discussed in Section 7.2.1, the velocity of observed echoes along the flow would correspond to the ion acoustic speed of the medium. In this case one would expect velocity increase with height (for all scales) and the difference between velocity at 12 and 50 MHz by a factor of 2 [*Haldoupis and Schlegel*, 1990]. If the velocity can be described by the linear theory, then one would also expect the velocity increase with height due to the collisional depression [e.g., *Uspensky et al.*, 1994]. For high-velocity 12-MHz echoes the model of Figure 7.3b predicts that the difference between 12- and 50-MHz velocities should not be large, since above 95 km the depression coefficient does not change drastically with height.

One consequence of low refraction at 50 MHz is that at short distances these echoes can only be received at nonzero aspect angles, so that their velocity would actually be less than the $\mathbf{E} \times \mathbf{B}$ electron drift velocity as explained by *Uspensky et al.* [1994], in contrast to 12-MHz echoes (experiencing significant refraction) that might have velocity equal either to the electron drift or the ion acoustic speed. At farther slant ranges, 50-MHz echoes can easily be received at zero aspect angles, so that their phase velocity should be about the same as for 12-MHz echoes. One expects that for some points, 12-MHz echoes would have slightly larger velocities because they might be coming from larger heights (if the electron density is enhanced). This effect can explain why 12-MHz velocities are quite often larger in magnitude than 50-MHz velocities.

Our measurements revealed one more important effect. All scatter plot diagrams show that the 12-MHz data spread is much stronger than the 50-MHz data spread, even though nearly simultaneous records have been considered. In our opinion this reflects the fact that refraction effects are much more significant at 12 MHz. Onset of local tilts in the ionospheric electron density contours might significantly change the path for 12-MHz radio waves, and this effect is much less for 50-MHz radio waves.

Another feature that is related to the scatter from top side of the E region for large ranges (in case of high-velocity 12-MHz echoes), Figure 7.3b, is that in the upper part of the electrojet layer, the intensity of electrojet irregularities (density fluctuations) is decreased because of poor conditions for excitation of electrojet instabilities [e.g., *Pfaff et al.*, 1984]. In addition, the electron density might be decreased, for example, as indicated by the electron density profiles in Figure 7a. Both factors would lead then to smaller echo power for the echoes at large slant ranges. If one recalls that these echoes have large velocity magnitudes (Figures 5.8 and 5.15b show that velocity increases with range) then it means that echoes with large velocities would have smaller power, which can explain the 12-MHz power saturation and even decrease at large velocities. The 50-MHz echoes are most probably coming from the central part of the electrojet layer and, therefore, though their velocity still increases with range/height their power does not start to go down as in the case of 12-MHz echoes, but steadily increases together with velocity.

7.3 High-Velocity HF Echoes: Lessons From the Multifrequency HF Experiment

New information on the properties of high-velocity decameter E-region irregularities was obtained in Chapter 6 where Prince George multifrequency observations at very close HF frequencies were considered.

We studied one event of evening measurements when, on the basis of the IMF intensity and orientation, one would expect a fairly uniform flow with a high degree of L-shell alignment. Calculations based upon the Institute of Terrestrial Magnetism, Ionosphere and Radiowave Propagation (IZMEM) electrodynamic model [*Papitashvili*

et al., 1994] indicate the possibility of a slightly curved flow, with a north-west rotation of about 10°–20° in the flow on the west side of the radar FOV and a 10°–20° north-east rotation in the flow on the east side of the radar FOV. Some regular flow departure from the L-shell alignment within the radar FOV would occur as well, though of less curvature than the above shifts. This prediction fits well with the E-region velocities measured by the Kodiak and Saskatoon SuperDARN radars, to the west and east of the PG radar FOV, respectively. The IZMEM model also predicts that the flow should increase slightly with latitude between 60° and 70° (PG radar FOV).

The limited amount of SuperDARN radar data during the event was not conducive to the production of accurate convection maps, but the estimated patterns with the available radar data agree with the assumption of slowly changing approximately L-shell-aligned flow. This conclusion is also supported by two DMSP crossings near the radar FOV areas (Figure 6.1) that show very stable ion velocities (a component perpendicular to the satellite path) of 700–800 m s^{-1} at latitudes 60°–65°. The passes are 1.5 hours apart but the intensity of the flow is comparable at those latitudes where the HF echoes were detected. Some difference between velocities for these passes can be explained by very weak and gradual variation in the flow intensity and orientation, as discussed above.

It should be emphasized that, though the maximum velocities observed during the event under study did not exceed 300 m s^{-1}, the $\mathbf{E} \times \mathbf{B}$ drift velocities observed by the DMSP satellites were well above the F-B threshold, meaning that the F-B instability was operational.

In the PG radar study we focused on wavelength effects in the irregularity phase velocity for the aspect angle and flow angle variations.

7.3.1 Velocity Versus Aspect Angle

In Chapter 6 we investigated whether the velocity of E-region HF echoes exhibits a decrease with aspect angle. This effect is well known for VHF echoes [*Ogawa et al.*, 1982; *Nielsen*, 1986; *Kustov et al.*, 1994]. We showed that, for the radar beam orientations closer to the flow (beams 0–3 of the Prince George radar), the velocity decrease with the aspect angle is slower than predicted by the standard linear theory but agrees well with the predictions if the regular electron-neutral collision frequencies are replaced by the anomalous values, greater by a factor of 5 for beams 0–1 and by a factor of 10 for beams 2–3. The first of these estimates matches well with earlier findings at VHF [*Ogawa et al.*, 1982; *Nielsen*, 1986] for measurements at low flow angles. The required factor of 10 increase in anomalous collision frequency for the beams 2–3 (that are further away from the electrojet direction) is an unexpected result. An even greater enhancement is required for larger L-shell angles, where the velocity decrease with aspect angle was not strong.

How can this result be explained? From one side, the Doppler velocity decrease with aspect angle that is slower than predicted by the standard linear theory and that becomes even slower with deviation from the flow direction, is consistent with the idea of electron collisions enhanced by the anisotropic quasi-linear effects [*Sudan*, 1983]. However, there are problems with this notion as discussed by *St-Maurice* [1987, 1988, 1990]. Also one would not expect an increase in anomalous collision frequency with the departure from the flow direction since for these directions the intensity of F-B fluctuations (ultimately related to the increase in collision frequency) is smaller. The result obtained perhaps indicates that other factors are important for the velocity of decameter irregularities.

In this view, it is worth noting that for large flow angles, beyond the F-B instability cone, the anomalous collision frequency interpretation would not apply, but

we observed a gradual weakening of the velocity decrease with the aspect angle as well, similar to observations within the instability cone. Moreover, for beams 12–13, almost perpendicular to the flow, no velocity aspect angle decrease was observed, and in fact there was even some increase. Analysis of measurements for individual scans shows that the velocities were quite often somewhat larger at the shortest and largest ranges within the echo band.

If one assumes that the fluid equations describe properly the velocity of electrojet irregularities at large flow angles, one can propose an explanation of the observed velocity stability over significant areas of the high-latitude ionosphere (Chapter 6, Figures 6.3 and 6.4). We expect that the aspect angles were quite large at those ranges where no velocity variations were observed. For this situation the effect of ion motions can be significant. From (2.58) one can immediately notice that for large flow angles (when $\mathbf{k} \cdot \mathbf{V}_d$ is close to zero) the phase velocity $V_{ph} = \omega_{\mathbf{k}r}/k$ would be completely defined by the second, ion term. This term does not depend on aspect angle α; for typical ionospheric parameters, it can be as high as 50–100 m s^{-1}, which agrees with the velocities measured on the high-numbered beams (large flow angles) of 60–90 m s^{-1}, Figure 6.3.

7.3.2 Velocity Versus L-Shell Angle

We showed that the velocity decrease with L-shell angle was fairly slow for angles 70°–100° and there was some velocity magnitude decrease with L-shell angle increase for smaller angles, Figure 6.10. We demonstrated that this decrease cannot be described by a cosine law, meaning that our data contradict predictions of the linear theory of the F-B and G-D instabilities [*Fejer and Kelley*, 1980] and experimental findings by *Villain et al.* [1990] and *Jayachandran et al.* [2000]. We should, however,

note that both the above experimental studies used data for directions almost perpendicular to the flow. For such directions, as their data indicate, the cosine variation does exist. Our observations refer to large flow angles for which there was no change in the sign of the velocity within radar FOV and for which the observed velocities were fairly high, up to 250 m s^{-1}. The observations nevertheless were still away from the electrojet direction since 2–3 times larger velocities along L shells were observed by the DMSP satellites.

One can relate the deviation of the observed variation of Doppler velocity with the L-shell angle from the cosine law to the rotation of the flow from the L-shell direction. For example, we can achieve a better match in Figure 7.4 if we take into account the fact that the flow was not exactly L-shell aligned but rather curved, as discussed above. However, significant improvement would be achieved only if the flow angle is changed strongly, say from current 60° to flow angle of 30°, which is very unlikely, given the observed velocity distribution within the radar near FOV, IZMEM prediction and SuperDARN estimates of the convection pattern for this event.

7.3.3 Velocity Versus Scale

Data presented in Section 6.3 showed that the flow angle variation is slightly different at various radar frequencies for smaller flow angles; the effect is more significant at higher radar frequencies. None of the previous HF experimental studies reported this feature and none of the theoretical papers predicted the effect. We attempt here to explore conclusions of one of the theories proposed for irregularity formation and compare it with our experimental data. Namely, we consider the theory by *Hamza and St.-Maurice* [1993a,b].

To compare the predictions of this theory with our measurements, we computed the expected irregularity phase velocity versus flow angle in a manner similar to

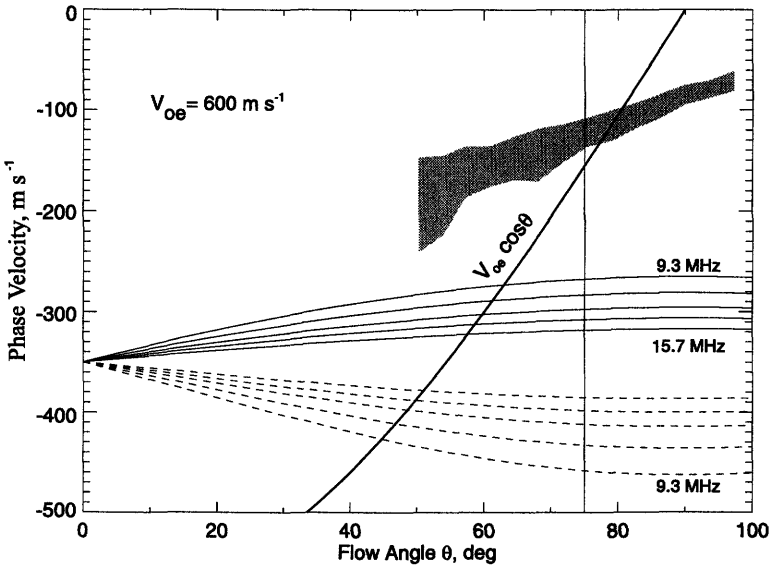

Figure 7.4: Theoretical curves of phase velocity versus flow angle at five radar frequencies. Typical E-region collision frequencies and density gradient scale of 10 km oriented parallel/antiparallel to the flow direction were assumed. Solid (dashed) line represents solution with phase velocity smaller (larger) than the ion acoustic speed. Shaded area indicates the span of measured velocities; data were taken from Figure 6.10. Vertical line indicates the line for which flow angle is equal to 75° (see Figure 7.5). Thick solid curve denotes "cosine" variation with electron drift velocity of 600 m s^{-1}.

calculations by *Milan at Lester* [2001] for a number of radar frequencies between 9.3 and 15.7 MHz.

Dividing (2.86) by k^2 one obtains the quadratic equation for the phase velocity $V_{ph} = \overline{\omega}_{\mathbf{k}}/k$:

$$V_{ph}^2 + \tau(\mathbf{k}) V_{ph} - C_s^2 + \Delta\omega_{\mathbf{k}}^2/k^2 = 0. \tag{7.1}$$

The coefficient

$$\tau(\mathbf{k}) = \frac{\nu_i |\Omega_e|}{\nu_e} \frac{\mathbf{k}\cdot\mathbf{K}}{k^3}$$

is a function of the wave number $\mathbf{k}$ and, therefore, the solutions of (7.1) are scale-dependent.

Figure 7.4 shows the result of calculations. Both possible solutions of the quadratic equation (7.1) for the plasma wave velocity were considered, and velocities were assumed negative for the convenience of comparison with the data. We assumed typical E-region collision frequencies (Section 2.1.5), both parallel and antiparallel to the flow background gradients of 10-km scale, an ion acoustic speed of 350 m s^{-1}, and zero spectral broadening ($\Delta\omega_{\mathbf{k}} = 0$).

Even though we present solutions for all flow angles, the theory is valid only within the linear instability cone, at angles $\theta <\sim 75°$ (vertical line) for electric field of ~ 60 mV m^{-1}. Both solutions show a change of expected velocity with flow angle within the linear instability cone, as noticed earlier by *Milan and Lester* [2001]. We also plotted in this diagram the cosine variation curve that is expected to be appropriate outside the linear instability cone, at flow angles more than 75°. Here we again used the electron drift magnitude of 600 m s^{-1}. To assess how well the data match theoretical predictions, we show in the top part of Figure 7.4 the range of velocities observed in our measurements, assuming that the L-shell angle equals the flow angle.

One can see that both theoretical solutions do not match the data very well. One can shift the theoretical curve up or down by assuming larger ion acoustic speed and some spectral broadening ($\Delta\omega_{\mathbf{k}} \neq 0$) as stipulated by the theory. In this way, one can match the absolute values of predicted and measured velocities. Matching the trend in the velocity variation with the flow angle is more problematic. The low-velocity theoretical solution (solid lines) appears to fit better to the measurements. In addition, this solution is preferable since for it, the magnitude of 9.3 MHz velocity is smaller than the magnitude of 15.7 MHz velocity, in agreement with measurements. The high-velocity solution (dashed lines), however, predicts the opposite velocity ratio to that observed.

The observed differences between HF velocities for various frequencies at small flow angles (the smallest L-shell angles calculated were 45° at leftmost part of the

shaded area) matches with the theory of *Hamza and St.-Maurice* [1993a,b], Figure 7.4. One can clearly see that, at smallest flow angles, the velocity differences at various radar frequencies (velocity spread) were of the order of 70–100 m s^{-1} in agreement with theoretical expectations. One should note that the statement is only partially correct because the data show a decreased spread with flow angle θ increase while the theory predicts an increase in the velocity spread with θ. On the other hand, this change in the amount of velocity spread may be associated with the fact that larger flow angles were outside the F-B instability cone.

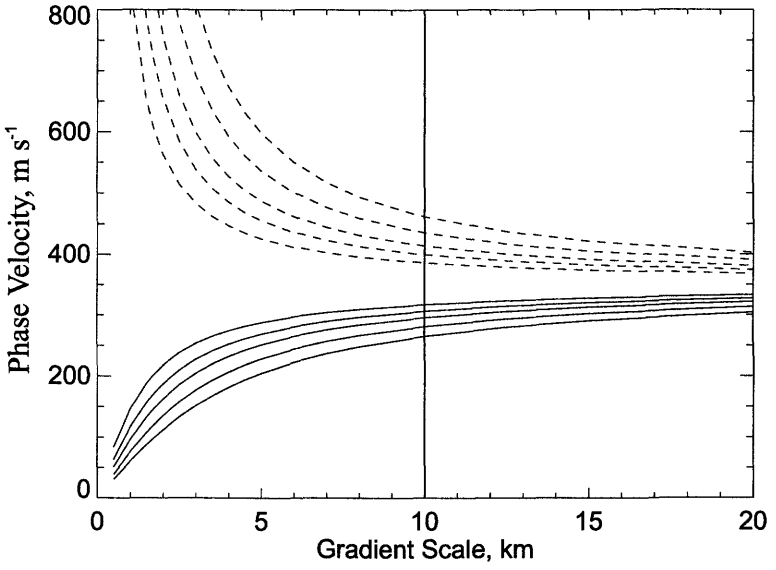

Figure 7.5: Theoretical predictions for the irregularity phase velocity as a function of density gradient for the flow angle of 75°. Solid (dashed) line shows solutions with phase velocity smaller (larger) than C_s.

One also should note that the conclusions of *Hamza and St.-Maurice*'s [1993a,b] theory are dependent on the size of background gradient chosen. In Figure 7.5 we presented theoretical predictions for the velocity of waves at various values of the plasma gradient. The flow angle was assumed to be 75°, which corresponds to the

size of the F-B instability cone for an electric field of 60 mV m^{-1}. The conclusion from this diagram is that one might expect stronger velocity spread for shorter plasma gradients, and it seems that scales of $\sim$ 10 km match the present observations the best.

Chapter 8

Conclusions and Suggestions for Future Research

8.1 Conclusions

In this thesis several aspects of the electrojet irregularity formation at high latitudes have been studied.

First of all, a review of existing theories of irregularity excitation has been given. We concentrated on the F-B and G-D plasma instabilities as the major mechanisms of irregularity formation at high latitudes. The main characteristics of unstable (in the linear regime) waves were described and various nonlinear effects leading to the saturation of such waves were reviewed. The analysis was focused on the phase velocity of electrojet irregularities. We showed that the expected irregularity velocity depends strongly on the nonlinear effect under consideration.

Analysis of various nonlinear theories showed that the mode coupling is an important process for the F-B and G-D instability evolution and that it should be taken into account if one wants to make a prediction on the properties of electrojet irregularities for all flow and aspect angles. It was noted that in spite of significant progress in the development of the theory of mode coupling, there is no definite answer with respect to the velocity. In the most advanced theory by *Hamza and St.-Maurice* [1993a,b] an expression for the irregularity phase velocity was proposed but the theory is two-dimensional while observations are always three-dimensional, which raises a question on the applicability of derived formulas to observations.

We also demonstrated that, in the past, a general assumption was that the nonlinear interaction between F-B modes (or between G-D modes) leads to the effective energy transfer from the unstable meter irregularities to the irregularities of shorter scales, the direct energy transfer. We argued that though these processes are very likely to occur, one might expect the opposite direction of the energy flow in a system of modes. Theory of such processes has been offered. It was shown that turbulent background of the F-B modes is unstable with respect to long-wavelength perturbations propagating along the flow. These perturbations can grow and absorb energy from the background turbulent fluctuations. Thus, in the combined system of primary, short-wavelength fluctuations and secondary, long-wavelength modes, the energy can be delivered from small to large structures meaning the inverse energy cascade. It was demonstrated that the properties of secondary, long-wavelength waves are significantly affected by the short-wavelength perturbations. In the absence of dispersion, the secondary waves are expected to propagate with the velocity predicted by the linear theory, contrary to the notion that all waves propagate along the flow with the ion acoustic speed C_s. It is assumed that the secondary waves constitute the long-wavelength part of the spectrum of electrostatic fluctuations regularly measured by

rockets, and it is anticipated that large-scale waves should be detectable by other techniques. No such observations are presently known for high latitudes. It is expected that such a scenario of the F-B instability evolution can explain the excitation of the decameter irregularities for the near threshold electric fields when such perturbations are linearly stable.

Experimentally, the phase velocity of irregularities of two significantly different wavelengths (3 and 12 m) was investigated. The thrust was on measurements for which both VHF and HF echoes were recorded nearly simultaneously. Several dependencies were studied. It was demonstrated that the HF echoes can clearly be divided into two populations, the high- and low-velocity echoes, while no separate populations of VHF echoes were evident. No other types or classes of HF and VHF echoes have been identified within the considered, relatively large data set. We have related the high-velocity HF and VHF echoes to the F-B and G-D plasma instabilities. We found that the phase velocity at both HF and VHF does not saturate at the ion acoustic speed; observed velocities were as large as 750 m s^{-1} and they were changing with the flow and aspect angles. The low-velocity HF echoes were associated with the F-B and G-D waves affected significantly by other sources. We argued that neutral wind and nonisothermality of plasma fluctuations in the lower E region can change the properties of ionospheric irregularities at these heights. We also noted a possibility of neutral turbulence effects.

The other conclusion from the HF/VHF experiment was that, in agreement with expectations, refraction significantly affects HF signals. Besides the well known effect of HF echo power maxima to be located closer to the radar site than the VHF echo power maxima, we showed that the HF power did not exhibit the monotonic increase with velocity that is seen at VHF. We argued that the observed power-velocity saturation at HF was due to the HF radio wave focusing onto the parts of the electrojet layer that are higher than the typical heights of VHF scatter. We also used this

hypothesis to explain the fact that 12-MHz velocities were, on average, larger than those at 50 MHz.

In the second experiment, multifrequency HF measurements at Prince George, the most important result was that measured Doppler velocity depends on irregularity wavelength but only for directions within the F-B instability cone. For observations inside the instability cone, maximum velocities measured at 15.7 MHz were about 30% larger than those at 9.3 MHz, which is stronger than the rate of the velocity increase with the radar frequency reported in the literature. Inside the cone, the velocity magnitude strongly decreased with aspect angle and the rate of the decrease was scale sensitive (greater at higher frequencies).

For observations outside the F-B instability cone, the Doppler velocity did not show significant variation with aspect angle. This result supports the notion that the ion motion contribution to the Doppler velocity of HF echoes can be quite significant for observations at large flow angles. Also it has been demonstrated that for the directions outside the cone, velocity change with the flow angle was insignificant and almost the same at all radar frequencies. The variation was not consistent with the expected cosine law. The theory by *Hamza and St.-Maurice* [1993a,b] of the F-B instability excitation in the presence of strong gradients was compared with the data and the expected spread in Doppler velocities was found to be in a reasonable agreement with the measurements. On the other hand, the theoretically expected flow angle variation was not easy to match with measurements.

8.2 Suggestions for Future Research

In the theoretical part of the thesis we considered the two-dimensional nonlinear theory of short- and long-wavelength wave interaction in the plane perpendicular to

the Earth's magnetic field. Experimentally, the plasma waves are usually observed in a range of off-orthogonality angles. In this sense, it is desirable to extend the proposed theory to 3-D case. One expectation is that the phase velocity of irregularities would be different from the phase velocity in the 2-D case since waves will be dispersive in 3-D case.

The other possibility is to incorporate gradients into the theory of scale-separation. The sharp gradients well might be present in the high-latitude E region. The previous theoretical attempts to include the effects of the strong gradients were quite successful [e.g., *Hamza and St.-Maurice*, 1993b]; it was shown that gradients can significantly change the properties of the E-region irregularities.

A self-consistent theory of short- and long-wavelength waves interacting with each other could be the next step in the theory development, though one can only wonder how difficult the theory would become to describe these processes quantitatively.

Experimentally, there are possibilities to expand this thesis work in several ways. First of all, one can do more thorough work with the data used for this study.

One of the questions is on the degree of meteor contamination in the Syowa radar data. One can attempt to evaluate how many of the low-velocity 12-MHz echoes are actually echoes associated with the meteor trails. To accomplish this, one can look at individual events in terms of spatial/temporal stability of echoes and coverage, and in terms of spectra (whether they are single- or multi-peaked). Of special interest would be running Syowa radars in new radar mode installed in October 2001 at the Syowa SuperDARN radars. This mode allows one to detect more efficiently the meteor echoes and use information about them to infer neutral wind velocities and decay time constants [*Yukimatu and Tsutsumi*, A new SuperDARN raw time series analysis method and its application to mesopause region dynamics, submitted to *Geophys. Res. Let.*, 2002]. Though we are confident that the echoes considered in this thesis were predominantly E-region scatter, the conclusion needs to be substantiated in a

more rigorous fashion.

To expand conclusions of this thesis one can look at the data of the newly installed SuperDARN HF radars in the northern hemisphere, the Kodiak and King Salmon radars. These two radars have FOVs sitting side-by-side, similar to the Syowa East and South radars, so that their combined azimuthal coverage is also very good (see Figure 1.6a). The geometric aspect conditions are not so favorable here, and it would be interesting to see whether the results of this thesis still hold for this new geometry.

Of special interest would be data of a forthcoming experiment at Syowa where a new VHF radar at 112 MHz is currently under construction [*Igarashi et al.*, 2001]. This radar will look along the Syowa East beams 13–15, and this arrangement is extremely convenient for comparison of velocities of HF and VHF echoes. This comparison could give more information on the irregularity phase velocity under the condition when the F-B instability is operational.

For further expansion of obtained in this thesis results the HF/VHF data with simultaneous measurements of other ionospheric parameters are needed. The fact is that electric field, collision frequencies, electron density, and ion acoustic speed are seldom known while the irregularity phase velocity is expected to depend on them. In this thesis, when considering the phase velocity variation with the flow angle we used a proxy for the flow angle, the L-shell angle, relying on various electric field estimates and models. It would be important to study the flow angle dependence of the Doppler velocity at two or more radar frequencies with simultaneous measurements of the ionospheric electric field. One can perform such an experiment by building new VHF and HF coherent radars and positioning them within the FOV of one of the SuperDARN pairs. Such arrangement is preferable in the European sector where the geometric aspect angles are convenient for VHF measurements.

One can also attempt to look at the data of presently available measurements. The Finland Co-ordinated UK Twin-Located Auroral Sounding System (CUTLASS)

HF radar, the Scandinavian Twin Auroral Radar Experiment (STARE) Finland radar (144 MHz) and the EISCAT radar potentially can have simultaneous data over the EISCAT spot near Tromso. The work is this direction is currently in progress [*Danskin et al.*, 2002; *Koustov et al.*, 2002; *Uspensky et al.*, 2002]. The results presented in this thesis indicate that it would be very interesting to incorporate the neutral wind data from either MF or EISCAT radar to verify the hypothesis on the ion drift and neutral wind contributions to the irregularity phase velocity. The neutral wind effects are expected to be more pronounced for the observations at large flow angles, therefore, the CUTLASS and STARE Finland coherent radars looking approximately perpendicular to the flow, should be very convenient for this kind of study. The STARE radar has some advantage over the CUTLASS HF radar since it regularly detects echoes over the EISCAT spot, while CUTLASS Finland E-region echoes are typically located about 300 km equatorward of this spot. The proposed multi-radar comparison would be focused on measurements at one point. To infer flow angle variation for the velocity one would need a significant data base to average over observations at various flow angle and flow intensity conditions. This is not an entirely unrealistic venue.

The above proposals, in no way, cover all other possibilities. It is our belief that, with so many coherent radars currently operational and under construction, fundamentally new results will be obtained in near future, and we are looking forward to seeing the unravelling of our knowledge of the small-scale processes in the high-latitude ionosphere.

References

André, D., G. J. Sofko, and A. V. Koustov, Aspect angle dependence of HF-backscatter from the E region, paper presented at International SuperDARN Workshop, Inst. di Fis. dello Spazio Interplanet., Venice, Italy, 21–25 May 2001.

Baker, K. B., and S. Wing, A new magnetic coordinate system for conjugate studies at high latitudes, *J. Geophys. Res., 94*, 9139–9143, 1989.

Balk, A. M., S. V. Nazarenko, and V. E. Zakharov, Nonlocal turbulence of drift waves, *Sov. Phys. JETP, Engl. Transl., 71*(2), 249–260, 1990.

Balsley, B. B., and D. T. Farley, Radar studies of the equatorial electrojet at three frequencies, *J. Geophys. Res., 76*, 8341–8351, 1971.

Bilitza, D., International Reference Ionosphere - Status 1995/96, *Adv. Space Res., 20*(9), 1751–1754, 1997.

Bourdillion, A., C. Haldoupis, and J. Delloue, High-Frequency Doppler radar observations of magnetic aspect sensitive irregularities in the midlatitude E-region ionosphere, *J. Geophys. Res., 100*, 21,503–21,521, 1995.

Buneman, O., Excitation of field-aligned sound waves by electron streams, *Phys. Rev. Lett., 10*, 285–287, 1963.

Cho, J. Y. N., and J. Rottger, An updated review of polar mesospheric summer echoes: observations, theory, and subvisible aerosols, *J. Geophys. Res., 102*, 2001–2020, 1997.

Clauer, C. R., and Y. Kamide, DP 1 and DP 2 current systems for the March 22, 1979 substorms, *J. Geophys. Res., 90*, 1343–1354, 1985.

Crochet, M., Radar studies of longitudinal differences in the equatorial elecrojet: A review, *J. Atmos. Terr. Phys., 39*, 1103–1117, 1977.

Danskin, D. W., A. V. Koustov, T. Ogawa, N. Nishitani, S. Nozawa, S. E. Milan, M. Lester, and D. Andre, On the factors controlling occurrence of F-region coherent echoes, *Ann. Geophys., 20*, 1385–1397, 2002.

del Pozo, C. F., J. C. Foster, and J.-P. St.-Maurice, Dual-mode E region plasma wave observations from Millstone Hill, *J. Geophys. Res., 98*, 6013–6032, 1993.

Dimant, Ya. S., and R. N. Sudan, Kinetic theory of low-frequency cross-field instability in a weakly ionized plasma. 1, *Phys. Plasma, 2*, 1157–1168, 1995a.

Dimant, Ya. S., and R. N. Sudan, Kinetic theory of low-frequency cross-field instability in a weakly ionized plasma. 2, *Phys. Plasma, 2*, 1169–1181, 1995b.

Dimant, Ya. S., and R. N. Sudan, Kinetic theory of Farley-Buneman instability in the E-region of the ionosphere, *J. Geophys. Res., 100*, 14,605–14,623, 1995c.

Dimant, Ya. S., and R. N. Sudan, Physical nature of a new cross-field current-driven instability in the lower ionosphere, *J. Geophys. Res., 102*, 2551–2563, 1997.

Drexler, J., J.-P. St.-Maurice, D. Chen, and D. R. Moorcroft, New insights from a nonlocal generalization of the Farley-Buneman instability problem at high latitudes, *Ann. Geophys., 20*, 2003–2025, 2002.

Dubois, J. R., Propagation and coupling of plasma waves in the E region, M.Sc. thesis, Univ. of Western Ontario, London, Ontario, Canada, 1989.

Ecklund, W. L., B. B. Balsley, and D. A. Carter, A preliminary comparison of F region plasma drifts and E region irregularity drifts in the auroral zone, *J. Geophys. Res., 82*, 195–197, 1977.

Eglitis, P., T. R. Robinson, I. W. McCrea, K. Schlegel, T. Nygren, and A. S. Roger, Doppler spectrum statistics obtained from three different-frequency radar auroral experiments, *Ann. Geophys., 13*, 56–65, 1995.

Farley, D. T., A plasma instability resulting in field-aligned irregularities in the ionosphere, *J. Geophys. Res., 68*, 6083–6093, 1963.

Farley, D. T., Theory of equatorial electrojet plasma waves: new developments and current status, *J. Atmos. Terr. Phys., 47*, 729–744, 1985.

Farley, D. T., and B. G. Fejer, The effect of the gradient drift term in type 1 electrojet irregularities, *J. Geophys. Res., 80*, 3087–3090, 1975.

Farley, D. T., and J. Providakes, The variation with Te and Ti of the velocity of unstable ionospheric two-stream waves, *J. Geophys. Res., 94*, 15,415–15,420, 1989.

Farley, D. T., W. E. Swartz, D. L. Hysell, and C. Ronchi, High-resolution radar observations of daytime kilometer-scale wave structure in the equatorial electrojet, *J. Geophys. Res., 99*, 299–307, 1994.

Fejer, B. G., and M. C. Kelley, Ionospheric irregularities, *Rev. Geophys., 18*, 401–454, 1980.

Fejer, B. G., D. T. Farley, B. B. Balsley, and R. F. Woodman, Vertical structure of the VHF backscattering region in the equatorial electrojet and the gradient-drift instability, *J. Geophys. Res., 80*, 1313–1324, 1975.

Fejer, B. G., R. W. Reed, D. T. Farley, W. E. Swartz, and M. C. Kelley, Ion cyclotron waves as a possible source of resonant auroral radar echoes, *J. Geophys. Res., 89*, 187–194, 1984a.

Fejer, B. G., J. F. Providakes, and D. T. Farley, Theory of plasma waves in the auroral E-region, *J. Geophys. Res., 89,* 7487–7494, 1984b.

Ferch, R. L., and R. N. Sudan, Numerical simulation of type II gradient drift irregularities in the equatorial electrojet, *J. Geophys. Res., 82*, 2283–2289, 1977.

Foster, J. C., D. Tetenbaum, C. F. del Pozo, J.-P. St-Maurice, and D. R. Moorcroft, Aspect angle variations in intensity, phase velocity and altitude for high-latitude 34 cm E region irregularities, *J. Geophys. Res., 97*, 8601–8617, 1992.

Fried, B. D., and S. D. Conte, *The Plasma Dispersion Function*, Academic Press, San Diego, 1961.

Fukumoto, M., N. Nishitani, T. Ogawa, N. Sato, H. Yamagishi and A.S. Yukimatu, Statistical analysis of echo power, Doppler velocity and spectral width obtained with the Syowa South HF radar, *Adv. Polar Upper Atmos. Res., 13*, 37–47, 1999.

Fukumoto, M., N. Nishitani, T. Ogawa, N. Sato, H. Yamagishi, and A. S. Yukimatu, Statistical study of Doppler velocity and echo power around 75 deg magnetic latitude using data obtained with the Syowa East HF radar in 1997, *Adv. Polar Upper Atmos. Res., 14*, 93–102, 2000.

Greenwald, R. A., et al., DARN/SuperDARN: A global view of the dynamics of high-latitude convection, *Space Sci. Rev., 71*, 763–796, 1995.

Gurevich, A. V., and A. N. Karashtin, Small-scale thermal diffusion instability in the lower ionosphere, *Geom. Aeron., 24*, 733–738, 1984.

Gurevitch, A. V., N. D. Borisov, and K. P. Zybin, Ionospheric turbulence induced in the lower part of the E region by the turbulence of the neutral atmosphere, *J. Geophys. Res., 102*, 379–388, 1997.

Haldoupis, C., A review on radio studies of auroral *E* region ionospheric irregularities, *Ann. Geophys., 7*, 239–258, 1989.

Haldoupis, C., and K. Schlegel, Direct comparison of 1-m irregularity phase velocity and ion-acoustic speeds in the auroral *E* region ionosphere, *J. Geophys. Res., 95*, 18,989–19,000, 1990.

Haldoupis, C. I., P. Prikryl, G. J. Sofko, and J. A. Koehler, Evidence for 50 MHz bistatic radio observations of electrostatic ion cyclotron waves in the auroral plasma, *J. Geophys. Res., 90*, 10,983–10,990, 1985.

Haldoupis, C., G. J. Sofko, J. A. Koehler, P. Prikryl, and A. G. McNamara, High resolution Doppler spectrum measurements of 3-meter auroral irregularities at large magnetic aspect angles, *Phys. Scripta, 35*, 910–916, 1987.

Haldoupis, C., E. Nielsen, and K. Schlegel, Dependence of radar auroral scattering cross section on the ambient electron density and the destabilizing electric field, *Ann. Geophys., 8*, 195–212, 1990.

Haldoupis, C., K. Schlegel, and E. Nielsen, On type 3 auroral VHF coherent radar backscatter, *J. Geophys. Res., 97*, 4109–4120, 1992.

Haldoupis, C., G. J. Sofko, G. C. Hussey, and J. Mu, An overview of type-3 radar auroral research: basic observational properties and new interpretation propositions, *Ann. Geophys., 13*, 10–24, 1995.

Haldoupis, C., A. Bourdillon, M. Six, and J. Delloue, Midlatitude *E* region coherent backscatter observed simultaneously at two HF radar frequencies, *J. Geophys. Res., 101*, 7961–7971, 1996.

Haldoupis, C., A. Bourdillon, J. Delloue, and G. Hussey, Wavelength dependence of Doppler spectrum broadening in midlatitude *E* region coherent backscatter, *J. Geophys. Res., 103*, 11,605–11,615, 1998.

Haldoupis, C., K. Schlegel, G. C. Hussey, and J. A. Koehler, Observations of kinetic effects at meter scales for Farley-Buneman plasma waves, *J. Geophys. Res., 107*(A10), 1272, doi:10.1029/2001JA009193, 2002.

Hall, G. E., and D. R. Moorcroft, Doppler spectra of the UHF diffuse radio aurora, *J. Geophys. Res., 93*, 7425–7440, 1988.

Hall, G., and D. R. Moorcroft, Magnetic aspect angle effects in radar aurora at 48.5 MHz, corrected for refraction, *J. Geophys. Res., 97*, 19,471–19,488, 1992.

Hall, G. E., J. W. MacDougall, D. R. Moorcroft, J.-P. St.-Maurice, A. H. Manson, and C. E. Meek, Super Dual Auroral Radar Network observations of meteor echoes, *J. Geophys. Res., 102*, 14,603–14,614, 1997.

Hamza, A. M., and J.-P. St.-Maurice, A turbulent theoretical framework for the study of current-driven *E* region irregularities at high latitudes: Basic derivation and application to gradient-free situations, *J. Geophys. Res., 98*, 11,587–11,599, 1993a.

Hamza, A. M., and J.-P. St.-Maurice, A self-consistent fully turbulent theory of auroral *E* region irregularities, *J. Geophys. Res., 98*, 11,601–11,613, 1993b.

Hamza, A., and J.-P. St-Maurice, Large aspect angles in auroral E region echoes: A self-consistent turbulent fluid theory, *J. Geophys. Res., 100*, 5723–5732, 1995a.

Hamza, A., and J.-P. St-Maurice, A fully self-consistent fluid theory of anomalous transport in Farley-Buneman turbulence, *J. Geophys. Res., 100*, 9653–9668, 1995b.

Hanuise, C., and M. Crochet, Multifrequency HF radar studies of plasma instabilities in Africa, *J. Atmos. Terr. Phys., 39*, 1097–1101, 1977.

Hanuise, C., J.-P. Villain, J. C. Cerisier, C. Senior, J. M. Ruohoniemi, R. A. Greenwald, and K. B. Baker, Statistical study of high-latitude *E* region Doppler spectra obtained with SHERPA HF radar, *Ann. Geophys., 9*, 273–285, 1991.

Hanuise, C., J. P. Villain, D. Gresillon, B. Cabrit, R. A. Greenwald, and K. B. Baker, Interpretation of HF radar ionospheric Doppler spectra by collective wave scattering theory, *Ann. Geophys., 11*, 29–39, 1993.

Hargreaves, J. K., *The solar-terrestrial environment*, Cambridge Univ. Press, Cambridge, 1992.

Hoh, F. C., Instability of Penning-type discharge, *Phys. Fluids, 6*, 1184–1191, 1963.

Huber, M., HF radar echo statistics and spectral studies using SuperDARN, M.Sc. thesis, Univ. of Saskatchewan, Saskatoon, Saskatchewan, Canada, 1999.

Hunsucker, R. D., *Radio Techniques for Probing the Terrestrial Ionosphere*, Springer-Verlag, Berlin, 1991.

Hussey, G. C., J. Delloue, C. Haldoupis, and A. Bourdillon, E region mid-latitude decameter irregularities observed at four radar frequencies. Experiment and first results, *Ann. Geophys., 15*, 918–924, 1997.

Hussey, G. C., C. E. Meek, D. Andre, A. H. Manson, and G. J. Sofko, A comparison of Northern Hemisphere winds using SuperDARN meteor trail and MF radar wind measurements, *J. Geophys. Res. 105*, 18,053–18,066, 2000.

Igarashi, K., K. Ohtaka, M. Kunitake, T. Tanaka, and T. Ogawa, Development of scanning-beam VHF auroral radar system, *Proc. NIPR Symp. Upper Atmos. Phys., 8*, 65–69, 1995.

Igarashi, K., K. Ohtaka, M. Kunitake, and T. Kikuchi, Scanning-beam VHF auroral radar at Syowa station, *Proc. NIPR Symp. Upper Atmos. Phys., 11*, 154–158, 1998.

Igarashi, K., K. Ohtaka, T. Obara, and K. Nozaki, Development of 112 MHz VHF auroral radar at Syowa station, Antarctica, The 25th Symposium on Coordinated Observations of the Ionosphere and Magnetosphere in the Polar Regions, Programs and Abstracts, NIPR, Tokyo, Japan, 30–31 July 2001.

Janhunen, P., Three-dimensional stabilisation mechanism for the auroral Farley-Buneman instability, *J. Atmos. Terr. Phys., 54*, 1633–1643, 1992.

Janhunen, P., Perpendicular particle simulation of the E-region Farley-Buneman instability, *J. Geophys. Res., 99*, 11,461–11,473, 1994.

Janhunen, P., On recent development in E-region irregularity simulations and a summary of related theory, *Ann. Geophys., 13*, 791–806, 1995.

Jayachandran, P. T., J.-P. St.-Maurice, J. W. MacDougall, and D. R. Moorcroft, HF detection of slow long-lived E region plasma structures, *J. Geophys. Res., 105*, 2425–2442, 2000.

Kadomtsev, B. B., *Plasma Turbulence*, Plenum, New York, 1965.

Kagan, L. M., and M. C. Kelley, A wind-driven gradient drift mechanism for mid-latitude E-region ionospheric irregularities, *Geophys. Res. Lett., 25*, 4141–4144, 1998.

Kagan, L. M., and M. C. Kelley, A thermal mechanism for generation of small-scale irregularities in the ionospheric E region, *J. Geophys. Res., 105*, 5291–5303, 2000.

Kamenetskaya, G. Kh., Quasi-linear theory of the formation of inhomogeneities in the equatorial electrojet, *Geom. Aeron., 11*, 71–75, 1971.

Kaw, P. K., Wave propagation effects on observations of irregularities, *J. Geophys. Res., 77*, 1323–1326, 1972.

Kelley, M. C., *The Earth's Ionosphere*, The Academic Press, San Diego, 1989.

Keskinen, M. J., Nonlinear stabilization of the Farley-Buneman instability by strong $\mathbf{E} \times \mathbf{B}$ turbulence in a plasma, *Phys. Rev. Lett., 47*, 344–348, 1981.

Keskinen, M. J., R. N. Sudan, and R. L. Ferch, Temporal and spatial power spectrum studies of numerical simulations of type 2 gradient drift irregularities in the equatorial electrojet, *J. Geophys. Res., 84*, 1419–1430, 1979.

Koehler, J. A., C. Haldoupis, K. Schlegel and V. Virvilis, Simultaneous observations of E region coherent radar echoes at 2-m and 6-m radio wavelengths at midlatitude, *J. Geophys. Res., 102*, 17,255–17,266, 1997.

Kofman, W., and E. Nielsen, STARE and EISCAT measurements: Evidence for the limitation of STARE Doppler velocity observations by the ion acoustic velocity, *J. Geophys. Res., 95*, 19,131–19,136, 1990.

Koustov, A. V., K. Igarashi, D. Andrè, K. Ohtaka, N. Sato, H. Yamagishi, and A. S. Yukimatu, Observations of 50- and 12-MHz auroral coherent echoes at the Antarctic Syowa station, *J. Geophys. Res., 106*, 12,875–12,887, 2001.

Koustov, A. V., D. W. Danskin, M. V. Uspensky, T. Ogawa, P. Janhunen, N. Nishitani, S. Nozawa, M. Lester, and S. Milan, Velocities of auroral coherent echoes at 12 and 144 MHz, *Ann. Geophys., 20*, 1647–1662, 2002.

Kraichnan, R. H., The structure of isotropic turbulence at very high Reynolds numbers, *J. Fluid Mech., 5*, 497–543, 1959.

Kustov, A. V., M. V. Uspensky, G. J. Sofko, J. A. Koehler, and J. Mu, Aspect angle dependence of the radar aurora Doppler velocity, *J. Geophys. Res., 99*, 2131–2144, 1994.

Lee, K., and C. F. Kennel, Effects of propagation parallel to the magnetic field on the type I electrojet irregularity instability, *Planet. Space Sci., 21*, 1339–1343, 1973.

Lee, K., C. F. Kennel, and J. M. Kindel, High-frequency Hall current instability, *Radio Sci., 6*, 209–213, 1971.

Machida, S., and C. K. Goertz, Computer simulation of the Farley-Buneman instability and anomalous heating in the auroral ionosphere, *J. Geophys. Res., 93*, 9993–10000, 1988.

Makarevitch, R. A., T. Ogawa, K. Igarashi, A. V. Koustov, N. Sato, K. Ohtaka, H. Yamagishi, and A. S. Yukimatu, On the power-velocity relationship for 12- and 50-MHz auroral coherent echoes, *J. Geophys. Res., 106*, 15,455–15,469, 2001.

Makarevitch, R. A., A. V. Koustov, G. J. Sofko, D. Andre, and T. Ogawa, Multifrequency measurements of HF Doppler velocity in the auroral E region, *J. Geophys. Res., 107*(8), 10.1029/2001JA000268, 2002a.

Makarevitch, R. A., A. V. Koustov, K. Igarashi, N. Sato, T. Ogawa, K. Ohtaka, H. Yamagishi, and A. S. Yukimatu, Comparison of flow angle variations of E-region echo characteristics at VHF and HF, *Adv. Polar Upper Atmos. Res., 16*, in press, 2002b.

McDonald, B. E., T. P. Coffey, S. L. Ossakow, and R. N. Sudan, Preliminary report of numerical simulation of type II irregularities in the equatorial electrojet, *J. Geophys. Res., 79*, 2551–2554, 1974.

McIlwain, C. E., Coordinates for Mapping the Distribution of Magnetically Trapped Particles, *J. Geophys. Res., 66*, 3681–3691, 1961.

McNamara, A. G., The occurrence of radio aurora at high latitudes: the IGY period, 1957-1959, *Geophysiske Publikasjoner, 29*, 135–149, 1972.

Milan, S. E., and M. Lester, Simultaneous observations at different altitudes of ionospheric backscatter in the eastward electrojet, *Ann. Geophys., 16*, 55–68, 1998.

Milan, S., and M. Lester, Spectral and flow angle characteristics of backscatter from decameter irregularities in the auroral electrojet, *Adv. Space Res., 23*(10), 1773–1776, 1999.

Milan, S. E., and M. Lester, A classification of spectral populations observed in HF radar backscatter from the E region auroral electrojets, *Ann. Geophys., 19*, 189–204, 2001.

Milan, S. E., M. Lester, N. Sato, and H. Takizawa, On the altitude dependence of spectral characteristics of decameter-wavelength E region backscatter and the relationship with optical auroral forms, *Ann. Geophys., 19*, 205–217, 2001.

Milan, S. E., N. Sato, M. Lester, T. K. Yeoman, Y. Murata, H. Doi, and T. Saemundsson, The spectral characteristics of E region radar echoes co-located with and adjacent to visual auroral arcs, *Ann. Geophys., 20*, 795–805, 2002.

Moorcroft, D. R., Propagation of plasma wave energy in the auroral E-region, *J. Geophys. Res., 89*, 2963–2970, 1984.

Moorcroft, D. R., Flow angle effects in E region 398-MHz auroral backscatter at small aspect angle, *J. Geophys. Res., 101*, 13,379–13,386, 1996.

Moorcroft, D. R., Outstanding issues in the theory of radar aurora: Evidence from the frequency dependence of spectral characteristics, *J. Geophys. Res., 107*(10), 10.1029/2001JA009218, 2002.

Moorcroft, D. R., and K. Schlegel, E region coherent backscatter at short wavelength and large aspect angle, *J. Geophys. Res., 93*, 2005–2010, 1988.

Moorcroft, D. R., and R. T. Tsunoda, Rapid scan Doppler velocity maps of the UHF diffuse radar aurora, *J. Geophys. Res., 83*, 1482–1492, 1978.

Nielsen, E., Aspect angle dependence of mean Doppler velocities of 1-m auroral plasma waves, *J. Geophys. Res., 91*, 10,173–10,177, 1986.

Nielsen, E., and K. Schlegel, A first comparison of STARE and EISCAT electron drift velocity measurements, *J. Geophys. Res., 88*, 5745–5750, 1983.

Nielsen, E., J. D. Whitehead, L. A. Hedberg, and T. B. Jones, A test of the cosine relationship using three-radar velocity measurements, *Radio Sci., 18*, 230–236, 1983.

Nielsen, E., C. Haldoupis, B. G. Fejer, and H. M. Ierkic, Dependence of auroral power spectra variations upon electron drift velocity in the eastward electrojet, *J. Geophys. Res., 89*, 253–260, 1984.

Nielsen, E., C. F. del Pozo, and P. J. S. Williams, VHF coherent radar signals from the E region ionosphere and the relationship to electron drift velocity and ion acoustic velocity, *J. Geophys. Res., 107*(1), 10.1029/2001JA900111, 2002.

Ogawa, T., Radar observations of ionospheric irregularities at Syowa station, Antarctica: A brief overview, *Ann. Geophys., 14*, 1454–1461, 1996.

Ogawa, T., B. B. Balsley, W. L. Ecklund, D. A. Carter, and P. E. Johnston, Aspect angle dependence of irregularity phase velocities in the auroral electrojet, *Geophys. Res. Lett., 7*, 1081–1084, 1980.

Ogawa, T., B. B. Balsley, W. L. Ecklund, D. A. Carter, and P. E. Johnston, Auroral radar observations at Siple Station, Antarctica, *J. Atmos. Terr. Phys., 44*, 529–537, 1982.

Ogawa, T., K. Igarashi, Y. Kuratani, R. Fujii, and T. Hirasawa, Some initial results of 50 MHz meteor radar observations at Syowa station, *Mem. Natl. Inst. Polar Res., Spec. Issue, 36*, 254–263, 1985.

Ogawa, T., N. Nishitani, M. Fukumoto, N. Sato, H. Yamagishi, and A. S. Yukimatu, Doppler velocity characteristics derived from the Syowa HF radar, paper presented at National Institute of Polar Research Workshop, NIPR, Tokyo, Japan, 3 August 2000.

Ogawa, T., N. Nishitani, N. Sato, H. Yamagishi, and A. S. Yukimatu, Implications of statistics of near-range Doppler velocity observed with the Syowa East HF radar, *Adv. Polar Upper Atmos. Res., 15*, 82–102, 2001.

Oppenheim, M., N. Otani, and C. Ronchi, Hybrid simulation of the saturated Farley-Buneman instability in the ionosphere, *Geophys. Res. Lett., 22*, 353–356, 1995.

Oppenheim, M., N. Otani, and C. Ronchi, Saturation of the Farley-Buneman instability via nonlinear electron $E \times B$ drifts, *J. Geophys. Res., 101*, 17,273–17,286, 1996.

Orszag, S. A., Analytical theories of turbulence, *J. Fluid Mech., 41*, 363–386, 1970.

Ossakow, S. L., K. Papadopoulos, J. Orens, and T. Coffey, Parallel propagation effects on the type I electrojet instability, *J. Geophys. Res., 80*, 141–148, 1975.

Otani, N. F., and M. Oppenheim, A saturation mechanism for the Farley-Buneman instability, *Geophys. Res. Lett., 25*, 1833–1836, 1998.

Papitashvili, V. O., B. A. Belov, D. S. Faermark, Y. I. Feldstein, S. A. Golyshev, L. I. Gromova, and A. E. Levitin, Electric potential patterns in the northern and southern polar regions parametrized by the interplanetary magnetic field, *J. Geophys. Res., 99*, 13,251–13,262, 1994.

Pfaff, R. F., M. C Kelley, B. G. Fejer, E. Kudeki, C. W. Carlson, A. Pedersen, and B. Hausler, Electric field and plasma density measurements in the auroral electrojet, *J. Geophys. Res., 89*, 236–244, 1984.

Reinleitner, L. A., and E. Nielsen, Self-consistent analysis of electron drift velocity measurements with the STARE/SABRE system, *J. Geophys. Res., 90*, 8477–8486, 1985.

Robinson, T. R., Towards a self-consistent nonlinear theory of radar aurora backscatter, *J. Atmos. Terr. Phys., 48*, 417–422, 1986.

Robinson, T. R., The effects of small scale field aligned irregularities on E-region conductivity: Implications for electron thermal instabilities, *Adv. Space Res., 22*(9), 1357–1360, 1998.

Robinson, T. R., and F. Honary, A resonance broadening kinetic theory of the modified-two-stream instability: Implications for radar auroral backscatter experiments, *J. Geophys. Res., 95*, 1073–1085, 1990.

Rogister, A., Nonlinear theory of 'type I' irregularities in the equatorial electrojet, *J. Geophys. Res., 76*, 7754–7760, 1971.

Rogister, A, and N. D'Angelo, Type 2 irregularities in the equatorial electrojet, *J. Geophys. Res., 75*, 3819–3887, 1970.

Rogister, A., and E. Jamin, Two-dimensional nonlinear processes associated with 'Type I' irregularities in the equatorial electrojet, *J. Geophys. Res., 80*, 1820–1828, 1975.

Ronchi, C., R. N. Sudan, and D. T. Farley, Numerical simulations of large-scale plasma turbulence in the daytime equatorial electrojet, *J. Geophys. Res., 96*, 21,263–21,279, 1991.

Ruohoniemi, J. M., and K. B. Baker, Large-scale imaging of high-latitude convection with Super Dual Auroral Radar Network HF radar observations, *J. Geophys. Res., 103*, 20,797–20,811, 1998.

Sahr, J. D., Observation and theory of the radar aurora, Ph.D. thesis, Cornell Univ., Ithaca, New York, USA, 1990.

Sahr, J. D., and D. T. Farley, Three wave coupling in the auroral E region, *Ann. Geophys., 13*, 38–44, 1995.

Sahr, J., and B. G. Fejer, Auroral electrojet plasma irregularity theory and experiment: A critical review of present understanding and future directions, *J. Geophys. Res., 101*, 26,893–26,909, 1996.

Sahr, J., D. T. Farley, W. E. Swartz, and J. F. Providakes, The altitude of type 3 auroral irregularities: Radar interferometer observations and implications, *J. Geophys. Res., 96*, 17,805–17,811, 1991.

Sato, T., Stabilization of the two-stream instability in the equatorial electrojet, *Phys. Rev. Lett., 28,* 732–734, 1972.

Sato, T., Nonlinear stabilization and nonrandom behaviour of macro-instabilities in plasmas. I. Theory, *Phys. Fluids, 17*, 621–627, 1974.

Sato, T., On mechanisms governing the electrojet plasma instabilities, *J. Geophys. Res., 81*, 539–546, 1976.

Schlegel, K., Interpretation of auroral radar experiments using a kinetic theory of the two-stream instability, *Radio Sci. 18,* 108–118, 1983.

Schlegel, K., Coherent backscatter from ionospheric *E* region plasma irregularities, *J. Atmos. Terr. Phys., 58*, 933–941, 1996.

Schlegel, K., and J.-P. St.-Maurice, Anomalous heating of the polar E region by unstable plasma waves. 1. Observations, *J. Geophys. Res., 86*, 1447–1452, 1981.

Schlegel, K., and J.-P. St.-Maurice, Short wavelength gradient-drift waves at high latitudes, *Ann. Geophys., 1*, 259–264, 1983.

Schlegel, K., and H. Thiemann, Particle-in-cell plasma simulations of the modified two-stream instability, *Ann. Geophys., 12*, 1091–1100, 1994.

Schmidt, M. J., and S. P. Gary, Density gradients and the Farley-Buneman instability, *J. Geophys. Res., 78*, 8261–8265, 1973.

Schunk, R. W., and A. F. Nagy, Electron temperatures in the F region of the ionosphere: Theory and observations, *Rev. Geophys. Space Phys., 16*, 355–399, 1978.

Schunk, R. W., and J. C. G. Walker, Theoretical ion densities in the lower ionosphere, *Planet. Space Sci., 21*, 1875–1896, 1973.

Shalimov, S. L., and C. Haldoupis, An electron thermal diffusion instability and type 3 echoes in the auroral E-region, *Ann. Geophys., 13*, 45–55, 1995.

Sharma, S. K., and P. K. Kaw, Modification of type II irregularities by finite amplitude type I waves in equatorial electrojet, *J. Geophys. Res., 91*, 12,118–12,120, 1986.

Simon, A., Instability of a partially ionized plasma in a crossed electric and magnetic fields, *Phys. Fluids, 6*, 382–388, 1963.

Smolyakov, A. I., and P. H. Diamond, Generalized action invariants for drift wave-zonal flow systems, *Phys. Plasmas, 6*, 4410–4413, 1999.

Smolyakov, A. I., A. V. Koustov, and R. A. Makarevitch, Secondary instabilities in the dynamics of the Farley-Buneman fluctuations, *J. Geophys. Res., 106*, 15,511–15,518, 2001.

St.-Maurice, J.-P., A nonlocal theory of the high latitude Farley-Buneman instability, *J. Geophys. Res., 90*, 5211–5225, 1985.

St.-Maurice, J.-P., A unified theory of anomalous resistivity and Joule heating effects in the presence of ionospheric E region irregularities, *J. Geophys. Res., 92*, 4533–4542, 1987.

St-Maurice, J-P, Wave-induced diffusion in the turbulent E-region, *Physics of Space Plasmas, SPI Conference Proceedings and Reprint Series, 8*, Cambridge, Ma, 323–348, 1988.

St-Maurice, J.-P., Electron heating by plasma waves in the high latitude E-region and related effects: Theory, *Ad. Space Res., 10*(6), 239–249, 1990.

St-Maurice, J.-P., and A. M. Hamza, A new nonlinear approach to the theory of E-region irregularities, *J. Geophys. Res., 106*, 1751–1760, 2001.

St.-Maurice, J.-P., and R. S. Kissack, The role played by thermal feedbacks in heated Farley-Buneman waves at high latitudes, *Ann. Geophys., 18*, 532–546, 2000.

St.-Maurice, J.-P., and R. Laher, Are observed broadband plasma wave amplitudes large enough to explain the enhanced electron temperatures of the high-latitude E-region?, *J. Geophys. Res., 90*, 2843–2850, 1985.

St.-Maurice, J.-P., and K. Schlegel, A theory of coherent radar spectra in the auroral E region, *J. Geophys. Res., 88*, 4087–4095, 1983.

St.-Maurice, J. P., K. Schlegel, and P. M. Banks, Anomalous heating of the polar E region by unstable plasma waves. 2. Theory, *J. Geophys. Res., 86*, 1453–1462, 1981.

St.-Maurice, J.-P., J. C. Foster, J. M. Holt, C. del Pozo, First results on the observations of 440 MHz high-latitude coherent echoes from the E region with the Millstone Hill radar, *J. Geophys. Res., 94*, 6771–6798, 1989.

St.-Maurice, J. P., P. Prikryl, D. W. Danskin, A. M. Hamza, G. J. Sofko, J. A. Koehler, A. V. Kustov, and J. Chen, On the origin of narrow non-ion- acoustic coherent spectra in the high-latitude E region, *J. Geophys. Res., 99*, 6447–6474, 1994.

Stubbe, P., Theory of electrostatic waves in an auroral E region plasma 1. General formulation, *J. Geophys. Res., 94*, 5303–5315, 1989.

Sudan, R. N., Unified theory of type 1 and type 2 irregularities in the equatorial electrojet, *J. Geophys. Res., 88*, 4853–4860, 1983.

Sudan, R. N., and M. J. Keskinen, Theory of strongly turbulent two-dimensional convection of low-pressure plasma, *Phys. Rev. Lett., 38*, 966–970, 1977.

Sudan, R. N., J. Akinrimisi, and D. T. Farley, Generation of small-scale irregularities in the equatorial electrojet, *J. Geophys. Res., 78*, 240–248, 1973.

Sudan, R. N., A. V. Gruzinov, W. Horton, and N. Kukharkin, Convective turbulence in weakly ionized plasma, *Phys. Rep., 283*, 95–119, 1997.

Tsunoda, R. T., High latitude irregularities: A review and synthesis, *Rev. Geophys., 26*, 719–760, 1988.

Unwin, R. S., and P. V. Johnston, Height dependence in the power spectrum of diffuse radar aurora, *J. Geophys. Res., 86*, 5733–5745, 1981.

Uspensky, M. V., A. V. Kustov, G. J. Sofko, J. A. Koehler, J.-P. Villain, C. Hanuise, J. M. Ruohoniemi, and P. J. S. Williams, Ionospheric refraction effects in slant range profiles of auroral HF coherent echoes, *Radio Sci., 29*, 503–517, 1994.

Uspensky, M. V., A. V. Koustov, P. Eglitis, A. Huuskonen, S. E. Milan, T. Pulkkinen, and R. Pirjola, CUTLASS HF radar observations of high-velocity E-region echoes, *Ann. Geophys., 19*, 411–424, 2001.

Uspensky, M., A. Koustov, P. Janhunen, R. Pellinen, D. Danskin, and S. Nozawa, STARE velocities: importance of off-orthogonality and ion motions, *Ann. Geophys.*, accepted, 2002.

Vedenov, A. A., A. V. Gordeev, and L. I. Rudakov, Oscillation and instability of a weakly turbulent plasma, *Plasma Phys., 9*, 719–735, 1967.

Villain, J. P., R. A. Greenwald, K. B. Baker, and J. M Ruohoniemi, HF radar observations of E region plasma irregularities produced by oblique electron streaming, *J. Geophys. Res., 92*, 12,327–12,342, 1987.

Villain, J.-P., C. Hanuise, R. A. Greenwald, K. B. Baker, and J. M. Ruohoniemi, Obliquely propagating ion acoustic waves in the auroral E region: Further evidence of irregularity production by field-aligned electron streaming, *J. Geophys. Res., 95*, 7833–7846, 1990.

Villain, J.-P., R. Andre, C. Hanuise, and D. Gresillon, Observation of the high latitude ionosphere by HF radars: Interpretation in terms of collective wave scattering and characterization of turbulence, *J. Atmos. Terr. Phys., 58*, 943–958, 1996.

Wang, T. N. C., and R. T. Tsunoda, On a crossed field two-stream plasma instability in the auroral plasma, *J. Geophys. Res., 80*, 2172–2182, 1975.

Appendix A

Wave Kinetic Equation

Dynamics of a wave packet in an inhomogeneous plasma is described by the wave kinetic equation for the wave action density [*Kadomtsev*, 1965; *Vedenov et al.*, 1967]. Here we review the derivation of the wave kinetic equation that considers the interaction of small-scale fluctuations with a slow varying mean flow, following *Smolyakov and Diamond* [1999]. We consider a generic equation for fluctuating field $F_{\mathbf{k}}$ in a form

$$\frac{\partial F_{\mathbf{k}}}{\partial t} + i\omega_{\mathbf{k}} F_{\mathbf{k}} + \int d\mathbf{p} M_{\mathbf{p},\mathbf{k}-\mathbf{p}} F_{\mathbf{p}} F_{\mathbf{k}-\mathbf{p}} = 0, \tag{A.1}$$

where $\omega_{\mathbf{k}} = \omega(\mathbf{k})$ is the frequency of the linear mode with a wave vector $\mathbf{k}$ (the frequency may include an imaginary part corresponding to the wave growth or decay). From (3.31) we find the coupling coefficient $M_{\mathbf{p},\mathbf{k}-\mathbf{p}}$

$$\begin{aligned} M_{\mathbf{p},\mathbf{k}-\mathbf{p}} = &-\frac{i}{B(1+\psi)} \mathbf{p} \times (\mathbf{k}-\mathbf{p}) \cdot \mathbf{e}_z \frac{p_y (\mathbf{k}-\mathbf{p})^2}{k^2} \\ &-\frac{i}{B(1+\psi)} (\mathbf{k}-\mathbf{p}) \times \mathbf{p} \cdot \mathbf{e}_z \frac{p^2 (\mathbf{k}-\mathbf{p})_y}{k^2}, \end{aligned} \tag{A.2}$$

where $\mathbf{k}$ and $\mathbf{p}$ are the wave vectors for two different wave modes.

To keep track of the scale separation explicitly, it is convenient to introduce new notations for the large-scale $F_{\mathbf{k}}^{<}$ and small-scale $F_{\mathbf{k}}^{>}$ components; $F_{\mathbf{k}}^{<} = 0$ for $|\mathbf{k}| > k_\epsilon$,

and $F^{>}_{\mathbf{k}} = 0$ for $|\mathbf{k}| < k_\varepsilon$, where $k_\varepsilon = k_0\varepsilon$ defines a boundary of the scale separation, $\varepsilon \ll 1$ is a scale separation parameter, and k_0 is the characteristic wave number; $F^{<}_{\mathbf{k}}$ corresponds to $\overline{F}$ in the real space, $F^{<}_{\mathbf{k}} \to \overline{F}$.

For a near-stationary case of an anisotropic drift-wave-type turbulence the interaction of small scales with a long-wavelength component is dominant [*Balk et al.*, 1990], so the self-interaction of small-scale fields can be neglected. Such interaction is important, however, to establish the stationary spectrum that is formed by balancing the linear growth rate with the nonlinear damping. These effects are described by the right-hand side of (3.32).

Retaining only the dominant interaction term, we write from (A.1) the following equation for the small-scale fluctuations:

$$\frac{\partial F^{>}_{\mathbf{k}}}{\partial t} + i\omega_{\mathbf{k}} F^{>}_{\mathbf{k}} + \int d\mathbf{p} M_{\mathbf{p},\mathbf{k}-\mathbf{p}} F^{<}_{\mathbf{p}} F^{>}_{\mathbf{k}-\mathbf{p}} = 0. \tag{A.3}$$

To derive the equation for the evolution of the wave spectrum, we multiply (A.3) by $F^{>}_{\mathbf{k}'}$ and then add it with a similar equation obtained by reversing $\mathbf{k}$ and $\mathbf{k}'$, yielding

$$\begin{aligned} &\frac{\partial}{\partial t}\left(F^{>}_{\mathbf{k}} F^{>}_{\mathbf{k}'}\right) + i\left(\omega_{\mathbf{k}} + \omega_{\mathbf{k}'}\right)\ F^{>}_{\mathbf{k}} F^{>}_{\mathbf{k}'} + \\ &+F^{>}_{\mathbf{k}'} \int d\mathbf{p}\ M_{\mathbf{p},\mathbf{k}-\mathbf{p}} F^{<}_{\mathbf{p}} F^{>}_{\mathbf{k}-\mathbf{p}} + \ F^{>}_{\mathbf{k}} \int d\mathbf{p} M_{\mathbf{p},\mathbf{k}'-\mathbf{p}} F^{<}_{\mathbf{p}} F^{>}_{\mathbf{k}'-\mathbf{p}} = 0. \end{aligned} \tag{A.4}$$

The small-scale turbulence is described by the spectral function (Wigner function) $I_{\mathbf{k}}(\mathbf{x}, t)$ and is defined as follows:

$$\frac{1}{(2\pi)^2} \int d\mathbf{q} \left\langle F^{>}_{-\mathbf{k}+\mathbf{q}} F^{>}_{\mathbf{k}} \right\rangle e^{i\mathbf{q}\cdot\mathbf{x}} = I_{\mathbf{k}}(\mathbf{x}, t). \tag{A.5}$$

Hereafter the dependence on fast variables is suppressed, and $(\mathbf{x}, t)$ is used for slow variables. The slow time and spatial dependence in $I_{\mathbf{k}}(\mathbf{x}, t)$ corresponds to modulations with a "slow" wave vector $q \ll k$. Angle brackets in (A.5) stand for ensemble average.

The evolution equation for $I_{\mathbf{k}}(\mathbf{x},t)$ is derived from (A.4) by averaging it over fast scales and by taking the Fourier transform over the slow variable $\mathbf{x}$. Setting $\mathbf{k}' = -\mathbf{k}+\mathbf{q}$ and applying the operator $\int d\mathbf{q}\, e^{i\mathbf{q}\cdot\mathbf{x}}$, we obtain

$$\frac{\partial}{\partial t} I_{\mathbf{k}}(\mathbf{x},t) + i\int d\mathbf{q} e^{i\mathbf{q}\cdot\mathbf{x}} \left(\omega_{\mathbf{k}} + \omega_{-\mathbf{k}+\mathbf{q}}\right) \left\langle F^{>}_{\mathbf{k}} F^{>}_{-\mathbf{k}+\mathbf{q}} \right\rangle + S_1 + S_2 = 0, \tag{A.6}$$

$$S_1 = \int\int d\mathbf{p}\, d\mathbf{q}\, e^{i\mathbf{q}\cdot\mathbf{x}} \left\langle F^{>}_{-\mathbf{k}+\mathbf{q}} F^{>}_{\mathbf{k}-\mathbf{p}} \right\rangle M_{\mathbf{p},\mathbf{k}-\mathbf{p}} F^{<}_{\mathbf{p}}, \tag{A.7}$$

$$S_2 = \int\int d\mathbf{p}\, d\mathbf{q}\, e^{i\mathbf{q}\cdot\mathbf{x}} \left\langle F^{>}_{\mathbf{q}-\mathbf{k}-\mathbf{p}} F^{>}_{\mathbf{k}} \right\rangle M_{\mathbf{p},\mathbf{q}-\mathbf{k}-\mathbf{p}} F^{<}_{\mathbf{p}}. \tag{A.8}$$

The second term in (A.6) gives

$$i\int d\mathbf{q}\, e^{i\mathbf{q}\cdot\mathbf{x}} \left(\omega_{\mathbf{k}} + \omega_{-\mathbf{k}+\mathbf{q}}\right) \left\langle F^{>}_{\mathbf{k}} F^{>}_{-\mathbf{k}+\mathbf{q}} \right\rangle = \frac{\partial \omega_{\mathbf{k}}}{\partial \mathbf{k}} \cdot \frac{\partial}{\partial \mathbf{x}}\, I_{\mathbf{k}}(\mathbf{x},t) - 2\gamma_{\mathbf{k}} I_{\mathbf{k}}, \tag{A.9}$$

where $\gamma_{\mathbf{k}}$ is the linear growth rate and only the real part of the frequency is presumed for $\omega_{\mathbf{k}}$ on the right-hand side of (A.9).

The ensemble average in S_1 can be transformed by using the inverse of (A.5)

$$\left\langle F^{>}_{-\mathbf{k}+\mathbf{q}} F^{>}_{\mathbf{k}-\mathbf{p}} \right\rangle = \left\langle F^{>}_{\mathbf{k}-\mathbf{p}} F^{>}_{-(\mathbf{k}-\mathbf{p})+\mathbf{q}-\mathbf{p}} \right\rangle = \int d\mathbf{x}' I_{\mathbf{k}-\mathbf{p}}(\mathbf{x}') e^{-i(\mathbf{q}-\mathbf{p})\cdot\mathbf{x}'}. \tag{A.10}$$

By using (A.10) and expanding in $p \ll k$, the expression for S_1 is transformed to

$$S_1 = \int d\mathbf{p}\, e^{i\mathbf{p}\cdot\mathbf{x}} M_{\mathbf{p},\mathbf{k}-\mathbf{p}} \left(I_{\mathbf{k}}(\mathbf{x}) - \mathbf{p}\cdot\frac{\partial I_{\mathbf{k}}(\mathbf{x})}{\partial \mathbf{k}} \right) F^{<}_{\mathbf{p}}. \tag{A.11}$$

Similarly, by using the identity analogous to (A.10) and expanding the interaction coefficient $M_{\mathbf{p},\mathbf{q}-\mathbf{k}-\mathbf{p}}$ in $q-p \ll k$, we transform S_2 to the form

$$\begin{aligned} S_2 &= \int\int d\mathbf{p}\, d\mathbf{q}\, e^{i\mathbf{q}\cdot\mathbf{x}} \left(M_{\mathbf{p},-\mathbf{k}} + (\mathbf{q}-\mathbf{p})\cdot\frac{\partial M_{\mathbf{p},-\mathbf{k}}}{\partial(-\mathbf{k})} \right) F^{<}_{\mathbf{p}} \int d\mathbf{x}'\, e^{-i(\mathbf{q}-\mathbf{p})\cdot\mathbf{x}'} I_{\mathbf{k}}(\mathbf{x}') = \\ &= I_{\mathbf{k}}(\mathbf{x}) \int d\mathbf{p}\, e^{i\mathbf{p}\cdot\mathbf{x}} M_{\mathbf{p},-\mathbf{k}} F^{<}_{\mathbf{p}} - i\int d\mathbf{p}\, e^{i\mathbf{p}\cdot\mathbf{x}} \frac{\partial M_{\mathbf{p},-\mathbf{k}}}{\partial(-\mathbf{k})} \cdot \frac{\partial I_{\mathbf{k}}}{\partial \mathbf{x}} F^{<}_{\mathbf{p}}. \end{aligned} \tag{A.12}$$

Combining expressions (A.11) and (A.12), one obtains

$$\begin{aligned} S_1 + S_2 &= I_{\mathbf{k}}(\mathbf{x}) \int d\mathbf{p}\, e^{i\mathbf{p}\cdot\mathbf{x}} \left(M_{\mathbf{p},\mathbf{k}-\mathbf{p}} + M_{\mathbf{p},-\mathbf{k}} \right) F^{<}_{\mathbf{p}} - \\ &- \int d\mathbf{p}\, e^{i\mathbf{p}\cdot\mathbf{x}} M_{\mathbf{p},\mathbf{k}-\mathbf{p}} \mathbf{p}\cdot\frac{\partial I_{\mathbf{k}}(\mathbf{x})}{\partial \mathbf{k}} F^{<}_{\mathbf{p}} - \\ &- i\int d\mathbf{p}\, e^{i\mathbf{p}\cdot\mathbf{x}} \frac{\partial M_{\mathbf{p},-\mathbf{k}}}{\partial(-\mathbf{k})} \cdot \frac{\partial I_{\mathbf{k}}}{\partial \mathbf{x}} F^{<}_{\mathbf{p}}. \end{aligned} \tag{A.13}$$

Using (A.2), we obtain

$$M_{\mathbf{p},\mathbf{k}-\mathbf{p}} + M_{\mathbf{p},-\mathbf{k}} = \frac{i}{B(1+\psi)} \mathbf{p} \times \mathbf{e}_z \cdot \mathbf{k} \frac{4\mathbf{k}\cdot\mathbf{p}}{k^2} p_y. \tag{A.14}$$

By making a Fourier transformation and using (A.14), the first term in (A.13) becomes

$$\begin{aligned} & I_{\mathbf{k}}(\mathbf{x}) \int (M_{\mathbf{p},\mathbf{k}-\mathbf{p}} + M_{\mathbf{p},-\mathbf{k}})\, d\mathbf{p}\; e^{i\mathbf{p}\cdot\mathbf{x}} F_{\mathbf{p}}^{<} = \\ & -\frac{1}{B(1+\psi)} \frac{\partial}{\partial \mathbf{x}} \left(\nabla \frac{\partial \overline{F}}{\partial y} \times \mathbf{e}_z \cdot \mathbf{k} \right) \cdot \frac{4\mathbf{k}}{k^2} I_{\mathbf{k}}. \end{aligned} \tag{A.15}$$

Similarly, the second term in (A.13) takes the form

$$-\int \mathbf{p} \cdot \frac{\partial I_{\mathbf{k}}(\mathbf{x})}{\partial \mathbf{k}} M_{\mathbf{p},\mathbf{k}-\mathbf{p}} d\mathbf{p}\; e^{i\mathbf{p}\cdot\mathbf{x}} F_{\mathbf{p}}^{<} = -\frac{1}{B(1+\psi)} \frac{\partial}{\partial \mathbf{x}} \left(\nabla \frac{\partial \overline{F}}{\partial y} \times \mathbf{e_z} \cdot \mathbf{k} \right) \cdot \frac{\partial I_{\mathbf{k}}}{\partial \mathbf{k}}, \tag{A.16}$$

and the last term in (A.13) transforms to

$$-i \int \frac{\partial M_{\mathbf{p},-\mathbf{k}}}{\partial(-\mathbf{k})} \cdot \frac{\partial I_{\mathbf{k}}}{\partial \mathbf{x}} d\mathbf{p}\; e^{i\mathbf{p}\cdot\mathbf{x}} F_{\mathbf{p}}^{<} = \frac{1}{B(1+\psi)} \frac{\partial}{\partial \mathbf{k}} \left(\nabla \frac{\partial \overline{F}}{\partial y} \times \mathbf{e}_z \cdot \mathbf{k} \right) \cdot \frac{\partial I_{\mathbf{k}}}{\partial \mathbf{x}}. \tag{A.17}$$

Finally, combining all terms and adding two identically equal to zero terms ($\sim \partial\omega_{\mathbf{k}r}/\partial\mathbf{x}$), we have

$$\begin{aligned} & \frac{\partial}{\partial t}\left(\left|\widetilde{F}_{\mathbf{k}}\right|^2\right) + \frac{\partial \omega_{\mathbf{k}r}}{\partial \mathbf{k}} \cdot \frac{\partial}{\partial \mathbf{x}}\left(\left|\widetilde{F}_{\mathbf{k}}\right|^2\right) - \\ - & \frac{\partial \omega_{\mathbf{k}r}}{\partial \mathbf{x}} \cdot \frac{\partial}{\partial \mathbf{k}}\left(\left|\widetilde{F}_{\mathbf{k}}\right|^2\right) - \frac{\partial \omega_{\mathbf{k}r}}{\partial \mathbf{x}} \cdot \frac{4\mathbf{k}}{k^2} \frac{\partial}{\partial \mathbf{k}}\left(\left|\widetilde{F}_{\mathbf{k}}\right|^2\right) + \\ + & \frac{\partial}{\partial \mathbf{k}}\left(\frac{1}{B(1+\psi)} \nabla \frac{\partial \overline{F}}{\partial y} \times \mathbf{e}_z \cdot \mathbf{k}\right) \cdot \frac{\partial}{\partial \mathbf{x}}\left(\left|\widetilde{F}_{\mathbf{k}}\right|^2\right) - \\ - & \frac{\partial}{\partial \mathbf{x}}\left(\frac{1}{B(1+\psi)} \nabla \frac{\partial \overline{F}}{\partial y} \times \mathbf{e}_z \cdot \mathbf{k}\right) \cdot \frac{4\mathbf{k}}{k^2} \left|\widetilde{F}_{\mathbf{k}}\right|^2 - \\ - & \frac{\partial}{\partial \mathbf{x}}\left(\frac{1}{B(1+\psi)} \nabla \frac{\partial \overline{F}}{\partial y} \times \mathbf{e}_z \cdot \mathbf{k}\right) \cdot \frac{\partial}{\partial \mathbf{k}}\left(\left|\widetilde{F}_{\mathbf{k}}\right|^2\right) = S_{\mathbf{k}}. \end{aligned}$$

Multiplying this equation by k^4 and combining the last two terms, we obtain the wave kinetic equation (3.34).